Semiconductors, Vol. 36, No. 8, 2002, pp. 837–840. Translated from Fizika i Tekhnika Poluprovodnikov, Vol. 36, No. 8, 2002, pp. 897–901.

ATOMIC STRUCTURE AND NONELECTRONIC PROPERTIES OF SEMICONDUCTORS

Measurements of Parameters of the Low-Temperature Molecular-Beam Epitaxy of GaAs

V. V. Preobrazhenskiĭ, M. A. Putyato, and B. R. Semyagin

Institute of Semiconductor Physics, Siberian Division, Russian Academy of Sciences, pr. Akademika Lavrent'eva 13, Novosibirsk, 630090 Russia

e-mail: pvv@isp.nsc.ru

Submitted December 24, 2001; accepted for publication December 28, 2001

Abstract—Phase diagrams of GaAs (001) surface structures were used to calibrate sensors of the substrate temperature and As flux in molecular-beam epitaxy systems. The sublimation temperature of amorphous layers of As adsorbed on GaAs was measured. It was shown that this temperature is constant and does not depend on the rate of substrate heating, layer thickness, or the degree of vacuum in the system. The sublimation temperature of amorphous As can be used as a reference point to calibrate the substrate temperature in the range of low growth temperatures. © *2002 MAIK "Nauka/Interperiodica".*

INTRODUCTION

The use of molecular-beam epitaxy (MBE) to grow GaAs layers with preset parameters requires accurate determination of the temperature of a substrate (T_s) and the flux density of As incident on the substrate. The problem of accurately measuring these parameters has existed since the inception of MBE, and it still remains urgent.

The widely used methods of measuring T_s (optical pyrometry and the use of a thermocouple that has no direct contact with a substrate) have a number of serious drawbacks. One of the major drawbacks of optical pyrometry is that it can be used only in a limited temperature range. Commercial infrared (IR) pyrometers make it possible to reliably measure temperatures no lower than 400°C [1]. In addition to this, the accuracy of IR pyrometers depends on how accurately the emissivity of the object of measurement is determined. Therefore, in order to increase the accuracy of pyrometric measurements, the measuring instruments should be systematically calibrated.

One of the drawbacks of the thermocouple method is the significant difference between thermocouple readings and actual substrate temperatures. This difference can be as large as 150°C [2]. Therefore, as in the case of pyrometry measurements, a thermocouple should be calibrated in order to accurately measure the substrate temperature.

In order to calibrate thermocouples and IR pyrometers, reliably determined temperatures of some processes are used. Among these are (1) the melting of substances deposited on the substrate surface (for example, the melting temperatures T_m of InSb and In are 525 and 163°C, respectively) and (2) the formation of eutectics Al–Si (at 577°C) and Al–Ge (at 424°C). However, this technique cannot be used under the conditions of radiative heating of a substrate. There is an increase in light absorption in areas where substances are deposited, which results in significant local overheating of the substrate [3]. Most often, the temperature at which an oxide layer evaporates from a GaAs substrate is used to calibrate T_s. Before carrying out MBE, it is necessary to thermally clean the substrate surface. The process of thermal cleaning is monitored by reflection high-energy electron diffraction (RHEED). This makes it possible to calibrate each substrate. One of the drawbacks of this technique is the heavy dependence of the sublimation temperature of the oxide on the method of its formation and on the period of time during which the oxidized substrate is stored. The oxide sublimation temperature can range from 515 to 640°C [3, 4].

Recent intensive studies of GaAs grown at low (below 300°C) temperatures (*LT* GaAs) have revealed another drawback that is inherent to all the above-mentioned methods. Namely, none of these methods makes it possible to accurately determine T_s in the temperature region below 350°C.

A flux of As in any MBE system is commonly monitored by a vacuum ionization gauge. However, it is a rather difficult task to derive the values of flux density from ionization gauge readings. Therefore, the value of the equivalent pressure in an As flux is usually reported in the literature, rather than the value of the flux itself.

In this study, we suggest a method for evaluating both the As flux incident on a growth surface and the T_s value in MBE systems. The proposed method is based on phase diagrams (PDs) of GaAs (001) surface structures (SSs). It is shown that the temperature of sublimation of amorphous As from the substrate surface is 250 ± 2°C. This value is constant and can be used as a reference point to determine the substrate temperature in the temperature range below 350°C.

1063-7826/02/3608-0837$22.00

Table 1. Expressions used to describe the position of boundaries in the static PD of a GaAs (001) surface

Transition	Expression
$c(4\times4) \longleftrightarrow (2\times4)$	$J_{As4} = 5.25\times10^{34}\exp(-3\times10^5/8.31T_s)$
$(2\times4) \longleftrightarrow (3\times1(6))$	$J_{As4} = 8.25\times10^{34}\exp(-3.5\times10^5/8.31T_s)$
$(3\times1(6)) \longleftrightarrow (4\times2)$	$J_{As4} = 7.25\times10^{31}\exp(-3.19\times10^5/8.31T_s)$

Note: J_{As4} is the As_4 flux density (molecules cm^{-2} s^{-1}); T_s is the substrate temperature (in K).

Table 2. Expressions used to describe the position of boundaries in the dynamic PD of a GaAs (001) surface

Growth rate of GaAs, monolayers/s	Boundary between SSs	Expression
0.95	$c(4\times4) \longleftrightarrow (2\times4)$	$J_{As4} = 5.25\times10^{34}\exp(-3\times10^5/8.31T_s)$ $+1.47\times10^{14}\times180\exp(-2.5\times10^4/8.31T_s) + 1.47\times10^{14}$
0.95	$(2\times4) \longleftrightarrow (3\times1(6))$	$J_{As4} = 8.25\times10^{34}\exp(-3.5\times10^5/8.31T_s)$ $+1.47\times10^{14}\times75\exp(-2.5\times10^4/8.31T_s) + 1.47\times10^{14}$
0.95	$(3\times1(6)) \longleftrightarrow (4\times2)$	$J_{As4} = 7.25\times10^{31}\exp(-3.19\times10^5/8.31T_s)$ $+1.47\times10^{14}\times50\exp(-2.5\times10^4/8.31T_s) + 1.47\times10^{14}$

Note: J_{As4} is the As_4 flux density (molecules cm^{-2} s^{-1}); T_s is the substrate temperature (in K).

DETERMINATION OF ARSENIC FLUX AND SUBSTRATE TEMPERATURE USING SURFACE PHASE DIAGRAMS OF GALLIUM ARSENIDE (001)

The PD of a GaAs (001) surface subjected to MBE shows areas where SSs exist. The position of boundaries between SSs depends only on T_s and the densities of incident fluxes. This makes it possible to use the PD of the GaAs (001) surface to calibrate sensors of temperature and As flux in MBE systems.

Let us consider how to determine the T_s and the As flux density using PDs of GaAs (001).

We previously obtained [5] static PDs (for the case when only an As flux is incident on the surface) and dynamic PDs (both As and Ga fluxes are incident) using direct measurements of the substrate temperature and incident fluxes. The position of boundaries between SSs in the static and dynamic PDs can be described by expressions obtained in [5]. These expressions are listed in Tables 1 and 2 for static and dynamic (the growth rate is 0.95 monolayers/s) PDs, respectively.

The As flux can be monitored either by the position of a shutoff valve (if a valve source of As is used) or by readings of an ionization vacuum gauge. The gauges are either installed on the walls of the vacuum chamber or clamped on manipulators and thus can be placed in the As flux. In any case, there is a relation between the As flux and the valve position or the readings of the vacuum gauge. The problem is how to derive this relation. The same problem arises when T_s is measured: it is necessary to determine the relation between temperature sensor readings and actual substrate temperatures. The value of T_s can be monitored by a pyrometer and/or a thermocouple at the substrate heater (the value of a current passed through the heating element can also be used if there is no thermocouple).

In order to determine these relations for any MBE system, the phase diagram of the GaAs (001) surface should be plotted on the basis of experimental data. The measured values of the As flux density and T_s should be plotted on the axes. A GaAs substrate can be mounted on the manipulator heater in any convenient way. In order to increase the calibration accuracy, the location of boundaries between all SSs on the static PD should be determined for as wide a range as possible for As flux densities and T_s values. In the case of the dynamic PD, it is sufficient to determine the location of the boundary between any two SSs and one value of the growth rate. By rescaling the *X* and *Y* axes, the obtained PDs can be unambiguously related to the PDs plotted using the expressions from Tables 1 and 2. This makes it possible to determine the relations between the readings of sensors of flux density and temperature and the actual values of these quantities.

Figure 1 shows an example of bringing into correspondence the SSs obtained for a Katun' MBE system with SSs, which was plotted using the expressions from Tables 1 and 2. A thermocouple (that was not in direct contact with a substrate) was used to measure T_s. The As flux was measured from the position of the As source valve.

When the size of a substrate and the method of its mounting change, the thermal parameters of the holder–heater system change as well. This requires the recalibration of T_s. It is much easier to make a new calibration when the relation between the readings of a vacuum gauge and the actual values of As flux are known. In this case, it is sufficient to determine the transition temperature for one pair of SSs in the static PD

(for one known value of As flux) and then to correct the calibration of T_s using this point. The use of several such points increases calibration accuracy.

Thus, the method of phase diagrams can be used to determine the As flux density and T_s in growth chambers of MBE systems, including those that have no sensors for directly measuring these parameters. The values of T_s and As flux density can be determined by this method with an error of ±10°C and ±20%, respectively.

The authors of [6] suggested using the temperatures of transitions between SSs on GaAs (100) as reference points for the calibration of thermocouples. It was found that, if a substrate is heated at a rate of 1 K/min, the transitions between SSs from $c(4 \times 4)$ to (2×3), from (2×3) to (2×4), from (2×4) to (3×6), and from (3×6) to (4×2) occur at T_s = 354, 395, 500, and 549°C, respectively. This technique has the following significant advantages: the method of heating (radiative or conductive) does not affect the transition temperature; there is no need to deposit other substances on the substrate surface; each substrate can be calibrated before the growth; and the RHEED technique (conventional for MBE systems) can be used to observe transitions. One of the drawbacks of the suggested technique is the influence of the rate of substrate heating on the transition temperature, which was observed in [5]. Modern tools for heating control make it possible to easily maintain the preset heating rate; therefore, the temperatures of transitions between SSs in the absence of incident fluxes can be used for the rapid determination of T_s.

DETERMINATION OF THE TEMPERATURE OF SUBLIMATION OF AMORPHOUS ARSENIC FROM THE SUBSTRATE SURFACE

Passivation of surfaces of structures by depositing layers of amorphous As on them is widely used in the production of semiconductor devices (see, for example, [7]). Many authors reported the value of 250°C as the temperature of sublimation of an amorphous As layer from the substrate surface. This fact, together with the simplicity of deposition of amorphous As layers on substrates in III–V MBE systems, prompted us to study the sublimation of amorphous As from the surface of GaAs in order to use the value of the sublimation temperature for the calibration of T_s in the temperature range below 350°C.

Experiments were carried out in an updated PMA-12 (Shtat) MBE system. Semi-insulating GaAs (001) substrates were used. The surface condition and the processes of deposition and sublimation of amorphous As were monitored by RHEED.

The substrate was mounted on a special-type holder (Fig. 2). A thermocouple, mounted on the holder, was in good thermal contact with the substrate. The latter was installed on a massive Mo base using indium. In accordance with the data reported in [8], the difference in the temperatures of the thermocouple and substrate was less than 0.2°C.

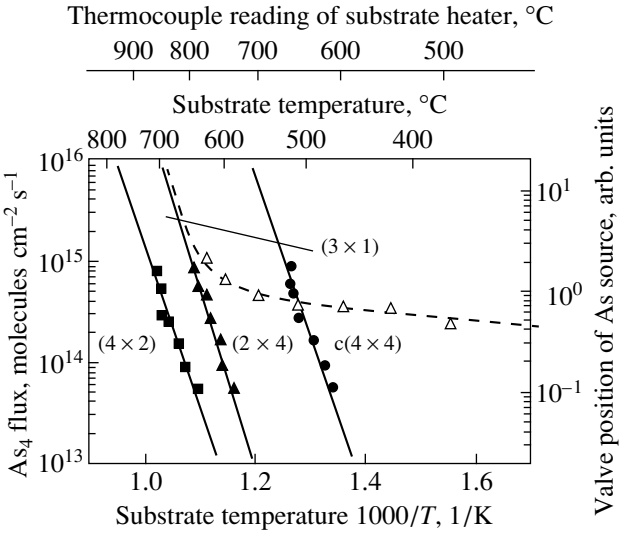

Fig. 1. Correlation between a PD of GaAs (001), obtained in experiments in a Katun MBE system, and a PD, plotted with the use of expressions from Tables 1 and 2. Dots, squares, and triangles mark experimentally obtained boundaries between SSs; solid lines indicate the boundaries between SSs, which were plotted using expressions listed in Table 1; and the dashed line indicates the boundary between (3×1) and (2×4) SSs, which was plotted using an expression from Table 2.

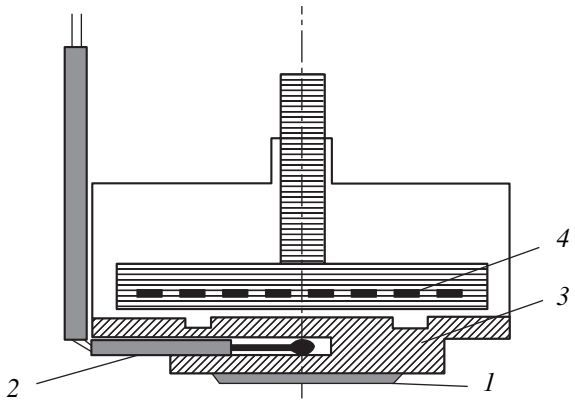

Fig. 2. Layout of a system for temperature measurements, including (*1*) substrate, (*2*) thermocouple, (*3*) Mo holder, and (*4*) heater.

In all experiments, in order to obtain an atomically smooth surface, a buffer GaAs layer of thickness in the range of 0.1–0.5 μm was grown on the GaAs substrate. After the buffer layer was grown, the substrate was cooled to 50–80°C in As_4 vapor. After that, the superstructure disappeared but clear strands of main reflexes remained. Then, the cracking zone of the As source was heated to supply a flux of As_2 molecules to the substrate. We chose As_2 because its adsorption rate exceeds that of As_4 [9, 10]. The flux density was $2–8 \times 10^{15}$ molecules cm^{-2} s^{-1}. Under these conditions, a layer of amorphous As condensed on the substrate surface. In a

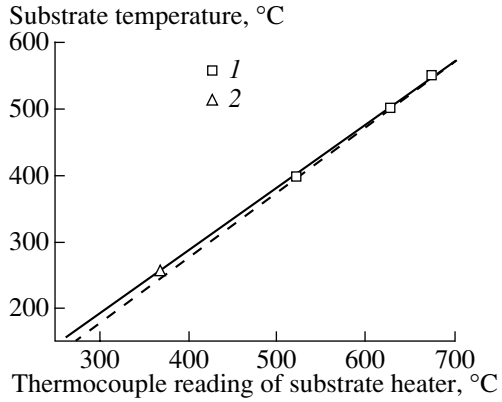

Fig. 3. Calibration curves for a thermocouple on a manipulator heater in a Katun MBE system; the curves were obtained from a PD of GaAs (001) (solid line) and from transitions between SSs without As flux and sublimation point of amorphous As (dashed line). Squares (*1*) correspond to the temperatures of transitions between SSs and a triangle (*2*) corresponds to the sublimation temperature of amorphous As.

period of 3–5 min, all features in the diffraction pattern disappeared and a uniform diffuse background arose which was stable in time. Then, the flux of As_2 molecules was switched off; the As source was cooled; and, after the pressure of residual gases in the growth zone was reduced to about 10^{-7} Pa, the substrate was heated. The sublimation temperature of As was determined from the appearance of diffraction features in the RHEED pattern. In the experiments, different exposure times of the substrates to As^2 vapor and different (from 4 to 20 K/min) heating rates were used. Under all experimental conditions, the sublimation temperature of As was constant and equaled 250 ± 2°C.

The fact that the sublimation temperature of As does not depend on the heating rate and layer thickness is probably caused by the phase transition that occurs at 250°C between amorphous (black) As and As in one of the crystalline phases (gray As). During this transition, the saturated-vapor pressure of As above the crystalline phase can greatly exceed that above the amorphous phase. This results in the fast sublimation of As from the substrate surface at 250°C. As is known, the phase transition between black and gray As occurs at 270°C under normal conditions [11]. The disagreement between the data in the literature and our results may be due to the fact that we determined the temperature of the phase transition in vacuum.

When radiative heating is used, the calibration of the temperature sensor should be carried out taking the following into account. The deposition of a thick (greater than 50 nm) layer of amorphous As on a substrate makes the substrate absorb radiation more intensively from the manipulator heater. This may result in a large error in determining T_s.

Figure 3 shows calibration curves for a thermocouple positioned on a substrate heater in a Katun' MBE system; these curve were obtained using either PDs (solid line) or transitions between SSs without an As flux or sublimation point of amorphous As (dashed line). The experiments were carried out on a GaAs (001) substrate mounted on a Mo holder with the use of In. As can be seen, there is good agreement between the calibration curves obtained by these two methods. Such agreement cannot be obtained in the low-temperature range without using the sublimation temperature of amorphous As. Therefore, the calibration obtained using transitions between SSs and the sublimation point of amorphous As can be used to determine T_s. Then, the sensor of the As flux can be calibrated using PDs of GaAs (001). In order to do this, it is sufficient to plot a boundary between two neighboring SSs in the static PD.

CONCLUSIONS

The results of this study show that the substrate temperature and As flux density in MBE systems can be determined using PDs of GaAs (001) surface structures. The substrate temperature can be measured with an error of ±10°C, while the As flux density can be measured with an error of ±20%. The sublimation temperature of amorphous As deposited on the surface of GaAs was measured. It was shown that this temperature is constant and does not depend on the heating rate, the thickness of the deposited layer, or the degree of vacuum in the MBE system. Therefore, this value can be used as a reference point to calibrate the substrate temperature in the region of low growth temperatures.

REFERENCES

1. S. L. Wright, R. F. Marks, and A. E. Goldberg, J. Vac. Sci. Technol. B **6**, 842 (1988).
2. R. Fernández, J. Cryst. Growth **116**, 98 (1992).
3. E. S. Hellman, P. M. Pitner, A. Harwit, *et al.*, J. Vac. Sci. Technol. B **4**, 574 (1986).
4. A. J. Spring Thorpe, S. J. Ingrey, B. Emmerstorfer, and P. Mandeville, Appl. Phys. Lett. **50** (2), 77 (1987).
5. V. V. Preobrazhenskii, M. A. Putyato, O. P. Pchelyakov, and B. R. Semyagin, J. Cryst. Growth **201/202**, 166 (1999).
6. V. V. Preobrazhenskiĭ, V. P. Migal', and D. I. Lubyshev, Poverkhnost', No. 9, 156 (1989).
7. N. J. Kawai, T. Nakagawa, T. Kojima, *et al.*, Electron. Lett. **20**, 47 (1984).
8. J. H. Neave and B. A. Joyce, J. Cryst. Growth **43**, 204 (1978).
9. V. V. Preobrazhenskii, M. A. Putyato, O. P. Pchelyakov, and B. R. Semyagin, J. Cryst. Growth **201/202**, 170 (1999).
10. B. S. Krusor and R. Z. Bachrach, J. Vac. Sci. Technol. B **1**, 138 (1983).
11. V. A. Rabinovich and Z. Ya. Khavin, in *Concise Chemical Handbook*, Ed. by A. A. Potekhin and A. I. Efimov (Khimiya, Leningrad, 1991), p. 432.

Translated by Yu. Sin'kov

Semiconductors, Vol. 36, No. 8, 2002, pp. 841–844. Translated from Fizika i Tekhnika Poluprovodnikov, Vol. 36, No. 8, 2002, pp. 902–906.

ATOMIC STRUCTURE AND NONELECTRONIC PROPERTIES OF SEMICONDUCTORS

Threshold of Inelastic Strain Formation in Si and GaAs Surface Layers under Multiple Pulsed Laser Irradiation

S. V. Vintsents*, A. V. Zoteev, and G. S. Plotnikov****

** Institute of Radio Engineering and Electronics, Russian Academy of Sciences (Fryazino Branch), pl. Vvedenskogo 1, Fryazino, Moscow oblast, 141120 Russia*

e-mail: alkeev@ms.ire.rssi.ru

*** Faculty of Physics, Moscow State University, Vorob'evy gory, Moscow, 119899 Russia*

Submitted January 16, 2002; accepted for publication January 16, 2002

Abstract—For the first time, a contactless local photoacoustic technique based on the spectroscopy of laser beam deviation was used to estimate maximal values of elastic shear strains φ_0 in micrometer-sized surface regions of Si and GaAs; the values obtained fall in the range of $10^{-5} < \varphi_0 < 10^{-4}$. The development of irreversible inelastic processes in the surface layers of semiconductors subjected to a series of focused laser pulses under photoinduced quasi-static strains $\varphi > \varphi_0$ is demonstrated. Studying the diffuse and Raman scattering of light near the thresholds φ_0 suggests that the early stage of the inelastic cyclic strain photoinduced in the surface layers is accompanied by the generation and spatial redistribution of point rather than extended defects (e.g., dislocations). A number of threshold values, such as the photoinduced increase in the temperature and the mean shear stresses that appear in the surface layers of Si and GaAs samples exposed to local submicrosecond radiation, are estimated. The physical nature of the low-threshold effects is discussed. © *2002 MAIK "Nauka/Interperiodica".*

INTRODUCTION

A variety of photoacoustic methods, including those involving totally reversible elastic strain of the surface [1, 2], for the nondestructive diagnostics of the surface layers of solids are well known. Along with this, special attention should be drawn to the controllable irreversible processes that can develop in inelastically strained irradiated surface layers of semiconductors. In our opinion, the most practically important of these processes are the laser-induced formation of point defects and, likely connected with this, the development of more sizable surface damage.

The most attractive aspect of the dosed laser effects is the possibility of controlling the photoinduced strain by varying a number of the parameters of pulsed laser radiation. As was previously shown [3–5], the pulse power fluences W suitable for such an effect range from the linear reversible photoacoustics region (the lower thresholds W_0) to the values that cause uncontrollable damage processes with an abrupt decrease in the reflectivity of the surface (the upper thresholds W_d). The number of pulses N used for the local laser-induced effects also plays an essential role.

The method of photothermal straining of the surface (PTSS) [2] was used to demonstrate that the multiple ($N \geq 10^6$) photoinduced inelastic strain of semiconductors (Ge, $In_{0.53}Ga_{0.47}As/InP$) [3, 4] and metals [3, 5] results in heavy local damage, in other words, catastrophes. At the final stage of damage under the action of a series of submicrosecond irradiations, microcraters as deep as several microns [6, 7] appear on the surface within a single-mode Gaussian spot (with the radius $\omega \approx 10$–100 μm) if the energy density W exceeds a relatively small threshold value $W_0 \approx 0.1$ J/cm^2. It should be noted that, at $N > 10^6$, in the conditions of a "size" effect [8, 9], the thresholds W_0 and W_d are close to each other [3] and the range of W values that are suitable for the controllable inelastic processes is narrow.

It is natural that, in order to clarify the mechanisms behind the photoinduced catastrophes, one should study the initial (rather than the final) surface changes, which occur long before the visible sites of damage appear at the surface, i. e., far from the thresholds W_d. The results of such studies may be of use for scanning laser microscopy of semiconductor materials and structures, for the analysis of the low-threshold degradation of semiconductor devices operating in the mode of pulse-repetitive local Joule heat release, as well as in cases when strains and thermal stresses appear in semiconductor microwave structures operating in the millimeter wavelength region [10, 11].

The initial stages of inelastic photoinduced strains in semiconductors (at $W \approx W_0$ and $N \leq 10^3$) were investigated by electrical (field effect) [12] and optical (photoluminescence of the adsorbed molecules, light scattering) [13] methods. In the vicinity of the elasticity deformation thresholds $\varphi_0(W_0) \equiv (dU_z/dr)_{max}$, where U_z is the normal displacement of the surface and r is the distance from the center along the beam radius [2], a considerably enhanced point defect formation was dis-

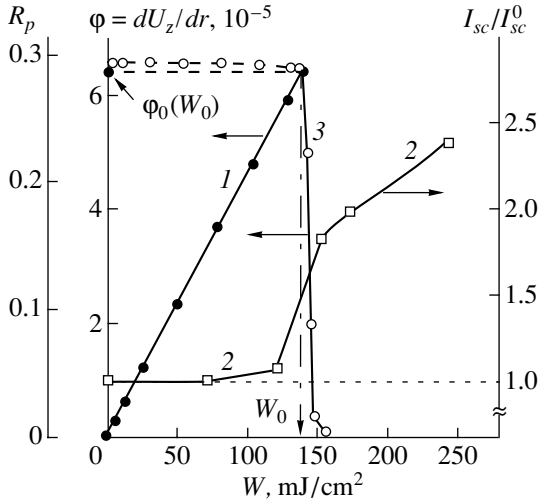

Fig. 1. For Si samples, *W*-dependences of (*1*) elastic photoinduced strain $\varphi = (dU_z/dr)_{max}$, (*2*) the intensity of diffuse-scattered light I_{sc}/I_{sc}^0 normalized to the scattering intensity I_{sc}^0 at $W = 0$, and (*3*) specular reflectance of the probe beam R_p in PTSS method.

covered at the actual germanium surfaces near the Ge/GeO_2 interfaces [12, 13].

This study contributes to the investigation of the initial stages of microplasticity in semiconductors; in particular, the lower thresholds W_0 of inelastic strain formation in the Si and GaAs surface layers are measured by PTSS technique, as well as by the diffuse and Raman scattering (RS) methods.

EXPERIMENTAL

As experimental samples, we used (111)-faced high-resistivity ($\rho \approx 2$–4 kΩ cm) dislocation-free *n*-Si single crystals doped with phosphorus and Gunn-type n–n^+-GaAs structures consisting of a 2.4-μm-thick film with an electron concentration $n \approx 10^{16}$ cm^{-3}. The crystals were grown by liquid-phase epitaxy on the (100) surface of a heavily doped ($n^+ \approx 10^{18}$ cm^{-3}) substrate with a thickness of ~250 μm. The GaAs surfaces were preliminarily cleaned [7]; the silicon samples were etched in a CP-4 fluorine-containing etchant [14].

Similarly to [12, 13], the scanning laser beam ($\lambda = 0.53$ μm, $2\omega \approx 70$ μm, $\tau \approx 0.4$–0.5 μs) was incident on the ~(20 × 5 × 0.25)-mm sample surfaces and produced irradiation zones corresponding to different energy densities at the center of the incident laser beam W [mJ/cm^2] = $E/\pi\omega^2$, where E is the total energy of the pulse. After that, each zone (with an area of ≈5 × 3 mm^2) obtained through scanning and characterized by a certain number of irradiation events $N \le 10^3$ was studied by Raman and diffuse scattering of light methods according to the technique outlined in [13]. Furthermore, the PTSS method [2–4] was used to measure the *W*-dependences of the intensity of a probing beam reflected specularly from the semiconductor surface and the maximal (in time *t* and along the radius *r* of the beam) elastic surface strains $\varphi = (dU_z/dr)_{max}$, which attained their maximums φ_0 [3] at the thresholds W_0.

RESULTS AND DISCUSSION

As an example, Fig. 1 presents the results of studying the Si samples by PTSS and diffuse scattering of light methods. Similar to the case with Ge [12, 13], at small *W* such that $W < W_0 \approx (130$–$140)$ mJ/cm^2, one can easily notice the existence of an elastic (or quasi-elastic) range of the irradiation dose at which the quasi-static (slow) strains $dU_z/dr(r, t)$ induced at the semiconductor surface are still reversible (up to $N \ge 10^8$ [2, 3]) and increase almost linearly with *W* up to the threshold $\varphi_0 \approx 6.5 \times 10^{-5}$ (Fig. 1, curve *1*). The diffuse component of the scattered light remains constant and relatively small (≈10^{-3}) since the defect-formation processes in the elastic strain range considered (corresponding to the linear photoacoustics $W < W_0$) still have a low efficiency [1–3] (Fig. 1, curve *2*). Upon exceeding the threshold strain $(dU_z/dr)_{max} > \varphi_0(W_0)$, the development of inelastic processes sets in at the Si (and GaAs) surface layers and, similar to the case of Ge [3, 13], at $N > 10^6$ and the threshold values W_d, an abrupt drop of the reflectivity R_p occurs, thus indicating a rapid degradation of the surface-layer structure (Fig. 1, curve *3*).

The relatively smooth rather than abrupt growth of the diffusive scattering at $W > W_0$ is worth noting (Fig. 1, curve *2*). Such behavior of the scattering intensity may be associated, as in the case of Ge [13], with a gradual accumulation of microplastic changes at the initial stages ($N \le 10^3$) of the inelastic photoinduced strain. Note in this context that the shape of curves *2* and *3* in Fig. 1 near the thresholds W_0 primarily depends on whether the initial (curve *2*, $N \le 10^3$) or the final (curve *3*, $N > 10^6$) stages of the inelastic change are considered.

A possible origin of the above-mentioned distinctions is illustrated by Fig. 2, from which it is seen that, at $N \le 10^3$, a considerable energy gap should exist between the lower threshold of inelastic strain W_0 and the energy density W_d corresponding to profound surface damage. In this case, at the energy densities within the range $W_0 < W < W_d$, one should expect fairly smooth (and, hence, controllable) changes in the characteristics of the modified layer (Fig. 1, curve *2*). In the other mode, when $N > 10^6$–10^7, the transition from an elastic (W_0) to a damaging (W_d) action should be rather sharp, implying the fast development of considerable changes at $W > W_0$ (Fig. 1, curve *3*). The distinctions indicated above can be attributed to the known phenomenon of a decrease in the values W_d with *N* and their asymptotic approach to the lower thresholds W_0 at $N \longrightarrow \infty$ [3, 6, 8, 9, 15] (Fig. 2).

As a result of the Raman studies on the silicon samples subjected to laser radiation with an energy density

in the range $W \approx (10–250)$ mJ/cm^2 < W_d, we obtained a Raman line with a nearly constant spectral position $\nu \approx 520$ cm^{-1} and a half-width $\nu_{1/2} \approx 4$ cm^{-1}, both corresponding to those of the optical phonons of single-crystal Si with low dislocation density. At constant parameters ν and $\nu_{1/2}$, an increase in the Raman line intensity did not start until $W \geq 240$ mJ/cm^2. Note that one result of the intensive generation of dislocations in silicon would be a considerable broadening of the Raman signals due to the influence of the local inhomogeneous fields of compression and tension, which are necessarily present near the extended defects [16]. In our case, the absence of such a broadening of the Raman signal supports the conclusion previously suggested by the electrical [12] and luminescence [13] studies of germanium that, at the initial stage ($N \leq 10^3$) of the photoinduced inelastic strain and at a temperature below the brittle point, the main role in the modification of the semiconductor surface layer is played by point-defect formation and the redistribution of point rather than extended defects [15, 17].

The table lists the values of φ_0 and W_0 measured for Si, GaAs, and some other semiconductor materials and structures. Silicon proved to be the most stable against cyclic strain in the micrometer-thick ($\omega \approx 10–100$ μm) surface layer. It should be noted in this context that silicon features not only higher values of φ_0 and W_0 compared to those previously obtained for germanium [13], but also displays radically different behavior in its Raman spectra (see above). Recall that, in germanium, which has a significantly higher initial (at $W = 0$) concentration of defects [14, 17], a change in the Raman spectra was observed in both the elastic (quasi-elastic) and elastoplastic modes and, in line with the "vacancy pump" model [17], was associated [13] with the possibility of an effective cyclic migration of the point defects from the surface to inherent sinks (microinclusions, dislocation loops, nanopores). Such migration is apparently hampered in dislocation-free single-crystal silicon, which is characterized by a structure of greater perfection. According to our data, the changes in the Raman spectra are not directly related to the strain thresholds φ_0 and appear more readily (i.e., at lower W) in the surface layers with an initially higher concentration of defects. Note also that, apart from the inherent-defect factor, the presence of stressed interfaces in heterostructures (e.g., thin-film $In_{0.53}Ga_{0.47}As$/InP samples [3]) may also lead to a reduction in the strength of the active semiconductor layers (see table).

Along with the experimental values of the critical strains $\varphi_0 \equiv (dU_z/dr)_{max}$, the table also presents the maximal possible (attained at the threshold W_0) surface shear strains $\varphi_0' = U_0'/\omega$, where U_0' is the amplitude of the so-called "quasi-one-dimensional" normal displacements of the surface corresponding to conventional thermoelasticity and an ideal "instantaneous" (i.e., reproducing the laser pulse shape) surface heat source with a Gaussian distribution along the r axis, as

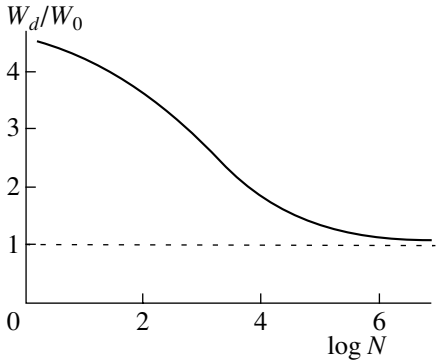

Fig. 2. Qualitative dependence of the threshold W_d (in W_0 units) in metals and semiconductors on the number of laser pulses N [3, 6, 8, 9, 15].

calculated by the method described in [5, 18] (variation of this technique for bulk characteristics can be found in [19, 20]). As one might expect [18], the quasi-one-dimensional configuration of the normal displacements is not realized in full measure in our experimental space-and-time conditions mainly due to the lateral (parallel to the surface) diffusion of heat; however, the estimates φ_0' (which are obviously larger than φ_0 [5] in the sense specified) comply with the experimental values φ_0 within one order of magnitude.

In view of the qualitative correlation obtained between φ_0' and φ_0, it turns out to be possible to estimate [3–5] the maximal values of the photoinduced local heating ΔT_{max} (at the center of the laser beam, at the inelastic strain threshold) and the mean shear stresses σ_0 that arise in the surface layers at the thresholds W_0 on the assumption of the ideal heat source specified above. The estimated maximal values are listed in the table. It should be emphasized that, at rather low (though inhomogeneous over the radial cross section of the beam) heating ΔT, the shear stress σ_0 in the surface layers attains several megapascals and, as was shown previously for germanium [12, 13], is sufficient to initiate point-defect generation near the insulator/semiconductor interfaces in a fairly thin (and, hence, low-strength) oxide layer on the actual semiconductor sample surfaces; i. e., the cyclic shear stresses $\sigma > \sigma_0$ can no longer be considered small in this context.

Thus, we applied a method of contactless photothermal surface strain (PTSS) [2, 3] to study the lower thresholds ($10^{-5} < \varphi_0 < 10^{-4}$) of inelastic strain initiation in silicon and gallium arsenide samples under the repetitive laser irradiation of their surface regions, which are micrometer-size. Silicon turned out to be the most resistant to pulsed periodic photoinduced shear strains and stresses (see table). Relatively low values of the local laser-induced heating $\Delta T_{max} \approx (10–100)$°C correspond to considerable shear stresses in the surface layers $\sigma_0 \geq (10^6–10^7)$ N/m^2, which can give rise to point-defect formation at the initial stage of the repetitive

Thresholds of the inelastic photoinduced strain formation in the surface layers of semiconductors under multiple local pulsed laser irradiation ($\lambda = 0.53$ μm, $\tau \approx 0.5$ μs, $N \geq 10^6$, $2\omega \approx 70$ μm)

Material	Thresholds				
	Experiment		Calculation		
	W_0, mJ/cm^2	$\varphi_0 \equiv (dU_z/dr)_{max}$	$\varphi_0' = U_0'/\omega$	ΔT_{max}, °C	σ_0, N/m^2
Si	130–140	6.5×10^{-5}	1.1×10^{-4}	50	4.0×10^6
GaAs	100–105	5.5×10^{-5}	9.7×10^{-5}	50	3.3×10^6
Ge*	65–70	4.7×10^{-5}	9.0×10^{-5}	30	2.0×10^6
$In_{0.53}Ga_{0.47}As/InP$	35–40	3.5×10^{-5}	–	–	–

Note: W_0 is the threshold energy density at the center of the incident beam, φ_0 is the maximal shear elastic strain, φ_0' is the threshold strain corresponding to the "quasi-one-dimensional" mode of the surface displacements [5, 18], ΔT_{max} is the maximal (at $W = W_0$) photoinduced heating of the semiconductor at the initial stage of inelastic changes, and σ_0 is the mean value of the threshold subsurface stresses. The data on Ge and $In_{0.53}Ga_{0.47}As/InP$ structures are reproduced from [3] for the sake of comparison.

($N \leq 10^3$) inelastic ($W > W_0$) deformation of the surface layer without producing additional heavy damage (the extended defects) in the crystal lattice. This is likely due to an increase in the concentration of the point defects produced and the development of instabilities [21], so that the further growth of W or N may result in the spatial redistribution of the point defects and their transformation into extended structures in the surface layer, which manifest themselves in the observed enhancement of the diffuse reflectivity of the surface. This gives evidence of the defect–deformation nature of the low-threshold phenomena that take place at the initial stage of the inelastic changes.

ACKNOWLEDGMENTS

S.V. Vintsents thanks V. E. Lyubchenko for valuable comments that contributed to the improvement of this paper.

REFERENCES

1. M. A. Almstead, N. M. Amer, S. Kohn, *et al.*, Appl. Phys. A **32**, 141 (1983).
2. S. V. Vintsents and S. G. Dmitriev, Zh. Tekh. Fiz. **67** (2), 105 (1997) [Tech. Phys. **42**, 216 (1997)].
3. A. G. Barskov and S. V. Vintsents, Fiz. Tverd. Tela (St. Petersburg) **36**, 2590 (1994) [Phys. Solid State **36**, 1411 (1994)].
4. S. V. Vintsents and S. G. Dmitriev, Pis'ma Zh. Tekh. Fiz. **21** (19), 1 (1995) [Tech. Phys. Lett. **21**, 767 (1995)].
5. S. V. Vintsents, S. G. Dmitriev, and O. G. Shagimuratov, Pis'ma Zh. Tekh. Fiz. **22** (8), 8 (1996) [Tech. Phys. Lett. **22**, 307 (1996)].
6. S. S. Cohen, J. B. Bernstein, and P. W. Wyatt, J. Appl. Phys. **71**, 630 (1992).
7. A. G. Barskov, S. V. Vintsents, G. G. Dvoryankina, *et al.*, Poverkhnost', No. 3, 79 (1995).
8. C. S. Lee, N. Koumvakalis, and M. Bass, Appl. Phys. Lett. **47**, 625 (1982); Opt. Eng. **22**, 419 (1983).
9. C. S. Lee, N. Koumvakalis, and M. Bass, J. Appl. Phys. **54**, 5727 (1983).
10. A. L. Polyakova, *Deformation of Semiconductors and Semiconductor Devices* (Énergiya, Moscow, 1979).
11. V. E. Lyubchenko, Radiotekhnika, No. 1, 87 (2000).
12. S. V. Vintsents, S. G. Dmitriev, R. A. Zakharov, and G. S. Plotnikov, Fiz. Tekh. Poluprovodn. (St. Petersburg) **31**, 513 (1997) [Semiconductors **31**, 433 (1997)].
13. S. V. Vintsents, V. B. Zaĭtsev, A. V. Zoteev, *et al.*, Fiz. Tekh. Poluprovodn. (St. Petersburg) **36** (8), 947 (2002) [Semiconductors **36**, 883 (2002)].
14. V. F. Kiselev, S. N. Kozlov, and A. V. Zoteev, *Basics of the Solid-Surface Physics* (Mosk. Gos. Univ., Moscow, 1999), Chap. 4.
15. B. L. Volodin, V. I. Emel'yanov, and Yu. G. Shlykov, Kvantovaya Élektron. (Moscow) **20**, 57 (1993).
16. I. I. Novak, V. I. Vettegren', and B. M. Tashpulatov, in *Proceedings of the II All-Union Conference "Spectroscopy of Raman Scattering", Moscow, 1978.*
17. V. P. Alekhin, *Physics of Strength and Plasticity of Surface Layers of Materials* (Nauka, Moscow, 1983).
18. S. V. Vintsents, S. G. Dmitriev, and K. I. Spiridonov, Fiz. Tverd. Tela (St. Petersburg) **39**, 2224 (1997) [Phys. Solid State **39**, 1985 (1997)].
19. *Tables of Physical Quantities*, Ed. by I. K. Kikoin (Atomizdat, Moscow, 1976).
20. Landolt-Börnstein: Numerical Data and Functional Relationships in Science and Technology, New Series (Springer-Verlag, Berlin, 1984), Group III, Vol. 17g.
21. V. I. Emel'yanov, Kvantovaya Élektron. (Moscow) **28**, 2 (1999).

Translated by A. Sidorova-Biryukova

Semiconductors, Vol. 36, No. 8, 2002, pp. 845–847. Translated from Fizika i Tekhnika Poluprovodnikov, Vol. 36, No. 8, 2002, pp. 907–909.

ATOMIC STRUCTURE AND NONELECTRONIC PROPERTIES OF SEMICONDUCTORS

Dissociation Energies of a C_iC_s Complex and the *A* Center in Silicon

N. I. Boyarkina*, S. A. Smagulova, and A. A. Artem'ev****

** Institute of Semiconductor Physics, Siberian Division, Russian Academy of Sciences, pr. Akademika Lavrent'eva 13, Novosibirsk, 630090 Russia*

*** Yakut State University, Yakutsk, 677891 Russia*

Submitted September 3, 2001; accepted for publication January 22, 2002

Abstract—Reactions of annealing of *A* centers (*V*O) and complex centers consisting of interstitial carbon atoms and substitutional carbon atoms (C_iC_s) in *n*-Si irradiated with fast electrons or ^{60}Co gamma quanta were analyzed. The kinetics of isochronous annealing of the above centers was evaluated. By comparing the results of calculations with published experimental data, which were obtained by measuring the concentration of centers with the level $E_c - 0.17$ eV in the course of isochronous heat treatment of irradiated *n*-Si, the dissociation energy *E* for the C_iC_s complex was estimated at 1.10 ± 0.05 eV. The activation energy for annealing of this center was found to be equal to $E_{aC_iC_s} \approx 2.0$ eV. The dissociation energy for the *A* center was estimated at $E_A = 1.94$ eV. © *2002 MAIK "Nauka/Interperiodica".*

The fabrication of silicon-based semiconductor devices is accompanied by a number of technological treatments, including irradiation. It is of interest to know the electrical parameters of defects introduced by irradiation into the silicon bulk.

When silicon is irradiated with fast electrons or ^{60}Co gamma quanta, electrically active defects are introduced into the crystal bulk. The most important of these defects are the complexes consisting of a silicon vacancy and either an oxygen atom *V*O (the *A* centers) or a donor *VD* (the *E* centers), divacancies (*VV*), or carbon-containing centers: interstitial carbon atoms C_i and the complexes composed of interstitial carbon and either substitutional carbon (C_iC_s) or interstitial oxygen (C_iO_i). The C_iC_s and *V*O complexes introduce acceptor levels in the vicinity of $E_c - 0.17$ eV, and, thus, it is difficult to differentiate between these complexes using electrical measurements. For example, the level at $E_c - 0.17$ eV that was observed by Vasil'ev *et al.* [1] was assumed to belong to the *A* center. The C_i and C_iC_s centers introduce the acceptor levels at $E_c - 0.12$ eV and $E_c - 0.16$ eV, respectively [2, 3].

According to Medvedeva *et al.* [4], radiation defects with a level at $E_c - 0.17$ eV are annealed out in two stages: at $T = 200$–240 and 300–380°C. The C_iC_s complexes and the *A* centers are annealed out at the first and second stages, respectively. The kinetics of annealing of the *A* centers was studied in detail by Svensson and Lindstrom [5]; the experimental data on the isothermal heat treatment of silicon irradiated with 2-MeV electrons were used to determine the activation energy for annealing of the *A* centers: $E_{aA} = 2.27$ eV.

In this study, we compared the results of calculating the kinetics of annealing of defects in silicon with experimental data that were obtained in the course of the isochronous heat treatment of *n*-Si irradiated with fast electrons or gamma quanta and we determined the dissociation energies for the C_iC_s complexes and *A* centers.

We first consider the annealing reaction for the C_iC_s complexes. We assume that the reaction proceeds via dissociation of the complex into its constituents with subsequent migration of the released interstitial carbon atom over the crystal; i.e.,

$$C_iC_s \xrightarrow{\nu_{C_iC_s}} C_i + C_s, \tag{1}$$

where $\nu_{C_iC_s}$ is the rate constant of this reaction. Thus, we have

$$\frac{dN_{C_iC_s}}{dt} = -\nu_{C_iC_s}N_{C_iC_s}, \tag{2}$$

where $N_{C_iC_s}$ is the concentration of complexes and *t* is time.

Boyarkina [6] suggested that it is possible to define the rate constant for the dissociation reaction of the C_iC_s complexes as

$$\nu_{C_iC_s} = \nu_0 \exp\frac{-E_{C_iC_s} - W^{el}_{C_iC_s}}{kT}, \tag{3}$$

where *k* is the Boltzmann constant, $E_{C_iC_s}$ is the dissociation energy for the C_iC_s complex, and $W^{el}_{C_iC_s}$ is the

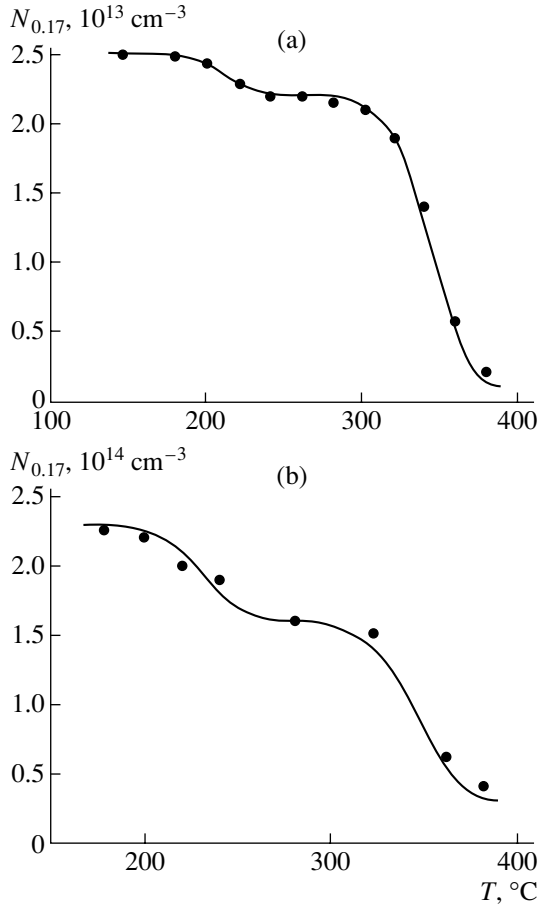

Fig. 1. Dependences of concentration of defects with a level at $E_c - 0.17$ eV on the temperature of a 30-min isochronous heat treatment of irradiated *n*-Si. The lines represent the results of calculations, and the dots correspond to experimental data [4]. (a) The phosphorus concentration is $N_P = 5 \times 10^{13}$ cm^{-3}, the oxygen concentration is $N_O = (6–9) \times 10^{17}$ cm^{-3}, and the carbon concentration is $N_C = (1–5) \times 10^{16}$ cm^{-3}; the sample was irradiated with ^{60}Co gamma quanta at room temperature (see Fig. 1 in [4]). (b) $N_P = 5 \times 10^{14}$ cm^{-3}, $N_O = (1–3) \times 10^{16}$ cm^{-3}, and $N_C \approx N_O$; the sample was irradiated with fast electrons at 0°C (see Fig. 3 in [4]).

energy contribution of the electronic subsystem of the crystal to the reaction rate,

$$W^{el}_{C_iC_s} = \varepsilon_{C_iC_s} f^-_{C_iC_s} - \varepsilon_{C_i} f^-_{C_i}. \quad (4)$$

Here, $\varepsilon_{C_iC_s} = 0.16$ eV and $\varepsilon_{C_i} = 0.12$ eV are the ionization energies for the C_iC_s and C_i centers in *n*-Si, respectively; and $f^-_{C_iC_s}$ and $f^-_{C_i}$ are the probabilities of finding these centers in the negatively charged state. The preexponential factor ν_0 in expression (3) is defined as (see formulas (1.30), (1.21), and (1.6) in [7])

$$\nu_0 = \theta D_{C_i} = \theta D_{0C_iC_s} \exp\frac{-W_{C_i}}{kT} = \nu_{0C_iC_s} \exp\frac{-W_{C_i}}{kT}. \quad (5)$$

Here, θ depends on the vibration frequency of the components of the complex and on its size and mass; D_{C_i} is the diffusion coefficient of the released carbon interstitial atom; and W_{C_i} is the activation energy for the migration of this atom. According to [8], $W_{C_i} = 0.87$ eV, whereas it was earlier stated that $W_{C_i} = 0.77 \pm 0.05$ eV [1].

Thus, we obtain the following expression for the rate constant of reaction (1):

$$\nu_{C_iC_s} = \nu_{0C_iC_s} \exp\frac{-E_{C_iC_s} - W^{el}_{C_iC_s} - W_{C_i}}{kT}. \quad (6)$$

The activation energy for annealing of C_iC_s complexes can be calculated as

$$E_{aC_iC_s} = E_{C_iC_s} + W^{el}_{C_iC_s} + W_{C_i}. \quad (7)$$

The kinetics of annealing for the *A* centers is defined by the following equation:

$$\frac{dN_A}{dt} = -\nu_{0A}\left(\exp\frac{-E_{aA}}{kT}\right)N_A. \quad (8)$$

The concentration of defects $D_{0.17}(N_{0.17})$, whose level is in the vicinity of $E_c - 0.17$ eV, is equal to the sum of concentrations of the C_iC_s ($N_{C_iC_s}$) complexes and the *A* centers (N_A). The kinetics of annealing of the $D_{0.17}$ defects is described by the equation

$$\frac{dN_{0.17}}{dt} = \frac{dN_{C_iC_s}}{dt} + \frac{dN_A}{dt}. \quad (9)$$

We determine the dissociation energy for the C_iC_s complex by comparing the calculated data on the kinetics of annealing of the $D_{0.17}$ defects with the data obtained in the experiments with isochronous heat treatment of *n*-Si irradiated with electrons or gamma quanta. As a result of this comparison, we determined the dissociation energy for the C_iC_s complex: $E_{C_iC_s} = 1.10 \pm 0.05$ eV

In Fig. 1, we show the dependences of $N_{0.17}$ on the temperature of the isochronous heat treatment of irradiated *n*-Si; these dependences were calculated by solving Eq. (9). It was assumed that the annealing of the C_iC_s center occurs by the decomposition of this center into the substitutional carbon C_s and interstitial carbon atom C_i, which migrates through the crystal with an energy of $W_{C_i} = 0.87$ eV. The dissociation energy for the C_iC_s center was assumed to be equal to 1.05 eV (Fig. 1a) and 1.13 eV (Fig. 1b). The annealing-activation energy for the *A* center was assumed to be equal to 2.27 eV. The dots represent the experimental data obtained using the isochronous heat treatment of *n*-Si irradiated with ^{60}Co gamma quanta (see Fig. 1a) and 4-MeV electrons (see Fig. 1b). Agreement between cal-

culated curves and experimental data supports the assumption that the dissociation energy for the C_iC_s complex is $E_{C_iC_s} = 1.10 \pm 0.05$ eV.

The activation energy $E_{aC_iC_s}$ for annealing of the C_iC_s center, on the assumption that this complex decomposes into its constituents (7), is equal to 1.10 + 0.87 + 0.02 = 1.99 eV ≈ 2.0 eV.

Knowing the activation energy for annealing of the *A* center E_{aA}, we can estimate the dissociation energy for this center E_A in the following manner. We assume that an *A* center is annealed out by decomposing into an interstitial oxygen atom O_i and a vacancy *V*, which migrates through the crystal; i.e.,

$$A \xrightarrow{\nu_A} O_i + V. \tag{10}$$

Then, similarly to (7), we have

$$E_{aA} = E_A + W_A^{el} + W_V. \tag{11}$$

Therefore,

$$E_A = E_{aA} - W_A^{el} - W_V, \tag{12}$$

where E_A is the dissociation energy for the *A* center;

$$W_A^{el} = \varepsilon_{V2} f_V^{--} + \varepsilon_A f_A^{-} \tag{13}$$

is the energy contribution of the electronic subsystem of the crystal to the rate of reaction (10); and

$$W_V = W_V^{--} f_V^{--} + W_V^0 f_V^0 \tag{14}$$

is the migration energy of the released vacancy. After simple algebraic transformations, we obtain

$$W_A^{el} = -0.39 \times 10^{-5} + 0.17 \times 3 \times 10^{-3}$$

$$= 0.51 \times 10^{-3} \text{ eV},$$

$$W_V = 0.18 \times 10^{-5} + 0.33 \times 1 = 0.33 \text{ eV},$$

$$E_A = 2.27 + 0.51 \times 10^{-3} - 0.33 = 1.94 \text{ eV}.$$

Thus, the dissociation energy for the *A* center is equal to $E_A = 1.94$ eV.

ACKNOWLEDGMENTS

We thank L.S. Smirnov, O.V. Naumova, and V.F. Stas' for their helpful participation in discussions.

This study was supported by the Russian Foundation for Basic Research, project no. 00-15-96801.

REFERENCES

1. A. V. Vasil'ev, V. I. Panov, S. A. Smagulova, and S. S. Shaĭmeev, Fiz. Tekh. Poluprovodn. (Leningrad) **21**, 573 (1987) [Sov. Phys. Semicond. **21**, 352 (1987)].
2. A. G. Litvinko, L. F. Makarenko, L. I. Murin, and V. D. Tkachev, Fiz. Tekh. Poluprovodn. (Leningrad) **14**, 776 (1980) [Sov. Phys. Semicond. **14**, 455 (1980)].
3. L. I. Murin, Phys. Status Solidi A **93**, K147 (1986).
4. I. F. Medvedeva, L. F. Makarenko, V. P. Markevich, and L. I. Murin, Izv. Akad. Nauk BSSR, Ser. Fiz.-Mat. Nauk, No. 3, 19 (1991).
5. B. G. Svensson and J. L. Lindstrom, Phys. Rev. B **34**, 8709 (1986).
6. N. I. Boyarkina, Fiz. Tekh. Poluprovodn. (St. Petersburg) **34**, 425 (2000) [Semiconductors **34**, 410 (2000)].
7. A. I. Baranov, A. V. Vasil'ev, V. F. Kuleshov, *et al.*, *Rate Constants of Reactions between Multiply Charged Centers in Semiconductors*, Preprint (Chernogolovka, 1985).
8. G. Davies, E. C. Lightowlerst, R. C. Newmant, and A. S. Oates, Semicond. Sci. Technol. **2**, 524 (1987).

Translated by A. Spitsyn

Semiconductors, Vol. 36, No. 8, 2002, pp. 848–851. Translated from Fizika i Tekhnika Poluprovodnikov, Vol. 36, No. 8, 2002, pp. 910–913.

ATOMIC STRUCTURE AND NONELECTRONIC PROPERTIES

Initial Stages of Growth of Diamond Island Films on Crystalline Silicon

N. A. Feoktistov*, V. V. Afanas'ev, V. G. Golubev*, S. A. Grudinkin*, S. A. Kukushkin***, and V. G. Melekhin***

** Ioffe Physicotechnical Institute, Russian Academy of Sciences, Politekhnicheskaya ul. 26, St. Petersburg, 194021 Russia*
e-mail: grudink@gvg.ioffe.rssi.ru
*** University of Leuven, Laboratory of Semiconductor Physics, B-3001 Leuven, Belgium*
**** Institute of Problems in Machine Science, Russian Academy of Sciences, Vasil'evskii ostrov, Bol'shoi pr. 61, St. Petersburg, 199178 Russia*
Submitted February 18, 2002; accepted for publication February 18, 2002

Abstract—The results of the investigation of the initial stages of growth of diamond island films, which were formed by hot-filament chemical-vapor deposition on optically polished crystalline silicon, are reported. Atomic force microscopy was used to study the evolution of islands, formed at the initial growth stages, during annealing. It was found that at the initial growth stages the island density changes due to the coalescence of closely spaced islands. Then, after the islands increase in size up to the critical value, Ostwald ripening of the islands sets in. *© 2002 MAIK "Nauka/Interperiodica".*

1. INTRODUCTION

In the last 20 years, considerable progress in the technique of growing diamond polycrystalline films by chemical-vapor deposition (CVD) has been attained [1]. The use of different modifications of CVD made it possible to form films with a high diamond-phase content on different substrates. Much attention is now being paid to the formation of diamond and diamond-like films on silicon substrates for field-emission cathodes [2]. As was noted in [3], diamond films grown on silicon substrates consist of hemispherical diamond islands of a few microns in size and have the highest emissivity and most uniform distribution of emissive centers. Since the field-emissive properties of films depend on their phase composition, surface density, and island size, the investigation of the growth mechanisms of island films is a necessary stage in the development of methods for manufacturing field-emission cathodes based on diamond films [4, 5].

It is worth noting that, in most studies of the initial stages of growth of diamond films on silicon, much attention was commonly paid to the effect of substrate pretreatment on the density of diamond nucleation centers [6] and to the phase composition of diamond nuclei [7, 8]. The mechanisms of interaction between islands have been virtually unexplored.

In order to determine the mechanisms of growth of diamond island films at the initial stages, we investigated the interaction between carbon islands on crystalline silicon using the technique suggested in [5]. We studied the evolution of the size and surface density of carbon islands, formed at the initial stages of diamond-film growth, during isothermal annealing in the absence of an external source of carbon.

2. EXPERIMENTAL

Diamond island films were formed by hot-filament chemical-vapor deposition (HFCVD) from a hydrogen–methane mixture [9] at 850°C. The content of methane, the gas pressure in the reactor, and the gas flow rate were 1%, 48 Torr, and 500 cm^3/min, respectively. The growth duration ranged from 15 to 30 min. Optically polished Si(100) substrates were used. In order to study the mass transport mechanism, films were annealed in an Ar flow at 850°C, i.e., at the same temperature at which HFCVD was carried out. In order to suppress evaporation of material from the substrate, the Ar pressure was chosen as 760 Torr. Annealing was carried out in a quartz cell; the annealing time ranged from 1 to 61 hours. Samples were temporarily extracted from the cell in order to carry out measurements, and then the annealing was continued.

The morphology of the film surface at the initial growth stages was analyzed using a Burleigh ARIS-3500 atomic-force microscope (AFM) with an ARIS-3005 scan module. We used the constant-force mode (a force of 5 pN was applied to the probe). In this mode, the vertical and horizontal resolutions were about 0.1 and 1 nm, respectively. The images of the diamond film surface were computer-processed using a software package that made it possible to determine the average island size and surface density. Raman spectra were recorded using a Ramanor U-1000 monochromator. An Ar laser

with a wavelength of 488 nm was used as a source of excitation light.

3. RESULTS AND DISCUSSION

The following stages of the heteroepitaxial growth of diamond films are commonly considered as the initial ones: incubation period, formation of diamond nuclei, final stage of nucleation, and incorporation of nuclei into crystallites [6].

During the incubation period, a set of carbon islands is formed on a substrate [4, 10]. It was shown in [11] that both islands consisting of sp^3 carbon (diamond phase) and islands consisting of sp^2 carbon (graphite phase) are present. During the growth, a structural phase transition from sp^2 carbon to sp^3 carbon is possible [12]. Since the size of the islands is less than the critical value, they are not stable. At the nucleation stage, diamond islands increase in size due to their coalescence, the adsorption of carbon from the gas phase, and the migration of carbon atoms over the substrate surface. When a diamond island reaches a critical size (i.e., the island becomes stable), it turns into a diamond nucleus [13]. During the next growth stage (final nucleation stage), the diamond nuclei increase in size and crystallize [6]. The authors of publications on HFCVD refer to the density of submicrometer islands at this growth stage as the density of diamond nucleation centers, suggesting that in the course of time these islands increase in size and form a continuous polycrystalline diamond film [4].

Figure 1 shows AFM images of C islands after 15-min growth, unannealed (Fig. 1a) and subjected to 61-h annealing (Fig. 1b). As can be seen, due to the annealing, the islands increase in size, their shape becomes smoother, and the density of islands decreases. Since AFM measurements do not make it possible to distinguish diamond from graphite and amorphous C, the phase composition of the observed islands remains unknown. At the same time, the complex use of different measurement methods (Raman spectroscopy and X-ray diffractometry) is not very effective during the initial growth stages because the thickness of the objects under investigation is small. Figure 2 shows the dependence of the average height and density of islands on the annealing time. As can be seen, the average island height ranges from 5 nm for an unannealed sample to 22 nm for a sample annealed for 61 hours. The surface density of islands decreased in the course of annealing from 3.5×10^9 to 1×10^9 cm^{-2}.

The experimental data indicate that the morphology of the film surface changes during the annealing as follows. At some initial moment (approximately after a 10-h annealing), the density of islands drastically decreases. Then, the density of islands decreases at a lower rate. Such behavior is typical of island films. Thus, at the initial moment, when the density of islands is high, they coalesce (merge), whereupon Ostwald rip-

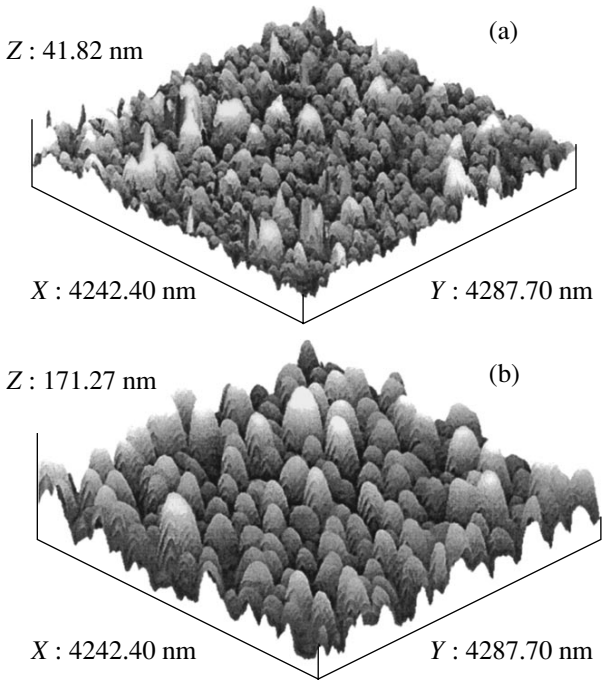

Fig. 1. AFM images of C islands formed after 15-min growth on a silicon substrate (a) before and (b) after annealing at 850°C for 61 h.

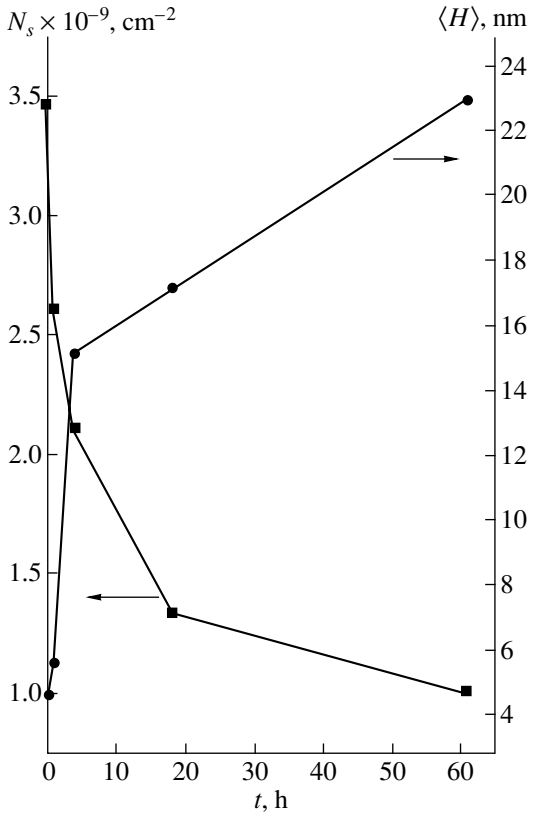

Fig. 2. Surface density N_s and average height $\langle H \rangle$ of C islands (growth time is 15 min) as functions of annealing time.

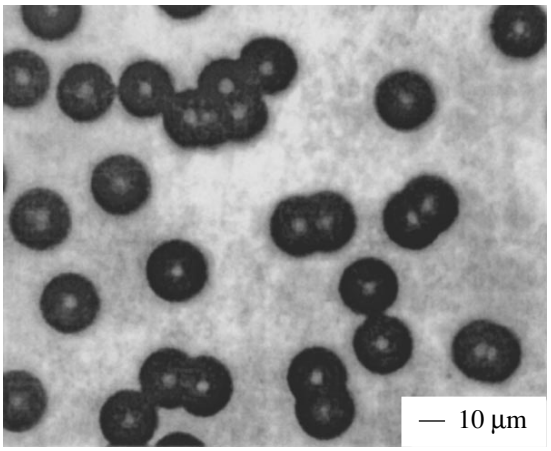

Fig. 3. Optical microscopy image of diamond island film after 8-h growth.

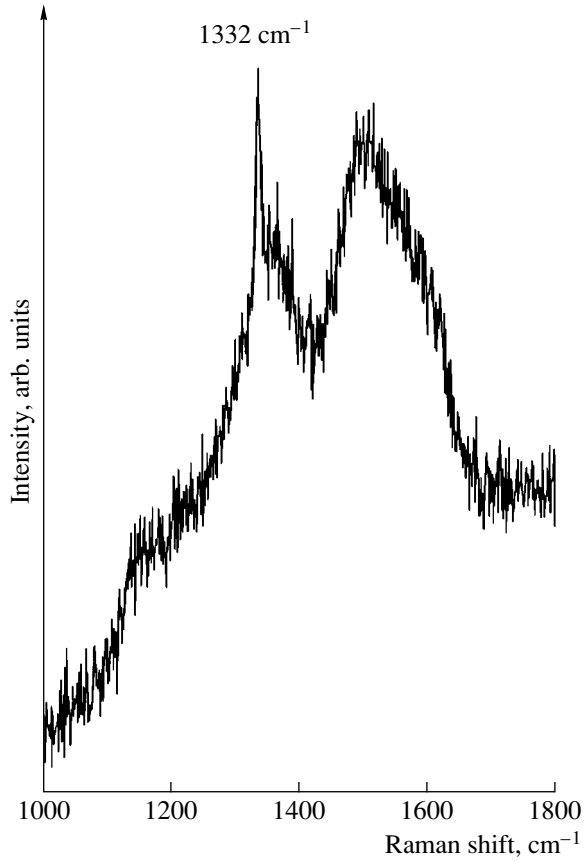

Fig. 4. Raman spectrum of diamond island film after an 8-h growth.

ening (OR) of islands sets in. This dependence of the density of islands on the annealing time is in good agreement with the data reported in [5]. The essence of OR is that the islands, forming a set, interact with each other via a generalized diffusion field. The islands whose radii exceed some critical value increase in size in the generalized field, while those with radii below the critical value dissolve. Under the OR, a universal distribution of islands over their sizes arises. If the system in which OR occurs contains several phases or different chemical compounds with common components, not only does relaxation of the excess surface energy occur but there is also evolution of the phase composition of the islands. The islands of thermodynamically stable phases increase in size, absorbing material from less stable compounds.

The authors of [5] developed a theory that made it possible to plot phase diagrams of island films formed during OR. However, in order to carry out a quantitative comparison between predictions based on theory and experimental data, it is necessary to know the exact values for a number of constants, such as the coefficient of diffusion of C atoms over the substrate surface and the equilibrium concentration of C atoms on the substrate. Consequently, we have omitted this issue in this publication.

In order to determine the morphology of the diamond-film surface after the formation of micrometer-size islands (Fig. 3), we also investigated diamond films using optical microscopy. After an 8-h growth, separately positioned diamond particles shaped as hemispherical segments were observed on the silicon substrate. The diameter of the particles was about 30 μm, they were virtually monodisperse, and their surface density was on the order of 10^5 cm^{-2}. Thus, the concentration of islands after the 8-h growth was 4 orders of magnitude lower than that of C islands after the 15-min growth. Such a difference indicates that not all islands that formed after the 15-min growth serve as diamond nucleation centers, in spite of the fact that, as was shown in [4], the density of nanosized diamond islands considerably exceeds that of micrometer-sized ones. Since, after 8 hours of growth, islands are located at a large distance from one another, they virtually do not interact via the generalized diffusion field and grow separately from each other.

The Raman spectrum of an island film after the 8-h growth (Fig. 4) contains a 1332-cm^{-1} peak, which is indicative of a rather high content of the diamond phase in the film [14]. A broad peak located at about 1580 cm^{-1} is related to sp^2 C. An analysis of the areas between the micron-sized islands showed that these areas contain nanosized islands. It seems likely that these nanosized islands contain a considerable amount of sp^2 C and that their contribution to the 1580-cm^{-1} peak in the Raman spectrum is the largest.

4. CONCLUSION

An explanation has been suggested for changes in the size and surface density of C islands at the early stages of growth of diamond films. It was shown that changes in the size and surface density of islands during the initial growth stages occur due to coalescence. After

islands attain a critical size, their growth is governed by Ostwald ripening.

ACKNOWLEDGMENTS

We thank A.Ya. Vul for helpful discussions.

This study was supported by the Russian research program "Fullerenes and Atomic Clusters" ("Film-2" project, no. 98059), and by the Linkage NATO HT (grant no. 973290).

REFERENCES

1. S. Shikata, MRS Bull. **23** (9), 61 (1998).
2. X. L. Peng, Thin Solid Films **372**, 292 (2000).
3. C.-F. Chen and W.-H. Huang, Thin Solid Films **308**, 85 (1997).
4. T. Lin, K. P. Loh, A. T. S. Wee, *et al.*, Diamond Relat. Matter. **9**, 1703 (2000).
5. S. A. Kukushkin and V. V. Slezov, *Disperse Systems on Solid Surface* (Nauka, St. Petersburg, 1996).
6. H. Liu and D. S. Dandy, Diamond Relat. Mater. **4**, 1173 (1995).
7. B. R. Stoner, G.-H. M. Ma, S. D. Wolter, and J. T. Glass, Phys. Rev. B **45**, 11067 (1992).
8. K. Komvopoulos and T. Xu, Diamond Relat. Mater. **9**, 274 (2000).
9. J. C. Angus and C. C. Hayman, Science **241**, 913 (1988).
10. M. Tomellini, R. Polini, and V. Sessa, J. Appl. Phys. **70**, 7573 (1991).
11. A. M. Bonnot, R. Schauer, and B. Weidner, Diamond Relat. Mater. **7**, 205 (1998).
12. S. Yugo, K. Semoto, N. Nakamura, and T. Kimura, Diamond Relat. Mater. **6**, 1047 (1997).
13. X. Jiang, K. Schiffmann, A. Westphal, and C.-P. Klages, Appl. Phys. Lett. **63**, 1203 (1993).
14. R. E. Shröder, R. J. Nemanich, and J. T. Glass, Phys. Rev. B **41**, 3338 (1990).

Translated by Yu. Sin'kov

Semiconductors, Vol. 36, No. 8, 2002, pp. 852–854. Translated from Fizika i Tekhnika Poluprovodnikov, Vol. 36, No. 8, 2002, pp. 914–916.

ELECTRONIC AND OPTICAL PROPERTIES OF SEMICONDUCTORS

Local Structure of Zinc Impurity Centers in Lead Chalcogenides and $Pb_{1-x}Sn_xTe$ Solid Solutions

S. A. Nemov and N. P. Seregin

St. Petersburg State Technical University, Politekhnicheskaya ul. 29, St. Petersburg, 195251 Russia

Submitted February 27, 2002; accepted for publication February 28, 2002

Abstract—The positions of zinc impurity atoms formed in lead chalcogenide lattices (PbS, PbSe, and PbTe) after the radioactive decay of ^{67}Cu and ^{67}Ga isotopes are defined by the positions of parent atoms. Therefore, stabilization of the zinc centers is possible both at the cation and interstitial sites. In both positions, the zinc centers are either electrically inactive or the impurity energy level has a low ionization energy and recharging of the impurity does not affect the isomeric shift of the Mössbauer spectrum. In zero-gap $Pb_{1-x}Sn_xTe$ solid solutions, changes in local symmetry of the cation sites and in the electron density at these sites are not observed.

Superconductivity with a critical temperature extraordinarily high for semiconductors has been discovered in $Pb_{1-x}Sn_xTe$ solid solutions with a high concentration of indium impurity [1]. At present, there is no explanation of this phenomenon within the microscopic theory of superconductivity. First of all, this is connected with the fact that the traditional methods of semiconductor physics cannot provide insight into variations in the electron structure of a material during the semiconductor–superconductor transition. Hence, any assumptions on the nature of the phase transition to the superconducting state in the $Pb_{1-x}Sn_xTe$ alloys are, to a large extent, speculative.

Mössbauer spectroscopy is a promising method for studying the electron structure of the solid-state. In particular, measurements of the temperature dependences of the centroid of the Mössbauer spectrum S at temperatures higher and lower than the superconducting transition temperature give information about the formation of Cooper pairs and Bose condensation [2]. However, the choice of the objects for research should take into account the necessity of introducing a Mössbauer ^{67}Zn probe into the lattice sites. If we use the Mössbauer emission spectroscopy of $^{67}Cu(^{67}Zn)$ and $^{67}Ga(^{67}Zn)$ isotopes, this condition can basically be fulfilled for the lead chalcogenides. It is possible to introduce the parent isotopes both into the cation (^{67}Ga) and interstitial (^{67}Cu) sites of the lead chalcogenide lattices. As a result, the daughter ^{67}Zn isotope will also occur either at the Pb sites or in the interstitial position (it is well known that Ga substitutes Pb in the lead chalcogenides, and it acts as an acceptor with low ionization energy, whereas Cu in the interstitial sites forms shallow donor levels [3]). In other words, there is an opportunity to study the spatial nonuniformity of the electron density caused by the Bose condensate of the Cooper pairs.

This study is devoted to the identification of the position of the Zn impurity atoms in lead chalcogenide lattices (PbS, PbSe, and PbTe) using emission Mössbauer spectroscopy of $^{67}Cu(^{67}Zn)$ and $^{67}Ga(^{67}Zn)$ isotopes. The $Pb_{1-x}Sn_xTe$ system is represented by a continuous series of solid solutions with an NaCl-type lattice in which the band inversion and zero-gap state occur for $x = 0.62$ and 0.40 at $T = 295$ and 80 K, respectively [3]. We employed the Mössbauer spectroscopy of the $^{67}Ga(^{67}Zn)$ isotope for the study of possible variations in the local symmetry of the cation sites in zero-gap $Pb_{1-x}Sn_xTe$ solid solutions ($0 < x < 1$).

Initial PbS, PbSe, and PbTe samples and the $Pb_{1-x}Sn_xTe$ solid solutions were grown using powder metallurgy. These compounds were synthesized through the melting of the components, which had a purity typical of semiconductor materials, in evacuated quartz cells. First the ingots and then the pressed samples were annealed at $T = 650°C$ for 120 h. The charge was prepared taking into account that the homogeneity region of the solid solutions, enriched with PbTe, corresponds to the tellurium excess in reference to the stoichiometric composition (~50.1 at. % of Te [3]). An X-ray diffraction analysis of the crystal structure showed that all samples under study contained a single phase (they had a structure of the NaCl-type). The samples of PbS, PbSe, and PbTe were either of the n-type (with excess of Pb; the electron concentration $n \sim 10^{18}$ cm^{-3}) or of the p-type (with excess of chalcogen; the hole concentration $p \sim 10^{18}$ cm^{-3}), while the $Pb_{1-x}Sn_xTe$ solid solutions were of the p-type (the hole concentration varied from 10^{17} cm^{-3} in PbTe to 10^{21} cm^{-3} in SnTe at $T =$ 80 K). We prepared the Mössbauer sources through diffusion doping of the samples with radioactive ^{67}Ga and ^{67}Cu isotopes in evacuated quartz cells at $T = 650°C$ for 2h; the concentration of the parent isotope did not exceed 5×10^{15} cm^{-3}.

For measurements of ^{67}Zn Mössbauer spectra, we used an MS-2201 commercial spectrometer with an updated system of transport. A piezoelectric transducer on the basis of PZT ceramics was used as a modulator. The maximum sweep velocity V was ±150 μm/s. The spectrometer was calibrated against the metallic ^{67}Zn spectrum with a ^{67}Cu source. The semiconductor Ge(Li) detector, having a maximum sensitivity at the energy of 100 keV, was used for the detection of gamma quanta. The Mössbauer spectra were recorded with the ^{67}ZnS absorber (its temperature was equal to 4.2 K). The centroids of the experimental spectra are shown in reference to the absorber. Typical ^{67}Ga(^{67}Zn) and ^{67}Cu(^{67}Zn) Mössbauer spectra for PbS are shown in Fig. 1. The results of the ^{67}Ga(^{67}Zn) spectra processing for the $Pb_{1-x}Sn_xTe$ solid solutions are shown in Fig. 2.

The spectra of ^{67}Ga(^{67}Zn) for the lead chalcogenide consist of single lines with a width at half-height which is close to the instrumental resolution (2.6 ± 0.3 μm/s). The isomeric shift of these lines increases in the following series of compounds: PbS (S = 2.2 ± 0.4 μm/s), ⟶ PbSe (S = 10.3 ± 0.4 μm/s), ⟶ PbTe (S = 33.7 ± 0.3 μm/s). The spectra are related to isolated impurity centers of Zn at the lead sites. The increase in the isomeric shift in the above-mentioned series is caused by variation in the ionicity of the chemical bond between the zinc atoms and the atoms in its first coordination sphere. The isomeric shift of the spectra is almost independent of the type of sample conductivity, and, therefore, the impurity center of Zn is either electrically inactive or recharging the shallow center does not affect the isomeric shift.

The spectra of ^{67}Cu(^{67}Zn) for lead chalcogenides also consist of single lines with the width at half-height close to the instrumental resolution. Their isomeric shift is appreciably displaced to the metallic Zn spectrum: S = 31.1 ± 0.4 μm/s for PbS, S = 32.5 ± 0.4 μm/s for PbSe, and S = 41.2 ± 0.4 μm/s for PbTe. The spectra correspond to isolated Zn centers that formed as a result of the radioactive decay of the interstitial parent Cu atoms in the lead chalcogenide lattices. At the same time, lead and chalcogen atoms occur as the nearest neighbors of the interstitial impurity atoms of Zn. Since the isomeric shift of the spectra is independent of the type of sample conductivity, we may conclude that, in this case, the Zn centers are also electrically inactive.

The Mössbauer spectra of ^{67}Ga(^{67}Zn) for the $Pb_{1-x}Sn_xTe$ solid solutions consist of single lines which are related to the Zn atoms at the sites of the cation sublattice. The line width in all spectra is close to the instrumental resolution. It slightly increases with x, approaching the maximum value for SnTe (Fig. 2). This fact is quite expected since the homogeneity region expands as the Sn content increases in the alloy. This causes an increase in the concentration of structural point defects and, as a result, an increase in the width of the Mössbauer spectrum. A similar effect was also observed for the Mössbauer spectrum of ^{119}Sn and ^{129}Te(^{129}I) in the $Pb_{1-x}Sn_xTe$ solid solutions [4].

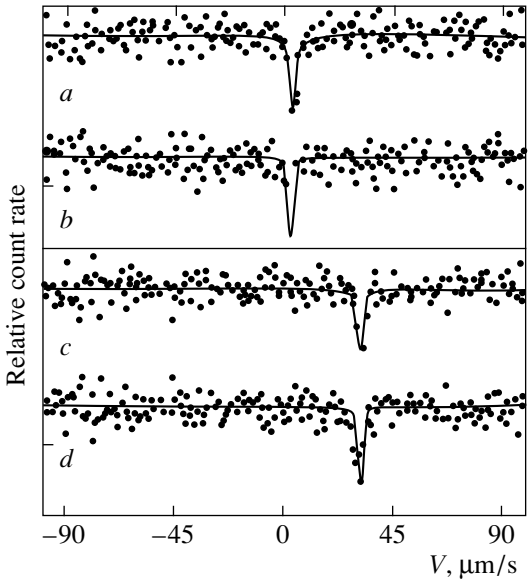

Fig. 1. Emission Mössbauer spectra of the impurity atoms: (*a*, *b*) ^{67}Ga(^{67}Zn) and (*c*, *d*) ^{67}Cu(^{67}Zn) in (*a*, *c*) *n*-PbS and (*b*, *d*) *p*-PbS at T = 4. 2 K.

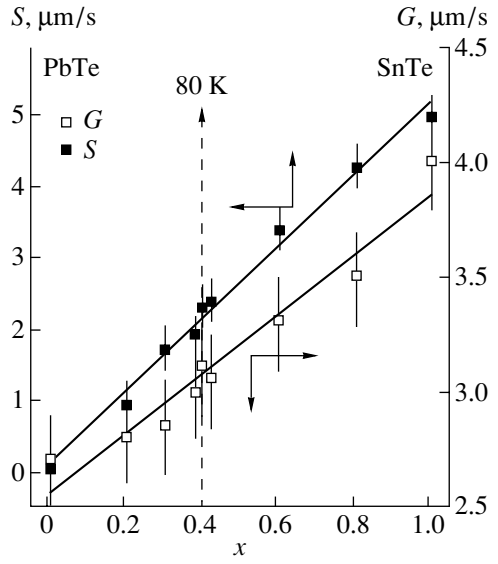

Fig. 2. The dependences of isomeric shift S (in reference to PbTe:^{67}Ga) and the spectrum width G on the composition of the $Pb_{1-x}Sn_xTe$ solid solution at T = 80 K. Dotted line indicates the composition with a zero gap at T = 80 K.

The isomeric shift of the Mössbauer spectra is governed by the chemical nature of atoms in the local environment of the Mössbauer probe. Since the variation in composition of the $Pb_{1-x}Sn_xTe$ solid solution does not affect the symmetry of the local environment of zinc atoms (tin atoms only substitute lead atoms in the second coordination shell), a weak dependence of the iso-

meric shift of the ^{67}Ga(^{67}Zn) Mössbauer spectra on the composition (Fig. 2) is quite expected.

It is essential that anomalous changes in both the isomeric shift and the spectrum width in the zero-gap state do not occur. In other words, we did not observe variation in the local symmetry of the cation sites and in the corresponding electron density in zero-gap $Pb_{1-x}Sn_xTe$ solid solutions at $T = 80$ K.

Thus, we have demonstrated that the position of zinc impurity atoms which formed in the lead chalcogenide lattices after the radioactive decay of ^{67}Cu and ^{67}Ga isotopes is defined by the position of parent atoms. The stabilization of zinc centers is possible at cation sites as well as at interstitial ones. In both positions, the zinc centers are either electrically inactive or the impurity energy level has a low ionization energy. Due to this fact, recharging of the impurity atom does not affect the isomeric shift of the Mössbauer spectrum. Variations in local symmetry of the cation sites and in the electron density at these sites were not observed in zero-gap $Pb_{1-x}Sn_xTe$ solid solutions.

ACKNOWLEDGMENTS

This study was supported by the Russian Foundation for Basic Research, project no. 02-02-17306.

REFERENCES

1. R. V. Parfeniev, D. V. Shamshur, and M. F. Shakhov, J. Alloys Compd. **219**, 313 (1995).
2. N. P. Seregin, F. S. Nasredinov, and P. P. Seregin, J. Phys.: Condens. Matter **13**, 149 (2001).
3. N. Kh. Abrikosov and L. E. Shalimova, *Semiconducting Materials Based on IV–VI Compounds* (Nauka, Moscow, 1975).
4. V. F. Masterov, F. S. Nasredinov, S. A. Nemov, and P. P. Seregin, Fiz. Tverd. Tela (St. Petersburg) **38**, 2973 (1996) [Phys. Solid State **38**, 1625 (1996)].

Translated by I. Kucherenko

Semiconductors, Vol. 36, No. 8, 2002, pp. 855–862. Translated from Fizika i Tekhnika Poluprovodnikov, Vol. 36, No. 8, 2002, pp. 917–924.

ELECTRONIC AND OPTICAL PROPERTIES OF SEMICONDUCTORS

Influence of Tellurium Impurity on the Properties of $Ga_{1-X}In_XAs_YSb_{1-Y}$ ($X > 0.22$) Solid Solutions

T. I. Voronina, T. S. Lagunova, E. V. Kunitsyna, Ya. A. Parkhomenko, M. A. Sipovskaya, and Yu. P. Yakovlev

Ioffe Physicotechnical Institute, Russian Academy of Sciences, Politekhnicheskaya ul. 26, St. Petersburg, 194021 Russia

Submitted December 18, 2001; accepted for publication December 20, 2001

Abstract—The influence of tellurium impurity on the electrical properties of $Ga_{1-X}In_XAs_YSb_{1-Y}$ ($X = 0.22$ and $X = 0.24$) solid solutions grown by liquid-phase epitaxy from lead-containing solution–melts was studied. Defect healing was shown to take place at low tellurium doping levels ($X_{Te}^{L} < 2 \times 10^{-5}$ at. %) in inhomogeneous highly compensated *p*-type solid solutions. Thus, it is possible to produce slightly compensated *p*-type materials with a low density of impurities and structural defects. High doping levels allow production of *n*-type materials with the electron density $n = 10^{17}$–10^{19} cm^{-3}. Electroluminescence spectra of *n*-GaInAsSb/*p*-GaSb heterostructures are promising for the development of light-emitting diodes with a wavelength $\lambda = 2.0$–2.5 μm. © *2002 MAIK "Nauka/Interperiodica"*.

1. INTRODUCTION

Solid solutions of $Ga_{1-X}In_XAs_YSb_{1-Y}$ ($X > 0.22$) with a band gap $E_g = 0.4$–0.5 eV can be used to develop optoelectronic devices in the wavelength range $\lambda = 2.5$–3 μm. The fabrication of such devices requires both *n*- and *p*-type materials with high electron and hole mobilities. Previously [1], we have shown that epilayers of $Ga_{1-X}In_XAs_YSb_{1-Y}$ solid solutions with a high indium content ($X = 0.22$–0.27) in the solid phase ($E_g = 0.5$–0.49 eV at $T = 77$ K) can be produced only when using lead in a solution–melt as a neutral solvent. As in $Ga_{1-X}In_XAs_YSb_{1-Y}$ solid solutions with a lower indium concentration, undoped layers always had the *p*-type conduction. To produce *n*-type layers, tellurium is most commonly employed as a donor impurity.

We studied tellurium as a dopant in $Ga_{1-X}In_XAs_YSb_{1-Y}$ ($X = 0.10$) solid solutions in [2]. A high temperature (650°C) of epitaxial growth made it possible to grow solid solutions about 100 μm thick on a *n*-GaSb:Te substrate; thus, the latter could be removed for the study of galvanomagnetic effects. It was shown that tellurium is readily dissolved in the solid solution (the segregation coefficient is $C = C_{sol}/C_{liq} = 0.7$) and gives rise to two donor levels: a shallow hydrogen-like one ($E_{D1} = 0.005$ eV), inherent to tellurium impurity, and a deeper one ($E_{D2} = 0.04$–0.05 eV), whose origin remains unclear.

In [3], it was shown that tellurium always diffused into thin undoped epilayers of solid solutions 3–5 μm thick grown on *n*-GaSb:Te substrates. In this case, on the one hand, tellurium gave rise to shallow donor levels. On the other hand, interacting with native defects (with activation energies $E_{A2} = 0.035$ eV and $E_{A3} = 0.07$ eV) inherent to gallium antimonide, tellurium produced new acceptor levels with the activation energy $E_{A4} = 0.1$ eV, which is related to the formation of a structural defect (V_{Ga}–Te).

Since tellurium can interact with vacancies and defects, it is of interest to study its behavior in $Ga_{1-X}In_XAs_YSb_{1-Y}$ solid solutions with $E_g = 0.4$–0.5 eV, which may have a wide application. In this study, we report the results of studying the transport and photoelectric properties of $Ga_{1-X}In_XAs_YSb_{1-Y}$ solid solutions with $X = 0.22$ and 0.24, which were grown from lead-containing solution–melts at various tellurium doping levels. Studies of the electrical conductivity σ, Hall coefficient *R*, Hall mobility μ in solid solutions in the temperature range 77–300 K, as well as electroluminescence in $Ga_{1-X}In_XAs_YSb_{1-Y}$ ($X = 0.22$ and 0.24) heterostructures with an active layer, allow us to analyze the impurity energy spectrum, determine the carrier scattering mechanism, and reveal the influence of tellurium on the properties of the solid solution.

2. SAMPLE PREPARATION

Epilayers of $Ga_{1-X}In_XAs_YSb_{1-Y}$ solid solutions with an indium content $X > 0.22$ were grown by liquid-phase epitaxy from lead-containing solutions–melts at the temperature $T = (560 \pm 3)$°C [1]. Single-crystal *n*- and *p*-GaSb wafers with the (100) orientation were used as substrates. As charge components, we used GaSb and InAs binary compounds, as well as In, Sb, and Pb of 99.999%, 99.999%, and 99.9999% purity, respectively.

Table 1. Characteristics of the studied samples of $Ga_{1-X}In_XAs_YSb_{1-Y}$ solid solutions with $X = 0.22$

Sample no.	X^L_{Te}, at. %	T = 300 K				T = 77 K			
		Conduction type	σ, Ω^{-1} cm^{-1}	n, p, 10^{17} cm^{-3}	μ, cm^2 V^{-1} s^{-1}	Conduction type	σ, Ω^{-1} cm^{-1}	n, p, 10^{17} cm^{-3}	μ, cm^2 V^{-1} s^{-1}
1	Undoped	*n*	13	0.3	3500	*p*	0.7	0.2	220
2	1.31×10^{-5}	*p*	23	2.8	500	*p*	26	0.7	2200
3	1.75×10^{-5}	*p*	50	6	520	*p*	27	0.46	3600
4	2.2×10^{-5}	*n*	15	3	300	*p*	0.46	0.5	60
5	1.09×10^{-4}	*n*	125	1.8	3500	*n*	60	20	180
6	2.2×10^{-4}	*n*	130	3	3700	*n*	75	1.2	4000
7	1.9×10^{-2}	*n*	2390	59	2526	*n*	1900	40	3050
8	6.9×10^{-2}	*n*	4550	170	1650	*n*	6000	180	1900

Note: X^L_{Te} is the Te impurity concentration in the melt.

As a result, two types of samples were prepared, with and without a GaSb buffer layer, to study the transport and electroluminescence properties, respectively.

2.1. Samples with a Buffer Layer

To avoid tellurium diffusion from the *n*-GaSb:Te substrate into the solid solution epilayer and the corresponding influence of this process on the electrical properties of the material, an additional buffer layer of *p*-GaSb with a low carrier concentration and a high resistivity ($p = 6 \times 10^{14}$ cm^{-3}, $\rho \gtrsim 400$ Ω cm) was preliminarily grown on the substrate from lead-containing solution–melts [4]. The GaSb buffer layer thickness was 4–5 μm. Then, 1- to 3-μm-thick epilayers of $Ga_{1-X}In_XAs_YSb_{1-Y}$ ($X = 0.22$ and 0.24) solid solutions were grown on this buffer layer from lead-containing solutions–melts. The solid solutions were doped with tellurium (as the donor impurity), which was introduced into the liquid phase in elemental form (with the concentration $X^L_{Te} < 10^{-2}$ at. % in the melt) and as a weighed *n*-GaSb:Te portion ($X^L_{Te} < 2.5 \times 10^{-4}$ at. %).

2.2. Samples without a Buffer Layer

To study the electroluminescence properties, $Ga_{1-X}In_XAs_YSb_{1-Y}$ solid solutions ($X = 0.22$ and 0.24) were grown from lead-containing solution–melts directly on the *p*-GaSb substrate with (100) orientation and were doped with tellurium to produce a free electron concentration $n = 1.2 \times 10^{17}$–10^{18} cm^{-3} at T = 77 K. Conventional photolithography was used to produce mesas 300 μm in diameter at the surface of the *n*-$Ga_{1-X}In_XAs_YSb_{1-Y}$/*p*-GaSb heterostructures.

3. TRANSPORT PROPERTIES OF $Ga_{1-X}In_XAs_YSb_{1-Y}$ SOLID SOLUTIONS

The electrical conductivity σ, Hall coefficient R, and mobility $\mu = R\sigma$ were measured in rectangular samples with six indium contacts in the temperature range of 77–300 K in a magnetic field of 0–20 kOe. We will consider the influence of tellurium doping on galvanomagnetic effects in samples with $X = 0.22$ and 0.24 separately.

3.1. Tellurium-Doped Samples with an Indium Content X = 0.22

The characteristics of the studied $Ga_{1-X}In_XAs_YSb_{1-Y}$ ($X = 0.22$) samples in relation to the tellurium doping level are listed in Table 1. The temperature dependences of the Hall coefficient R and the mobility μ are shown in Figs. 1 and 2, respectively.

One can see from Table 1 that the undoped solid solution (sample 1) at the liquid nitrogen temperature has *p*-type conduction with low density and mobility of holes. The temperature dependences of the Hall coefficient (Fig. 1a) and the mobility (Fig. 2) at $T < 150$ K in sample 1 indicate conduction over shallow acceptor levels. At $T > 150$ K, the Hall voltage changes sign and the Hall mobility drastically increases, which can be caused by the onset of the transition to intrinsic conduction. At $T > 250$ K, the Hall coefficient R decreases and the high Hall mobility $\mu > 2000$ cm^2 V^{-1} s^{-1} is totally controlled by electron conduction; i.e., intrinsic conduction sets in. However, the dependence of $RT^{3/2}$ on inverse temperature at $T > 250$ K is not exponential and does not correspond to the band gap of the solid solution. Such a nonexponential dependence in the case of intrinsic conduction, as well as the low temperature of the transition to intrinsic conduction ($T \approx 150$ K), may indicate deep "tails" of impurity states, which distort the valence and conduction bands. Such tails are char-

acteristic of highly compensated materials with a great number of nonuniformly distributed impurities and structural defects [5]. The properties of such solid solutions are drastically changed as a result of doping with tellurium and depend heavily on the doping level.

Light doping ($X^L_{\mathrm{Te}} < 1.75 \times 10^{-5}$ at. %) causes a certain inhomogeneity of the material. However, all the grown samples had *p*-type conduction both at $T = 77$ and ≈300 K with low density and high mobility of holes (see Table 1, samples 2, 3). The temperature dependence of the Hall coefficient (Fig. 1a, samples 2, 3) was controlled by three energy levels: the shallow impurity level $E_{A1} < 0.01$ eV ($T < 120$ K), which is related to uncontrollable impurities, as well as the deeper levels $E_{A2} = 0.03$ eV and $E_{A3} = 0.07$ eV, which can be related to the structural defect $(V_{\mathrm{Ga}}\mathrm{Ga}_{\mathrm{Sb}})^{++}$ inherent to GaSb and solid solutions close to GaSb in composition. The temperature dependence of the mobility in these samples (Fig. 2, samples 2, 3) is characteristic of the transition to scattering by impurity ions (μ_I) at $T < 100$ K and, at higher temperatures, by lattice vibrations (μ_L). Setting the experimental mobilities μ_{77} at 77 K equal to μ_I and comparing them with the calculated values μ^t_I [6], we can estimate the concentration of ionized shallow impurities; i.e.,

$$N^{77}_I = \mu^t_I p_{77}/\mu_{77}.$$

For shallow impurity levels, we have $N^{77}_I = 2N_D + p_{77}$, from which the donor concentration N_D can be found. We set the hole concentration p_{77} at 77 K equal to $p_{\mathrm{depl}} = N_{A1} - N_D$, where p_{depl} is the hole concentration at depleted shallow levels, and estimate the quantity N_{A1}.

In sample 2 with $X^L_{\mathrm{Te}} = 1.31 \times 10^{-5}$ at. %, we have $N_{A1} = 1.5 \times 10^{17}$ cm^{-3}, $N_D = 10^{16}$ cm^{-3}, and the compensation factor is $K = N_D/N_{A1} = 0.07$. In sample 3 with $X^L_{\mathrm{Te}} = 1.75 \times 10^{-5}$ at. %, we have $N_{A1} = 8 \times 10^{16}$ cm^{-3}, $N_D = 10^{16}$ cm^{-3}, and $K = 0.12$. The above values of N_{A1} and N_D indicate that we have grown a normal low-compensated *p*-type material as a result of light doping with tellurium. This may be attributed to "healing" of defects, where tellurium interacts with charged clusters of impurities and defects and neutralizes them. The potential fluctuations at the valence band bottom diminish, and the concentration and mobility in the sample are mainly controlled by holes at shallow impurity levels with the activation energy $E_{A1} = 0.01$ eV and by doubly charged structural defects with $E_{A2} = 0.03$ eV and $E_{A3} = 0.07$ eV, whose concentration is lower than that of shallow impurity levels ($N_{A2} = 10^{16}$ cm^{-3}) by an order of magnitude.

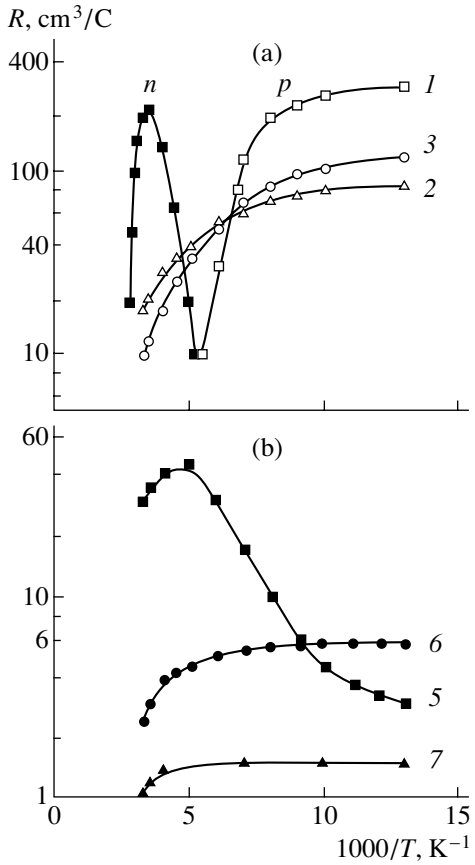

Fig. 1. Dependences of the Hall coefficient on the inverse temperature in the (a) *p*-type samples at $T \approx 77$ K (open symbols) and (b) *n*-type samples (closed symbols) of $\mathrm{Ga}_{1-X}\mathrm{In}_X\mathrm{As}_Y\mathrm{Sb}_{1-Y}$ ($X = 0.22$) solid solutions. Numbers at curves correspond to sample numbers in Table 1.

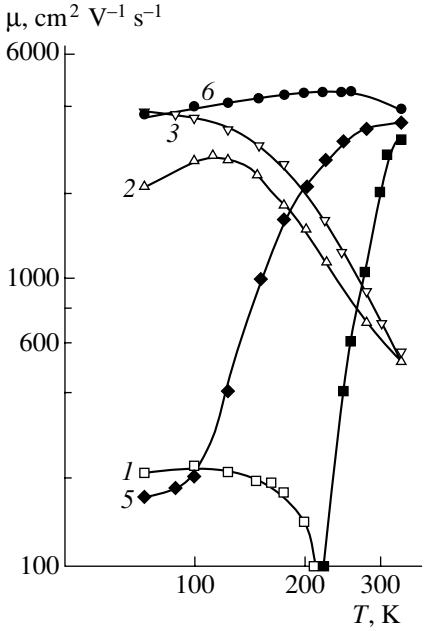

Fig. 2. Hall mobility versus temperature in the *p*- (open symbols) and *n*-type (closed symbols) samples of $\mathrm{Ga}_{1-X}\mathrm{In}_X\mathrm{As}_Y\mathrm{Sb}_{1-Y}$ solid solutions with $X = 0.22$. Numbers at curves correspond to sample numbers in Table 1.

Table 2. Characteristics of the studied samples of $Ga_{1-X}In_XAs_YSb_{1-Y}$ solid solutions with $X = 0.24$

Sample no.	X^L_{Te}, at. %	$T = 300$ K				$T = 77$ K			
		Conduction type	σ, Ω^{-1} cm^{-1}	n, p, 10^{17} cm^{-3}	μ, cm^2 V^{-1} s^{-1}	Conduction type	σ, Ω^{-1} cm^{-1}	n, p, 10^{17} cm^{-3}	μ, cm^2 V^{-1} s^{-1}
9	Undoped	*p*	140	14	550	*p*	190	4	2800
10	9.9×10^{-5}	*p*	200	23	540	*p*	205	4.8	2680
11	1.98×10^{-4}	*n*	950	30	2000	*p*	420	1.8	1460
12	1.3×10^{-2}	*n*	550	13	2660	*n*	327	7.4	2760
13	3.4×10^{-2}	*n*	1400	43	2000	*n*	1430	26	3300

Note: X^L_{Te} is the Te impurity content in the melt.

Thus, tellurium, as a dopant introduced in small amounts, improves the properties of $Ga_{1-X}In_XAs_YSb_{1-Y}$ solid solutions with $X = 0.22$ and, while retaining the *p*-type conduction, allows production of a material with high hole mobility and low density of structural defects.

Heavy doping with tellurium ($X^L_{Te} > 2 \times 10^{-5}$ at. %) causes overcompensation of impurities in the solid solution. One can see from Table 1 that the *p*-type conduction is still retained (but with very low mobility) at the tellurium content $X^L_{Te} = 2.2 \times 10^{-5}$ at. % in sample 4 at $T = 77$ K. At $T = 300$ K, the solid solution begins to exhibit *n*-type conduction. At $X^L_{Te} = 1.09 \times 10^{-4}$ at. % (sample 5), the material becomes *n*-type both at $T = 77$ and 300 K. In this case, the electron mobility at $T = 77$ K is very low, which may be caused by high compensation of the material and by impurity clusters. The temperature dependences $R(T)$ and $\mu(T)$ (Figs. 1b, 2, curves 5) exhibit a steep increase of the Hall coefficient and the mobility with temperature, as well as a peak at $T \approx 200$ K. This run of the dependences $R(T)$ and $\mu(T)$ is typical of a transition to conduction over the impurity band at low temperatures. The anomalously small Hall coefficient R and low mobility μ at the liquid nitrogen temperature may be explained by high compensation of the material, in which case the distribution of impurities becomes significantly nonuniform; the latter gives rise to a distortion of the conduction band bottom and a "tail" of the density of states in the band gap [5]. Electrons are localized in the deepest valleys of the potential relief, which are surrounded with high potential humps. The Hall coefficient is defined by the volume-average concentration $\bar{n}$ [7]. The conductivity σ in an inhomogeneous sample is defined by the concentration at the percolation level; at high compensation, this concentration depends on temperature as

$$n_c \propto \exp\left(-\frac{E_P - E_F}{kT}\right),$$

where E_P is the energy at the percolation level and E_F is the energy at the Fermi level [8]. The effective Hall mobility $\mu = R\sigma$ in an inhomogeneous material does not represent the behavior of true (drift) mobility and differs from it by the factor $n_c/n < 1$, which decreases drastically as the temperature is lowered. It is evident that the difference of the measured Hall mobility from the drift one will increase with the magnitude of sample inhomogeneities.

At a higher doping level ($X^L_{Te} > 2.2 \times 10^{-4}$ at. %), the electron concentration increases, the compensation factor decreases, and the potential relief is smoothed. The Hall coefficient is related to the electron density in the conduction band. One can see from Table 1 (samples 6, 7) that the solid solution both at $T = 77$ and 300 K always has the *n*-type conduction and high mobility. The temperature dependence of the Hall coefficient (Fig. 1b, samples 6, 7) exhibits a decrease in R at $T > 250$ K, which indicates that there is a donor level with an activation energy $E_D = 0.05$ eV. This donor level was previously observed in *n*-$Ga_{1-X}In_XAs_YSb_{1-Y}$ solid solutions ($X = 0.10$) at low electron densities [2]; the origin of it remains obscure.

The temperature dependence of the mobility (Fig. 2, sample 6) is characteristic of scattering by impurity ions at $T < 200$ K and by lattice vibrations at higher temperatures. By comparing the experimental mobility at $T = 77$ K with the theory [6], the impurity compensation factor in samples 6 and 7 was estimated as $K = 0.2$.

At a very high doping level ($X^L_{Te} = 6.9 \times 10^{-2}$ at. %, sample 8), an electron density above 10^{19} cm^{-3} can be attained. In this case (see Table 1), the Hall coefficient remains virtually unchanged in the entire temperature range from 77 to 300 K, which is typical of high degeneracy. The Fermi level position is $E_F = 50$ meV at $T \longrightarrow 0$.

We note that the Hall coefficient does not increase with temperature at any concentration in *n*-$Ga_{1-X}In_XAs_YSb_{1-Y}$ solid solutions with $X = 0.22$, in contrast to *n*-GaSb and

n-$Ga_{1-X}In_XAs_YSb_{1-Y}$ with $X = 0.10$. This indicates that there is no second (111)-type conduction subband slightly above the (000) minimum [6] ($E_c^{(111)} - E_c^{(000)} \approx$ 0.08 eV for GaSb).

Thus, the use of tellurium as a dopant in $Ga_{1-X}In_XAs_YSb_{1-Y}$ solid solutions with $X = 0.22$ makes it possible to "heal" existing defects with light doping ($X_{Te}^L \lesssim 1.75 \times 10^{-5}$ at. %) and to produce a *p*-type material with a low concentration and high mobility of holes ($p_{77} \approx 4 \times 10^{16}$ cm^{-3}, $\mu_{77} = 3600$ cm^2 V^{-1} s^{-1}). At heavy doping ($X_{Te}^L > 2 \times 10^{-4}$ at. %), *n*-type material with a high electron mobility may be produced in a wide concentration range from 10^{17} to 10^{19} cm^{-3}.

3.2. Tellurium-Doped Samples with an Indium Content X = 0.24

The characteristics of the studied samples are listed in Table 2. The temperature dependences of the Hall coefficient and the mobility are shown in Figs. 3 and 4.

The initial undoped samples of $Ga_{1-X}In_XAs_YSb_{1-Y}$ solid solutions ($X = 0.24$) were *p*-type at $T = 77$ and 300 K and had higher hole densities and mobilities (sample 9, Table 2) than in solid solutions with $X = 0.22$ (sample 1, Table 1). The high hole mobilities at $T = 77$ and 300 K indicate that the impurities are compensated only slightly ($K \approx 0.1$) and the impurity clusters are absent. Overcompensation of this material occurs at a higher tellurium content. In particular, at the tellurium content $X_{Te}^L = 9.9 \times 10^{-5}$ at. % in the liquid phase (sample 10), the material remained virtually unchanged and retained *p*-type conduction at $T = 77$ and 300 K, in contrast to sample 5 with $X = 0.22$ at the same doping level.

It is evident from Fig. 3a that the temperature dependence of the Hall coefficient for undoped sample 9 and lightly doped sample 10 exhibits slopes typical of *p*-type samples with an activation energy of 0.02 eV. The mobility in these samples (Fig. 4) is lowered as temperature increases and is controlled by scattering by impurity ions and lattice vibrations. The high mobilities at $T = 77$ K indicate a low impurity-compensation level in these samples ($K = N_D/N_A < 0.1$).

With doping at the level $X_{Te} = 1.98 \times 10^{-4}$ at. % (sample 11), the temperature dependence of the Hall coefficient (Fig. 3a) exhibits a conduction-type inversion at $T = 100$ K, which is typical of a transition to intrinsic conduction. The dependences of $RT^{3/2}$ on the reciprocal temperature at $T > 250$ K is exponential (Fig. 5). The activation energy calculated from the exponential dependences corresponds to the band gap $E_g = 0.42$ eV, which agrees closely with the values calculated in [1]. This result confirms the absence of fluctuations of the conduction band bottom and the valence band top, in contrast to sample 1 with a lower indium content in the solid solution.

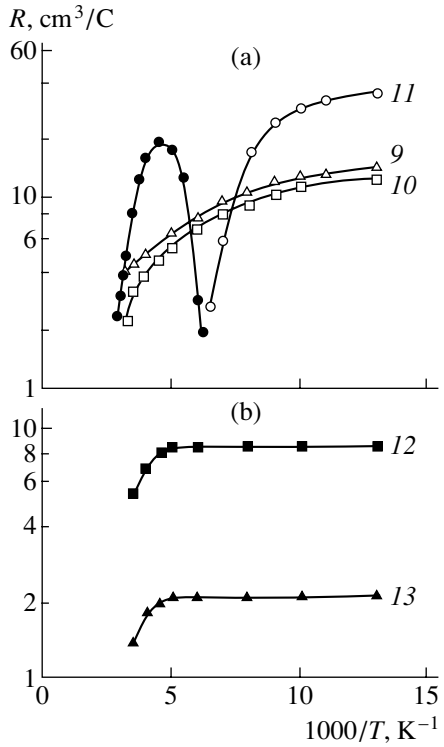

Fig. 3. Dependences of the Hall coefficient on the inverse temperature in the (a) *p*-type samples at $T \approx 77$ K (open symbols) and (b) *n*-type samples (closed symbols) of $Ga_{1-X}In_XAs_YSb_{1-Y}$ solid solutions with $X = 0.24$. Numbers at curves correspond to sample numbers in Table 2.

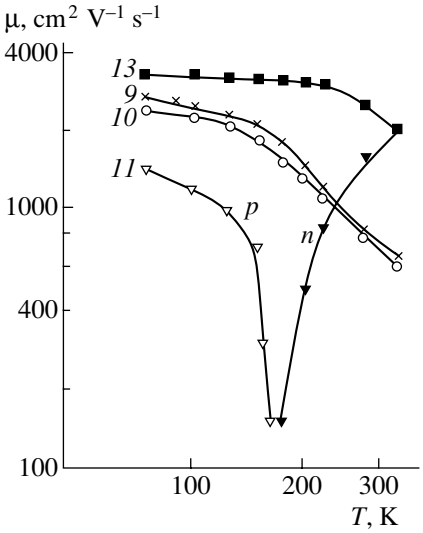

Fig. 4. Hall mobility versus the temperature in $Ga_{1-X}In_XAs_YSb_{1-Y}$ solid solutions with X = 0.24. Numbers at curves correspond to sample numbers in Table 2.

In samples 12 and 13 with $X_{Te}^L = 1.3 \times 10^{-2}$ and 3.4×10^{-2} at. %, complete overcompensation is observed. The temperature dependence of the Hall coefficient (Fig. 3b) in these samples, as in the n-type

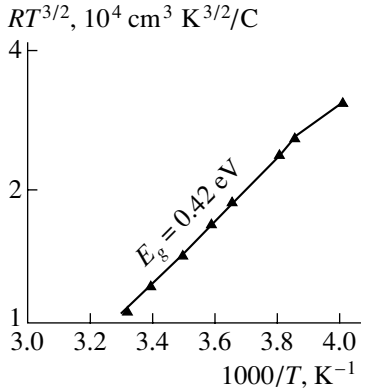

Fig. 5. Dependence of $RT^{3/2}$ on the inverse temperature for sample 11 at $T > 250$ K.

samples with a lower indium content (samples 7 and 8) at $T > 200$ K, exhibits slopes with the activation energy $E_D = 0.05$ eV. The temperature dependence of the electron mobility (Fig. 4, sample 13) is characteristic of a degenerate material when there is scattering by impurities and lattice vibrations. The electron mobility at $T =$ 77 K allows us to estimate the compensation factor for shallow impurities as $K = 0.1$.

Thus, in $Ga_{1-X}In_XAs_YSb_{1-Y}$ solid solutions with $X =$ 0.24, in which there are no fluctuations of the valence- and conduction-band edges, tellurium manifests itself as an ordinary donor impurity, which compensates holes and allows production of the *n*-type material in a wide concentration range.

4. ELECTROLUMINESCENCE OF *n*-$Ga_{1-X}In_XAs_YSb_{1-Y}$/*p*-GaSb HETEROSTRUCTURES (X = 0.22 AND 0.24)

Electroluminescence spectra of *n*-$Ga_{1-X}In_XAs_YSb_{1-Y}$/*p*-GaSb heterostructures (X = 0.22 and 0.24) emitting in the spectral region of 2–2.5 μm were studied at T = 77 and 300 K. Epilayers of *n*-GaInAsSb:Te were grown from a lead-containing solution–melt at various levels of tellurium doping. The possibility of developing LEDs based on these was studied.

The samples were prepared on the basis of *n*-$Ga_{1-X}In_XAs_YSb_{1-Y}$:Te solid solutions grown on a *p*-GaSb (100) substrate with a hole concentration $p =$ 10^{17} cm^{-3} without a buffer layer. The sample constituted a mesa with a continuous contact to *p*-GaSb and a point contact to the *n*-GaInAsSb layer. The spectral characteristics of LEDs were measured with an MDR-2 monochromator using a synchronous detection scheme. The measurements were carried out in a quasi-continuous mode by applying meander-type pulses with a repetition rate of 400 Hz to the *p–n* junction.

The spectra of the most intense signals of radiative recombination were measured for the samples grown at $X^L_{Te} \approx (2 \times 10^{-4}–2 \times 10^{-2})$ at. % (Figs. 6a–6c). According to the data obtained using the Hall effect, the free electron density in the layer at $T = 77$ K was $n = 1.2 \times 10^{17}$ cm^{-3} (sample 6, Table 1) and $n = 4.0 \times 10^{18}$ cm^{-3} (sample 7, Table 1). The spectra exhibit a number of peaks corresponding to recombination mechanisms that involve interband transitions and various levels.

First, we analyze the emission spectra of LEDs based on the material with $X = 0.22$ (Figs. 6a, 6b). Figure 6a ($T = 300$ K) displays the spectra for two samples with different doping levels: $X^L_{Te} = 2.2 \times 10^{-4}$ at. % (curve *1*) and $X^L_{Te} = 1.9 \times 10^{-2}$ at. % (curve *2*). The emission peaks at the wavelength $\lambda = 2.35$ μm ($E_g =$ 0.525 eV, curve *1*) and $\lambda = 2.24$ μm ($E_g = 0.55$ eV, curve *2*) may be related to the interband recombination of free carriers. The shift of the peak in curve *2* is caused by the higher position of the Fermi level in the conduction band due to a higher doping level. The peak related to the recombination level $E_{A2} = 0.035$ eV is observed at $\lambda = 2.5$ μm in the case of a lighter doped sample (curve *1*). This is probably the first charge state caused by the native structural defect $V_{Ga}Ga_{Sb}$, which distinctly manifests itself in the temperature dependence of the Hall coefficient in the *p*-type material. The run of curve *2* indicates that there is a center with an ionization energy $E_{A3} = 0.07$ eV. This is the second charge state of the same acceptor. The first charge state $E_{A2} = 0.035$ eV does not manifest itself in curve *2*. The introduction of tellurium with $X^L_{Te} = 2 \times 10^{-2}$ at. % probably changes the charge state of the doubly charged acceptor, and the first level disappears. This effect was observed in [9] in the case of tellurium-doped GaSb. According to the peak of radiative recombination observed at $\lambda = 1.99$ μm for the same sample (Fig. 6b) at the liquid nitrogen temperature, the band gap is $E_g = 0.62$ eV. The signals at $\lambda = 2.04$ and 2.18 μm, observed in the same spectrum, can be caused by the donor levels $E_{D1} = 0.01–0.012$ eV (detected in [9]) and $E_{D2} = 0.05$ eV. It may be assumed that hole injection into the narrow-gap region increases at a rather high (at $T = 77$ K) current of 200 mA through the *p–n* junction, the acceptor levels E_{A1} and E_{A2} become saturated, and the 0.012- and 0.05-eV donor centers begin to participate in recombination. The same level with $E_{D2} = 0.05$ eV manifests itself in the temperature dependences of the Hall coefficient (Figs. 1, 3). Shallow acceptor centers can also be involved in this process.

Now, we consider the emission spectra of the material with $X = 0.24$ (Fig. 6c). Its tellurium content was $X^L_{Te} = 1.9 \times 10^{-2}$ at. %, as in the solid solution with $X =$ 0.22 considered above. The band gap at $T = 77$ K was 0.6 eV. Two peaks are also easily detected in the spectrum at wavelengths longer than 2.1 μm. In this case, both charge states of the doubly charged impurity

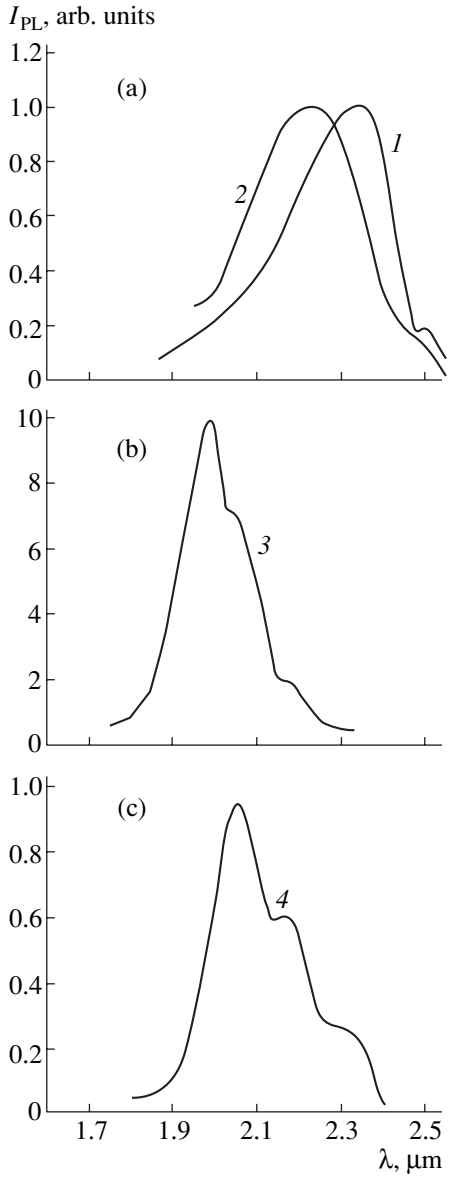

Fig. 6. Spectral dependences of the electroluminescence yield of LEDs based on n-$Ga_{1-X}In_XAs_YSb_{1-Y}$/p-GaSb with X = (a, b) 0.22 and (c) 0.24, measured at T = (a) 300 and (b, c) 77 K; X^L_{Te} = (*1*) 2.2×10^{-4} and (*2–4*) 1.9×10^{-2} at. %.

acceptor manifest themselves, in contrast to the sample with X = 0.22 with the same concentration (curve *3* in Fig. 6b). This indicates that the total concentration of acceptors was higher in the initial undoped material with X = 0.24; hence, complete compensation of acceptors requires a higher tellurium concentration, which conforms to the Hall measurements.

Thus, the radiative recombination spectra, which were measured when studying the electroluminescence of n-$Ga_{1-X}In_XAs_YSb_{1-Y}$/p-GaSbb (X = 0.22 and 0.24) heterostructures, have revealed levels identical to those detected when studying the transport properties of tellurium-doped n-type solid solutions; moreover, they have shown the prospect of developing LEDs based on these structures.

5. CONCLUSION

The influence of a tellurium impurity on the electrical properties of $Ga_{1-X}In_XAs_YSb_{1-Y}$/p-GaSb (X = 0.22 and 0.24) solid solutions grown from lead-containing solution–melts were studied for the first time, as were the electroluminescence spectra of heterostructures based on these solid solutions. These studies allow the following conclusions.

(i) The Te-undoped $Ga_{1-X}In_XAs_YSb_{1-Y}$ solid solution with X = 0.22 (E_g = 0.5 eV) represents a compensated p-type inhomogeneous material with a low concentration and mobility of holes at T = 77 K: $p_{77} = 2 \times 10^{16}$ cm^{-3} and $\mu_{77} \approx 200$ cm^2 V^{-1} s^{-1}. At light doping ($X^L_{Te} \le 1.75 \times 10^{-5}$ at. %), defects are "healed"; thus, it becomes possible to produce a low-compensated p-type material with a low concentration and high mobility of holes ($p_{77} = 5 \times 10^{16}$ cm^{-3} and $\mu_{77} \approx 3500$ cm^2 V^{-1} s^{-1}, as well as with a low density of structural defects.

(ii) In contrast to solid solutions with X = 0.22, undoped solid solutions with X = 0.24 are always characterized by a higher concentration and mobility of holes at T = 77 K ($p_{77} = 4 \times 10^{17}$ cm^{-3} and $\mu_{77} \approx 3000$ cm^2 V^{-1} s^{-1}, are more homogeneous, and do not involve significant fluctuations of impurities and defects. Therefore, light doping ($X^L_{Te} < 10^{-4}$ at. %) of $Ga_{1-X}In_XAs_YSb_{1-Y}$ (X = 0.24) solid solutions does not appreciably change the properties of the material.

(iii) At high doping ($X^L_{Te} > 10^{-4}$ at. % and $X^L_{Te} > 2 \times 10^{-4}$ at. % for compositions with X = 0.24 and 0.22, respectively), ordinary overcompensation of acceptor levels occurs in $Ga_{1-X}In_XAs_YSb_{1-Y}$ solid solutions. Thus, it becomes possible to produce n-type epilayers in a wide concentration range from $n = 10^{17}$ to 10^{19} cm^{-3} with a high electron mobility $\mu_{77} \approx 4000$ cm^2 V^{-1} s^{-1}.

(iv) In contrast to n-GaSb, the second (111)-type conduction subband does not manifest itself in n-type Te-doped $Ga_{1-X}In_XAs_YSb_{1-Y}$ solid solutions (X = 0.22 and 0.24) up to concentrations $n \approx 10^{19}$ cm^{-3}; i.e., these solid solutions can be used as direct-gap semiconductors in a wide concentration range.

(v) The studies of the electroluminescence of n-$Ga_{1-X}In_XAs_YSb_{1-Y}$/p-GaSb (X = 0.22 and 0.24) heterostructures confirm the data obtained from the galvanomagnetic effects and show the prospect of developing LEDs with a wavelength λ = 2–2.5 μm.

REFERENCES

1. T. I. Voronina, T. S. Lagunova, E. V. Kunitsyna, *et al.*, Fiz. Tekh. Poluprovodn. (St. Petersburg) **35**, 941 (2001) [Semiconductors **35**, 904 (2001)].
2. T. I. Voronina, B. E. Dzhurtanov, T. S. Lagunova, and Yu. P. Yakovlev, Fiz. Tekh. Poluprovodn. (Leningrad) **25**, 283 (1991) [Sov. Phys. Semicond. **25**, 171 (1991)].
3. A. N. Baranov, T. I. Voronina, A. N. Dakhno, *et al.*, Fiz. Tekh. Poluprovodn. (Leningrad) **24**, 1072 (1990) [Sov. Phys. Semicond. **24**, 676 (1990)].
4. A. N. Baranov, T. I. Voronina, T. S. Lagunova, *et al.*, Fiz. Tekh. Poluprovodn. (Leningrad) **23**, 780 (1989) [Sov. Phys. Semicond. **23**, 490 (1989)].
5. B. I. Shklovskiĭ and A. L. Éfros, *Electronic Properties of Doped Semiconductors* (Nauka, Moscow, 1979; Springer-Verlag, New York, 1984).
6. O. Madelung, *Physics of III–V Compounds* (Wiley, New York, 1964; Mir, Moscow, 1967).
7. B. I. Shklovskiĭ and A. L. Éfros, Zh. Éksp. Teor. Fiz. **60**, 867 (1971) [Sov. Phys. JETP **33**, 468 (1971)].
8. M. K. Sheĭkman and A. Ya. Shik, Fiz. Tekh. Poluprovodn. (Leningrad) **10**, 209 (1976) [Sov. Phys. Semicond. **10**, 128 (1976)].
9. A. S. Kyuregyan, I. K. Lazareva, V. M. Stuchebnikov, and A. Yu. Yunovich, Fiz. Tekh. Poluprovodn. (Leningrad) **6**, 242 (1972) [Sov. Phys. Semicond. **6**, 208 (1972)].

Translated by A. Kazantsev

Semiconductors, Vol. 36, No. 8, 2002, pp. 863–868. Translated from Fizika i Tekhnika Poluprovodnikov, Vol. 36, No. 8, 2002, pp. 925–931.

ELECTRONIC AND OPTICAL PROPERTIES OF SEMICONDUCTORS

Optical Properties of Bulk and Epitaxial Unordered $Ga_xIn_{1-x}P$ Semiconductor Alloys

Ya. I. Vyklyuk*, V. G. Deĭbuk, and S. V. Zolotarev

Fedkovich Chernovtsy National University, Chernovtsy, 58012 Ukraine

** e-mail: vyklyuk@mail.ru*

Submitted July 16, 2001; accepted for publication January 15, 2002

Abstract—The electron band structure of $Ga_xIn_{1-x}P$ bulk solid solutions was calculated by the local model pseudopotential method taking into account lattice mismatch. The resulting local strain of the lattice was taken into account in calculations of effective mass and deformation potential. The main optical characteristics of $Ga_xIn_{1-x}P$ alloys can be explained by the presence of internal local strains and antisite defects. In comparison with bulk samples, the concentration dependences of the spectral peaks E_1 and $E_1 + \Delta_1$ in pseudomorphic thin films were found to be more sensitive than the fundamental absorption edge E_0 to deformations caused by the substrate. © *2002 MAIK "Nauka/Interperiodica".*

INTRODUCTION

In recent years, $Ga_xIn_{1-x}P$ alloys have been attracting particular interest in connection with their application in various devices. In this context, it is important to study the strain dependences of the optical properties of both bulk and epitaxial samples. In particular, unique heterostructural properties have made $Ga_xIn_{1-x}P$-based systems attractive for the development of electronic and optical devices such as bipolar and field-effect heterojunction transistors, solar cells, light-emitting diodes, as well as semiconductor injection lasers of the visible region of the spectrum [1, 2].

However, the basic parameters of $Ga_xIn_{1-x}P$ have not yet been studied in sufficient detail. This is due to difficulties encountered in the production of high-quality crystals, since the mismatch of the GaP and InP lattice constants (5.424 and 5.869 Å, respectively) is 7.6%, which is the highest value among III–V compounds.

Ternary semiconductor III–V-based alloys with a zinc blende structure are typically crystallized as unordered alloys, where one of the two fcc sublattices (anionic or cationic) is chemically unordered. The studies [3] of the crystal structure of III–V-based ternary solid solutions using the extended X-ray absorption fine structure (EXAFS) method allowed for the determination of distinctive features in these materials. On the one hand, the sublattice, which contains atoms of two types, is structurally close to a virtual crystal and obeys the Vegard law. On the other hand, the other sublattice is significantly deformed; therefore, the distances to the nearest atoms depend only slightly on the solution composition. Local internal stresses arising in this case can cause phase transformations: destruction on the one hand and superstructure formation on the other [4]. Furthermore, it is well known that deformations often give rise to optical activity in semiconductors [5]. It is common knowledge that biaxial deformation in epitaxial films from the substrate side also has an effect on the optical characteristics of an alloy. Isotropic deformation causes shifts of the valence and conduction band energies, whereas anisotropic deformation lowers the crystal symmetry and, hence, splits degenerate bands of heavy and light holes at the point Γ. Although the strain dependence of the band gap E_0 was studied in detail [6], the experimental data on the strain dependences of the spectral peaks $E_1$and E_2 [7] have not yet been adequately explained. Therefore, in this study, we analyze the effect of internal local and biaxial deformations on E_1 and E_2 in $Ga_xIn_{1-x}P$ bulk and epitaxial samples. The electron band structure was calculated by the method of the local model pseudopotential including a strain-dependent correction [8]. This allowed us to calculate the real and imaginary parts of the dielectric function, as well as to study the dependence of the main peak positions for the imaginary part of the dielectric function on the solution composition for both a bulk sample and for thin pseudomorphic films on GaP and GaAs substrates.

ELECTRON BAND STRUCTURE

The conventional empirical pseudopotentials $v(q)$ which are specified only for discrete wave-vector values cannot adequately represent experimentally measured effective masses, deformation potentials, and other electronic characteristics of various semiconductor structures. Therefore, in this study we used the local

Table 1. Pseudopotential parameters used in the calculations for GaP and InP

Parameter	GaP		InP	
	Ga	P	In	P
a_0, eV	1.485	0.0587	0.692	0.0406
a_1, $4\pi^2/a^2$	6.268	7.644	5.820	9.010
a_2	62.023	1.217	14.049	1.204
a_3, $a^2/4\pi^2$	0.0406	0.126	0.0798	0.114
a_4	7.9	0	3.32	0
λ^S, eV	0.0001		0.00203	
λ^A, eV	0.00034		0.0005	

Note: a is the lattice constant.

model pseudopotential method, which, on the basis of plane waves, leads to the secular problem [9]

$$\det\left|\left(\frac{\hbar^2}{2m}(\mathbf{k}+\mathbf{G})^2 - E(\mathbf{k})\right)\delta_{G,G'}\delta_{s,s'} + V_{ps}(|\mathbf{G}-\mathbf{G}'|)\delta_{s,s'} + V_{SO}^{ss'}(\mathbf{G},\mathbf{G}')\right| = 0, \quad (1)$$

where $\mathbf{G}$ and $\mathbf{G}'$ are the reciprocal lattice vectors. The first and second terms correspond to the kinetic energy and the local model pseudopotential $V_{ps}(|\mathbf{G}-\mathbf{G}'|)$; the third term accounts for the spin–orbit coupling

$$V_{SO}^{ss'}(\mathbf{G},\mathbf{G}') = (\mathbf{G}\times\mathbf{G}')\sigma_{s,s'} \times\{-i\lambda^S\cos(\mathbf{G}-\mathbf{G}')\boldsymbol{\tau} + \lambda^A\sin(\mathbf{G}-\mathbf{G}')\boldsymbol{\tau}\}, \quad (2)$$

where s and s' are the spin states, $\boldsymbol{\tau} = (a/8)[1,1,1]$, a is the lattice constant, σ are the Pauli matrices, and λ^S and λ^A are the adjustable parameters of the spin–orbit coupling.

We take into account local strains in alloys by supplementing the atomic pseudopotential $v_\alpha(G)$ with the factor $[1+\delta v_\alpha(\epsilon)]$ (see [8]); then we have

$$V_{ps}(\mathbf{G},\epsilon) = \frac{1}{\Omega}\sum_{\alpha,n}\{v_\alpha(|\mathbf{G}|)[1+\delta v_\alpha(\epsilon)]\} \times\exp(i\mathbf{G}\mathbf{R}_{\alpha,n}), \quad (3)$$

where ϵ is local strain, Ω is the unit cell volume, and $\mathbf{R}_{\alpha,n}$ is the position of the nth atom of type α.

In the approximation that is linear with respect to strain,

$$\delta v_\alpha(\epsilon) = \sum_{ij} a_{ij}\epsilon_{ij}, \quad (4)$$

the conditions

$$a_{xx} = a_{yy} = a_{zz}, \quad a_{ij} = 0 \quad \text{at} \quad i \neq j \quad (5)$$

are met for the zinc blende structure.

Then, (4) can be rewritten as

$$\delta v_\alpha(\epsilon) \propto \mathrm{Tr}(\epsilon). \quad (6)$$

The choice of the functional form of the screened pseudopotential is governed by the condition of its sufficient versatility when describing the largest possible number of physical characteristics. In this case, the number of pseudopotential parameters should be within reasonable limits and the parameters themselves should not vary significantly when optimizing the electronic structure. We chose the following pseudopotential form (see [10]):

$$v_\alpha(\mathbf{G}) = a_{0\alpha}\frac{(\mathbf{G}^2 - a_{1\alpha})}{a_{2\alpha}\exp(a_{3\alpha}\mathbf{G}^2) - 1} \quad (7)$$

with

$$\delta v_\alpha(\epsilon) = a_{4\alpha}\mathrm{Tr}(\epsilon). \quad (8)$$

Table 1 lists the pseudopotential parameters a_0, a_1, a_2, a_3, a_4, as well as λ^S and λ^A. The pseudopotential determination procedure amounted to fitting the equilibrium band structure for InP and GaP binary semiconductors. Thereafter, the coefficients a_4 for cations were selected in such a way so as to fit the calculated hydrostatic deformation potentials to the experimental ones. Table 2 lists the calculated energy interband distances of InP and GaP at several high-symmetry points of the Brillouin zone in comparison with those found by the nonlocal pseudopotential method [9] and experimental values. One can see that the calculated effective masses of the electrons (m_e) at the conduction band bottom and those of heavy holes (m_{hh}) adequately conform to the experimental data.

The hydrostatic deformation potential of the band gap (E_g) at the point Γ is given by

$$a_g = \Omega\frac{\partial E_g}{\partial\Omega}. \quad (9)$$

The deformation potential a_v of the valence band maximum is determined in a similar way; then, the deformation potential of the conduction band minimum is written as $a_c = a_g + a_v$. Our calculations exhibit a rather good fit of the deformation potentials to the experimental ones [11] both in magnitude and sign.

The influence of the temperature on the band structure of $Ga_xIn_{1-x}P$ solid solutions was taken into account using the Brooks–Yu theory [9] and was described in our preceding publication [20] in detail. According to the Vegard rule and the virtual crystal approximation (VCA), the lattice constant and pseudopotentials in a $Ga_xIn_{1-x}P$ solid solution are defined as linear combinations of the corresponding values for InP (a_{InP}, V_{InP}) and GaP (a_{GaP}, V_{GaP}):

$$a_{ss} = a_{GaP}x + a_{InP}(1-x), \quad V_{ss} = V_{GaP}x + V_{InP}(1-x), \quad (10)$$

Table 2. Interband-distance energies at some symmetry points of the Brillouin zone, effective masses of electrons (m_e) and heavy holes (m_{hh}), and deformation potentials at 0 K for GaP and InP

Parameter	GaP			InP		
	Calculated data		Experimental data	Calculated data		Experimental data
	our data	[9]		our data	[9]	
Γ_{6c}–Γ_{8v}	3.06	2.88	2.86 [12]	1.51	1.50	1.46 [16]
X_{6c}–X_{7v}	4.50	4.89	5.05 [13, 14]	4.42	4.50	4.62 [16]
L_{6c}–$L_{4,5v}$	3.53	3.85	3.91 [13, 15]	3.06	3.13	3.22 [17]
X_{6c}–Γ_{8v}	2.52	2.16	2.35 [14]	2.84	2.44	2.38 [16]
Δ_0	0.211	–	–	0.377	–	–
m_e	0.17	–	0.127 [18]	0.068	–	0.077 [19]
m_{hh} [100]	0.42	–	0.45 [18]	0.45	–	0.56 [19]
a_g	–9.3	–	–9.3 [11]	–6.4	–	–6.4 [11]
a_v	–10.4	–	–10.6 [11]	–11.6	–	–11.6 [11]
a_c	–19.7	–	–19.9 [11]	–18.0	–	–18.0 [11]

Note: The energies, deformation potentials, and effective masses, are given in electronvolts, electronvolts, and free-electron masses m_0, respectively.

where a_{ss} and V_{ss} are the lattice constant and the pseudopotential form factor of the substitutional solid solution.

The slight difference between the anion pseudopotentials (P) in InP and GaP compounds confirms the experimental fact of the weak dependence of the anion sublattice parameter on the ternary solid solution composition [3].

All of the aforesaid allows us to determine the dielectric function and optical characteristics using the calculated $Ga_xIn_{1-x}P$ band structure and taking into account internal local strains.

OPTICAL CHARACTERISTICS

The calculated electron band structure is closely related to the complex dielectric function $\varepsilon(E) = \varepsilon_1(E) + i\varepsilon_2(E)$ of a semiconductor, which describes the optical response of a medium for any photon energy $E = \hbar\omega$. The complex dielectric function allows the determination of other optical characteristics, in particular, the refractive index of the medium (n), absorptivity (α), reflectance (R), and other related values. The imaginary part of the dielectric function is given by (see [9])

$$\varepsilon_2(E) = \frac{4\pi^2\hbar^2e^2}{m^2E^2} \times \sum_{vc}\int_{ZB}\frac{2d\mathbf{k}}{(2\pi)^3}|\mathbf{e}\cdot\mathbf{M}_{vc}(\mathbf{k})|^2\delta[E_c(\mathbf{k}) - E_v(\mathbf{k}) - E], \quad (11)$$

where

$$\mathbf{e}\cdot\mathbf{M}_{vc}(\mathbf{k}) = \langle\psi_{ck}|\mathbf{ep}|\psi_{vk}\rangle, \quad (12)$$

e is the polarization vector, and **p** is the momentum operator. Summation is carried out over the initial indices of the valence bands (v) and the final states of the conduction bands (c). Eight upper valence bands and four lower conduction bands were also taken into account. Integration was carried out over the first Brillouin zone using the method of tetrahedra [21]; the Brillouin zone was partitioned into 3000 equivoluminar tetrahedra. The matrix elements (12) were calculated for the obtained pseudowave functions and controlled using the selection rules [22]. In the calculation of $\varepsilon_2(E)$, exciton effects were neglected. Since GaP is an indirect-gap semiconductor compound, indirect interband transitions were taken into account when calculating $\varepsilon_2(E)$. Then, in the case of phonon absorption $\hbar\omega_q$ (see [22]), we have

$$\varepsilon_2(E) = \frac{4\pi^2h^2e^2}{m^2E^2}\int_{ZB}\int_{ZB}\frac{2d\mathbf{k}_1d\mathbf{k}_2}{(2\pi)^3(2\pi)^3} \times \left|\frac{\langle\psi_{ck_2}|V_p(\mathbf{q},\mathbf{r})|\psi_{\beta k_1}\rangle n_q^{1/2}\langle\psi_{\beta k_1}|\mathbf{ep}|\psi_{vk_1}\rangle}{E_\beta(\mathbf{k}_1) - E_v(\mathbf{k}_1) - E}\right|^2 \times \delta[E_c(\mathbf{k}_2) - E_v(\mathbf{k}_1) - E - \hbar\omega_q], \quad (13)$$

where n_q are the occupation numbers of the phonon states involved in transitions.

The real part $\varepsilon_1(E)$ of the dielectric function was calculated using the Kramers–Kronig relation. Figures 1 and 2 display the results of calculations of $\varepsilon_1(E)$ and $\varepsilon_2(E)$ for InP and GaP in comparison with the experimental dependences [23]. The interband transitions were analyzed in detail, and the main peaks were identified in our previous publication [24].

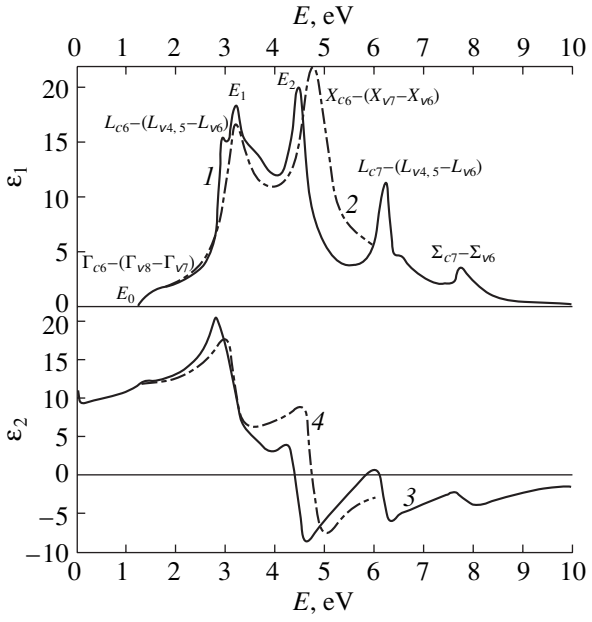

Fig. 1. Real (ε_1) and imaginary (ε_2) parts of the InP dielectric function at 300 K: (*1*, *3*) our calculations and (*2*, *4*) the experimental data of [23].

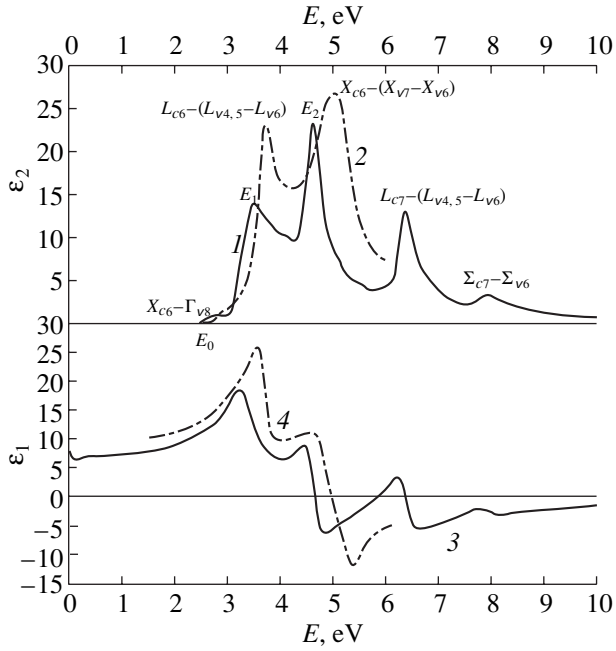

Fig. 2. Real (ε_1) and imaginary (ε_2) parts of the GaP dielectric function at 300 K: (*1*, *3*) our calculations and (*2*, *4*) the experimental data of [23].

As is known from the general theory of optical interband transitions, the $\varepsilon_2(E)$ spectrum is quantitatively defined by the correctness of the band dispersion calculations, the probability of electron transitions, and consideration of all Brillouin zone points.

BULK CRYSTAL

Having obtained a good fit of the real and imaginary parts of the GaP and InP dielectric function with the experiment, we pass on to the consideration of the behavior of the imaginary part $\varepsilon_2(E)$. First, we study variations in the E_1 peak position, which we accurately determined by analyzing the second derivative $d^2(\varepsilon_2)/d\omega^2$ (the E_0 behavior was studied in [20]). Using the Vegard law, we found that the linear dependence $E_1(x)$ (see Fig. 3) significantly differs from the experimental one. The latter can be approximated as $E_1(x) = 3.18 + 0.58x + 0.86x(x - 1)$ [25]. To explain the curve deflection, we initially took into account the fact that the alloy lattice constant varies by the nonlinear law [26], which is caused by local strains [8]. The latter, in turn, can be taken into account by the modified pseudopotential (3) with the relative change of the unit cell volume given by

$$\mathrm{Tr}(\epsilon) = \frac{\Delta\Omega}{\Omega}. \qquad (14)$$

One can see from Fig. 3 that this contribution to the deviation of the dependence $E_1(x)$ from the linear one is insignificant. The significant difference between the InP and GaP lattice constants is also caused by antisite defects [27], whose effect on the alloy band structure was taken into account in our previous paper [20]. Antisite defects give rise to the deflection of the dependences $E_1(x)$ and $E_1(x) + \Delta_1$, which conforms satisfactorily to the experimental data [24] (see Figs. 3, 4). The results of calculations of $E_2(x)$ and $E_2(x) + \Delta_2(x)$ are presented in Fig. 4. In this case, the deflection is less pronounced than that of $E_1(x)$ and $E_1(x) + \Delta_1(x)$ and its minimum is at the point $x = 0.5$. Furthermore, $\Delta_2 < \Delta_1$. This is explained by the fact that the splitting of the upper valence band at the point X is slighter than that at the point L [20]. A detailed analysis of the interband transitions showed that the transitions in the direction Λ of the Brillouin zone (where the valence and conduction bands are almost parallel) mainly contribute to the peaks E_1 and $E_1 + \Delta_1$. The transitions at the point X and in the direction Σ contribute to E_2.

EFFECT OF BIAXIAL DEFORMATION IN FILMS

The epitaxial growth of semiconductor alloys with lattice parameters differing from those of the substrate causes mismatch deformation in the epilayer. The mismatch strain can elastically relax due to tetragonal distortion on condition that the epilayer is not too thick (pseudomorphic film). As the mismatch between the layer and substrate lattice constants increases, the layer will relax in the direction of its bulk structure; as a result, the misfit dislocations are generated.

The optical characteristics of thin pseudomorphic InGaP films determined experimentally [7, 28, 29] differ from those of bulk samples, depend on the substrate

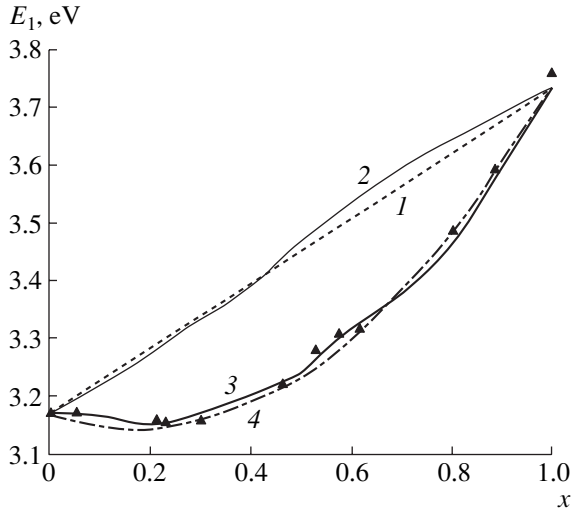

Fig. 3. Concentration dependence of the E_1 peak for the bulk alloy taking into account (*1*) only the Vegard law, (*2*) the lattice constant nonlinearity, (*3*) the lattice constant nonlinearity and antisite defects, (*4*) the approximation of the experimental data of [25] (triangles).

material, and have singularities in the concentration dependence $E_1(x)$. To explain these singularities, in addition to the abovementioned factors taking place in bulk samples, we considered the epilayer biaxial strain caused by the substrate. The chosen pseudopotential also allows for the consideration of film biaxial strain. In this case, the strain tensor components can be written as (see [1])

$$\epsilon_{xx} = \epsilon_{yy} = -\delta,$$
$$\epsilon_{zz} = \frac{2C_{12}}{C_{11}}\delta, \qquad (15)$$

where $\delta = (a_{InGaP} - a_{sub})/a_{sub}$; and a_{InGaP} and a_{sub} are the lattice constants of the bulk alloy and the substrate, respectively.

As our calculations and the theoretical studies [1] have shown, biaxial deformation changes the band structure in the following way. Under compressive deformation (the substrate lattice constant is smaller than that of the film), the band gap increases due to a rise of the conduction band, while the position of the upper valence band is virtually unchanged. The case of tensile deformation is opposite: the lower conduction band goes down, while the position of the upper valence band is also virtually unchanged, and the band gap narrows.

We studied GaAs and GaP substrates. In the case of the GaP substrate, compressive strains arise in the InGaP alloy, since the lattice constant of the film exceeds that of the substrate. As indicated above, the compressive strain widens the band gap, which in turn shifts the peaks E_1 and E_2 to higher energies. Hence, the $E_1(x)$ and $E_2(x)$ deflection will be slighter for the case

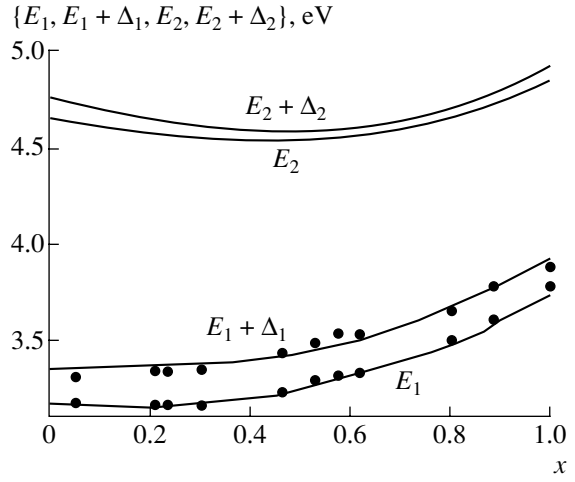

Fig. 4. Concentration dependences of the peaks $E_1(x)$, $E_1(x) + \Delta_1(x)$, $E_2(x)$, and $E_2(x) + \Delta_2(x)$ for $Ga_xIn_{1-x}P$ bulk samples; dots are the experimental data of [25].

of the GaP substrate than that for bulk samples. Figure 5 shows the results of our calculations in comparison with the experimental data of [7] for $Ga_xIn_{1-x}P/GaP$.

The case of GaAs substrate is somewhat different. The lattice constant of the alloy coincides with that of the substrate at $x = 0.4815$. Hence, compressive and tensile strains arise in the substrate at $x < 0.4815$ and $x > 0.4815$, which shifts the E_1 and E_2 peaks to higher and lower energies, respectively. This results in that the deflection of the concentration dependences $E_1(x)$ and $E_2(x)$ significantly decreases in the film relative to that of the bulk sample, while the peak E_2 and $E_2 + \Delta_2$ positions remain virtually unchanged at $x = 0.45$–0.7. This range is much wider for E_1 and $E_1 + \Delta_1$, $x = 0.2$–0.9, which is also confirmed experimentally [7] (see Fig. 6). Thus, the optical characteristics, as well as the band

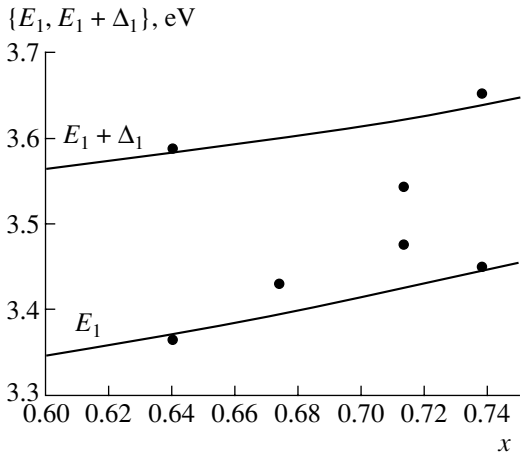

Fig. 5. Concentration dependences of the peaks $E_1(x)$ and $E_1(x) + \Delta_1(x)$ for $Ga_xIn_{1-x}P/GaP$; dots are the experimental data of [7].

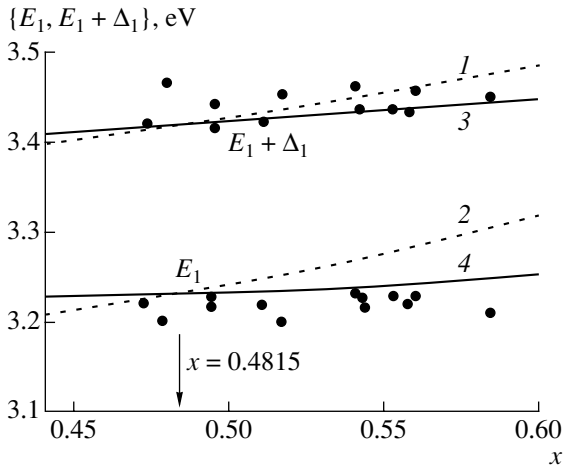

Fig. 6. Concentration dependences of the peaks $E_1(x)$ and $E_1(x) + \Delta_1(x)$ for the (*1*, *2*) $Ga_xIn_{1-x}P$ bulk sample and (*3*, *4*) $Ga_xIn_{1-x}P$/GaAs film; dots are the experimental data of [7].

structure of thin films, significantly differ from those inherent to bulk samples. Consideration of the biaxial strain allows for a correct explanation of the special features of the optical characteristics of thin films.

CONCLUSION

The electron band structure of bulk $Ga_xIn_{1-x}P$ solid solutions was studied using the local model pseudopotential method taking into account the lattice mismatch. The arising local strain of the lattice was taken into account when calculating the effective masses and deformation potentials. The consideration of internal local strains and antisite defects in $Ga_xIn_{1-x}P$ alloys allows for an explanation of their basic optical characteristics.

In comparison with bulk samples, the concentration dependences of the peaks $E_1(x)$ and $E_1(x) + \Delta_1(x)$ in pseudomorphic thin films are more sensitive than the fundamental absorption edge E_0 to deformations from the substrate side.

REFERENCES

1. S. C. Jain, M. Willander, and H. Maes, Semicond. Sci. Technol. **11**, 641 (1996).
2. G. M. Cohen, P. Zisman, G. Bahir, and D. Ritter, J. Vac. Sci. Technol. B **16**, 2639 (1998).
3. J. C. Mikkelsen, Jr. and J. B. Boys, Phys. Rev. B **28**, 7130 (1983).
4. R. Asomoza, V. A. Elyukhin, and S. G. Konnikov, Semicond. Sci. Technol. **10**, 1122 (1995).
5. B. Koopmans, P. V. Santos, and M. Cardona, Phys. Status Solidi B **205**, 419 (1998).
6. K. Ozasa, M. Yuri, S. Tanaka, and H. Matsunami, J. Appl. Phys. **68**, 107 (1990).
7. H. Lee, D. Biswas, M. V. Klein, *et al.*, J. Appl. Phys. **75**, 5040 (1994).
8. T. Matilla, L.-W. Wang, and A. Zunger, Phys. Rev. B **59**, 15270 (1999).
9. M. L. Cohen and J. R. Chelikowsky, *Electronic Structure and Optical Properties of Semiconductors* (Springer-Verlag, Berlin, 1988).
10. M. Schluter, J. R. Chelikowsky, S. G. Louis, and M. L. Cohen, Phys. Rev. B **12**, 4200 (1975).
11. A. Blacha, H. Presting, and M. Cardona, Phys. Status Solidi B **126**, 11 (1984).
12. D. Nelson, L. Johnson, and M. Gershenzon, Phys. Rev. **135**, A1399 (1964).
13. L. Ley, R. Pollak, R. McFeely, *et al.*, Phys. Rev. B **9**, 600 (1974).
14. D. Kyser and V. Rehn, Phys. Rev. Lett. **40**, 1038 (1978).
15. D. Aspnes, C. Olson, and D. Lynch, Phys. Rev. B **12**, 1371 (1975).
16. J. Camassel, P. Merle, L. Bayo, and H. Mathieu, Phys. Rev. B **22**, 2020 (1980).
17. E. Matatagui, A. Thompson, and M. Cardona, Phys. Rev. **176**, 950 (1968).
18. S.-G. Shen and X.-Q. Fan, J. Phys.: Condens. Matter **8**, 4369 (1996).
19. M. Helm, W. Knap, W. Seidenbusch, *et al.*, Solid State Commun. **53**, 547 (1985).
20. S. V. Korolyuk, Ya. I. Vyklyuk, and V. G. Deĭbuk, Ukr. Fiz. Zh. **45**, 318 (2000).
21. G. Lehmann and M. Taut, Phys. Status Solidi B **54**, 469 (1972).
22. F. Bassani and G. Pastori Parravicini, *Electronic States and Optical Transitions in Solids* (Pergamon, New York, 1975; Nauka, Moscow, 1982).
23. D. E. Aspnes and A. A. Studna, Phys. Rev. B **27**, 985 (1983).
24. Ya. I. Vyklyuk and V. G. Deĭbuk, Ukr. Fiz. Zh. **46**, 1185 (2001).
25. C. Alibert, G. Bordure, A. Laugier, and J. Chevallier, Phys. Rev. B **6**, 1301 (1972).
26. J. L. Martins and A. Zunger, Phys. Rev. B **30**, 6217 (1984).
27. A. N. Georgobiani and I. M. Tiginyanu, Fiz. Tekh. Poluprovodn. (Leningrad) **22**, 3 (1988) [Sov. Phys. Semicond. **22**, 1 (1988)].
28. A. Bensaada, A. Chennouf, R. W. Cochrane, *et al.*, J. Appl. Phys. **75**, 3024 (1994).
29. F. H. Pollak and M. Cardona, Phys. Rev. **172**, 816 (1968).

Translated by A. Kazantsev

Semiconductors, Vol. 36, No. 8, 2002, pp. 869–873. Translated from Fizika i Tekhnika Poluprovodnikov, Vol. 36, No. 8, 2002, pp. 932–936.

ELECTRONIC AND OPTICAL PROPERTIES OF SEMICONDUCTORS

Electrical and Thermoelectric Properties of *p*-Ag_2Te

F. F. Aliev*, E. M. Kerimova, and S. A. Aliev

Institute of Physics, Academy of Sciences of Azerbaijan, pr. Dzhavida 33, Baku, 370143 Azerbaijan

**e-mail: physic@physics.ab.az*

Submitted November 26, 1999; accepted for publication January 25, 2002

Abstract—Temperature dependences of the Hall coefficient R, electrical conductivity σ, and thermopower α_0 are investigated in the range of 4–300 K. The specific features observed in temperature dependences $R(T)$, $\sigma(T)$, and $\alpha_0(T)$ are interpreted in the context of a model with two types of charge carriers. © *2002 MAIK "Nauka/Interperiodica".*

INTRODUCTION

Numerous studies have been devoted to the investigation of the electrical and thermoelectric properties of Ag_2Te [1–8]. It was demonstrated that the electron dispersion law for *n*-Ag_2Te is governed by the Kane model [1, 2]. In the range of 4–300 K, the fundamental mechanisms of charge carrier scattering are scattering by ionized impurities and optical phonons [1–4].

In contrast with *n*-Ag_2Te, electrical and thermoelectric properties of *p*-Ag_2Te have specific features which are not observed for *n*-Ag_2Te. Their analysis requires more precise knowledge of the properties of charge carriers in *p*-Ag_2Te. Despite the series of studies which are devoted to this issue for *p*-Ag_2Te [4–8], the problem can not be considered as resolved.

This study is devoted to the investigation of temperature dependences of the Hall coefficient $R(T)$, conductivity $\sigma(T)$, and thermopower $\alpha_0(T)$ with the purpose of determining a number of properties of charge carriers in *p*-Ag_2Te.

EXPERIMENTAL

The *p*-Ag_2Te samples were obtained according to the single technique [9] with the Te excess as high as ~1 at. % [10]. The homogeneity in the solid state was investigated by the dilatometry technique [9]. For measurements, the samples were fabricated in the form of parallelepipeds $2 \times 3 \times 10$ mm in size. The experimental data obtained on the temperature dependences of kinetic coefficients $R(T)$, $\sigma(T)$, and $\alpha_0(T)$ are shown in Fig. 1.

The temperature dependence of the Hall coefficient $R(T)$ is shown by curve *1* in Fig. 1. It can be seen that $R(T)$ is independent of T up to $T \approx 45$ K. After that, it decreases with increasing temperature; and at $T \approx 65$ K, it changes its sign to a negative one and attains the peak absolute value $|R|$ at $T \approx 80$ K. Further, $|R|(T)$ decreases gradually, and, in the temperature range of 200–300 K, the decrease in $|R|$ diminishes. The temperature dependence of conductivity σ is shown by curve *2* in Fig. 1. From a comparison of $\sigma(T)$ and $R(T)$, it can be seen that $\sigma(T)$ at $T \lesssim 45$ K repeats the run of $R(T)$. At the temperature $T \approx 65$ K, which corresponds to the temperature of reversal of the sign of R, this curve passes through a minimum and further increases as the temperature increases, and at $T \approx 200$ K, it passes through a maximum. Curve *3* in Fig. 1 demonstrates the temperature dependence of thermopower $\alpha_0(T)$, which increases linearly up to $T \lesssim 45$ K and then changes its sign. At $T \approx 80$ and 270 K, the peaks of the dependence $|\alpha_0(T)|$ manifest themselves.

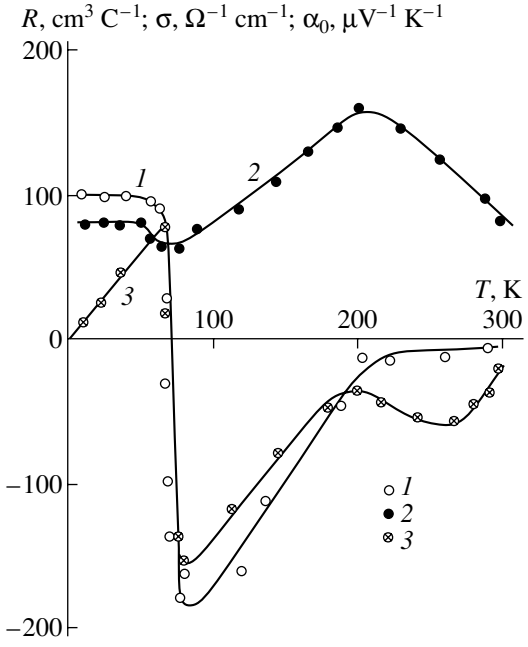

Fig. 1. Temperature dependences of (*1*) the Hall coefficient R for $H = 12$ kOe, (*2*) conductivity σ, and (*3*) thermopower α_0. Solid lines represent the results of calculations.

DISCUSSION

The temperature dependences $\sigma(T)$, $R(T)$, and $\alpha_0(T)$ for p-Ag_2Te were discussed previously [5–8]. The authors of [5] tried to explain the plateaus observed in the $R(T)$ dependence in the region $T \simeq 230$–300 K. The slope of $R(T)$ at $T \gtrsim 80$ K was used [5] to estimate the activation energy at 0.04 ± 0.01 eV, assuming that local energy levels emerge in the band gap. The presence of the plateau in the $R(T)$ curve is caused by the depletion of these energy levels [5]. It was concluded [6] that the charge carrier density for the region of the intrinsic conductivity of p-Ag_2Te is governed by the power-law dependence $n_i \propto T^3$. This dependence corresponds to the band-to-band activation of charge carriers with a substantially nonparabolic energy spectrum of electrons and holes. It is believed [6] that a sharp weakening of the increase in the electron density, namely, the emergence of the plateau in the $R(T)$ curve in the temperature range of ~250–300 K, can be explained by the presence of an additional valence band with a higher density of states.

It was assumed [7] that the presence of a conductivity peak and certain anomalies of thermopower in the range $T \simeq 248$–283 K could be associated with a possible phase transition. A decrease in the $|\alpha_0|$ quantity at $T > 283$ K is more characteristic of impurity conduction. In contrast with this, a decrease in $|\alpha_0|$ with decreasing temperature is related to variation in the scattering mechanism and phonon drag of charge carriers. It has been demonstrated [8] that, in the temperature range of 140–200 K, the $\alpha_0(T)$ quantity varies according to the law $|\alpha_0| \propto T^3$ and that the charge carriers are dragged by phonons in this temperature range.

The authors of [5–8], with the absence of low-temperature investigations of R, σ, and α_0, and with no allowance made for the temperature dependence of band parameters, made, according to our opinion, unjustified conclusions. In order to clarify this issue, the complex analysis of temperature dependences $\sigma(T)$, $R(T)$, and $\alpha_0(T)$ should be carried out with allowance made for the dispersion law of the electron spectrum and scattering mechanisms.

Such an analysis was carried out as follows.

The experimental data (Fig. 1) indicate that the low-temperatures hole gas is degenerate at $T \lesssim 50$ K. The Hall coefficient R and conductivity σ are independent of temperature, whereas the temperature dependence of thermopower $\alpha_0(T)$ is linear. Actually, it is known that the thermopower α_0 for each degree of degeneracy of the charge-carrier gas in a conventional band is expressed as follows:

$$\alpha_0 = -\frac{k_0}{e}\left[\frac{F_{r+2}(\mu^*)}{F_{r+1}(\mu^*)} - \mu^*\right]. \quad (1)$$

Here, μ is the Fermi level; $\mu^* = \mu/k_0T$; $F_r(\mu^*)$ is the Fermi-Dirac integral, defined in [11] as

$$F_r = \int_0^\infty \left(-\frac{\partial f_0}{\partial x}\right) x^r dx;$$

$x = \varepsilon/k_0T$; and the subscript r is determined from the $\tau(\varepsilon)$ dependence, which is the dependence of the relaxation time of charge carrier momentum on energy ε:

$$\tau(\varepsilon) = \tau_{0r}(T)\left(\frac{\varepsilon}{k_0T}\right)^{r-1/2}, \quad (2)$$

where $r = r_{ac} = 0$ for scattering by acoustic phonons; and $r = r_i = 2$ for scattering by impurity ions. From formula (1), for $\mu^* \gtrsim 10$, we derive $\alpha_0 \propto T$.

Let us use the value for the effective mass of holes $m_p = 0.12m_0$ [3] and assume that the donor density $N_d = 0$. In this case, from the Hall coefficient at $T < 50$ K, we find the acceptor density $N_a = 6.25 \times 10^{16}$ cm^{-3} and the temperature of eliminating the degeneracy of the hole gas $T_{hd} \approx 56$ K.

At $T \gtrsim 60$ K, the degeneracy of holes is eliminated and intrinsic conduction manifests itself, which is shown by the experimental data shown in Fig. 1. Using the temperature dependence of the band gap for Ag_2Te [12, 13],

$$E_g(T) = (0.035 - 7 \times 10^{-5}T) \text{ eV},$$

and the equation of neutrality $N_a = p - n$ for the region of intrinsic conduction, we can make an estimation and demonstrate that the intrinsic electron density n_i at approximately $T \gtrsim 200$ K increases to such a degree that the degeneracy of the electron gas manifests itself, which is characteristic of narrow-gap semiconductors. Such an estimation is confirmed by the temperature dependences $R(T)$, $\sigma(T)$, and $\alpha(T)$ at $T \gtrsim 200$ K.

In the region of intrinsic conduction, for two types of charge carriers, the quantities $R(T)$, $\sigma(T)$, and $\alpha_0(T)$ in a weak magnetic field H for $(U_pH)^2 \ll 1$, $(U_nH)^2 \ll 1$, where U_p and U_n are the mobilities of electrons and holes, are determined from the following formulas [14]:

$$R = \frac{1}{N_a e}\frac{(1-c)(1-b^2c)}{(1+bc)^2}, \quad (3)$$

$$\sigma = N_a e U_n \frac{1+bc}{b(1-c)}, \quad (4)$$

$$\alpha_0 = \frac{\alpha_{0p}\sigma_p - \alpha_{0n}\sigma_n}{\sigma_p + \sigma_n}. \quad (5)$$

Here, $N_a = p(1-c)$ is the acceptor concentration; $b = U_n/U_p$ is the ratio of mobilities for electrons and holes; $c = n/p$ is the ratio of densities of electrons n and holes p; and σ_p, σ_n, α_{0p}, and α_{0n} are the conductivities and thermopowers for holes and electrons, respectively.

We now turn our attention to the determination of the ratio of mobilities $b(T)$. With the reversal of the sign of the Hall coefficient R, the ratio of mobilities is equal to $b = 1/c^2$, whereas for the minimum $|R(T)| = |R_{min}|$ ($T \approx 80$ K), $b = 1/c$ [14], so that

$$|R_{min}| = \frac{(1-b)^2}{4beN_a}.$$

Above $T \approx 80$ K, the value of b was selected so that the calculated R values coincided with the experimental data (see Fig. 1, curve *1*, and Fig. 2). The dependence $c(T)$ was calculated according to the relationship

$$c = \frac{n_i}{N_a + p_i}.$$

If $b(T)$ and $c(T)$ are known, we can use relations (3)–(5) and the data on $\sigma(T)$ (Fig. 1, curve *2*) to determine the dependences $U_n(T)$ and $U_p(T) = U_n(T)/b(T)$ (Fig. 3).

The calculated temperature dependences of electron mobility at $T > 50$ K, when the electron contribution to kinetic coefficients begins to become noticeable against the background of the hole conduction (Fig. 1), were determined for two cases. These are the cases of nondegenerate electron gas (at $T < 200$ K) and degenerate electron gas, both for the conventional (parabolic) conduction band and for the nonparabolic one (at $T > 200$ K). The temperature dependence of mobility has the form

$$U(T) = \frac{e\langle\tau_{eff}(T, \varepsilon)\rangle}{m^*}. \quad (6)$$

Here, τ_{eff} is the momentum-relaxation time and m^* is the effective mass of charge carriers. Averaging the electrons by energy is denoted by broken brackets.

When two scattering mechanisms with the parameters r_i and r_{ac} exist, the effective transport time for relaxations is calculated using a representation of $\tau(\varepsilon)$ in the form of (2) [11]; i.e.,

$$\tau_{eff}(T, \varepsilon) = \frac{\tau_{0i}(T)\tau_{0ac}(T)\left(\frac{\varepsilon}{k_0T}\right)^{r_{ac}-1/2}}{\tau_{0i}(T) + \tau_{0ac}(T)\left(\frac{\varepsilon}{k_0T}\right)^{r_{ac}-r_i}}. \quad (7)$$

When determining $\tau_{0i}(T)$ for scattering by ionized impurity atoms, we can use the formula

$$\tau_{0i}(T) = \frac{\chi^2(2m_n)^{1/2}(k_0T)^{3/2}}{\pi e^4 N_i F}. \quad (8)$$

Here, $m_n = 0.025m_0$ [1], $\chi = 16$ is the dielectric constant of the crystal, and N_i is the concentration of impurity ions;

$$F = \ln(1+\xi) - \frac{\xi}{1+\xi}; \quad \xi = 4k^2r_S^2,$$

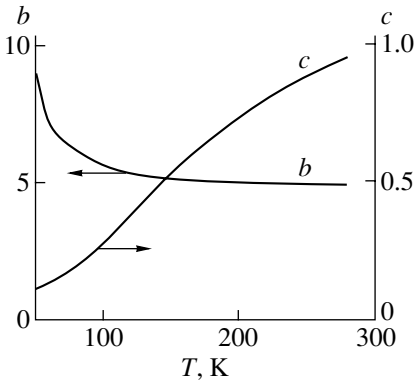

Fig. 2. Temperature dependences of the ratio of electron and hole mobilities $b = U_n/U_p$ and the ratio of electron and hole densities $c = n_i/(N_a + p_i)$.

where r_S is the screening length defined for nondegenerate semiconductors as

$$r_S = \left(\frac{\chi k_0 T}{4\pi e^2 n}\right)^{1/2};$$

n is the electron density; and k is the momentum of the electron with the energy $\varepsilon = \hbar^2k^2/2m_n$.

The formula for $\tau_{0ac}(T)$, which is the temperature coefficient in formula (2) for electron scattering by the deformation potential of lattice acoustic vibrations with a conventional band, has the form

$$\tau_{0ac}(T) = \frac{9\pi}{2}\frac{\rho U_0^2\hbar^4}{C^2(2m_nk_0T)^{3/2}}, \quad (9)$$

where ρ is the density of the crystal, C is a constant, and U_0 is the velocity of sound in the crystal. It was found [15] that the C quantity is related to the constant of the deformation potential of the lattice E_d as follows: $E_d = \frac{2}{3}C$. Taking into account the values $\rho = 8.32$ kg/cm^3 [9], $U_0 = 5 \times 10^5$ cm/s [16], and assuming that $E_d = 10$ eV, it is possible to calculate $\tau_{0ac}(T)$.

Substituting expressions (8) and (9) into formula (7), we determine $\tau_{eff}(T) = \langle\tau_{eff}(T, \varepsilon)\rangle$ for simultaneous electron scattering by ionized impurities and acoustic lattice vibrations, and, using relationship (6), we determine the temperature dependence of mobility U_{0n}' for a nondegenerate electron gas (Fig. 3).

Using

$$r_S = \left[\frac{\chi\hbar^2}{4m_ne^2}\left(\frac{\pi}{3n}\right)^{1/2}\right],$$

we can similarly calculate the mobility U_{0n}'' for a degenerate electron gas (Fig. 3).

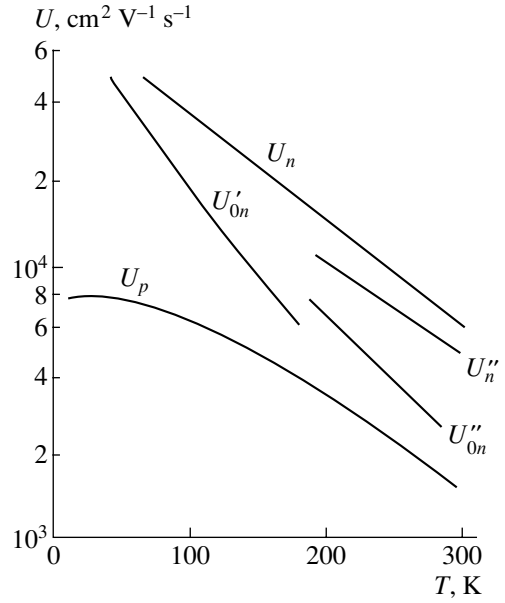

Fig. 3. Temperature dependences of mobilities of electrons U_n and holes U_p determined from the experimental data using formulas (3)–(5). The calculated dependences for the electron mobility: U'_{0n} for a nondegenerate electron gas, U''_{0n} for a degenerate electron gas and parabolic band, and U''_n for a degenerate electron gas and a nonparabolic band (expressions (10)–(12)).

When high degeneracy and the Kane dispersion law for scattering by acoustic phonons ($r_{ac} = 0$) and impurity ions ($r_i = 2$) are present, the charge-carrier mobility is given by [17]

$$U''_{ac} = \left(\frac{\pi}{3}\right)^{1/3} \frac{e\rho U_0^2 \hbar^3 n^{-1/3}}{E_d k_0 T (m^*)^2} \frac{1}{f_{ac}}, \quad (10)$$

$$U''_i = \frac{3\pi^2 \hbar^3 \chi^2}{2em^*} \frac{1}{f_i}. \quad (11)$$

Here, f_i are the factors which account for the influence of nonparabolicity on scattering probability. These factors are calculated using the following formulas [18]:

$$f_{ac}(P/P_0) = \frac{2.3}{12} - \frac{1}{20}\frac{P}{P_0} + \frac{10.3}{12}\left(\frac{P}{P_0}\right)^2,$$

$$f_i(P/P_0) = a - \frac{b'}{2} + \frac{1}{16}(b' + 3c')$$

$$+ \left[\frac{b'}{2} - \frac{1}{8}(b' + 3c')\right]\left(\frac{P}{P_0}\right) + \frac{b' + 3c'}{16}\left(\frac{P}{P_0}\right)^2.$$

Here,

$$a = \ln\left(1 + \frac{1}{\xi'}\right) - \frac{1}{1 + \xi'}, \quad b' = 4 + \frac{4\xi'}{1 + \xi'} - 8\xi' \ln\left(1 + \frac{1}{\xi'}\right),$$

$$c' = 2 - 12\xi' + \frac{4\xi'}{1 + \xi'} + 12\xi'^2 \ln\left(1 + \frac{1}{\xi'}\right),$$

$$P = \left(\frac{m_0}{m^*} - 1\right),$$

$$P_0 = \left(\frac{m_0}{m_n} - 1\right), \quad \xi' = \frac{e^2 m^*}{\pi\hbar^2 \chi (3\pi n)^{1/3}} = \frac{1}{4k_F^2 r_S^2},$$

where m^* and m_n are the effective electron masses at the Fermi level and at the conduction band bottom [1, 2], and k_F is the quasi-momentum at the Fermi level. The calculated temperature dependences of mobility for a degenerate electron gas with allowance made for (10) and (11),

$$U''_n(T) = \left(\frac{1}{U''_{ac}} + \frac{1}{U''_i}\right)^{-1}, \quad (12)$$

are shown in Fig. 3.

It can be seen from Fig. 3 that the calculated dependences $U'_{0n}(T)$ at $T \lesssim 200$ K and $U''_{0n}(T)$, $U''_n(T)$ at $T \gtrsim 200$ K are in qualitative agreement with the dependence $U_n(T)$, which was determined from formulas (3)–(5) and experimental data. The similarly determined hole mobility $U_p(T)$ at $T \lesssim 50$ K is independent of temperature, as it should be for a highly degenerate hole gas when there is scattering by impurity ions. With increasing temperature, hole scattering by phonons prevails.

The comparison of the data on $U_n(T)$ with theoretical calculations demonstrates that the calculated electron mobilities are lower than the experimental ones. This can be associated with the fact that the screening length for Ag_2Te is close to the lattice constant.

Taking into account the results of calculations of $c(T)$, $b(T)$, and $U_n(T)$, and using formulas (3)–(5), we calculated the dependences $R(T)$, $\sigma(T)$, and $\alpha_0(T)$, which are shown in Fig. 1 by solid lines.

Thus, at $T \lesssim 50$ K, the Ag_2Te sample investigated has *p*-type conductivity with a high degeneracy of the hole gas. The temperature range 50 K $\lesssim T \lesssim$ 200 K corresponds to the region of intrinsic conductivity, and the temperature dependences of the kinetic coefficients $R(T)$, $\sigma(T)$, and $\alpha_0(T)$) are determined by two types of carriers.

At $T > 200$ K, the electrons start to make the main contribution to the conduction and a progressively higher degeneracy of the electron gas manifests itself with increasing temperature. Correspondingly, the signs of the Hall effect and thermopower correspond to the *n*-type conduction (Fig. 1). In this case, the Hall coefficient $R = 1/en$; it depends only slightly on temperature. The dependence $\sigma(T)$ is governed by the temperature dependence of electron mobility $U_n(T) \propto T^{-1.2}$ when there is scattering by acoustic phonons. In the range of 200 K < T < 270 K, the dependence of ther-

mopower on temperature is determined by expression (1) if the nonparabolicity of the conduction band is disregarded. In this temperature range, the reduced chemical potential $\mu^* = \mu/kT$ is determined by a rapid increase in the value of $\mu > 0$, which is measured from the conduction-band bottom. In these conditions, formula (1) predicts a decrease in the magnitude of $|\alpha_0|$. On reaching T = 270 K and with a sufficiently high degeneracy (magnitude $\mu^* > 5$), the chemical potential μ varies only slightly with increasing temperature. As a result, $|\alpha_0(T)| \propto 1/\mu^* = kT/\mu$ [11]; i.e., the absolute value of the thermopower increases linearly with temperature, similarly to the region of low-temperature hole conduction.

CONCLUSION

Thus, the causes for decreasing σ, the dependence $R(T)$, and the emergence of the $|\alpha_0|$ peak in the temperature range of ~200–300 K are clarified.

From the aforesaid it can be concluded that the suggested model with two types of charge carriers adequately describes the electrical and thermoelectric properties of p-Ag_2Te.

REFERENCES

1. S. A. Aliev, U. Kh. Suyunov, and M. I. Aliev, Fiz. Tekh. Poluprovodn. (Leningrad) **7** (10), 2024 (1973) [Sov. Phys. Semicond. **7**, 1353 (1974)].
2. S. A. Aliev and Z. F. Agaev, Izv. Akad. Nauk SSSR, Neorg. Mater. **19** (12), 2050 (1983).
3. S. A. Aliev and F. F. Aliev, Izv. Akad. Nauk SSSR, Neorg. Mater. **24** (2), 341 (1988).
4. S. A. Aliev, F. F. Aliev, S. G. Abdinova, *et al.*, Izv. Vyssh. Uchebn. Zaved., Fiz., No. 6, 41 (1990).
5. V. V. Gorbachev and I. M. Putilin, Izv. Akad. Nauk SSSR, Neorg. Mater. **11** (9), 1556 (1975).
6. A. S. Koroleva, V. Yu. Martynov, and P. P. Petrov, in *Proceedings of the 2nd Conference of Chernovtsy State University "Materials Science of Chalcogenide Oxygen-Containing Semiconductors", Chernovtsy, 1996*, p. 47.
7. O. P. Astakhov, Izv. Akad. Nauk SSSR, Neorg. Mater. **10** (9), 1614 (1974).
8. V. P. Zhuze, I. M. Tsidil'kovskiĭ, and T. S. Bartnitskaya, Zh. Tekh. Fiz. **8**, 1646 (1958).
9. V. M. Glazov and N. M. Makhmudova, Izv. Akad. Nauk SSSR, Neorg. Mater. **6** (8), 1409 (1970).
10. S. A. Aliev and F. F. Aliev, Izv. Akad. Nauk SSSR, Neorg. Mater. **25** (2), 241 (1989).
11. B. M. Askerov, *Kinetic Effects in Semiconductors* (Nauka, Leningrad, 1970).
12. F. F. Aliev, Izv. Inst. Fiz. Akad. Nauk Resp. Az., Fiz. **11** (4), 15 (1996).
13. F. F. Aliev, in *Proceedings of Second International Symposium on Mathematical and Computational Applications, Baku, 1999*, p. 80.
14. C. Hilsum and A. C. Rose-Innes, *Semiconducting III–V Compounds* (Pergamon, Oxford, 1961; Inostrannaya Literatura, Moscow, 1963).
15. G. E. Pikus, Zh. Tekh. Fiz. **28**, 2390 (1958) [Sov. Phys. Tech. Phys. **3**, 2194 (1958)].
16. *Physicochemical Properties of Semiconductor Materials: Handbook* (Nauka, Moscow, 1979).
17. T. A. Aliev, F. M. Gashim-zade, S. A. Aliev, *et al.*, Fiz. Tekh. Poluprovodn. (Leningrad) **5** (2), 323 (1971) [Sov. Phys. Semicond. **5**, 274 (1971)].

Translated by N. Korovin

Semiconductors, Vol. 36, No. 8, 2002, pp. 874–877. Translated from Fizika i Tekhnika Poluprovodnikov, Vol. 36, No. 8, 2002, pp. 937–940.

ELECTRONIC AND OPTICAL PROPERTIES OF SEMICONDUCTORS

Photoconductivity of Coarse-Grained CdTe Polycrystals

S. A. Medvedev, Yu. V. Klevkov, S. A. Kolosov, V. S. Krivobok, and A. F. Plotnikov

Lebedev Physical Institute, Russian Academy of Sciences, Leninskiĭ pr. 53, Moscow, 119991 Russia

Submitted January 30, 2002; accepted for publication February 13, 2002

Abstract—The photoconductivity spectra of textured coarse-grained CdTe polycrystals grown by low-temperature synthesis from deeply purified components are investigated. It is shown that photoconductivity is controlled by complexes of extended defects with segregated impurities. *© 2002 MAIK "Nauka/Interperiodica".*

1. INTRODUCTION

For years, widespread use of polycrystalline semiconductors in microelectronics was hindered by the presence of large amounts of extended defects (such as grain boundaries and dislocations) in these materials. It is known that not only are such defects responsible for a significant reduction in the majority-carrier mobility and in the minority-carrier lifetime, but, during growth, may act as centers for secondary-phase formation and impurity segregation as well. At one time, these systems became so well-studied that their polycrystalline structure presented promise rather than problems [1].

Currently, it is understood that the properties of these semiconductors can be altered considerably by varying the grain size or the orientation of the grain boundaries and by controlled doping, which, during the growth, can lead to deviations from stoichiometry or to changes in the impurity-segregation mechanism [2]. However, correct characterization of the local disorder in elemental, as well as compound polycrystalline, semiconductors is a problem that remains to be solved, since it is difficult to distinguish between random clusters of impurity atoms and extended defects. Fortunately, extended defects, as a rule, represent a source of electric and elastic-stress fields in their vicinity; this makes a considerable difference between the electronic states of extended defects and those of local impurity clusters. The problem is also simplified significantly when crystals with a low impurity content are studied.

The electronic states of extended defects (mainly those in silicon) were experimentally investigated by the techniques of photoluminescence, optical absorption, double-spin resonance, high-frequency conductivity, and photoconductivity [3, 4]. In this paper, we report the results of studying the steady-state photoconductivity and its kinetics in coarse-grain textured CdTe polycrystals grown by a new technology [5].

It should be noted that the photoconductivity technique holds an important place among different methods for studying the physical properties of semiconductors, because, in addition to data on the energy levels of local defects, it enables one to obtain information on lifetimes and mobilities of nonequilibrium charge carriers in semiconductors with moderate concentrations of impurities (about $\sim 10^{15}$–10^{16} cm^{-3}) [6].

Unfortunately, the interpretation of the photoconductivity spectra becomes rather complicated in crystals with various kinds of extended defects (dislocations and grain boundaries); as a rule, the cutoff of the intrinsic photoconductivity signal is shifted to longer wavelengths in such crystals [7]. This indicates the presence of local compressive and tensile strain fields that may significantly alter the spectrum of deep electronic states in the band gap, the local distribution of these strain fields over the crystal being inhomogeneous. Under such conditions, important parameters characterizing the quality of the material are the lifetimes and mobilities of the charge carriers, which can be determined quite reliably from measurements of steady-state photoconductivity and its kinetics.

2. EXPERIMENTAL

Measurements were carried out for high-purity stoichiometric polycrystalline *p*-CdTe samples (resistivity 10^5–10^6 Ω cm) having a textured structure with the [111] growth direction of single-crystal grains. The mean size of the grains was no smaller than 1.5–2 mm. The samples were cut from polycrystalline ingots grown at temperatures of 600–620°C in the course of the final purification of CdTe. Samples with a size of $5 \times 5 \times 1.5$ mm^3 were prepared by the mechanical grinding and polishing of the {111} surface crosswise to the growth direction.

After etching the samples in bromomethanol solution, contacts on the {111} surfaces were formed by gold deposition from an auric chloride solution.

The photoconductivity was measured at 65 K in the region of the fundamental absorption edge (in the photon energy range $h\nu$ = 1.3–1.6 eV); the layout made it possible to illuminate the sample from its two opposite sides (*A* and *B*, see Fig. 1). It should be noted that the photoconductivity of CdTe polycrystals is determined

by free nonequilibrium electrons, since the mobility–lifetime product $\mu_p\tau_p$ for holes is small [8].

3. RESULTS AND DISCUSSION

Figure 2 represents the photoconductivity spectrum of one of the samples measured in the ac mode (the incident light flux was modulated at 12.5 Hz). This spectrum is typical of high-purity CdTe crystals. It demonstrates, first, the high quality of the crystal surface treatment as indicated by the low surface recombination rate (revealed by the fact that the signal drop beyond the intrinsic absorption edge is small); second, the absence of any significant amount of impurity centers forming energy levels in the vicinity of the conduction and valence band edges (whose presence we observed studying similar samples with a somewhat higher content of impurities [9]); and, third, the absence of the spectral structure in the signal beyond the fundamental edge.

It should be stressed that the spectra recorded under the illumination of the sample from side *A* and side *B* are identical. Also note that the estimation of the electron lifetime–mobility product from the ac photoconductivity data yields 3×10^{-3} cm^2 V^{-1}, which is characteristic of high-resistivity detector-quality CdTe crystals [10].

However, this spectrum does not provide complete information about the electronic states of the defects present in the material, since ac photoconductivity measurements carried out at a frequency f cannot reveal slow traps characterized by the time of carrier exchange with the allowed bands $\tau > 1/f$. As a rule, it is this type of traps which is formed by extended defects.

The photoconductivity spectra of the same sample measured in the dc mode (without modulation of the incident light flux) under the illumination of the sample from side *A* and side *B* are shown in Figs. 3a and 3b, respectively. These curves differ considerably from the spectrum in Fig. 1: the maximum of the signal is shifted to longer wavelengths and a spectral structure appears in a photon energy range larger than the material band gap E_g. In addition, the spectra in Figs. 3a and 3b differ from each other.

Interpretation of the results obtained presents certain difficulties; this is related first of all to the absence of similar data in the literature. Moreover, there are no wholly convincing concepts on the processes of charge accumulation at extended defects even for the case of dislocations, let alone grain boundaries. Nevertheless, we think that our results can be explained on the assumption that the photoconductivity is controlled by extended defects, which accumulate substantial charge during illumination.

The following facts corroborate our assumption.

First, it is difficult to believe that residual substitutional impurities or intrinsic point defects have such a considerable effect on the band structure as to form local electron states in the conduction band, which could explain the presence of the spectral structure in the photoconductivity signal beyond the fundamental absorption edge.

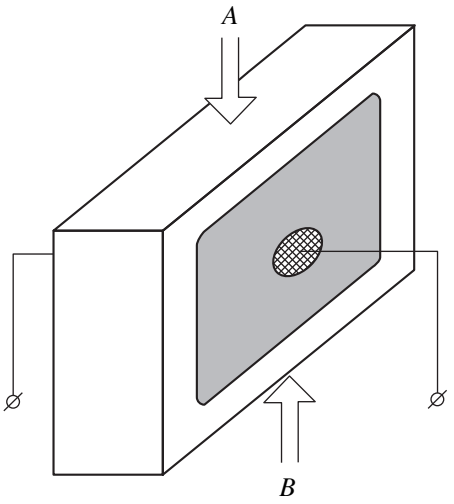

Fig. 1. Typical configuration of the samples for the photoconductivity measurements.

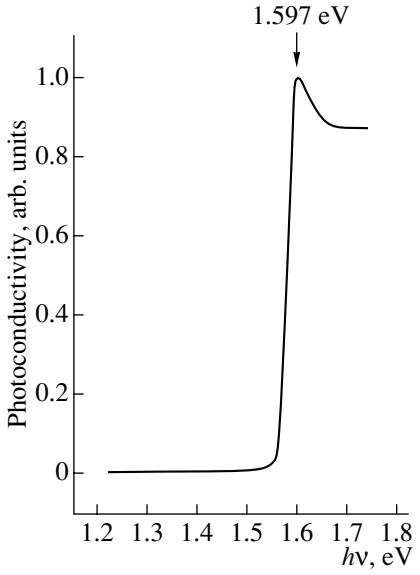

Fig. 2. The photoconductivity spectrum measured in the ac mode (light flux is modulated).

Second, the method that we used to grow and prepare the polycrystals could not have resulted in such a considerable gradient in the distribution of impurities or intrinsic point defects, by which the differences in the photoconductivity spectra obtained under illumination of the samples from the opposite sides might be explained. These differences are, evidently, related to the spatial variations in the structure of extended defects [11], e.g., with the arrangement of the grain

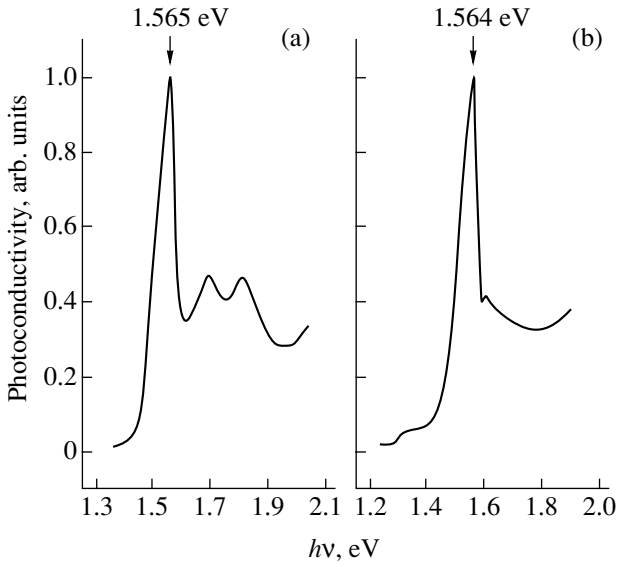

Fig. 3. The photoconductivity spectra measured in the dc mode (light flux is not modulated); light is incident on the sample (a) from side *A* and (b) from side *B*.

boundaries in the bulk of the sample or their different orientation along the texture direction.

Using all data found in the literature to explain the results obtained, we suggest the following model. It was shown long ago [12] that charged dislocation tubes cause local modification of the semiconductor energy bands, which leads to the formation of potential barriers for the capture or emission of nonequilibrium charge carriers.

Apparently, dips in the photoconductivity spectra beyond the fundamental absorption edge originate from the capture of electrons excited to the conduction band by the extended-defect traps, this process being possible when the electrons overcome certain barriers of height E_b (see Fig. 4). We note that a similar model was proposed to explain the appearance of a *Z* band in the photoluminescence spectra of CdTe [13].

In Fig. 5, we present the photoconductivity spectrum of the same sample after a 72-h annealing in a saturated Cd vapor at 650°C. In this case, the structure of the signal obtained under the illumination of the sample from opposite sides is the same. However, annealing leads to a significant change in the electronic states of traps present in the sample.

First, one can see that, in the energy range above E_g, excited electrons can be captured only by one type of traps, with the spread in their energy being insignificant (note that the narrow dip in the signal cannot be explained by excitonic absorption, since it is absent in the spectra measured in the ac mode).

Second, the appearance of a clearly resolved shoulder in the photoconductivity signal indicates that the second trap evolved into an electron capture center with a level at $E_v + (0.035 \pm 0.02)$ eV, which is already known for CdTe.

These results provide evidence that long-term annealing leads either to the reconstruction of dangling bonds in the region of extended defects or to the consid-

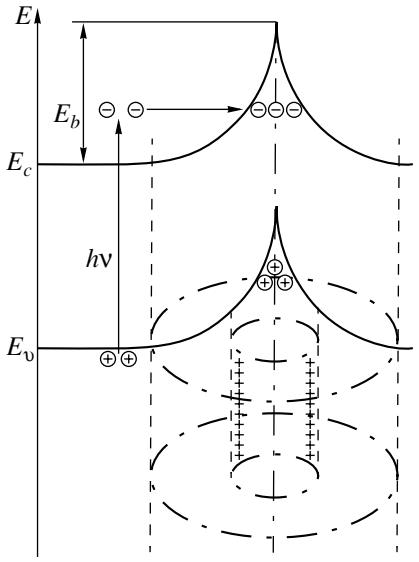

Fig. 4. Suggested diagram of electronic transitions (see text).

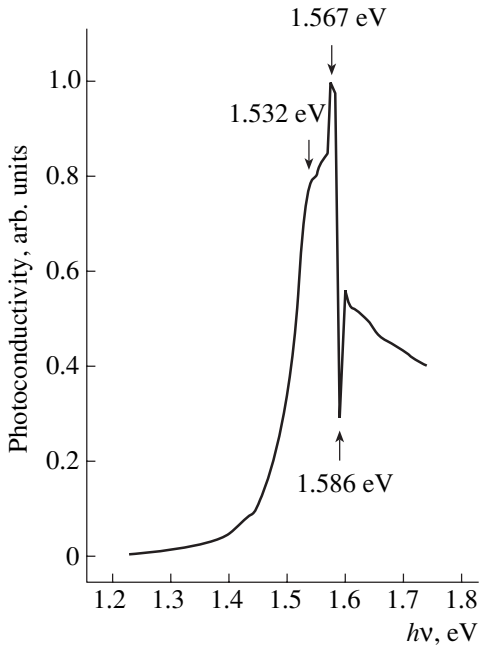

Fig. 5. The photoconductivity spectrum of the sample annealed in Cd vapor.

erable redistribution of background impurities in the vicinity of extended defects. It remains to be seen which of the two hypotheses is more realistic.

4. CONCLUSION

Until relatively recently, the use of polycrystalline materials was limited to selenium rectifiers and powder luminophors. However, the situation changed radically during the last ten years. More and more applications of polycrystals and polycrystalline films of III–V and II–VI compounds have been found in micro- and optoelectronics and solar-power engineering. Unfortunately, reproducible manufacturing of polycrystalline semiconductors with desirable properties is severely hampered by the structural features inherent to these materials, specifically, by the presence of extended defects (grain boundaries and dislocations). Depending, for example, on the type of the boundaries and the nature of their interaction with background and dopant impurities, the electronic properties of polycrystals may vary dramatically. The cause of these variations has yet to be established. There are two more or less clearly formulated points of view. In [12], where germanium bicrystals were investigated, it was suggested that the electronic states of extended defects, which induce electric and stress fields in their vicinity, are determined by the atomic structure of a defect, in particular, by the presence of dangling bonds; a similar conclusion was made in [2], where dislocations in silicon were studied. On the other hand, the authors of [1], who also studied dislocations in silicon, argue that the spectrum of electronic states is governed by the nature of interaction of grain boundaries with background impurities.

Most likely, our results give evidence in favor of the former suggestion. For its final verification, more sophisticated techniques (first of all, local structural methods) should be used in future investigations.

ACKNOWLEDGMENTS

We are grateful to Prof. V.S. Bagaev for valuable comments.

This study was supported by the Russian Foundation for Basic Research (project nos. 99-02-1861 and 01-02-16500).

REFERENCES

1. S. Pizzini, N. Butta, M. Acciary, and M. Acciarri, Springer Proc. Phys. **54**, 178 (1991).
2. W. Schröter, I. Kronewitz, U. Gnauert, *et al.*, Phys. Rev. B **52**, 13726 (1995).
3. V. Celli, A. Golf, and R. Thomson, Phys. Rev. Lett. **8**, 96 (1962).
4. H. Teichler, in *Lattice Defects in Semiconductors, 1974: Invited and Contributed Papers from the International Conference on Lattice Defects in Semiconductors, Freiburg, 1974* (Institute of Physics, London, 1975), Conf. Ser. -Inst. Phys., No. 23.
5. S. A. Medvedev, Yu. V. Klevkov, V. S. Bagaev, and A. F. Plotnikov, Nauka Proizvod. **6** (31), 16 (2000).
6. R. H. Bube, *Photoconductivity of Solids* (Wiley, New York, 1960; Inostrannaya Literatura, Moscow, 1962).
7. H. F. Matare and K. S. Cho, J. Appl. Phys. **36**, 3427 (1965).
8. V. E. Loshkarev, M. K. Sheĭnkman, and A. V. Lyubchenko, *Nonequilibrium Processes in Photoconductors* (Naukova Dumka, Kiev, 1981), p. 264.
9. Yu. V. Klevkov, S. A. Kolosov, S. A. Medvedev, and A. F. Plotnikov, Fiz. Tekh. Poluprovodn. (St. Petersburg) **35**, 1192 (2001) [Semiconductors **35**, 1139 (2001)].
10. Y. Eisen and A. Shor, J. Cryst. Growth **184/185**, 1302 (1998).
11. *Polycrystalline Semiconductors: Physical Properties and Applications: Proceedings of the International School of Materials Science and Technology, Erice, 1984*, Ed. by G. Harbeke (Springer-Verlag, Berlin, 1985; Mir, Moscow, 1989), Part 1.
12. H. F. Matare, J. Appl. Phys. **56**, 2605 (1984).
13. J. Krustok, J. Mödasson, and J. Hiie, Phys. Status Solidi A **165**, 517 (1998).

Translated by M. Skorikov

Semiconductors, Vol. 36, No. 8, 2002, pp. 878–882. Translated from Fizika i Tekhnika Poluprovodnikov, Vol. 36, No. 8, 2002, pp. 941–946.

ELECTRONIC AND OPTICAL PROPERTIES OF SEMICONDUCTORS

Time-Resolved Photoluminescence of Polycrystalline GaN Layers on Metal Substrates

A. V. Andrianov*, K. Yamada, H. Tampo**, H. Asahi**, V. Yu. Nekrasov*, Z. N. Petrovskaya*, O. M. Sreseli*, and N. N. Zinov'ev***

** Ioffe Physicotechnical Institute, Russian Academy of Sciences, Politekhnicheskaya ul. 26, St. Petersburg, 194021 Russia*

e-mail: Olga.Sreseli@pop.ioffe. rssi.ru

*** Institute of Scientific and Industrial Research, Osaka University, 567-0047 Osaka, Japan*

Submitted February 14, 2002; accepted for publication February 14, 2002

Abstract—The low-temperature time-resolved photoluminescence of polycrystalline GaN layers grown by molecular beam epitaxy on metal substrates (Mo and Ta) was investigated. The photoluminescence spectra observed include two emission bands in the ultraviolet spectral region. We assign one of these bands to recombination processes inside cubic nanocrystallites, which are formed in the hexagonal polycrystalline GaN host. The recombination radiation of cubic nanocrystallites is enhanced due to predominant trapping of the nonequilibrium electron–hole pairs in these crystallites. © *2002 MAIK "Nauka/Interperiodica".*

1. INTRODUCTION

At present, Group III nitrides are being investigated intensively in many research centers in connection with prospects for their application in optoelectronic devices operating in the blue and ultraviolet spectral regions, as well as in high-temperature electronic devices. Despite certain advances in the development of a number of devices, for example, lasers for the blue and violet regions of the spectrum [1] and high-power microwave field transistors [2], the technology of obtaining Group III nitrides remains complex and very expensive. This is associated partially with the problem of substrates [3] and partially with the specifics of the epitaxial growth of Group III nitrides [4]. For this reason, the search for ways of reducing the cost of obtaining Group III nitrides and devices based on them is a very important problem in the context of both applied and basic research. Recent advances in the technique of growing layers of Group III nitrides using molecular-beam epitaxy (MBE) made it possible to obtain GaN polycrystalline layers with an efficient photoluminescence (PL) [5, 6]. Moreover, the preparation of *n*- and *p*-type conduction layers was demonstrated [7]. High-quality polycrystalline GaN layers were also obtained on metal substrates (Mo, Ta, W, Nb) [8]. These results open up the prospect of developing relatively inexpensive polycrystalline layers of nitrides. On the other hand, further investigations of the mechanism for high-efficiency luminescence of polycrystalline GaN are required.

In this study, the spectra and kinetics of the PL decay for polycrystalline GaN layers grown by MBE on Mo and Ta substrates are investigated.

2. EXPERIMENTAL

The GaN layers 0.4–0.5 μm thick were grown on metal substrates (Mo, Ta) according to the MBE procedure described elsewhere [8]. The layers obtained were investigated by X-ray diffraction and atomic-force microscopy. The results indicate that the layers contain mainly hexagonal crystallites 400–800 and 100–300 nm in size for GaN/Mo and GaN/Ta, respectively. The details associated with these measurements can be found in publication [8].

The PL was investigated on a spectrometry installation which included a DFS-24 double-grating monochromator, an FEU-100 photomultiplier, a BCI-280 box-car integrator, as well as a controlling and recording computer system. The spectral resolution of measurements was 3 meV. The time resolution of the system was about 10 ns. The PL was excited by the radiation of a pulsed N laser (λ = 337 nm, τ_p = 6 ns). The excitation intensity was ~10^3 W/cm^2. The measurements were carried out at 78 and 4.2 K.

3. RESULTS AND DISCUSSION

Typical PL spectra measured at the peak of the laser pulse at T = 78 K for the two types of investigated layers, namely, GaN/Mo and GaN/Ta, are shown in Fig. 1.

The samples investigated produced PL mainly in the violet and near-ultraviolet spectral regions. The PL intensity for the yellow-green region was very low for all samples investigated. For this reason, we consider here only the high-energy part of the emission spectrum.

The spectra are characterized by two fundamental emission bands with peaks at 3.465 and 3.259 eV in the case of GaN/Mo, and at 3.470 and 3.260 eV in the case of GaN/Ta. The emission in both PL bands is characterized by rapid decay (Fig. 2), which repeats the shape of the laser pulse. This indicates that the PL decay time for both bands is shorter than several nanoseconds. The PL bands with peaks at 3.465 and 3.470 eV can be attributed to the edge emission of hexagonal GaN crystallites.

Rapid decay of the second PL band (3.26 eV) does not permit one to assign it to donor–acceptor recombination, as was done in study [8] based on measurements of steady-state PL. It is known [9] that the donor–acceptor recombination in GaN is characterized by a nonexponential and relatively slow PL decay. In addition, the time-resolved PL spectra demonstrate no variation in the position and shape of this band with the prolongation of the delay time between the instant of detecting the spectrum and the peak of the laser pulse (Fig. 3). The fact that the difference in the peak energies of PL bands for 3.46–3.47 and 3.26 eV is close to 200–210 meV has engaged our attention. This value corresponds to the difference in band gaps of hexagonal (*h*-GaN) and cubic (*c*-GaN) GaN [10]. Based on these data, we assume that the band with the peak at 3.26 eV is related to the edge emission from cubic GaN crystallites. This emission is caused mainly by exciton recombination.

X-ray measurements [8] have not revealed a cubic phase in the GaN/Mo and GaN/Ta samples, which were investigated in this study. This can be explained by the small volume fraction of *c*-GaN in epilayers. However, the PL from the cubic phase can be detected even if this phase occupies much less volume when compared with the hexagonal phase (see, for example, [11]). If *c*-GaN consists of small nanocrystallites, which are surrounded by considerably larger hexagonal crystallites, preferential trapping of the nonequilibrium charge carriers, which are generated by external excitation, is possible in nanocrystallites of the cubic phase. Due to a substantially narrower band gap for *c*-GaN, the carriers will move from crystallites of the *h* phase to crystallites of the *c* phase. This situation is similar to the preferential trapping of the charge carriers by quantum dots, which are incorporated into the wide-gap host (see, for example, [12, 13]). Due to such trapping, the PL of the cubic phase can be considerably enhanced.

Let us consider a simple phenomenological model which describes this effect of PL enhancement.

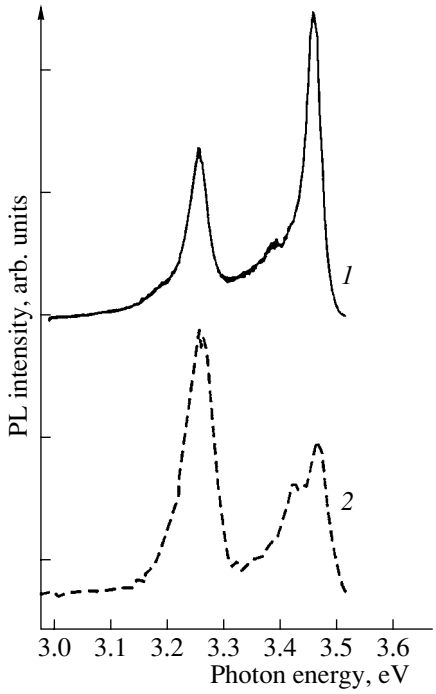

Fig. 1. Time-resolved photoluminescence spectra of GaN epilayers on metal substrates at $T = 77$ K with the zero delay relative to the laser pulse. (*1*) GaN/Mo and (*2*) GaN/Ta.

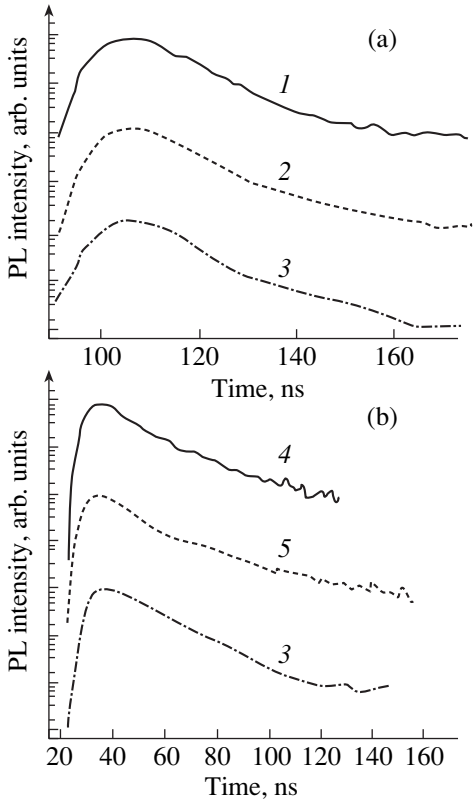

Fig. 2. Kinetics of photoluminescence pulses for structures (a) GaN/Mo and (b) GaN/Ta at 77 K. The wavelengths of PL detected: (*1*) 3578, (*2*) 3800, (*4*) 3610, and (*5*) 3802 Å; (*3*) laser pulse. The curves are shifted relative to each other along the ordinate axis.

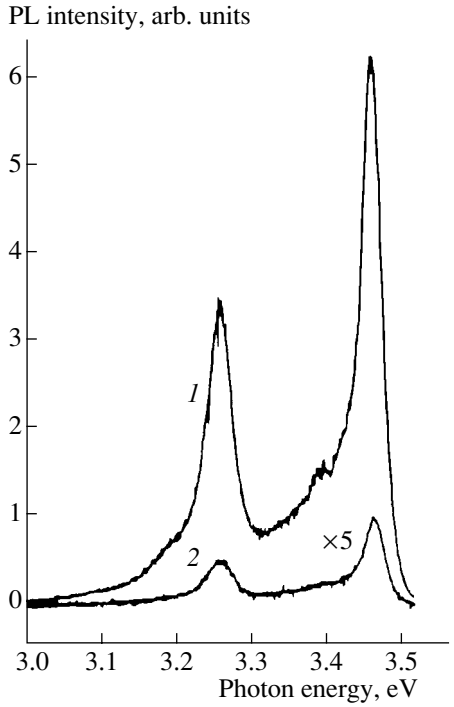

Fig. 3. Time-resolved photoluminescence spectra of the GaN/Mo structure at $T = 77$ K. (*1*) The spectrum for the zero delay between the instant of spectrum detection and a peak of the laser pulse; (*2*) the delay is equal to 100 ns.

Let us write the balance equations for electrons and excitons in the crystallites of the hexagonal phase while making allowance for carrier escape to neighboring crystallites of the cubic phase. We assume that the interfaces between crystallites are ideal, i.e., with no carrier trapping, and the temperature is so low that it is possible to neglect the thermal decomposition of excitons:

$$\frac{dn_{eh}}{dt} = \alpha J - \beta n_{eh}^2 - \frac{n_{eh}}{\tau_e} - \gamma_e n_{eh}, \quad (1)$$

$$\frac{dn_{xh}}{dt} = \beta n_{eh}^2 - \frac{n_{xh}}{\tau_x} - \gamma_x n_{xh}. \quad (2)$$

Here, n_{eh} and n_{xh} are the electron and exciton densities in the *h* phase, respectively; αJ is the rate of electron generation from the light; β is the coefficient of combining the carriers into the exciton; γ_e is the frequency of electron trapping by cubic crystallites; γ_x is the frequency of exciton trapping by cubic crystallites; τ_x is the exciton lifetime, including radiative and nonradiative recombination processes; and τ_e is the electron lifetime, which accounts for the recombination processes other than those combining into the exciton. In Eqs. (1) and (2), it is also implied that the excitation level is high and the electron density is equal to the hole density. In addition, relative to trapping into the *c* phase, electrons and holes are assumed to behave similarly. The solutions to Eqs. (1) and (2) for the steady-state case, with the proviso that the excitation levels are high ($\alpha J \gg 1/4\beta^2\tau_e^2$), have the form

$$n_{eh} = \sqrt{\frac{\alpha J}{\beta}}, \quad (3)$$

$$n_{xh} = \frac{\alpha J \tau_x}{1 + \gamma_x \tau_x}. \quad (4)$$

If we write similar balance equations for the cubic phase,

$$\frac{dn_{ec}}{dt} = \alpha J - \beta n_{ec}^2 - \frac{n_{ec}}{\tau_e} + \gamma_e n_{eh}, \quad (5)$$

$$\frac{dn_{xc}}{dt} = \beta n_{ec}^2 + \gamma_x n_{xh} - \frac{n_{xc}}{\tau_x}, \quad (6)$$

and assume that the light generates electrons and holes with the same efficiency as in the *h* phase, the electron and exciton lifetimes become independent of the phase of their location. With the assumption of high excitation levels, we have for the steady-state case

$$n_{ec} \cong \sqrt{\frac{\alpha J}{\beta}} \quad (7)$$

and, using expression (4),

$$n_{xc} = \alpha J \tau_x \left(1 + \frac{\gamma_x \tau_x}{1 + \gamma_x \tau_x}\right) = \frac{\alpha J \tau_x (1 + 2\gamma_x \tau_x)}{1 + \gamma_x \tau_x}. \quad (8)$$

Using expressions (4) and (8), we derive the ratio between exciton densities in the cubic and hexagonal phases:

$$\frac{n_{xc}}{n_{xh}} = 1 + 2\gamma_x \tau_x. \quad (9)$$

Assuming that the radiative lifetime of excitons is the same for the *c* and *h* phases and taking into account different volumes (V_c and V_h) of the luminescent material, we can derive the following ratio of intensities of the exciton PL I_{pl} in the *c* and *h* phases:

$$\frac{I_{pl}^c}{I_{pl}^h} = \frac{V_c}{V_h}(1 + 2\gamma_x \tau_x). \quad (10)$$

The product $\gamma_x \tau_x$ in expression (10) is the number of exciton captures which were generated in hexagonal crystallites by the cubic phase during the exciton lifetime. This quantity can be substituted by the ratio of the exciton diffusion length L_d to the size of the hexagonal crystallite L. For this reason, expression (10) can be written as follows:

$$\frac{I_{pl}^c}{I_{pl}^h} = \frac{V_c}{V_h}\left(1 + 2\frac{L_d^2}{L^2}\right). \quad (11)$$

It can be seen from expression (11) that, for small crystallite sizes and large enough exciton diffusion lengths, the PL of the cubic phase can be comparable with the PL of the hexagonal phase even in the case of a small volume fraction of cubic crystallites. As was noted above, the size of the hexagonal crystallites for the GaN/metal layers, which were investigated in this study, is several hundreds of nanometers. The exciton diffusion length for GaN should be on the order of the free-carrier diffusion length, which is as large as several micrometers for high-quality GaN samples [14]. For this reason, the factor of enhancement of PL from cubic crystallites $(1 + 2(L_d/L)^2)^2$ in expression (11) can be as large as several tens.

The PL spectra of the GaN/metal samples at T = 4.2 K (Fig. 4) make it possible to identify radiative transitions more exactly.

In the case of the GaN/Mo samples, the narrow PL line with a peak at 3.468 eV and a half-width of ~13 meV is dominant in the emission spectrum of hexagonal crystallites. The spectral position and rapid PL decay allowed us to attribute this line to the recombination of excitons bound at neutral donors (D^0–X transition). A certain low-energy shift of the peak of this line (of about 4–8 meV) from the value 3.472–3.476 eV, which is known from the literature for the D^0–X transition in hexagonal GaN [15, 16], is most likely associated with strain effects in the polycrystalline structure.

In the emission region of cubic crystallites, two emission lines with peaks at 3.264 and 3.187 eV and half-widths of 30 and 60 meV, respectively, can be observed. The line with a peak at 3.264 eV, which is characterized by a PL decay time shorter than several nanoseconds, can be attributed to the recombination of excitons bound at neutral donors (D^0–X) in the c-GaN phase [16, 17]. In contrast with this, the emission of the line at 3.187 eV is characterized by a substantially nonexponential and slow PL decay. More specifically, the PL signal decays from the level of 0.9 to the level of 0.1 in about 400 ns. In addition, time-resolved PL spectra demonstrate the low-energy shift of the peak of this line with increasing delay time between the moment of detecting the spectrum and the peak of the laser pulse. These facts indicate that this line is related to the donor–acceptor recombination in cubic crystallites.

In the case of GaN/Ta samples, two emission lines from hexagonal crystallites, namely at 3.472 and 3.430 eV with a half-width of 18 and 30 meV, respectively, are observed in the low-temperature PL spectrum (Fig. 4, curve *2*). Both lines are also characterized by rapid PL decay. We attribute the line at 3.472 eV to the recombination of excitons bound by neutral donors (D^0–X). In contrast with this, the line at 3.430 eV can be caused by the recombination of a hole with an electron bound by a deep donor (h–D^0 transition) with a bonding energy of about 70 meV. This energy E_i can be estimated from the relation $h\nu = E_g - E_i + kT/2$ taking into account that

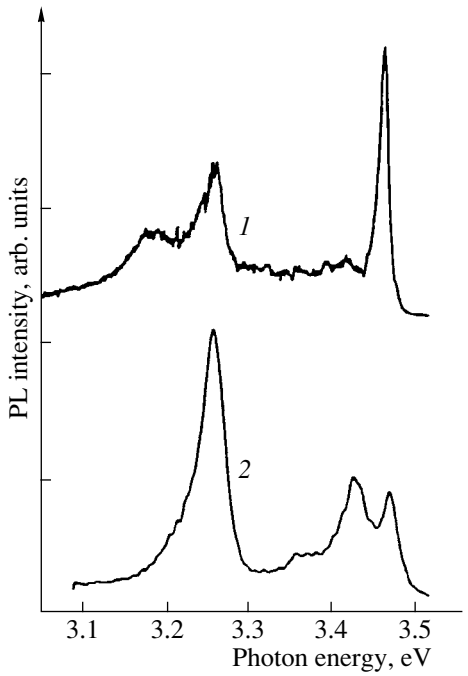

Fig. 4. Photoluminescence spectra of GaN epilayers on metal substrates at T = 4.2 K. (*1*) GaN/Mo and (*2*) GaN/Ta.

E_g ~ 3.50 eV for h-GaN [10]. The h–D^0 transition with the participation of a donor with an energy of about 80 meV was observed in many studies, and many authors assign this donor to the O impurity in GaN (see, for example, [18, 19]). It is possible that the donor center in our samples has the same nature, and a decrease in its bonding energy is explained by specific features of behavior of the O impurity in polycrystalline GaN.

The emission of cubic crystallites in the GaN/Ta samples at 4.2 K comprises an asymmetric line with a peak at 3.261 eV and a half-width of ~27 meV. The spectral position of this line allows one to assign it to D^0–X transitions in cubic crystallites. The asymmetry of this line can be caused by the contribution of an additional weaker emission line with a peak at 3.24 eV.

Variation in the epitaxial growth conditions for polycrystalline GaN layers on metal substrates strongly affects the structure of GaN crystallites. The PL spectra at 78 K for two GaN/Mo samples, *N1* and *N2*, are shown in Fig. 5. The *N1* sample was prepared according to the procedure described in study [8] and was considered above. For the *N2* sample, growth conditions were varied; namely, we changed the source of activated N (N_2 for *N1* and NH_3 for *N2*), and the temperature of growth and thickness of the buffer layer (3-nm-thick layer grown at 400°C for *N1* and 40 nm at 550°C for *N2*). It can be seen that a change in the growth conditions of the *N2* sample led to the almost complete disappearance of the band at 3.26 eV and the emergence of a shoulder at 3.43 eV for the line at 3.465 eV. The emission both at 3.43 eV and at 3.465 eV is characterized by

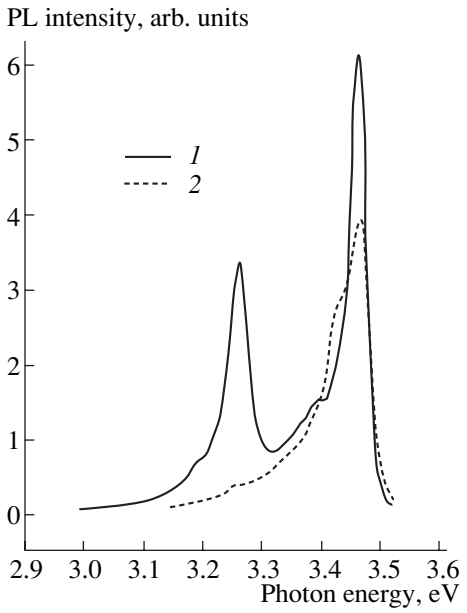

Fig. 5. Photoluminescence spectra of two GaN/Mo samples at $T = 77$ K. (*1*) Sample *N1* and (*2*) sample *N2*.

rapid decay. These variations in the emission spectra can be explained by the fact that change in the growth conditions led to the almost complete disappearance of the cubic crystallites. However, the concentration of impurity centers in hexagonal crystallites increased substantially in this case. Specifically, the line at 3.43 eV is related to the h–D^0 transition in which the O impurity is involved, as was discussed above.

4. CONCLUSION

Thus, the PL kinetics for polycrystalline GaN layers grown by the MBE technique on metal substrates was investigated. These investigations allowed us to identify the recombination processes in GaN. The PL spectra observed include two emission bands in the ultraviolet spectral region. We relate one of these bands to recombination processes inside cubic nanocrystallites, which are formed in the hexagonal polycrystalline GaN host, and the other one to the recombination inside hexagonal crystallites. The emission from cubic GaN crystallites is found to be enhanced, which makes it possible to observe the PL signal from the cubic phase despite its small volume fraction in the GaN layers investigated. The enhancement of the recombination emission for cubic nanocrystallites is caused by the preferential trapping of the nonequilibrium electron–hole pairs in these crystallites.

ACKNOWLEDGMENTS

This study was supported in part by the program of the Ministry of Industry and Science, “Physics of Solid-State Nanostructures” and the Russian Foundation for Basic Research, project no. 00-15-96750.

REFERENCES

1. S. Nakamura and G. Fasol, *The Blue Laser Diode* (Springer-Verlag, Berlin, 1997).
2. N. Q. Zhang, B. Moran, S. P. DenBaars, *et al.*, Phys. Status Solidi A **188**, 213 (2001).
3. S. Strite and M. Marcoc, J. Vac. Sci. Technol. B **10**, 1237 (1992).
4. F. A. Ponce, MRS Bull. **22**, 51 (1997).
5. K. Iwata, H. Asahi, K. Asami, *et al.*, J. Cryst. Growth **188**, 98 (1998).
6. M. Hikori, H. Asahi, H. Tampo, *et al.*, J. Cryst. Growth **209**, 209 (2000).
7. H. Asahi, K. Iwata, H. Tampo, *et al.*, J. Cryst. Growth **201/202**, 371 (1999).
8. K. Yamada, H. Asahi, H. Tampo, *et al.*, in *Proceedings of IWN2000, Nagoya, Japan, 2000*, p. 553; IPAP Conf. Ser., Vol. 1, p. 556.
9. R. Dingle and M. Ilegems, Solid State Commun. **9**, 175 (1971); V. Yu. Nekrasov, L. V. Belyakov, O. M. Sreseli, and N. N. Zinov’ev, Fiz. Tekh. Poluprovodn. (St. Petersburg) **33** (12), 1428 (1999) [Semiconductors **33**, 1284 (1999)].
10. B. Monemar, Phys. Rev. B **10**, 676 (1974); G. Ramírez-Flores, H. Navarro-Contreras, A. Lastras-Martínez, *et al.*, Phys. Rev. B **50**, 8433 (1994).
11. A. V. Andrianov, D. E. Lacklison, J. W. Orton, *et al.*, Semicond. Sci. Technol. **11**, 366 (1996).
12. S. Marcinkevicius and R. Leon, Phys. Rev. B **59**, 4630 (1999).
13. L. Zhang, Thomas F. Boggess, K. Gundogdu, *et al.*, Appl. Phys. Lett. B **79**, 3320 (2001).
14. L. Chernyak, A. Osinsky, H. Temkin, *et al.*, Appl. Phys. Lett. **69**, 2531 (1996).
15. G. D. Chen, M. Smith, J. Y. Lin, *et al.*, Appl. Phys. Lett. **68**, 2784 (1996).
16. J. Menniger, U. Jahn, O. Brandt, *et al.*, Phys. Rev. B **53**, 1881 (1996).
17. A. V. Andrianov, D. E. Lacklison, J. W. Orton, *et al.*, Semicond. Sci. Technol. **12**, 59 (1997).
18. B. C. Chung and M. Gershenzon, J. Appl. Phys. **72**, 651 (1992).
19. G. D. Chen, M. Smith, J. Y. Lin, *et al.*, J. Appl. Phys. **78**, 2675 (1995).

Translated by N. Korovin

Semiconductors, Vol. 36, No. 8, 2002, pp. 883–888. Translated from Fizika i Tekhnika Poluprovodnikov, Vol. 36, No. 8, 2002, pp. 947–952.

SEMICONDUCTOR STRUCTURES, INTERFACES, AND SURFACES

Low-Threshold Defect Formation and Modification of Ge Surface Layer under Elastic and Elastoplastic Pulsed Laser Effects

S. V. Vintsents*, V. B. Zaitsev, A. V. Zoteev**, G. S. Plotnikov**, A. I. Rodionov**, and A. V. Chervyakov****

** Institute of Radio Engineering and Electronics, Russian Academy of Sciences (Fryazino Branch), pl. Vvedenskogo 1, Fryazino, Moscow oblast, 141120 Russia*

e-mail: alkeev@ms.ire.rssi.ru

*** Faculty of Physics, Moscow State University, Vorob'evy gory, Moscow, 119899 Russia*

Submitted July 23, 2001; accepted for publication November 28, 2001

Abstract—Changes in the spectra of fluorescence of dye (rhodamine B) molecules adsorbed on a Ge surface and modification of the parameters of Raman and diffuse scattering of light by a semiconductor surface subjected to elastic and elastoplastic effects of pulsed laser radiation are studied. Using contactless photoacoustic measurements based on the laser beam deflection technique, the amplitude of the threshold surface strain is estimated at $\sim 5 \times 10^{-5}$. An appreciable quenching of the fluorescence of the adsorbed probe molecules, an abrupt broadening of the molecular spectra, and an above-threshold increase in the intensity of the diffusively scattered light are observed upon the transition to the range of energy densities corresponding to the inelastic strain formation. The larger the laser-induced strain, the smaller the frequency and the width of the Raman lines, and the higher their intensities. The physical nature of these effects is discussed. *© 2002 MAIK "Nauka/Interperiodica".*

INTRODUCTION

Previously, the final stages of the controllable damage of semiconductors and metals exposed to multiple laser pulses were observed at relatively low threshold energy densities $W_0 \lesssim 0.1$ J/cm^2 [1–4], which, in the conditions of local (Gaussian beam radius $\omega \approx 10$–100 μm) short-term heat release, are characterized by the so-called size effect: $W_0 \propto \omega$ [2, 5–8]. Most of the experiments were based on the techniques that are sensitive only to the macrodamage of semiconductors (see, e. g., [2, 3] and the references therein). It was not until recently that the initial stages of microscopic changes, whose accumulation within small regions (10–100 μm) may cause macrodamage, have received the attention they deserve [9–11].

It has been shown already that, under the local effect of a relatively small number of laser pulses ($N \lesssim 10^3$), the thermal stress produced in the surface layer of a semiconductor results in plastic microstrains, which cause (at the energy density $W \approx W_0$) a significant threshold change in the parameters of the insulator slow states (ISS) localized in the oxide layer on the germanium surface [10]. However, in the conditions specified, the microscopic defect formation in the oxide film is not the only result of the photoinduced deformation; a considerable change in the microstructure of the semiconductor surface layer, a radical restructuring of the deeper layers [7, 8, 10], and the formation of superstructures on the surface [3, 12] are also possible.

For a complex investigation of the early stages of microplastic changes produced near the actual (i.e., covered with a thin oxide film) germanium surface, we combined several optical nondestructive techniques; namely, molecular luminescence probing, diffuse and Raman scattering, and photothermal deformation of the surface were used.

EXPERIMENTAL

Similar to [10], we studied the (111) surfaces of high-resistivity (resistivity $\rho = 25$–30 Ω cm) *n*-Ge single crystals doped with Sb and etched in H_2O_2 at room temperature. After the etching, the germanium samples were kept in air for more than a day, during which a 20- to 30-Å-thick GeO_2 layer of hexagonal structure was formed on the Ge surface. Then, the "real" surfaces thus obtained were subjected to pulsed laser radiation in air. A laser beam of micrometer size, similar to that described in [10], was used in the scanning mode; for the experimental techniques implying nonlocal action, five-to-six regions of $\sim 3 \times 5$ mm^2 area were formed by scanning the sample surface (we used the samples of size $20 \times 5 \times 0.3$ mm^3). Each of the regions was characterized by its specific energy density W of the laser radiation with $\lambda = 0.53$ μm, the Gaussian spot of the size $2\omega \approx 70$ μm, the pulse duration $\tau_0 \gtrsim 350$ ns, and the number of pulses $N \lesssim 10^3$. The range of W variation was chosen between 10 and 250 mJ/cm^2, which is much

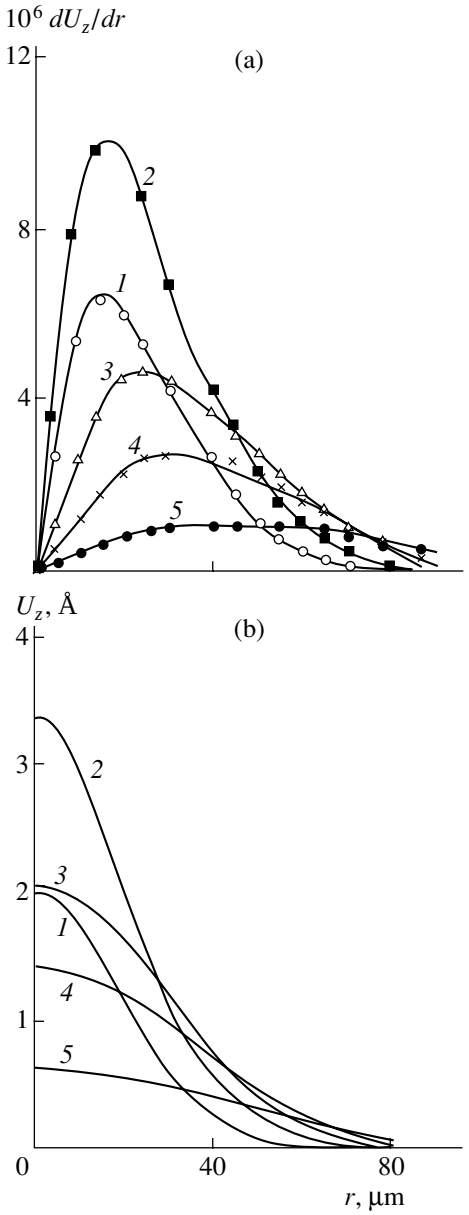

Fig. 1. Kinetics of the spatial profiles of (a) quasi-static strains $dU_z/dr = f(r)$ and (b) the effective normal displacements $U_z(r)$ of the actual Ge surfaces at the elastic stage of the focused laser-beam effect $W \approx 8$–10 mJ/cm$^2 \ll W_0$. The profiles were measured at the time t counted from the beginning of the laser pulses, which recurred within intervals $\Delta t \approx 100$ μs and featured the following coordinate r and time t dependence of the intensity [15]: $I(r, t) = W\exp(-r^2/\omega^2)(t/\tau_0^2)\exp(-t/\tau_0)$ with the characteristic time constant $\tau_0 \geq 350$ ns. $t =$ (*1*) 1, (*2*) 2, (*3*) 6, (*4*) 10, and (*5*) 18 μs.

lower than the melting threshold $W_m \gtrsim 1.2$ J/cm^2 [13] calculated at $\tau_0 \gtrsim 350$ ns [13].

The fluorescence spectra were measured using a hyperspectrometer, which is a system with a position-sensitive sensor and ensures a wavelength resolution of ~0.8 nm and a spatial resolution along a sample of ~10 μm. As the position-sensitive device, we used a microchannel plate and a CCD array for detecting the fluorescence spectra and for studying the Rayleigh scattering, respectively. A halogen lamp (1000 W) with an interference filter adjusted to 530 nm excited the fluorescence of the probe molecules.

Probe molecules were those of rhodamine B deposited on the semiconductor surface from an alcoholic solution. The surface concentration of the dye molecules amounted to 2×10^{13} cm^{-2}, which corresponds to a ~0.2 monolayer according to the data obtained using a piezo-resonance balance. Special experiments indicated that neither the adsorption of the dye at the surface nor the radiation with intensities used in the experiments changed the degree of homogeneity of the surface or the spectrum of surface electron states (SES).

Additional study of Raman and diffuse scattering spectra of the probing light was carried out using a DFS-52 spectrograph for the germanium samples excited by an argon laser with $\lambda = 0.488$ μm. The resolution of the Raman scattering (RS) spectral measurements was improved by using *p* polarization of the laser beam incident upon the sample surface at the Brewster angle with an intensity of ~0.5 W/cm^2.

Instantaneous spatial profiles of the quasi-static strains on the germanium surface $dU_z/dr = f(r)$ and the effective normal elastic displacements $U_z(r)$ were detected using an advanced method of photothermal surface strain (PTSS) in accordance with the technique employed in [14, 15].

RESULTS AND DISCUSSION

The results will be outlined by proceeding mainly from the lower to higher densities of laser pulse energy *W*.

The profiles of $dU_z/dr = f(r)$ and $U_z(r)$ obtained in germanium *in situ* under the nondestructive (elastic) pulsed laser effect at $W \approx 8$–10 mJ/cm$^2 \ll W_0$ are plotted in Fig. 1. The profiles have the shape of a hump appearing at the semiconductor surface and turned out to be similar to those previously obtained for metals [14, 15]. The kinetics of the displacement profiles makes it clear that the intervals between laser pulses ($\Delta t \approx 100$ μs) is sufficient for the sample surface to cool entirely and return to its unperturbed (unstrained) "horizontal" state. When *W* increased to $W_0 \gtrsim 70$ mJ/cm^2, the displacement profiles retained their smooth shape and no small-size (on the order of micrometers) spatial fluctuations U_z appeared. As in [2], the profiles at W_0 corresponded to the largest (along the beam radius *r* and for the time *t*) shear strain $\varphi_0 \equiv (dU_z/dr)_{max} \approx 5 \times 10^{-5}$ (Fig. 2, curve *1*). Note that the drop in the photostrain signal at the thresholds W_0 is mostly caused by the development of the final stages of damage in germanium (at $N \geq 10^6$) accompanied by an abrupt decrease in the fraction of mirror-reflected light [2].

The results of studying the fluorescence of the dye on the germanium surface are shown in Fig. 3. It is clearly seen that, at small W ($W < W_0$), both the intensity (I_{PL}) and the half-width of the rhodamine B spectral line ($\lambda_{1/2}$) are nearly constant. This corresponds with the data previously obtained from electrical measurements of the slow states in an insulator [10], which suggest that no dramatic changes are produced under the thermoelastic local laser effect either in the germanium layer (Ge) or in the oxide film (GeO_2). We observed only a slight quenching of the fluorescence from the adsorbed rhodamine B molecules (at $W \approx 50$–70 mJ/cm^2), which was attributed to the prethreshold laser-induced generation of a small number of deep slow states in the oxide layer [10]. Such states may apparently arise from the elastic bending flexure of the thin insulator films during the multiple photostimulated expansion of the surface-layer bulk with the vertical displacement amplitude $U_z \approx 1$–10 nm [2, 8]. As is known [16], the deep traps in an insulator can act as acceptors of the electron excitation energy transferred from the probe molecules, thus, promoting moderate quenching of the molecular fluorescence observed at $W < W_0$.

The most abrupt changes in the rhodamine B molecular spectra of fluorescence are observed at $W \approx$ 70–85 mJ/cm^2, i. e., at the thresholds W_0 [10]. These changes comprise an appreciable (from five to ten times) quenching of the fluorescence intensity (Fig. 3, curve *1*) and a simultaneous broadening of the fluorescence spectra of the probe molecules (Fig. 3, curve *2*). Let us emphasize that, at $W \approx W_0$, no shift of the fluorescence peak (λ_{max}) was noticed at the threshold. In our opinion, this may be explained by the fact that the irreversible plastic strain induced at the energy densities in the vicinity of W_0 (Fig. 2) results in the additional electronic states in the damaged oxide layer on the germanium surface. Along with an increase in the concentration of the deep electron traps (the ISS), we observed a pronounced increase in the concentration of shallow fluctuation states in GeO_2 in the vicinity of the allowed band edges. The latter circumstance is indicated by an abrupt drop in the ISS charging threshold upon the photoinjection of charge carriers from Ge [10].

Similar to the deep traps in insulators [16], the fluctuation states in GeO_2 are likely to be effective acceptors of the probe-molecule photoexcitation energy that is nonradiatively transferred into the solid medium. In fact, the critical radius of the energy transfer by the Forster–Dexter mechanism in such structures equals ~5 nm, and the most intense generation of the fluctuation states is in the oxide region (with a thickness $\lesssim$3–5 nm) that is directly adjacent to the germanium interface; this region is the most disordered [17]. It should be noted that the local electric fields that appear upon the recharging of such defects could produce only a slight effect on the position of the fluorescence peak λ_{max} of the probe molecules, because the Coulomb charged centers affect only the molecules which are located in their vicinity, i.e., within 1 nm [18].

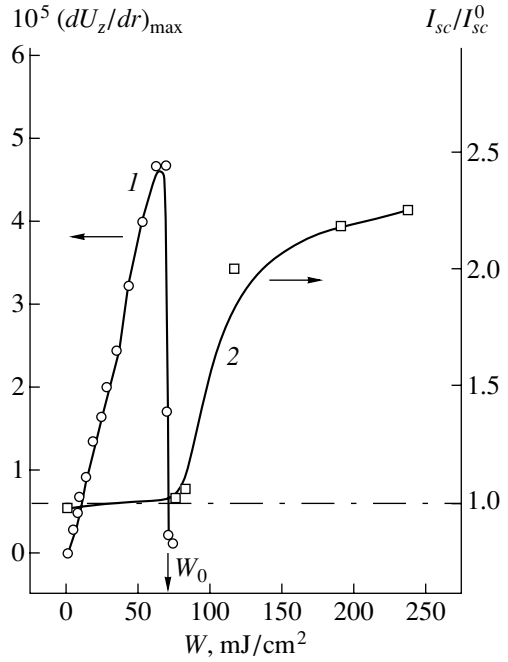

Fig. 2. (*1*) The increase in the largest (along the radius r and for the time t) elastic strain $(dU_z/dr)_{max}$ with increasing W and the drop of the PTSS [2] signal at the thresholds W_0 (*1*); (*2*) W-dependence of the intensity of light diffusely scattered from the Ge surface I_{sc}/I_{sc}^0, where I_{sc}^0 is the intensity of light scattered from an unirradiated surface ($W = 0$).

The considerable (from 1.5 to 2 times) broadening exhibited by the fluorescence spectra of probe molecules at the thresholds W_0, i. e., upon the transition from the elastic to the elastoplastic straining of the semiconductor, may be attributed to the pronounced growth of the geometric heterogeneity of the surface, which presents direct evidence of the initiated irreversible (residual) displacements ΔU_z of the real germanium surface. The amplitude of these displacements is apparently close (within an order of magnitude) to the amplitude of the maximal reversible elastic displacements of the germanium surfaces $U_{z\,max} \sim 1$–10 nm, which were previously studied by the PTSS method [2, 8]. Note that, at the thresholds W_0, the value $U_{z\,max}$ is comparable to the mean radius of the induction-resonant Forster–Dexter transfer of the electron excitation energy $r_0 \approx 5$–6 nm [16] and the inhomogeneous broadening of spectra is maximal; therefore, the molecular probe technique turned out to be especially effective in this case.

A distinct increase in the intensity of the diffuse scattering was observed at $W \gtrsim 85$–100 mJ/cm^2 and tended to level off at higher energy densities (Fig. 2, curve *2*). In contrast to the short-range testing of the surface by the luminescent molecular probes, the scattered light allows one to probe the germanium surface to a depth that is essentially larger than r_0 and can be as large as $R_0 \sim 100$ nm for the excitation wavelength λ

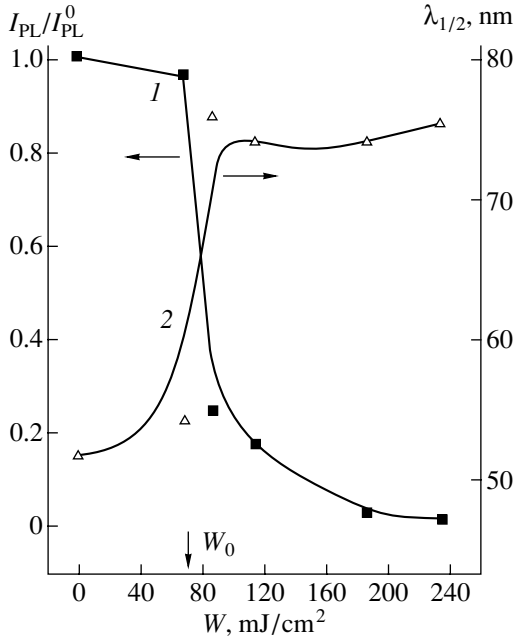

Fig. 3. (*1*) Threshold quenching of rhodamine B molecular fluorescence and (*2*) threshold broadening of the fluorescence spectra of the probe molecules on the actual germanium surface that was preliminarily subjected to elastic ($W < W_0$) or elastoplastic ($W > W_0$) strains as a result of pulsed laser irradiation. I^0_{PL} is the fluorescence intensity of an unirradiated sample.

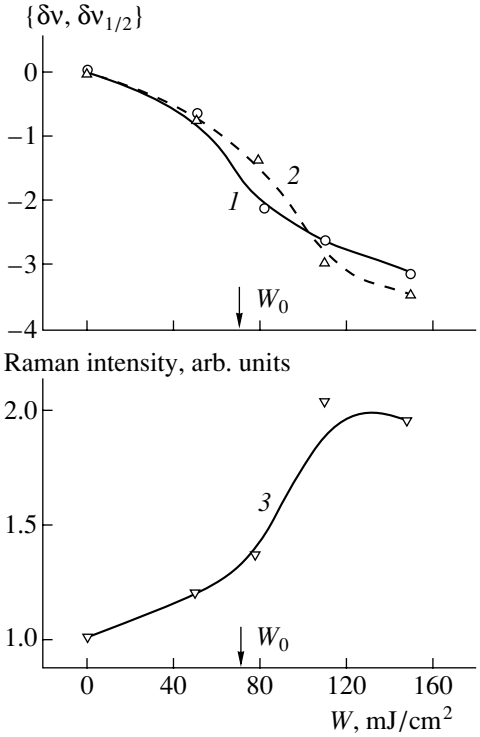

Fig. 4. Changes in the parameter of Raman scattering from actual germanium surfaces subjected to preliminary pulsed laser irradiation versus the energy density at the center of the laser spot W: (*1*) Raman line frequency shift $\delta\nu$, (*2*) narrowing of the linewidth $\delta\nu_{1/2}$, and (*3*) an increase in the intensity of Raman scattering.

used in the experiment. In these conditions, the enhancement of the diffuse scattering observed at $W \gtrsim (1.2–1.5)W_0$ most likely reflects the kinetics of the gradual accumulation of the microplastic changes, when the scattering inhomogeneities induced in the surface layer grow with W and become comparable in size with R_0 or λ.

We believe that, at the initial stages of the microplastic changes (i. e., in the vicinity of W_0), the inhomogeneities grow mainly due to pulse-to-pulse accumulation and the subsequent diffusion of point rather than extended defects [3]. This is because the local laser irradiation with an energy density near the threshold W_0 induces the thermal stresses $\sigma_0 \approx 2–3$ MN/m^2 [2, 8], which are far below the minimal stresses that give rise to the heterogeneous nucleation and motion of dislocations at room temperature and the related dislocation-related plasticity of germanium $\sigma > 20–200$ MN/m^2, as determined from the experiments with contact loading of germanium [19]. In fact, in our experimental conditions, the local laser-induced heating does not exceed $\Delta T \lesssim 100$°C [2, 8] at the thresholds W_0, while the brittle point in germanium is $T \approx 500$°C. In accordance with the well-known classification of the microplasticity phenomena ([19], p. 243), in the range of a relatively low photoinduced stress, which is the case, the heterogeneous–dislocation mechanism of microplastic strain gives way to a defect–diffusion mechanism: both the initial nucleation of the plastic microstrains (dislocation loops) and their further growth are entirely governed by the diffusion processes in the field of the point defects.

The significant role of the kinetics of defects in the observed microplastic processes is also indicated by the somewhat unexpected behavior of the Raman spectra. As W grows, the RS line (~301 cm^{-1}) shifts to lower frequencies by $\delta\nu$, which is usually observed during amorphization, when the degree of crystallinity decreases and microcrystals appear in the material [20] (Fig. 4, curve *1*). Along with this, the full width of the RS line at half maximum decreases with W by $\delta\nu_{1/2}$ (Fig. 4, curve *2*), which is typical of a growing degree of order. It should be emphasized that the aforementioned changes in the RS spectra of the germanium samples were observed in both the elastic ($W < W_0$) and the elastoplastic ($W > W_0$) modes of the multiple ($N \lesssim 10^3$) laser-induced straining and did not feature a pronounced threshold character (Fig. 4).

The RS spectrum narrowing observed in the entire W range may be caused by the existence of an initial (at $W = 0$) inhomogeneous broadening of the RS spectra in the studied samples due to the overlapping of local

stress fields that exist in the vicinity of various growth-related microinclusions and extended defects, e. g., dislocations. Is it well known that such local fields of compression and tension of the crystal lattice in the vicinity of defects give rise to a considerable broadening of the RS spectra [21]. In fact, the initial RS linewidth for unirradiated samples was $\nu_{1/2} \approx 7.5$ cm^{-1}, whereas the RS line of the reference germanium single crystal with a low concentration of growth dislocations had a width of ~ 5.5 cm^{-1}. In the conditions of multiple laser irradiation realized in our experiment (in both the elastic and elastoplastic modes), an increase in W resulted in the increase of the concentration of "frozen" vacancies ("vacancy pump" model [19, 22]), whose migration to dislocations or other sinks may effectively reduce the fluctuations of microstresses existing before exposure in the vicinity of defects. To illustrate such a positive influence of defects, we may recall the well-known relaxation of microstresses in the elastic model of interstitial precipitate, where the discrepancy in the size of an inclusion and semiconductor void (for example, the inclusion is larger than the void) is significantly reduced because the "excess" material of the host is removed in the course of the diffusive absorption (emission) of point defects: vacancies, interstitial atoms, etc. ([19], p. 203).

Another argument in favor of the noticeable contribution of vacancies (and other point defects) to the observed defect–diffusion microplasticity [19] is presented by an increase in the intensity of RS (Fig. 4, curve *3*). According to the theory of RS for an anharmonic crystal containing vacancies [23], the presence of vacancies should produce an additional polarization of the lattice around the point defect, thus making additional contributions to the dipole moment and renormalizing the spectral width and position of both the fundamental and combination absorption lines. Usually, the defects make only a moderate contribution to these parameters; however, the laser-induced cyclic thermal strains may cause a considerable accumulation of defects (vacancies) [3], which can contribute significantly to both the frequency shifts and the increase in the intensities of the Raman scattering and the fundamental absorption [23].

It should also be noted that, when the concentration of the point defects is high, various types of instabilities might develop and give rise to the formation of a microcrystalline superstructure, which is possibly the case in our experimental conditions [3, 12]. In order to verify the latter statement, one has to perform a direct study of the changes induced in the micromorphology of the surface by the elastoplastic laser effect. This may be done using scanning atomic-force microscopy, which we are planning to perform.

CONCLUSION

(1) We studied the changes in the fluorescence spectra of dye (rhodamine B) molecules adsorbed on a germanium surface and in the parameters of the Raman and diffuse scattering of light, which were the result of elastic ($W < W_0$) and elastoplastic ($W > W_0$) pulsed laser effects with a threshold strain amplitude of $\sim 5 \times 10^{-5}$ [2].

(2) Along with the deep traps in the insulator (GeO_2), the slow fluctuation states appearing in the oxide layer at the thresholds $W_0 \approx 70$ mJ/cm^2 [10] effectively absorb the electron photoexcitation energy from the adsorbed probe molecules and cause a pronounced quenching of their fluorescence at $W \geq W_0$. The energy transfer to the fluctuation states near the insulator/semiconductor interface is accompanied by a threshold (with respect to W) broadening of the fluorescence spectra of the dye, which suggests a steep rise in the geometric heterogeneity of the germanium surface due to irreversible (residual) surface displacements $\Delta U_z \sim$ 1–10 nm that arise at the thresholds W_0.

(3) The observed behavior of the Raman and the diffuse scattering parameters indicates that a gradual accumulation of microplastic changes occurs in the surface layer of the semiconductor (Ge). The initial stage of modifications includes primarily the generation, the accumulation (from pulse to pulse), and the diffusion to sinks of the point defects (presumably, vacancies), which, at $W \geq (1.2–1.5)W_0$, (i) lead to the growth of scattering irregularities thus enhancing the intensity of the diffuse scattering and (ii) effectively reduce the inhomogeneous broadening of the RS spectra caused by local microstress fields.

(4) High concentrations of point defects in germanium are attainable in the elastoplastic mode of multiple local laser effects; therefore, irradiation in this mode may cause an instability in the point defect field with the subsequent formation of periodic surface superstructures.

REFERENCES

1. P. M. Fauchet, Phys. Lett. A **93**, 155 (1983).
2. A. G. Barskov and S. V. Vintsents, Fiz. Tverd. Tela (St. Petersburg) **36** (9), 2590 (1994) [Phys. Solid State **36**, 1411 (1994)].
3. B. L. Volodin, V. I. Emel'yanov, and Yu. G. Shlykov, Kvantovaya Élektron. (Moscow) **20** (1), 57 (1993).
4. C. S. Lee, N. Koumvakalis, and M. Bass, Appl. Phys. Lett. **47**, 625 (1982); Opt. Eng. **22**, 419 (1983).
5. C. S. Lee, N. Koumvakalis, and M. Bass, J. Appl. Phys. **54**, 5727 (1983).
6. S. S. Cohen, J. B. Bernstein, and P. W. Wyatt, J. Appl. Phys. **71**, 630 (1992).
7. S. V. Vintsents and S. G. Dmitriev, Pis'ma Zh. Tekh. Fiz. **21** (19), 1 (1995) [Tech. Phys. Lett. **21**, 767 (1995)].
8. S. V. Vintsents, S. G. Dmitriev, and O. G. Shagimuratov, Pis'ma Zh. Tekh. Fiz. **22** (8), 8 (1996) [Tech. Phys. Lett. **22**, 307 (1996)].
9. A. G. Barskov, S. V. Vintsents, G. G. Dvoryankina, *et al.*, Poverkhnost, No. 3, 79 (1995).

10. S. V. Vintsents, S. G. Dmitriev, R. A. Zakharov, and G. S. Plotnikov, Fiz. Tekh. Poluprovodn. (St. Petersburg) **31** (5), 513 (1997) [Semiconductors **31**, 433 (1997)].
11. I. V. Ostrovskiĭ, L. P. Steblenko, and A. B. Nadtochiĭ, Fiz. Tekh. Poluprovodn. (St. Petersburg) **34** (3), 257 (2000) [Semiconductors **34**, 251 (2000)].
12. V. I. Emel'yanov, Kvantovaya Élektron. (Moscow) **28**, 2 (1999).
13. R. F. Wood, C. W. White, and R. T. Young, Semicond. Semimet. **23**, 1 (1984).
14. S. V. Vintsents and S. G. Dmitriev, Zh. Tekh. Fiz. **67** (2), 105 (1997) [Tech. Phys. **42**, 216 (1997)].
15. S. V. Vintsents, S. G. Dmitriev, and O. G. Shagimuratov, Fiz. Tverd. Tela (St. Petersburg) **38** (4), 993 (1996) [Phys. Solid State **38**, 552 (1996)].
16. S. V. Vintsents, V. F. Kiselev, and G. S. Plotnikov, Phys. Status Solidi A **85**, 273 (1984).
17. V. F. Kiselev, S. N. Kozlov, and A. V. Zoteev, *Foundations of Solid Surface Physics* (Mosk. Gos. Univ., Moscow, 1999), Chap. 6.
18. V. B. Zaĭtsev, S. G. Zhidomirova, and G. S. Plotnikov, Khim. Fiz. **9** (4), 485 (1990).
19. V. P. Alekhin, *Physics of Strength and Plasticity of Surface Layers of Materials* (Nauka, Moscow, 1983).
20. M. M. Sushchinskiĭ, *Raman Scattering and Structure of Materials* (Nauka, Moscow, 1981).
21. I. I. Novak, V. I. Vettegren', and B. M. Tashpulatov, in *Spectroscopy of Raman Scattering* (Nauka, Moscow, 1978), p. 191.
22. N. V. Karlov, N. A. Kirichenko, and B. S. Luk'yanchuk, *Laser Thermochemistry* (Nauka, Moscow, 1992), Chap. 15.
23. A. A. Adkhamov, V. I. Lebedev, and Kh. Nasrullaev, in *Spectroscopy of Raman Scattering* (Nauka, Moscow, 1978), p. 10.

Translated by A. Sidorova-Biryukova

Semiconductors, Vol. 36, No. 8, 2002, pp. 889–894. Translated from Fizika i Tekhnika Poluprovodnikov, Vol. 36, No. 8, 2002, pp. 953–958.

SEMICONDUCTOR STRUCTURES, INTERFACES, AND SURFACES

Electron Tunneling through a Double Barrier in a Reverse-Biased Metal–Oxide–Silicon Structure

G. G. Kareva*^, M. I. Vexler, I. V. Grekhov**, and A. F. Shulekin****

** Institute of Physics, St. Petersburg State University, St. Petersburg, 198504 Russia*

^ e-mail: galina.kareva@pobox.spbu.ru

*** Ioffe Physicotechnical Institute, Russian Academy of Sciences, St. Petersburg, 194021 Russia*

Submitted December 27, 2001; accepted for publication December 28, 2001

Abstract—A number of effects in metal/(tunnel-thin SiO_2)/p^+-Si structures associated with electron tunneling from the valence band of bulk Si into a metal have been studied. The tunneling occurs through two successively arranged tunnel-transparent barriers: that of the depleted space charge region in Si and the SiO_2 barrier, with the possible intermediate involvement of a quantum well formed by the Si conduction band. The current–voltage characteristics of the structures are calculated in terms of a simple model that considers these mechanisms for the purely depletion mode, i.e., with the inversion layer charge neglected. The relationship between the structure parameters (*p*-Si doping level and oxide thickness) and the relative contributions of nonresonant and resonant (via quantum-well levels in the Si conduction band) tunneling to the overall current through an MOS structure is discussed. The conditions most favorable for the observation of resonance effects are formulated.

1. INTRODUCTION

In [1], we reported on the experimental observation of steps and peaks in current–voltage (*I–V*) characteristics of metal/SiO_2/p^+-Si structures ($N_A \approx 10^{19}$ cm^{-3}, $d_{ox} \approx$ 3 nm). These features were attributed to the resonant tunneling transport of electrons along the path of the (valence band of Si)–(discrete levels in the quantum well (QW) in the conduction band of Si)–metal.

Interest in these kinds of features of the electrical characteristics of metal/oxide/silicon (MOS) tunnel structures based on relatively heavily doped silicon is stimulated by two different factors. First, the thickness of the gate insulator in modern FETs may already be less than 3 nm [2], and the channel doping level may exceed 10^{18} cm^{-3}, so that the integrated study of the various operation features of tunnel MOS structures with the corresponding parameters is of high practical importance. Second, the above features allow us to regard, under certain conditions, a MOS structure as a resonant-tunneling nanostructure, which makes the variety of its properties much wider and improves the prospects for its application.

A necessary stage in studying electron tunneling through a double barrier (first, in the depleted layer in Si and then through SiO_2, possibly via a QW in the Si conduction band) consists in systematizing the effects associated with this type of transport and the requirements for the structural parameters, which, when satisfied, allow observation of these effects. This is the aim of the present study. We restrict our analysis to a consideration of the depletion mode and ignore the build-up of electrons in the QW.

2. POSSIBLE EFFECTS AND FORMAL CONDITIONS FOR THEIR OBSERVATION

In a MOS structure based on p^+-Si, the following effects associated with tunneling transport of electrons in the band gap of Si may occur (Fig. 1):

(i) nonresonance tunneling of electrons from the Si bulk through the tunnel-transparent barriers in the space charge region (SCR) of Si and the insulator (Fig. 1a);

(ii) resonance tunneling of electrons from the Si bulk through the double barrier via the discrete quantum-well levels in the SCR of Si and in the QW lying between these two barriers. In previous experiments, resonant tunneling manifested itself as a sharp rise in current, which was observed when each new quantum level became involved in the charge transport (Fig. 1b) [1];

(iii) resonance tunneling of electrons from the metal, which is responsible for a current peak appearing when one of the QW levels lying below the Fermi level of the metal coincides with the valence band edge of the bulk Si [1];

(iv) ingress of tunneling electrons into the Si conduction band and their build-up in the QW, which may presumably make the voltages corresponding to the occurrence of resonances somewhat higher but does not significantly change the general situation.

The first two tunneling processes, nonresonance and resonance transfer of electrons from the Si bulk to the

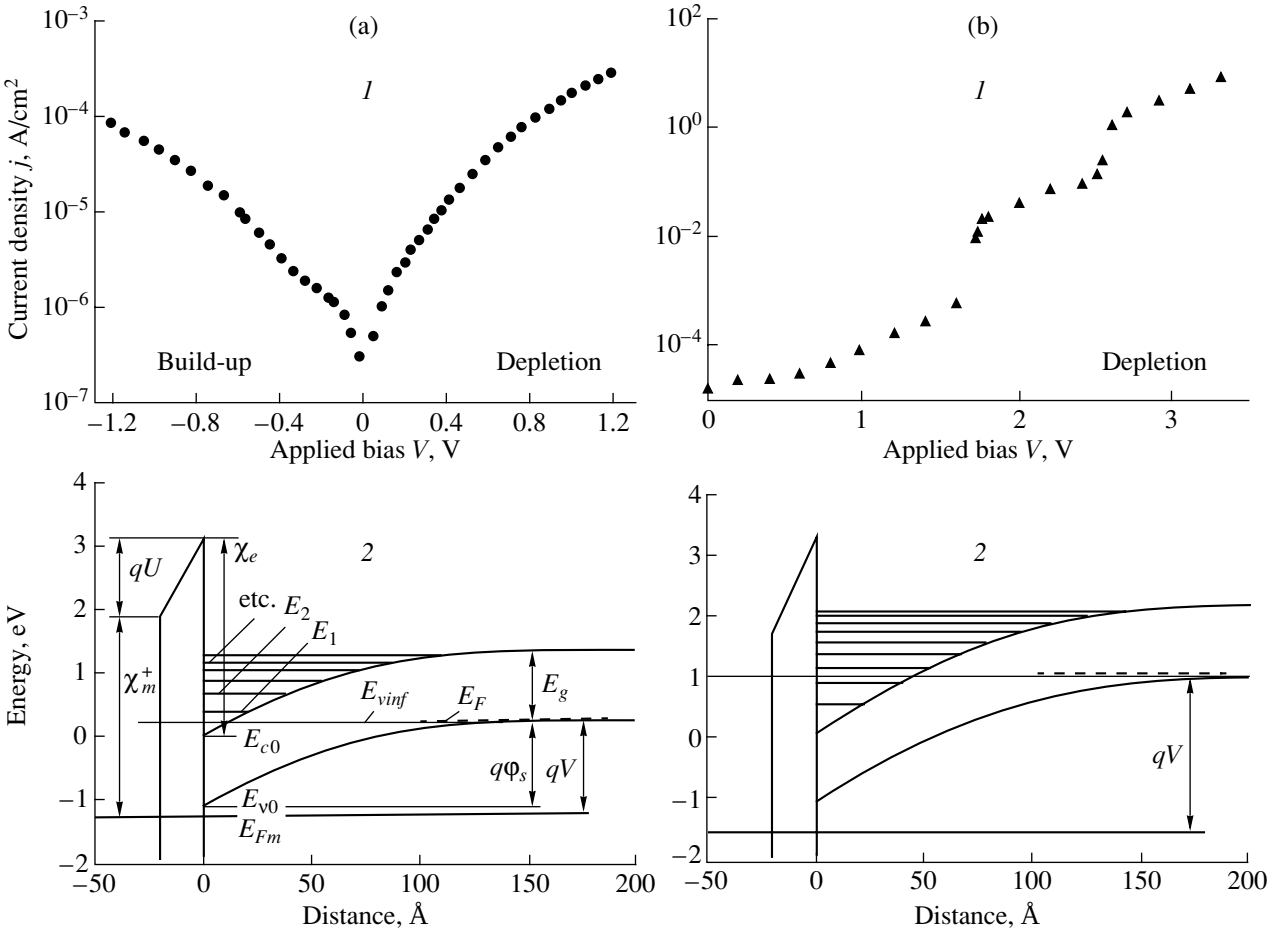

Fig. 1. *I–V* characteristics of a Al/SiO_2/p^+-Si (111) structure at $N_A = 2 \times 10^{19}$ cm^{-3} and $d_{ox} \approx 2.5$ nm under forward (a, *1*) and reverse (b, *1*) bias and the corresponding band diagrams (in scale) for a Al/SiO_2/p^+-Si structure with $N_A = 10^{19}$ cm^{-3} and $d_{ox} \approx 2$ nm (a, *2*; b, *2*): (a) at low voltages ensuring only nonresonant electron tunneling through the double barrier, $V < 1.5$ V; (b) at higher voltages, $V > 1.8$ V, inducing resonant as well as nonresonance tunneling.

metal, are responsible for the high reverse currents, making them close to the forward currents. In what follows, we discuss these two processes in more detail.

Apparently, the double barrier described above exists in any MOS structure in any mode, with the exception of the flat band case. In other words, if, for example, the electron exchange between the Si valence band and the metal is discussed with quantitative details neglected, then it is E_{vinf}, and not E_{v0} (Fig. 1a), that must be the upper limit of the energies considered.

A necessary condition for resonance tunneling from Si is that at least one of the QW levels should coincide with or lie below the valence band edge in the Si bulk, E_{vinf}. This condition can be satisfied for any N_A and d_{ox} at a sufficiently high reverse bias *V*. Apparently, this is impeded in thick structures by the small band bending $q\varphi_s$, because virtually the entire applied voltage *V* falls on the insulator [3]. However, the current flow into the metal grows with increasing *V*, and, as soon as this rise can no longer be compensated for by thermal generation, $q\varphi_s$ becomes high enough.

For resonance tunneling from the metal to occur, at least the ground level E_1 in the QW must be equal to or lower than E_{Fm} at the instant of its coincidence with E_{vinf}. Analysis shows that this condition cannot be satisfied in the Al/SiO_2/Si system in the absence of charge at the Si/SiO_2 interface: the E_1 level always lies above E_{Fm}. However, we can imagine a structure with a very low work function of the metal, or with a strongly positively charged interface, in which the necessary conditions could be fulfilled.

The above-mentioned build-up of electrons in the QW invariably occurs even in the case when thermal generation cannot maintain the inversion layer ($d_{ox} <$ 3.5 nm) and the structure is defect-free (tunneling is not upset). The fact is that each tunneling electron makes a contribution $q|\psi(z)|^2$ to the two-dimensional density of a charge (ψ is the wave function, and *z* is the direction of tunneling). There arises a kind of analogue with the

case of space-charge-limited current. This also occurs in conventional resonant-tunneling diodes [4, 5].

3. SEMIQUANTITATIVE MODEL

The presented qualitative analysis does not suggest any definite limitations, so that resonant and nonresonant tunneling may occur in any structure. The model presented below was developed and applied to the calculation of the *I–V* characteristics and to the evaluation of MOS structure parameters at which effective tunneling occurs.

In the framework of the model, we assume that the device operates in the depletion mode and disregard the build-up of electrons in the QW. A tunnel MOS structure itself is a rather complex object, and we decided to ignore charge build-up for the time being, the more so as the self-consistent consideration of it (as in [5]) may prove irrelevant because of the use of simplified formulas for tunneling.

The energy levels E_i in the QW and the corresponding lifetimes τ_i can be found using a quasi-classical approach (from the relation $2\int p_z\,dz \approx (i - 1/4)h$, $\tau = 2\int v_z^{-1}\,dz$, where p_z is momentum and v_z is velocity). This leads, in the case of depletion, to the following analytical expressions:

$$w\sqrt{w^2 - a^2} - a^2 \ln\frac{w + \sqrt{w^2 - a^2}}{a} = \left(i - \frac{1}{4}\right)\frac{\alpha h}{(2m_{n,z})^{1/2}},$$
$$\tau_i^n = \frac{\sqrt{2m_{n,z}}\alpha}{2}\ln\frac{w + \alpha(E_i^n)^{1/2}}{w - \alpha(E_i^n)^{1/2}}, \quad (1)$$

where w is the width of the depletion region, $m_{n,z}$ is the electron mass in the tunneling direction, and

$$a^2 = w^2 - \frac{2E_i^n\varepsilon_0\varepsilon_s}{q^2N_A}, \quad \alpha = \left(\frac{2\varepsilon_0\varepsilon_s}{q^2N_A}\right)^{1/2}. \quad (2)$$

The additional index n ($n = he, le$) is introduced to distinguish the subsystems of levels for heavy and light electrons. The degeneracy factors are as follows: $\nu_{he} = 2$, $\nu_{le} = 4$ for (100)Si; and $\nu_{he} = 6$, $\nu_{le} = 0$ for (111)Si. The ground level E_1 always corresponds to the "heavy" subsystem ($E_1 = E_1^{he}$). Examples of band diagrams with levels for (111)Si are presented in Fig. 1.

The energy levels are the levels of the quantity $E - E_\perp$, which, as applied to a QW, is usually designated as E_z. Here E, E_z, and $E_\perp$ are, respectively, the total energy of a particle and its components in the tunneling direction and in the perpendicular plane. The designation E_i^n or E_i (instead of $E_{z,i}^n$) is used for brevity. The current through the structure comprises four components:

$$j = j_{v0} + j_{vdt} + j_{vrez} + j_{c0}, \quad (3)$$

where j_{v0} and j_{c0} are the currents of electron tunneling from the valence and conduction bands of Si only through SiO_2, and j_{vdt} and j_{vrez} are the currents of nonresonant and resonant tunneling through the SCR and oxide. The expression for j_{c0} is well known and has been given, e.g., in [6]; actually, j_{c0} is limited by the current of thermal generation.

In practice, j_{v0} and j_{vdt} can be calculated together:

$$j_{v0} + j_{vdt} = \frac{4\pi q}{h^3}\sum_{p,n}\left(m_{p,\perp}\frac{v_n}{6}\int_{-\infty}^{E_{vinf}}(f_P(E) - f_M(E)) \times \int_0^{E_{vinf}-E} T_{ox}(E - E_\perp)T_s^{p,n}(E, E_\perp)\,dE_\perp\,dE\right). \quad (4)$$

In this case, the product of tunneling probabilities $T_{ox} \cdot T_s$ through, separately, SiO_2 and Si is used as the probability of "double" tunneling. T_s depends on E and $E_\perp$ [3], and T_{ox}, only on the difference $E - E_\perp$. In calculating T_{ox}, we assume that electrons always interact with the conduction band of the oxide. As the limits of integration with respect to energy, we take $-\infty$ and E_{vinf} for E (see Fig. 1a), and zero and $E_{vinf} - E$ for $E_\perp$. The Fermi functions for the semiconductor bulk and the metal are denoted by $f_P(E)$ and $f_M(E)$. The summation includes light and heavy electrons and holes (the distinction is necessary, because T_s depends on the mass $2(m_{n,z}^{-1} + m_{p,z}^{-1})^{1/2}$ [3]). The principal contribution to the current is made by tunneling from the light hole subband.

If j_{v0} is to be found separately, E_{v0} should be substituted for E_{vinf} in relation (4) (naturally, $T_s \equiv 1$ in this case). It is in this form that the current between the metal and the Si valence band is written with the "double" tunneling disregarded. The resonant component is the sum of currents via levels (for each level, the peak value $T_{\max}$ is multiplied by the peak width ΔE_i):

$$j_{vrez} = \frac{4\pi q}{h^3}\sum_{p,n}\left(m_{p,\perp}\frac{v_n}{6}\sum_{i=1,2,\ldots} T_{\max}^{p,n,i}\Delta E_i^{p,n} \times \int_0^{1/2(E_{vinf}-E_i^n)}(f_P(E_i^n + E_\perp) - f_M(E_i^n + E_\perp)) \times \exp(-\lambda E_\perp)\,dE_\perp\right). \quad (5)$$

The upper limit in the integral (5) takes into account the conservation of $E_\perp$. Nevertheless, its significance

should not be overestimated, because, in view of the smallness of $\lambda = 2\pi E_g^{1/2}(q\hbar F(E))^{-1}(m_{n,z}^{-1} + m_{p,z}^{-1})^{-1/2}$ (F is the average field for an electron with energy $E = E_i^n + E_\perp$ in its tunneling in Si), only particles with low $E_\perp$ can overcome the barrier. Therefore, even replacing the upper limit of integration by $+\infty$ leads to only minor changes.

As follows from the above analysis, the probability of tunneling in the maximum is

$$T_{\max}^{p,n,i} = T_{ox}(E_i^n)T_s^{p,n}(E_i^n, 0)\frac{1}{(1 - b_i^{p,n})^2}, \qquad (6)$$
$$b_i^{p,n} = \sqrt{1 - T_{ox}(E_i^n)}\sqrt{1 - T_s^{p,n}(E_i^n, 0)},$$

and the level broadening

$$\Delta E_i^{p,n} = \frac{2\hbar}{\tau_i^n}\sqrt{-2 + \frac{1}{b_i^{p,n}} + b_i^{p,n}}. \qquad (7)$$

For all the cases of interest, $\Delta E_i^{p,n}$ is much smaller than the energy spacing between the two neighboring levels ($E_i^{n+1} - E_i^n$). The *I–V* characteristics of MOS structures, calculated in terms of this model, are discussed in the next section.

4. PRACTICAL CONDITIONS FOR THE OBSERVATION OF EFFECTS

Apparently, the experimental study of tunneling through a double barrier may be complicated if

(a) the probability of tunneling through the oxide is too small;
(b) the probability of tunneling in the semiconductor is too small;
(c) the necessary mode cannot be achieved owing to structure degradation;
(d) the current j_{vdt} is not small, but is much smaller than the currents $j_{v0} + j_{c0}$;
(e) the current j_{vrez} is much smaller than $j_{v0} + j_{c0} + j_{vdt}$ (in the theory of resonance tunneling, this sum is called the excess current).

The calculation we performed answers the question as to how these problems can be eliminated by the proper selection of structure parameters (Fig. 2). Thick structures with small T_{ox} are not considered here, because an inversion layer, ignored in our model, would be formed in such structures. Thus, $d_{ox} < 3.5$ nm in all cases and, therefore, the problem of the excessively low probability of tunneling through the oxide is formally resolved.

The probability of tunneling through the valence band in the SCR of Si is governed by the doping level N_A. At $N_A < 5 \times 10^{17}$ cm^{-3} and under reasonable conditions (V of several volts), the fields in the SCR and the probability T_s are so small that the tunneling currents (j_{vdt}, j_{vrez}) are virtually zero. However, at higher N_A (up to about 5×10^{18} cm^{-3}), tunneling of electrons with energies close to E_{vinf} from the valence band is also nearly impossible: the barrier at the SCR boundary farthest from the interface is too high. Consequently, the instants when the conditions for the occurrence of resonances, $E_i = E_{vinf}$, are satisfied may be indiscernible in the *I–V* characteristics (see below).

The breakdown of SiO_2 under an internal field of $\approx 2 \times 10^7$ V cm^{-1} places the upper limit for N_A at 3×10^{19} cm^{-3} for the case of resonant tunneling; at heavier doping, the oxide degrades even at a bias V corresponding to the mode $E_1 = E_{vinf}$. The lower "degradation limit" $N_A = 2 \times 10^{17}$ cm^{-3} is associated with the avalanche in Si. The background on which the current j_{vdt} may or may not be discernible is mainly created by j_{v0} (j_{c0} is small). As long as $E_{v0} < E_{Fm}$, i.e., $qU < E_g + \chi_e - \chi_m^+$, the current j_{v0} is also close to zero, because the quantum states with energies below E_{v0} are filled on both sides of the oxide. With increasing V, the voltage U grows, but $q\varphi_s$ grows too, which hampers the formation of the component j_{v0}. For a given bias V, an increase in N_A and/or d_{ox} results in higher U and smaller $q\varphi_s$, thus creating more favorable conditions for j_{v0} flow. In this context, mention should be made of a seemingly paradoxical result: for the same doping level ($N_A = 10^{19}$ cm^{-3}), the reverse current in the semiconductor (found with tunneling disregarded) increases, rather than decreases, with d_{ox} growing in a certain thickness range (compare Figs. 2b and 2a).

A relatively large contribution of j_{vdt} to the total current would be expected for the minimal thickness d_{ox}. As for doping, raising its level favors an increase in j_{vdt} owing to a rise in T_s (at any d_{ox}), but j_{v0} grows simultaneously. As a result, the component j_{vdt} is exceedingly important at $N_A \approx 10^{19}$ cm^{-3} and $d_{ox} \longrightarrow 0$ (Fig. 2b), and taking it into account in calculations yields high reverse currents that are in agreement with the experiment, whereas at higher N_A, its role decreases somewhat.

Figures 2a–2c give an answer to the question of the relative contribution of the resonant component compared to that of the excess current. Figure 2d shows an approximate ratio of the current j_{vrez} to $j_{c0} + j_{v0} + j_{vdt}$ at the instant when the first resonance ($E_1 = E_{vinf}$) appears. The current j_{vrez} was evaluated as a term in relation (5) and corresponded to $p = lh$, $n = he$, $i = 1$, with $+\infty$ as the upper limit of integration. The contribution of j_{vrez} to the total current grows with increasing d_{ox}. Moreover, as seen in Fig. 2c, the resonances are not always manifested as clear steps. At $N_A < 5 \times 10^{18}$ cm^{-3}, they simply provide an additional contribution, more or less monotonic, to the total current j. In this case, they manifest themselves at a voltage V higher than that correspond-

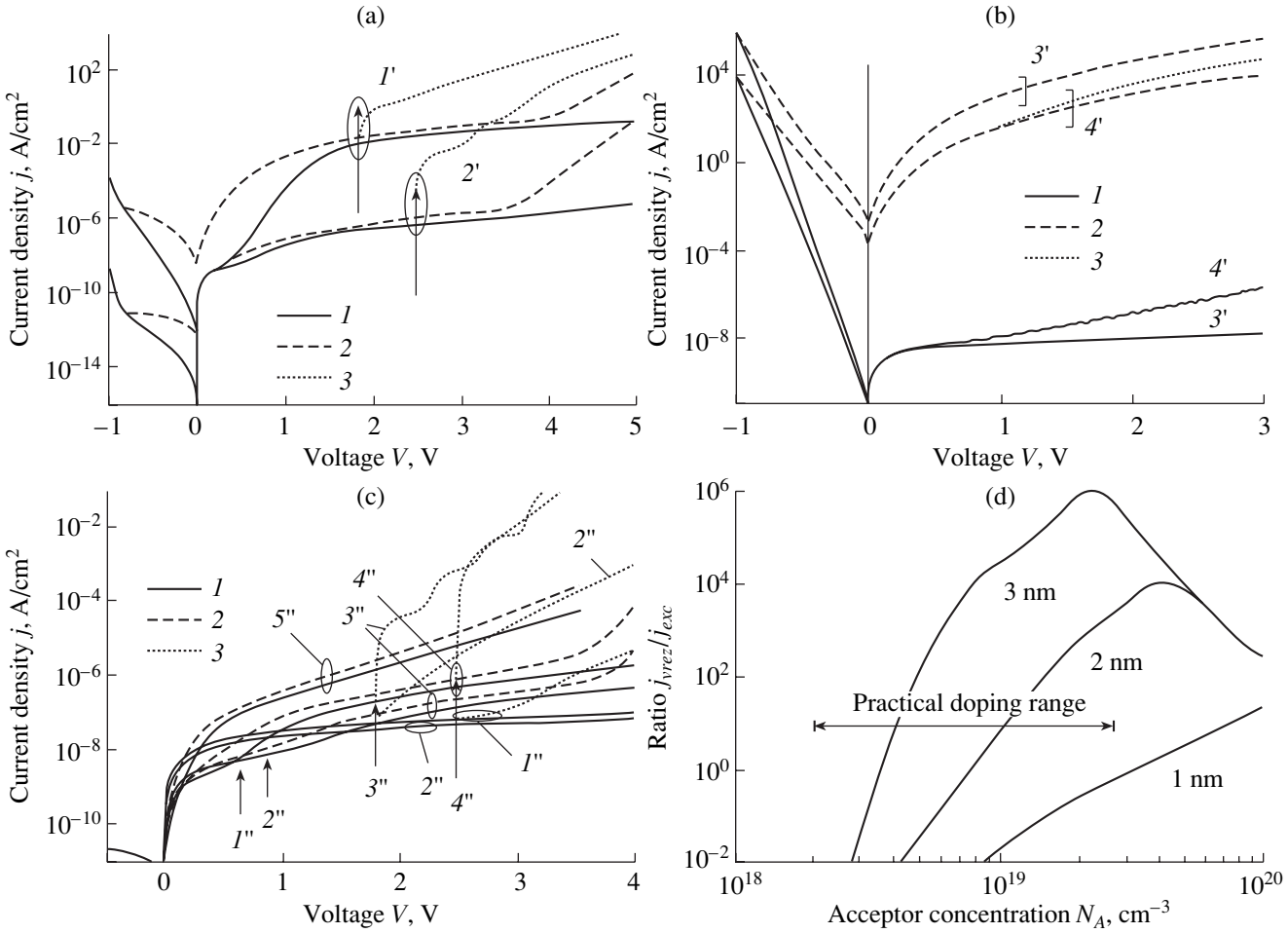

Fig. 2. (a–c) Calculated I–V characteristics of Al/SiO_2/p^+-(111)Si structures: (*1*) solid curves for $j_{v0} + j_{c0}$ with nonresonance and resonance tunneling disregarded; (*2*) dashed curves for $j_{vdt} + j_{v0} + j_{c0}$ only nonresonance tunneling taken into account; (*3*) dotted curves for $j_{rez} + j_{vdt} - j_{v0} + j_{c0}$ with account of both nonresonance and resonance tunneling. (a, b) At $N_A = 10^{19}$ cm^{-3} and varied oxide thickness d_{ox}, nm: (*1'*) 2.0, (*2'*) 3.0, (*3'*) 0.1, and (*4'*) 0.5 nm. (c) At $d_{ox} = 3$ nm and varied N_A, cm^{-3}: (*1"*) 5×10^{17}, (*2"*) 10^{18}, (*3"*) 5×10^{18}, (*4"*) 10^{19}, and (*5"*) 5×10^{19} cm^{-3}. Arrows in (a) and (c) indicate the voltages V corresponding to the condition $E_1 = E_{vinf}$ for the given N_A. (d) Calculated ratio of the resonance current j_{vrez} to the excess current $j_{exc} = j_{v0} + j_{c0} + j_{vdt}$ at the instant when the condition $E_1 = E_{vinf}$ is satisfied.

ing to $E_1 = E_{vinf}$. Therefore, the range of Si doping in which resonance effects should be observed in the way presented in Fig. 1b is rather narrow; for example, at $d_{ox} = 3$ nm, it does not exceed 5×10^{18}–3×10^{19} cm^{-3}. In this range, problems with the voltage resolution do not arise, since the difference $V_2 - V_1$ between the voltages corresponding to $E_2 = E_{vinf}$ and $E_1 = E_{vinf}$ is several fractions of a volt.

5. CONCLUSION

The conditions for the observation of resonant and nonresonant tunneling of electrons from the valence band of the Si bulk to a metal have been studied. The tunneling occurs through a double barrier formed successively by the tunnel-transparent barriers of the space charge region in a semiconductor and the insulator. The process also involves quantum-well levels in a QW formed by the conduction band of the semiconductor in Me/SiO_2/p^+-Si structures. A simple model that takes this transport mechanism into account was developed, and the I–V characteristics of MOS structures ($d_{ox} <$ 3.5 nm) in the purely depletion mode were calculated in terms of this model. Nonresonant tunneling is shown to be significant at $N_A > 5 \times 10^{17}$ cm^{-3}. It plays an important part in ensuring transport when $N_A \approx 10^{19}$ cm^{-3} and when the oxide thickness is minimal ($d_{ox} \longrightarrow 0$). It is demonstrated that the occurrence of resonant transport does not necessarily lead to the appearance of steps in the current. For example, at $d_{ox} = 3$ nm, the resonances emerge in the range of 5×10^{17}–3×10^{19} cm^{-3}, with clear steps expected only at $N_A > 5 \times 10^{18}$ cm^{-3}. At lower

N_A or d_{ox}, the resonances are not distinct and merely result in a smooth increase of current with voltage V.

ACKNOWLEDGMENTS

We are grateful to the state scientific program "Nanostructures" and the Russian Foundation for Basic Research (project no. 99-02-18079a) for financial support.

REFERENCES

1. G. G. Kareva, Fiz. Tekh. Poluprovodn. (St. Petersburg) **33**, 969 (1999) [Semiconductors **33**, 883 (1999)].
2. H. S. Momose, M. Ono, T. Yoshitomi, *et al.*, IEEE Trans. Electron Devices **43**, 1233 (1996).
3. S. Sze, *Physics of Semiconductor Devices* (Wiley, New York, 1981; Mir, Moscow, 1984), Vol. 1, Chap. 7.
4. J. Pozela, *Physics of High-Speed Transistors* (Mokslas, Vilnius, 1989; Plenum, New York, 1989).
5. K. Brennan, J. Appl. Phys. **62**, 2392 (1987).
6. A. F. Shulekin, M. I. Vexler, and H. Zimmermann, Semicond. Sci. Technol. **14**, 470 (1999).

Translated by D. Mashovets

Semiconductors, Vol. 36, No. 8, 2002, pp. 895–898. Translated from Fizika i Tekhnika Poluprovodnikov, Vol. 36, No. 8, 2002, pp. 959–963.

LOW-DIMENSIONAL SYSTEMS

Structure of Heterointerfaces and Photoluminescence Properties of GaAs/AlAs Superlattices Grown on (311)*A* and (311)*B* Surfaces: Comparative Analysis

G. A. Lyubas*^, N. N. Ledentsov, D. Litvinov***, B. R. Semyagin*, I. P. Soshnikov**, V. M. Ustinov**, V. V. Bolotov*, and D. Gerthsen*****

** Institute of Semiconductor Physics, Siberian Division, Russian Academy of Sciences, Novosibirsk, 630090 Russia*

^ e-mail: lubas@isp.nsc.ru

*** Ioffe Physicotechnical Institute, Russian Academy of Sciences, Politekhnicheskaya ul. 26, St. Petersburg, 194021 Russia*

**** University of Karlsruhe, D-76128 Karlsruhe, Germany*

Submitted December 10, 2001; accepted for publication December 18, 2001

Abstract—The photoluminescence properties of type II GaAs/AlAs superlattices grown on the (311) surface are determined by their polarity. Previous HRTEM investigations demonstrated a corrugation (with height of 1 nm and period of 3.2 nm) of both GaAs/AlAs and AlAs/GaAs interfaces in samples grown on the (311)*A* surface. In the present study, a lateral periodicity of 3.2 nm is also revealed in HRTEM images of a superlattice grown on the (311)*B* surface and in their Fourier transforms. However, this periodicity is poorly pronounced, which is due to fuzzy corrugation and the presence of a long-wavelength (>10 nm) disorder. Photoluminescence spectra of the GaAs/AlAs superlattice on the (311)*A* surface are strongly polarized relative to the direction of interface corrugation, in contrast to the (311)*B* superlattice, in which the corrugation is weakly pronounced. It was found that the strong mixing between the Γ and *X* minima of the conduction band, occurring only in sublattices with strongly corrugated interfaces, allows generation of bright red luminescence at 650 nm up to room temperature. The distinctions revealed between the superlattices grown on the (311)*A* and (311)*B* surfaces confirm that it is precisely the interface corrugation, and not crystallographic orientation, that governs the optical properties of (311) superlattices. © *2002 MAIK "Nauka/Interperiodica".*

Recently, much attention has been given to studying the effect of periodic faceting of the (311)*A* GaAs surface, which was discovered in 1991 [1]. Under typical conditions of molecular beam epitaxy (MBE), the (311)*A* GaAs surface is reconstructed into a periodic array of microfacets (microgrooves) directed along the crystallographic direction $[\bar{2}33]$ with a period of 32 Å along the direction $[01\bar{1}]$ [1]. The microgroove depth is 10.2 Å [1]. Heteroepitaxial growth of alternating GaAs and AlAs layers on such a faceted surface yields superlattices (SLs) with layers having a periodically modulated thickness. Such superlattices are commonly named lateral superlattices (LSLs), and the modulation of the layer thickness is termed "corrugation" of layers or heterointerfaces. LSLs are quasi-one-dimensional systems with strong quantum confinement of carriers. This is important for studying quantum phenomena at room temperature and creating devices that operate on intersubband transitions at high temperature. Recently, the polarization anisotropy of photoluminescence (PL) [2–4] has been observed in structures of this kind and it was found that dissimilar kinds of polarization anisotropy are observed at different GaAs layer thicknesses [3, 4]. At thicknesses exceeding ~35 Å, the nature of polarization is mainly accounted for by the orientation anisotropy of the (311) surface, and at thicknesses less than ~35 Å, predominantly by heterointerface corrugation [3, 4]. The observed polarization anisotropy of PL is in good agreement with data of high-resolution transmission electron microscopy (HRTEM) [5], according to which both GaAs/AlAs and AlAs/GaAs interfaces are corrugated with a lateral period of 3.2 nm and a corrugation height of 1 nm in samples grown on the (311)*A* surface. The present study is concerned with a comparative analysis of the PL and structure of GaAs/AlAs SLs grown on (311)*A*- and (311)*B*-oriented surfaces.

The GaAs/AlAs SLs under study were grown by MBE on GaAs substrates with (311)*A*, (311)*B*, and (100) orientations. The directions *A* and *B* were determined from anisotropy of chemical etching. The period of the SLs under study was 4 nm, with the mean thickness of GaAs and AlAs layers being the same and equal to 2 nm. The samples were studied using PL spectroscopy in the temperature range 77–300 K. An Ar^+ laser (488 nm) with a typical pumping power of 10–20 mW (incident power density 5–10 W/cm^2) served as the PL excitation source. The PL spectra were recorded using an SDL-1 double monochromator with a resolution of 0.4 nm and a photomultiplier with an S-20 cathode.

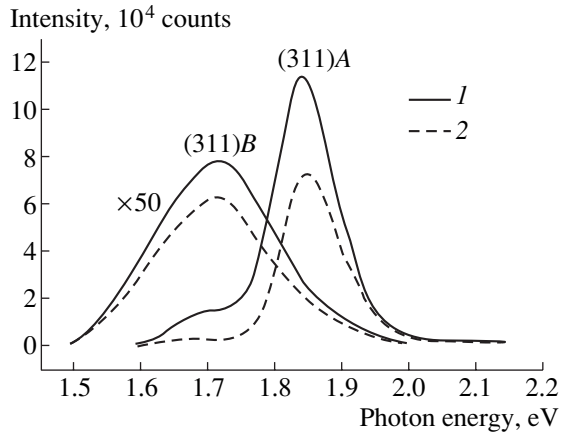

Fig. 1. PL spectra of GaAs/AlAs SLs grown on (311)*A* and (311)*B* surfaces in a single run. The spectra of the (311)*B* SL are enlarged by a factor of 50. T = 300 K. Polarization of light emitted by the samples was analyzed in the SL layer plane for two cases: along (*1*—*S* component) and across (*2*—*P* component) the corrugation grooves.

A Glan prism was used as the analyzer of light emitted by the samples. A depolarizing wedge was placed at the monochromator input. The SL structure was studied by HRTEM, with the images processed to enhance the contrast associated with different coefficients of electron extinction for AlAs and GaAs.

Figure 1 shows PL spectra of GaAs/AlAs SLs grown on (311)*A* and (311)*B* surfaces in the same run and, consequently, under identical conditions. The measurements were done at room temperature. Effective room-temperature PL was observed from a GaAs/AlAs SL grown on a faceted (311)*A* surface. The red luminescence from this SL could be seen with the naked eye, and its intensity was 50 times that in the case of an SL grown on a (311)B surface (the spectra of the latter in Fig. 1 are multiplied by a factor of 50). The difference is accounted for by the formation in the (311)*A* SL of well-structured corrugated layers of gallium arsenide, whose presence in the given sample was confirmed by direct electron-microscopic studies. Lateral localization of electrons in LSLs (for the most part, electron motion is only possible along corrugation grooves) reduces the nonradiative surface recombination, and it is this fact that results in high PL intensity at room temperature. The light exciting this PL was incident at some angle with respect to the plane of the SL layers. The direction of the electric field vector **E** (polarization of the exciting light) in the plane of the SL layers made an angle of 45° with the direction of the corrugation grooves ($[\bar{2}33]$ direction). The PL was recorded in the direction normal to the plane of layers. The polarization of light emitted by the samples was analyzed in the plane of the SL layers for two cases: along (solid line—*S* component) and across (dashed line—*P* component) the grooves. As expected, strong polarization anisotropy is observed in the PL spectra of

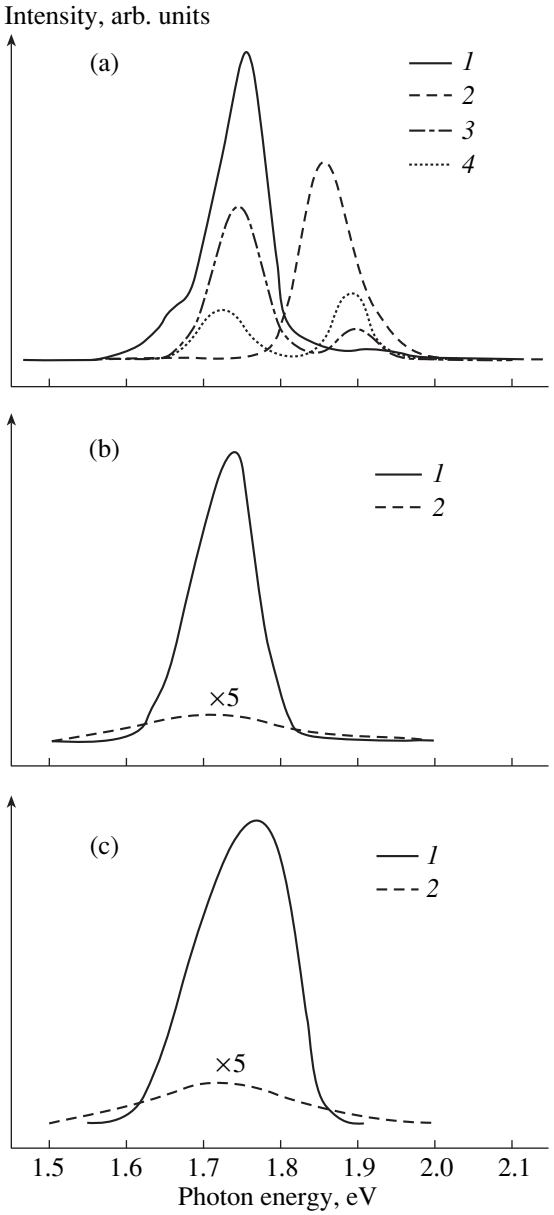

Fig. 2. PL spectra of GaAs/AlAs SLs grown on (a) (311)*A*, (b) (311)*B*, and (c) (100) surfaces in the same run. Temperature: (*1*) 77, (*2*) 295, (*3*) 117, and (*4*) 150 K. The spectra were recorded without an analyzer. The room temperature spectra of (311)*B* and (100) SLs are enlarged by a factor of 5.

(311)*A* LSLs. The degree of polarization $(S-P)/(S+P)$ is more than 60% for the peak at 1.69 eV and approximately 22% for the peak at 1.84 eV (Fig. 1). As seen from the same figure, the PL anisotropy is much weaker (~10%) in the case of a (311)*B* SL (peak at 1.71 eV). The decrease in the polarization anisotropy for the (311)*B* SL is quite understandable, being due to the fact that the corrugation in this SL is not so clearly pronounced as that in the (311)*A* SL. Thus, in the case of a (311)*B* SL, the effect of heterointerface corrugation is slight and the nature of polarization is mainly determined by the valence band anisotropy. It is noteworthy

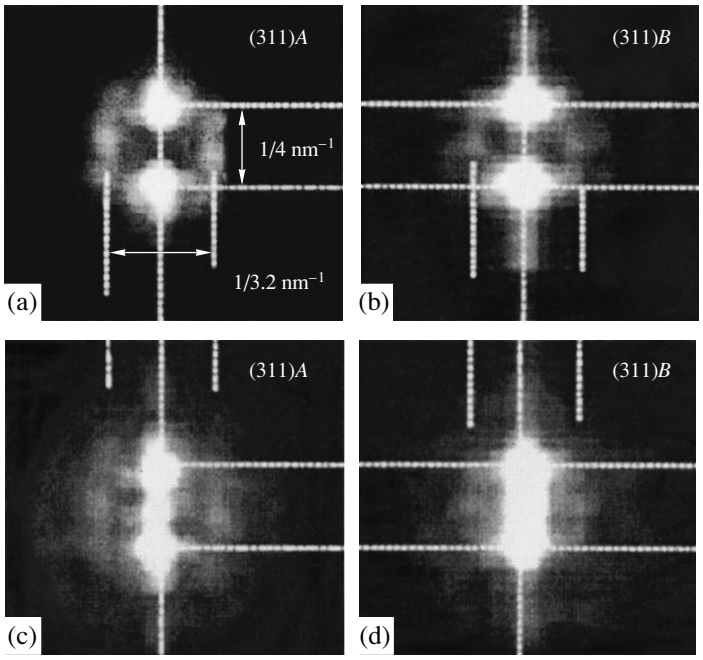

Fig. 3. Fourier transforms of HRTEM images obtained for (a) (311)*A* and (b) (311)*B* SLs with subtraction of the long-wavelength component. (c and d) Fourier transforms of, respectively, the same SLs but without subtraction. A lateral period of 3.2 nm is observed for both SLs but is much more obscure in the (311)*B* case, compared with (311)*A*, because of the strong overlapping by the long-wavelength component.

that the polarization anisotropy does not vary significantly with temperature.

Let us consider the PL spectra of SLs with orientations (311)*A*, (311)*B*, and (100), which are presented in Fig. 2 for different temperatures. The SLs were grown in a single run. A comparison of the spectra of (311)*B* and (100) SLs (Figs. 2b and 2c, respectively) shows that they are closely similar to one another and, at the same time, fundamentally different from the spectra of (311)*A* SLs (Fig. 2a). In contrast to the latter, the spectra of (311)*B* and (100) SLs contain one peak each, and the intensity of this peak grows with decreasing temperature. The similarity of PL from (311)*B* and (100) SLs means that, in contrast to the (311)*A* case, there is no pronounced modification of the electronic and optical properties of the (311)*B* SL as a result of heterointerface corrugation. This is due to the weaker corrugation and the presence of a long-wavelength disorder in (311)*B*. At the same time, the additional quantum confinement of carriers, which appears due to the layer thickness modulation in the (311)*A* LSL, leads to the strong modification of its electronic, optical, and quantum properties. Mixing[1] occurs between the Γ and *X* minima of the conduction band. As a result, two peaks are observed in the PL spectrum of the (311)*A* LSL; these are associated both with transitions involving the *X* minimum of the conduction band and with those from the mixed Γ–*X* states. It is noteworthy that such a strong mixing, which was observed here for the first time, is due to clearly pronounced heterointerface corrugation with a period of 3.2 nm and a height of 1 nm in the (311)*A* LSL under study.

The strong difference between the PL spectra of (311)*A* and (311)*B* SLs, revealed in the present study, is in agreement with the results of direct HRTEM investigations. Figure 3 shows the Fourier transforms of HRTEM images obtained for (311)*A* (Fig. 3a) and (311)*B* SLs (Fig. 3b) with the subtraction of the long-wavelength component in order to reveal the lateral periodicity. Figures 3c and 3d present the Fourier transforms of images for the same (311)*A* and (311)*B* SLs but without subtraction. It can be seen that there is a lateral period of 3.2 nm in both the (311)*A* and (311)*B* cases. In (311)*B* SLs, this periodicity is much less pronounced, being strongly overlapped by the long-wavelength component, but an intensity peak still exists. The existence of such a lateral period for the (311)*B* SL is in agreement with recent investigations using scanning tunnel microscopy [6]. It is noteworthy that the 3.2-nm lateral periodicity is not so clearly pronounced in the (311)*B* SL, compared with (311)A, and is adequately discerned only after the removal of the long-wavelength component. Moreover, as follows from the HRTEM image in Fig. 4, there is virtually no vertical correlation of GaAs- and AlAs-rich regions in the SL grown on the (311)*B* surface.

Thus, Fourier analysis of the HRTEM images of (311)*A* and (311)*B* SLs shows that a 3.2-nm lateral period is present in both SLs, but is less noticeable in the latter case because of weaker corrugation and a

[1] The phenomenon of mixing was first observed in [2].

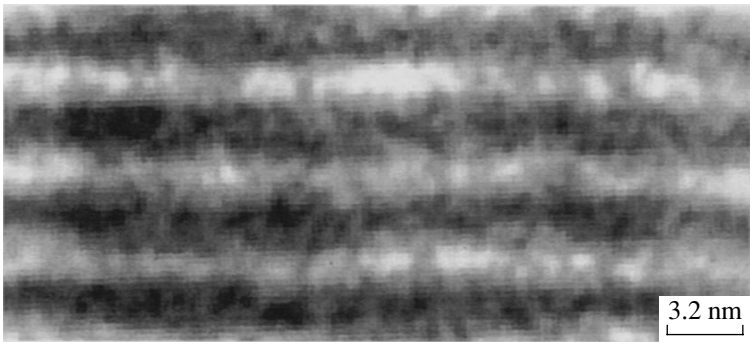

Fig. 4. HRTEM image of the structure of (311)*B* SL heterointerfaces. Vertical direction—[311], horizontal direction—[$01\bar{1}$]. Light layers—AlAs. Image height 16 nm. Weak corrugation with a lateral period of 3.2 nm and long-wavelength disorder with a characteristic lateral size of more than 10 nm are visible in the figure.

large amount of long-wavelength disorder. The (311)*A* SL shows a very distinct corrugation with a height of 1 nm and a clearly pronounced periodicity of 3.2 nm. Strong mixing between the Γ and *X* minima of the conduction band occurs only for SLs with strongly corrugated interfaces and makes it possible to obtain bright red luminescence at around 650 nm even at room temperature. The PL spectra of the (311)*A* SL show strong polarization anisotropy (the intensity of light polarized along the interface corrugation grooves greatly exceeds that for the transverse case). The anisotropy in the spectra of (311)*B* SLs is much less pronounced. This confirms the conclusion [3] that for the (311)*A* LSL the nature of polarization cannot be accounted for by only the orientation anisotropy of the (311) surface, rather, it is mainly determined by the corrugation of heterointerfaces. In contrast to the (311)*A* case, corrugation does not noticeably modify the electronic and optical properties of the (311)*B* SL, which is more similar to the conventional (100) SL in its electronic properties. The results presented above are important both for fundamental science and for the development of devices that may be used, e.g., in designing planar IR detectors with polarization-sensitive detection and normal incidence of light (operating on intersubband transitions), IR emitters, and planar Esaki–Tsu SLs for microwave applications (including three-terminal devices with a gate, e.g., microwave amplifiers).

ACKNOWLEDGMENTS

G.A.L. is grateful to the Zamaraev International Charitable Scientific Foundation.

REFERENCES

1. R. Nötzel, N. N. Ledentsov, L. A. Däweritz, *et al.*, Phys. Rev. Lett. **67**, 3812 (1991).
2. R. Nötzel, N. N. Ledentsov, L. A. Däweritz, *et al.*, Phys. Rev. B **45**, 3507 (1992).
3. G. A. Lyubas and V. V. Bolotov, Pis'ma Zh. Éksp. Teor. Fiz. **72**, 294 (2000) [JETP Lett. **72**, 205 (2000)].
4. G. A. Lyubas and V. V. Bolotov, in *Abstracts of the 9th International Conference on Defects: Recognition, Imaging and Physics in Semiconductors, Rimini, Italy, 2001*, p. 214.
5. N. N. Ledentsov, D. Litvinov, A. Rosenauer, *et al.*, J. Electron. Mater. **30**, 463 (2001).
6. Z. M. Wang, L. Däweritz, and K. H. Ploog, Appl. Phys. Lett. **78**, 712 (2001).

Translated by M. Tagirdzhanov

Semiconductors, Vol. 36, No. 8, 2002, pp. 899–902. Translated from Fizika i Tekhnika Poluprovodnikov, Vol. 36, No. 8, 2002, pp. 964–968.

LOW-DIMENSIONAL SYSTEMS

Wavelength of Emission from InGaAsN Quantum Wells as a Function of Composition of the Quaternary Compound

A. E. Zhukov*^, A. R. Kovsh*, E. S. Semenova*, V. M. Ustinov*, L. Wei, J.-S. Wang**, and J. Y. Chi****

** Ioffe Physicotechnical Institute, Russian Academy of Sciences, St. Petersburg, 194021 Russia*

^ e-mail: zhukov@beam.ioffe.rssi.ru

*** Industrial Technology Research Institute, Chutung, Hsinchu 310, Taiwan, Republic of China*

Submitted December 27, 2001; accepted for publication December 28, 2001

Abstract—The spectral position of the peak of photoluminescence from an InGaAsN quantum well has been studied as a function of the chemical composition of the quaternary compound. An empirical equation is proposed which describes with good precision the experimentally observed dependences and allows prediction of the composition necessary to obtain a required wavelength. © *2002 MAIK "Nauka/Interperiodica".*

The interest in light emitting devices on GaAs substrates, which can operate at room temperature in the 1.3 μm wavelength range, is due to their potentially better device characteristics as compared with conventional InP structures, and also to the simpler technology of fabrication of a vertical-cavity surface-emitting structure [1]. In the last two years, vertical-cavity surface-emitting lasers (VCSELs) for the 1.3-μm range have been fabricated using different approaches to the creation of the active region: forming an array of InAs/InGaAs quantum dots [2] or InGaAsN [3, 4] and GaAsSb [5, 6] quantum wells (QW).

For InGaAs QWs, the wavelength range of interest (1.3 μm) can be reached by adding a relatively small amount of nitrogen (several percent). As shown in [7], the strong narrowing of the band gap in the quaternary $In_xGa_{1-x}As_{1-y}N_y$ compound results from the interaction between the conduction band states of the InGaAs matrix and nitrogen states localized in a narrow resonance band. The parameters controlling the emission wavelength are the indium and nitrogen content, *x* and *y*, in the quaternary compound, and also the QW width. Raising any of these parameters must result in a long-wavelength shift of the emission peak. However, as seen from the table, the presently available published data show significant scatter. In this connection, investigation of the emission wavelength of InGaAsN QWs as a function of the chemical composition of this quaternary compound has not lost its topicality. It is worth noting that the energy of an optical transition can be calculated on the basis of certain models of the band structure of a quaternary compound (see, e.g., [8]). However, the lack of generalizing formulas hinders practical calculations.

In this communication, we report the results of a systematic study of how the wavelength of emission from MBE-grown InGaAsN QWs on GaAs substrates depends on the In and N content; we also present empirical relations allowing us to describe the dependences we observed in a simple analytical form.

The structures under study comprised a single 6.2-nm-thick InGaAsN QW, or a 0.2-μm-thick GaAsN layer in a GaAs matrix, confined by thin (50 nm) $Al_{0.3}Ga_{0.7}As$ layers. The structures were grown in a Riber Epineat MBE machine equipped with an Applied-EPI UNI-Bulb high-frequency plasma source of active nitrogen. In all the structures, the active region was deposited at a temperature of 450°C at a growth rate of 0.35 nm s^{-1}. The photoluminescence (PL) spectra were recorded at room temperature (20°C). The PL was excited with an Ar^+-ion laser (100 mW) and detected with a cooled InGaAs diode. The structural properties were studied using double-crystal X-ray diffractometry on a Bede D1 instrument.

We believe that the strong scatter of data on the dependence of the wavelength on the InGaAsN composition is largely due to inaccurate evaluation of the N and In content in the QW. Direct determination of the chemical composition of the InGaAsN QW by X-ray

Interrelation between the indium and nitrogen content *x* and *y*, QW width *L* in quaternary $In_xGa_{1-x}As_{1-y}N_y$ compound, and emission wavelength λ of a VCSE

x, %	*y*, %	*L*, nm	λ, μm	Reference
30	2	7	1.2	Larson [11]
35	1.8	6.5	1.28	Steinle [4]
34	1	6	1.295	Choguette [3]

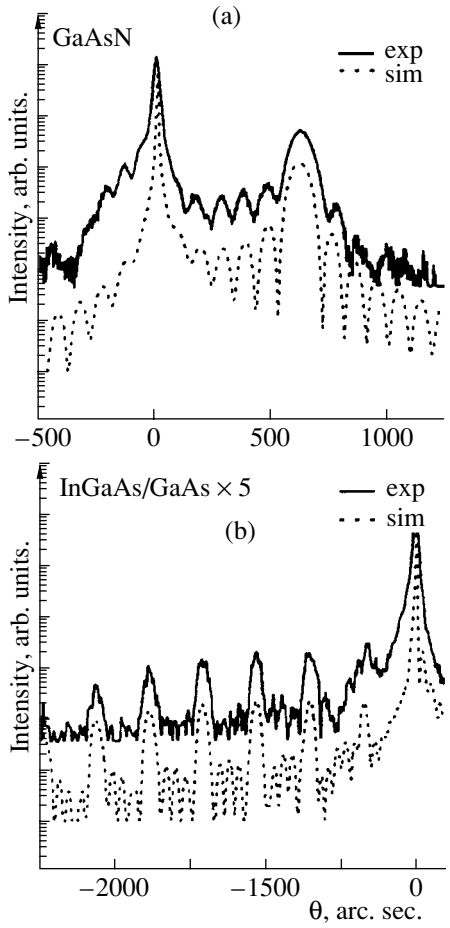

Fig. 1. Double-crystal X-ray rocking curves near GaAs (004) reflection for (a) 0.2-μm-thick $GaAs_{0.988}N_{0.012}$ epitaxial layer and (b) five-period $In_{0.35}Ga_{0.65}As$ (6 nm)/GaAs (48 nm) superlattice. Solid lines, experiment; dashed lines, simulation.

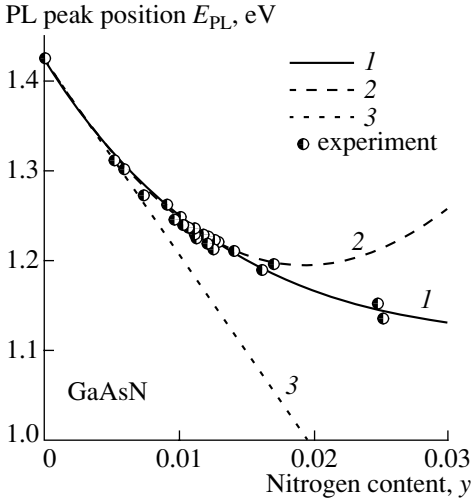

Fig. 2. Optical transition energy vs. nitrogen content in $GaAs_{1-y}N_y$ layers. Points, experiment; approximation: (*1*) with relation (2); (*2*) with relation (1), with the forbidden band parameter and the GaN band gap varied; and (*3*) with relation (1), with only the forbidden band bending parameter varied.

diffraction is impossible, since addition of both N and In changes the strain in GaAs. Moreover, there remains an open question of how indium in the InGaAsN layer affects the efficiency of atomic nitrogen incorporation from the plasma source, compared with the case of GaAsN. It is commonly believed, when considering quaternary QWs, that, at a constant total growth rate, the molar fraction of nitrogen in InGaAsN corresponds to the nitrogen content in GaAsN (see, e.g., [9]). However, some experimental facts cast doubt on the validity of this assumption. For example, it has been shown that the efficiency of nitrogen incorporation into InAs is much less than that into GaAs [10]. This fact indicates that the efficiency of nitrogen incorporation into InGaAs layers may depend on the molar fraction of indium in this compound. On the other hand, the model proposed below allows us to circumvent the problem of determining precisely the molar fraction of nitrogen in a QW and to relate the emission wavelength of an InGaAsN QW directly to parameters that can be determined by preliminary calibrations. In what follows, by the nitrogen content of a QW is meant the molar fraction of nitrogen, which is determined by the *X*-ray diffraction method for a ternary GaAsN compound grown under identical growth conditions at the same overall growth rate.

In the growth of InGaAs(N) QWs, the atomic flows of In and Ga were chosen so as to maintain constant the overall growth rate. The chemical composition of $GaAs_{1-y}N_y$ layers was determined from the distance between GaAsN and GaAs(004) diffraction peaks, with a lattice constant of 0.452 nm assumed for cubic GaN. The indium content and the thickness of the $In_xGa_{1-x}As$ QW were found by modeling the X-ray diffraction spectra of structures containing a periodic sequence of five QWs separated by 45-nm-thick GaAs barriers. Figure 1 presents examples of experimental spectra and the results of modeling.

Figure 2 shows an experimental dependence of the PL peak position on the nitrogen content *y* measured in $GaAs_{1-y}N_y$ layers. The band gap in a ternary compound of this type is commonly described by a quadratic dependence,

$$E_{GaAsN} = E_{GaN}y + E_{GaAs}(1-y) - C_{GaN-GaAs}y(1-y), \quad (1)$$

where E_{GaN} and E_{GaAs} are the band gaps of binary compounds forming the solid solution, and $C_{GaN-GaAs}$ is the parameter of the forbidden band bending, which describes the interaction of components in the solid solution. Figure 2 exemplifies an approximation of the experimental dependence with an expression of type (1). As seen, the above relation describes the compositional dependence of the PL peak position for ternary compound GaAsN only at a very small nitrogen content (<1%), which is insufficient for achieving the 1.3-μm wavelength in InGaAsN QWs. At a higher nitrogen content, the dependence of the PL peak position on

composition is weaker and tends to level off. This means that, being dependent on the nitrogen content in the ternary compound, the parameter of the forbidden band bending is not constant over the entire range of compositions.

As shown in Fig. 2, the experimental data can be formally described in the range y = 0–2% by a quadratic dependence (1) if E_{GaN} is considered a second fitting parameter. In this case, however, the physical meaning of both E_{GaN} and $C_{GaN–GaAs}$ is lost. Moreover, the predicted increase in the optical transition energy at $y >$ 2.5% is not observed experimentally.

To describe the experimental dependence of the PL peak position on the nitrogen content of $GaAs_{1-y}N_y$ layers, we propose the expression

$$E_{GaAsN} = E_{GaAs} - \Delta[1 - \exp(-y/y_0)], \quad (2)$$

where Δ and y_0 are the fitting parameters jointly describing the band gap variation at low nitrogen content ($E_{GaAsN} \approx E_{GaAs} - (\Delta/y_0)y$) and the decrease in the influence exerted by nitrogen at high nitrogen content ($E_{GaAsN} \longrightarrow E_{GaAs} - \Delta$). The best fit in the entire composition range studied is ensured by the following parameters: Δ = 321 meV and y_0 = 1.21% (Fig. 2).

The dependence of the PL peak position on the nitrogen content y in the range 0–2.8% is shown in Fig. 3a by points for $In_xGa_{1-x}As_{1-y}N_y$ QWs with an In molar fraction x of 21, 27, and 35%. In all cases, the QW width was 6.2 nm. A similar dependence from [8] is shown by the squares. We found that, similarly to the case of bulk GaAsN layers, the experimental data can be satisfactorily described by relation (2) if the width of the GaAs forbidden band is replaced with the energy of optical transition in a nitrogen-free InGaAs QW and if the parameters Δ and y_0 are assumed to depend on the In content:

$$E_{InGaAsN} = E_{InGaAs} - \Delta(x)[1 - \exp(-y/y_0(x))]. \quad (3)$$

The results of approximation are shown by solid lines in Fig. 3a, and the dependences of fitting parameters on x, by points in Fig. 3b.

As follows from Fig. 3b, the extrapolation of Δ and y_0 to a low In content in a QW yields values coinciding with those obtained for thick GaAsN layers. This means that the parameters Δ and y_0 depend weakly on the quantum confinement effects related to the QW width and reflect the dependence of the forbidden band width on the composition of the nitrogen-containing compound. It is necessary to note that the parameter Δ remains virtually the same, 310–320 meV, over the entire In range studied. At the same time, y_0 strongly grows with increasing In content, up to 2.8% at x = 35%, which reflects the decreasing effect of nitrogen on the position of the PL line in indium-containing structures. This effect was described in [7, 8] in terms of a decrease in the band-bending parameter with increasing In content. On the other hand, the decrease in y_0 can also be accounted for by a decrease in the actual nitrogen content because of a decline in the efficiency of incorporation of atomic nitrogen with an increasing molar fraction of In. Therefore, the proposed empirical dependence reflects the resultant influence of both effects.

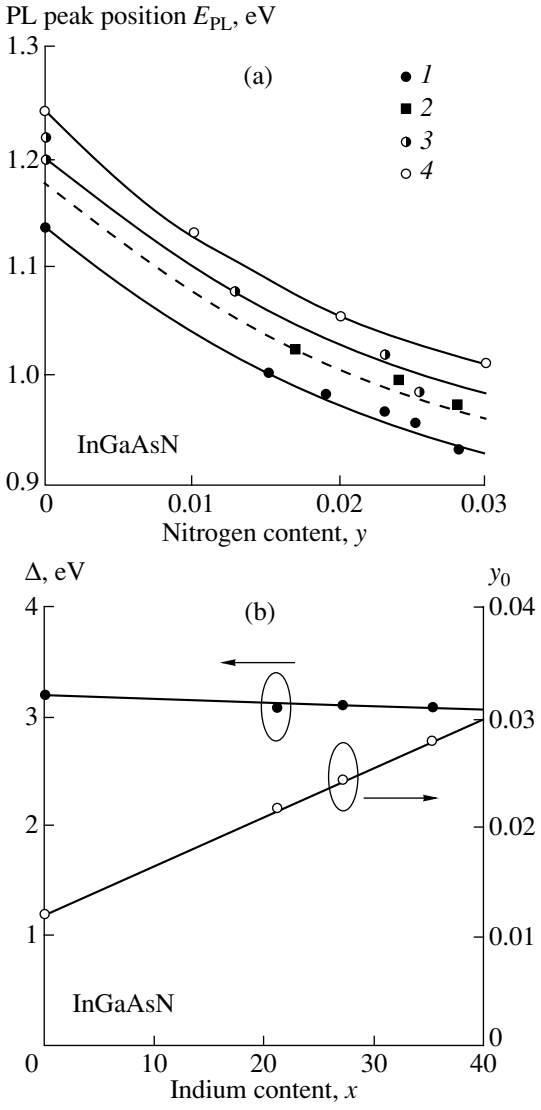

Fig. 3. (a) Experimental dependences of the optical transition energy on nitrogen content for 6.2-nm-wide $In_xGa_{1-x}As_{1-y}N_y$ QWs with indium content x: (*1*) 0.35, (*2*) 0.30 [8], (*3*) 0.27, and (*4*) 0.21. Lines, approximation by relation (3). (b) Points, parameters Δ and y_0 vs. indium content for the compositions studied experimentally; lines, linear interpolation.

To verify the proposed approach to the description of the PL peak position for InGaAsN QWs as a function of composition, we analyzed the experimental data for $In_{0.3}Ga_{0.7}As_{1-y}N_y$ QWs [8], which are represented by squares in Fig. 3a. Based on the dependences of Δ and y_0 on the molar fraction of In (Fig. 3b), we found the values of these parameters, corresponding to 30% indium content, to be, respectively, 312 meV and

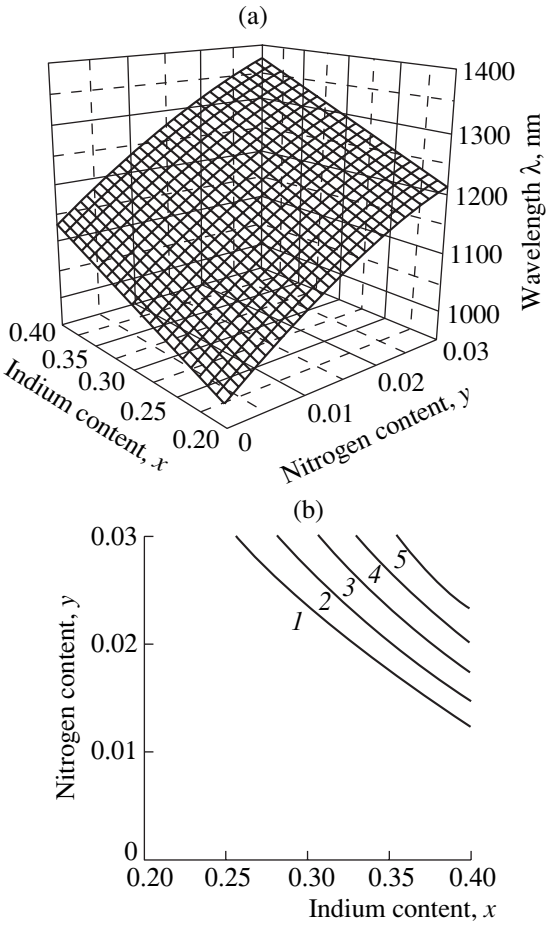

Fig. 4. (a) Wavelength of emission from $In_xGa_{1-x}As_{1-y}N_y$ QWs vs. chemical composition; (b) relationship between the nitrogen and indium content in the QW necessary for obtaining the prescribed emission wavelength λ: (*1*) 1.25, (*2*) 1.27, (*3*) 1.29, (*4*) 1.31, and (*5*) 1.33 μm.

2.56%. The dashed line in Fig. 3a was obtained by substituting these values in formula (3). As seen, the obtained dependence is in good agreement with independent experimental data, thus confirming the validity of the empirical approach we proposed.

The three-dimensional plot in Figure 4a demonstrates the dependence of the PL line position on the composition of an $In_xGa_{1-x}As_{1-y}N_y$ QW, which was calculated using (3). The values of Δ and y_0 were extrapolated to a lower and higher In content (x = 20–40%) with respect to the range of experimental values (27–35%). As seen, a wide spectral range from 1.1 to 1.37 μm can be covered by varying the chemical composition of the $In_xGa_{1-x}As_{1-y}N_y$ QW.

Figure 4b shows the relationship between the nitrogen and indium content necessary for obtaining a prescribed wavelength. To obtain emission in the 1.28–1.33 μm range, which is important for fiber-optics communication, both the indium and nitrogen content in a QW should be rather high. It is noteworthy that it is still unclear which composition is preferable from the standpoint of the device characteristics of 1.3-μm lasers: raising the indium content allows reduction of the required nitrogen content, thus precluding possible damage to the surface from nitrogen ions, but is limited, however, by the formation of misfit dislocations and the transition to island-growth mode. On the other hand, the use of too strongly strained QWs may impair the service life of devices based on these.

To conclude, we studied experimentally the PL from epitaxial GaAsN layers and InGaAsN QWs as a function of the nitrogen and indium content. The empirical relation we proposed can describe the emission wavelength in a wide range of compositions (0–40% In, 0–3% N) with due account of the nonparabolic dependence of the energy of optical transitions in these compounds on the N content and the decrease in the effect of nitrogen on the forbidden band width with increasing In content.

ACKNOWLEDGMENTS

This study was supported by the Joint Program of the Ioffe Institute and the Industrial Technology Institute "Research and Development of Advanced Light Sources for Application in the Next Generation of Optoelectronic Systems," and also by the programs "NATO Science for Peace" (grant SfP-972484) and "Physics of Solid-State Nanostructures."

REFERENCES

1. V. M. Ustinov and A. E. Zhukov, Semicond. Sci. Technol. **15**, R41 (2000).
2. J. A. Lott, N. N. Ledentsov, V. M. Ustinov, *et al.*, Electron. Lett. **36** (16), 1384 (2000).
3. K. D. Choquette, J. F. Klem, A. J. Fischer, *et al.*, Electron. Lett. **36** (16), 1388 (2000).
4. G. Steinle, H. Riechert, and A. Yu. Egorov, Electron. Lett. **37** (2), 93 (2001).
5. F. Quochi, J. E. Cunningham, M. Dinu, and J. Shah, Electron. Lett. **36** (25), 1469 (2000).
6. T. Anan, M. Yamada, K. Nishi, *et al.*, Electron. Lett. **37** (9), 405 (2001).
7. W. Shan, W. Walukiewicz, J. W. Ager, III, *et al.*, Phys. Rev. Lett. **82** (6), 1221 (1999).
8. H. Riechert, A. Yu. Egorov, G. Dumitras, and B. Borchert, in *Abstracts of the International Conference on Physics of Semiconductors, ICPS 25, Osaka, 2000*, p. ca314UO4.
9. H. P. Xin, K. L. Kavanagh, and C. W. Tu, J. Cryst. Growth **208**, 145 (2000).
10. J. S. Wang, H. H. Lin, L. W. Sung, and G. R. Chen, J. Vac. Sci. Technol. B **19** (1), 202 (2001).
11. M. C. Larson, C. W. Coldren, S. G. Spruytte, *et al.*, IEEE Photonics Technol. Lett. **12** (12), 1598 (2000).

Translated by D. Mashovets

Semiconductors, Vol. 36, No. 8, 2002, pp. 903–907. Translated from Fizika i Tekhnika Poluprovodnikov, Vol. 36, No. 8, 2002, pp. 969–973.

LOW-DIMENSIONAL SYSTEMS

Two-Dimensional *p–n* Junction under Equilibrium Conditions

A. Sh. Achoyan, A. É. Yesayan, É. M. Kazaryan, and S. G. Petrosyan*

Erevan State University, Erevan, 375049 Armenia

** e-mail: stpetros@www.physdep.r.am*

Submitted April 11, 2001; accepted for publication January 8, 2002

Abstract—For the first time, the idea of a two-dimensional *p–n* junction formed as a contact between two regions of a quantum-dimensional film with different types of conductivity is proposed. Under equilibrium conditions, the potential distribution and the potential-barrier height were determined. An expression was derived for the width of the surface-charge layer, which depends linearly on the contact potential (external bias) in contrast to the three-dimensional case. The specific capacitance of a two-dimensional *p–n* junction is virtually independent of the applied potential and depends only on the ambient permittivity. It was shown that, in spite of the fact that the junction electric field is screened only slightly, the Schottky approximation can be used for a description of the properties of such *p–n* junctions. © *2002 MAIK "Nauka/Interperiodica".*

INTRODUCTION

In connection with recent developments in the physics of low-dimensional systems, the investigation of the physical properties of various junctions formed near an interface between two electronic systems with a different dimensionality (the so-called heterodimensional junctions) [1–3] is of a great interest. A particular example of such a low-dimensional junction is the two-dimensional (2D) *p–n* junction formed, for example, by the molecular-beam epitaxy of thin quantum-dimensional GaAs or $Ga_xAl_{1-x}As$ films on nonplanar substrates; the films are doped with an amphoteric impurity (for example, Si), whose type (donor or acceptor) depends on the crystallographic orientation of the substrate [4].

In contrast to conventional *p–n* junctions, such 2D junctions have a number of specific properties induced both by the nature of a 2D gas and by features of the junction-field screening by low-dimensional electrons. Due to the fact that ionized donors and acceptors, as well as free charge carriers, are in the plane of the 2D gas, whereas the junction electric field is concentrated in the environment, this field is weakly screened, while the formed depleted domains of the "spatial" (more precisely, surface) charge are relatively extended. Correspondingly, the 2D *p*–n junction must also be characterized by a higher breakdown voltage than conventional *p–n* junctions. Due to the smallness of the effective cross section of the quantum-dimensional film, the 2D *p–n* junction must have a very low capacitance. Furthermore, taking into account that the 2D electron gas is, as a rule, very mobile, we may hope that the 2D *p–n* junctions will open a new field of research in the physics of 2D systems and lead to prospects for designing a new family of high-frequency diodes, varicaps, mixers, etc. [3].

The contact phenomena in a two-dimensional electron gas (2DEG) have already found a number of interesting applications. For example, the metal–2DEG junction was used as the basis of such devices as high-electron-mobility field-effect transistors [5], photodetectors at a wavelength of 1.3 μm with a record-wide operating band [6], and varactor diodes with a very high capacitance ratio C_{max}/C_{min} and a high breakdown voltage [7, 8].

In this study, we suggest a 2D *p–n* junction and investigate the voltage and electric-field distribution in such a junction without applying an external voltage.

POTENTIAL DISTRIBUTION AND ENERGY-BAND DIAGRAM OF A TWO-DIMENSIONAL *p–n* JUNCTION

In Fig. 1a, we display the schematic diagram of a 2D *p–n* junction, which constitutes a thin quantum-dimensional film with a thickness d. One half-plane ($y = 0$, $x > 0$) of the film is doped with acceptors with a surface concentration N_{AS} (for example, by the δ-doping). The other half-plane ($y = 0$, $x < 0$) is doped with donors with a surface concentration N_{DS}. The y axis is directed along the normal to the film, and its origin is in the film-symmetry plane. For the sake of simplicity, we further assume that $N_{AS} = N_{DS} = N_S$. Also, we consider the temperatures at which all the impurities are ionized, while away from the interface (i.e., in the quasi-neutral regions) equilibrium concentrations n_{S0} and p_{S0} of electrons and holes are equal to N_S.

When a junction is formed, a fraction of the electrons passes from the *n* region into the *p* region, while the holes, on the contrary, pass from the *p* region to the *n* region. Owing to this fact, surface-charge depleted layers are formed near the interface.

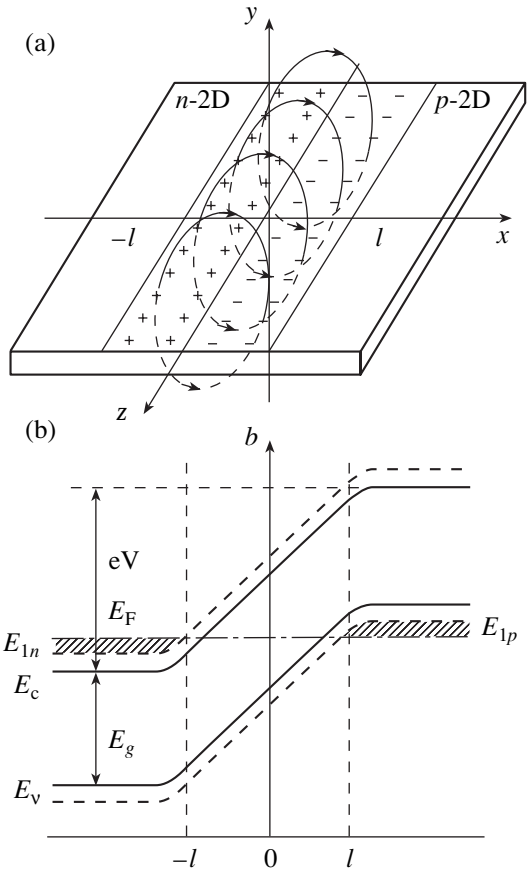

Fig. 1. (a) Schematic representation and (b) energy-band diagram of a two-dimensional *p–n* junction under equilibrium conditions. E_{1n} and E_{1p} are the levels of dimensional quantization for electrons and holes, and E_F is the Fermi level.

Due to the electric field that arises, energy bands and levels of dimensional quantification are bent until an equilibrium state is established. This state is characterized by a constant Fermi level throughout the entire semiconductor film (Fig. 1b). Correspondingly, the potential barriers V_c are formed along the x axis for electrons and holes. Their height V_c is equal to the contact potential

$$V_c = \frac{1}{e}\left[E_g + \pi\hbar^2\left(N_S + \frac{\pi}{2d^2}\right)\frac{m_n + m_p}{m_n m_p}\right], \qquad (1)$$

where e is the electron charge, E_g is the semiconductor band gap, and m_n and m_p are the effective electron and hole masses. It follows from (1) that the potential-barrier height always exceeds the band gap in contrast to the case of the three-dimensional (3D) *p–n* junction. From the band diagram of the *p–n* junction in Fig. 1b, it can be seen that, due to the band bending, there is always a certain region $-l \le x \le l$ where the dimensional-quantization levels are arranged relative to the Fermi level in the conduction valence bands so that there are no free electrons and holes in this region at low temperatures.

First, we determine the potential distribution in the complete-depletion approximation, in which case it is possible to assume that the region of negative surface charge is formed only by ionized acceptors located in the layer $0 < x \le l$, while the region of positive surface charge is formed by ionized donors in the layer $-l \le x < 0$. These surface charges generate the built-in contact electric field, which is primarily located in the environment. In order to determine the potential distribution $\varphi(x, y, z)$ for this field, we should solve the Laplace equation

$$\Delta\varphi(x, y, z) = 0. \qquad (2)$$

It is clear from the symmetry of the problem that the potential is independent of the coordinate z (we assume that the film size along the z axis far exceeds the surface-layer width $2l$ and the edge effects can be neglected).

It is necessary to solve Eq. (2) in the complete-depletion approximation with the following boundary conditions:

$$\varphi(x, 0) = \begin{cases} 0, & x \le -l, \\ V_c, & x \ge l, \end{cases}$$
$$\frac{\partial\varphi(x, 0)}{\partial y} = \begin{cases} -\dfrac{2\pi e}{\varepsilon}N_S, & -l \le x \le 0, \\ \dfrac{2\pi e}{\varepsilon}N_S, & 0 < x \le l, \end{cases} \qquad (3)$$

where ε is the permittivity of ambient regions.

The formulated problem can be solved by the method of conformal mapping using the function

$$w = 2\ln\frac{\xi + \sqrt{\xi^2 - l^2}}{l}, \qquad (4)$$

which transforms the first quadrant of the plane $\xi = x + iy$ into a semiband of the plane $w = u + iv$ ($0 \le v \le \pi$, $u > 0$). It is more convenient to find the solution $\varphi(x, y)$ in the plane $w(u, v)$ because we arrive at an identical type of boundary conditions at the region boundaries. In such a way, it is possible to find the function $\varphi(x, y)$, which has the following form in the first quadrant ($x > 0$ and $y > 0$):

$$\varphi_0(x, y) = V_c\left\{1 - \frac{1}{\pi}\arcsin\left[\frac{\sqrt{F(x, y) - (x^2 + y^2 - l^2)}}{l\sqrt{2}}\right]\right.$$
$$- \frac{1}{2\pi}\left[\frac{x}{l}\ln\frac{x - G(x, y)}{x + G(x, y)}\right. \qquad (5)$$
$$\left.\left. + \frac{2y}{l}\arctan\left(\frac{x^2 + y^2 + l^2 - F(x, y)}{l\sqrt{2}\sqrt{x^2 - y^2 - l^2 + F(x, y)}}\right)\right]\right\},$$

where we introduce the designations

$$F(x, y) = \sqrt{(x^2 + y^2 - l^2)^2 + 4l^2y^2},$$
$$G(x, y) = \frac{\sqrt{(x^2 + y^2)F(x, y) - (x^2 + y^2)^2 + l^2(x^2 - y^2)}}{l\sqrt{2}}. \quad (6)$$

Similar expressions for $\varphi(x, y)$ can also be written for other quadrants.

On the basis of the above formulas, it is easy to also determine the width of the surface-charge region. Since the region $y = 0$ and $x \geq l$ is equipotential, it is necessary that the solution obtained satisfies the condition

$$\frac{\partial\varphi}{\partial x}(l, 0) = 0. \quad (7)$$

The last requirement is fulfilled if the parameter l in formula (5) is given by the expression

$$l = \frac{\varepsilon V_c}{4\pi e N_S}. \quad (8)$$

It can be seen that the thickness of the spatial-charge-layer $L_{2D} = 2l$ in the 2D *p–n* junction also depends linearly on the contact potential as in the case of a metal–2DEG junction [1]. With an external voltage V, a similar formula is valid for the quantity l; however, it is necessary to write $(V_c - V)$ instead of V_c.

We obtained potential distribution (5) in the complete-depletion approximation (the Schottky approximation). However, the screening of the built-in field is known to be weaker in the 2DEG case than in the 3D case [2], due to which the falloff of the potential is less steep outside the surface-charge region. For this reason, on closer inspection, it is necessary to take into account that there are potential-distribution "tails" beyond the points $x = \pm l$.

In the general case, we can write the following expression for the surface-charge density in the 2D *p–n* junction:

$$\rho(x) = \frac{ekT}{\pi\hbar^2}[-m_n\ln(1 + e^{\varepsilon_1/kT}) + \theta(-x)m_n\ln(1 + e^{\varepsilon_2/kT}) + m_p\ln(1 + e^{\varepsilon_3/kT}) - \theta(x)m_p\ln(1 + e^{\varepsilon_4/kT})]. \quad (9)$$

Here,

$$\varepsilon_1 = -(E_{1n} + e\varphi(x, 0) - E_F),$$
$$\varepsilon_2 = -(E_{1n} - E_F),$$
$$\varepsilon_3 = -E_g - E_{1p} + e\varphi(x, 0) - E_F,$$
$$\varepsilon_4 = E_{Fp} = \frac{\pi\hbar^2 N_S}{m_p}.$$

As the energy origin, we take $E_c = (-\infty) = 0$, $\theta(x < 0) = 0$, and $\theta(x > 0) = 1$.

In this case, it is no longer possible to exactly solve the Laplace equation analytically. However, we can use (9) to write the following expression, which is valid to a high accuracy, for the surface-charge density at low temperatures in the region $x > 0$:

$$\rho(x) = \frac{em_p}{\pi\hbar^2}\begin{cases} e\varphi(x, 0) - V_c, & x \geq l, \\ -E_{Fp}, & 0 < x < l. \end{cases} \quad (10)$$

The unknown length l is now determined from the condition $e\varphi(l, 0) - V_c = -E_{Fp}$ (see Fig. 1b).

Correspondingly, it is now necessary to solve the Laplace equation in the first quadrant with the following boundary conditions:

$$\varphi(+\infty, 0) = V_c, \quad \varphi(0, y) = \frac{V_c}{2},$$
$$\frac{\partial\varphi}{\partial y}(x, 0) = \frac{2}{a_{Bp}}\begin{cases} \varphi(x, 0) - V_c, & x \geq l, \\ \gamma_p, & 0 < x < l. \end{cases} \quad (11)$$

Here,

$$a_{Bp} = \frac{\varepsilon\hbar^2}{m_p e^2}$$

is the Bohr radius for holes, and

$$\gamma_p = -\frac{E_{Fp}}{e}.$$

The problem can be solved again with the conformal-mapping method using function (4). In the approximation $l \gg a_{Bp}$, it is possible to represent $\varphi(x, y)$ as follows:

$$\varphi(x, y) = \varphi_0(x, y) - V_c\frac{a_{Bp}}{2\pi l}\arctan\frac{x^2 + y^2 + l^2 - F(x, y)}{l\sqrt{2}\sqrt{x^2 - y^2 - l^2 + F(x, y)}}, \quad (12)$$

where $\varphi_0(x, y)$ and $F(x, y)$ are given by expressions (5) and (6).

Again, using the requirement of continuity for the x component of the electric-field strength at the point $x = l$,

$$\frac{\partial\varphi}{\partial x}(l, 0)\Big|_{x \to l+} = \frac{\partial\varphi}{\partial x}(l, 0)\Big|_{x \to l-}, \quad (13)$$

and taking into account that $eV_c \gg E_{Fp}$, we obtain the following expression for l:

$$l = -\frac{V_c a_{Bp}}{4\gamma_p}. \quad (14)$$

Substituting the values for γ_p and a_{Bp}, we again arrive at expression (8) for the length l.

It should be noted that the potential distribution for $x < 0$ can be given by an expression similar to (12) only if we replace a_{Bp} and γ_p by the corresponding electron-gas quantities a_{Bn} and γ_n.

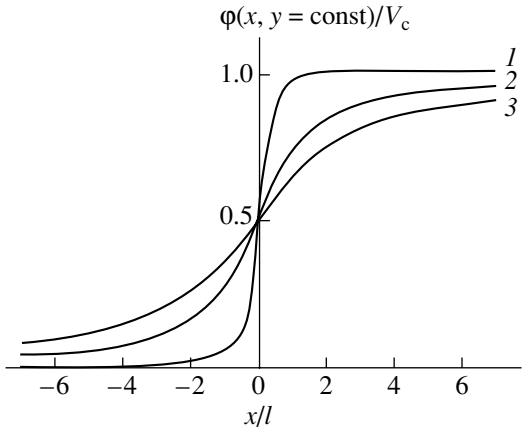

Fig. 2. Potential distribution φ(*x*, *y* = const) at fixed distances *y* from the plane of the *p*–*n* junction: *y* = (*1*) 0, (*2*) *l*, and (*3*) 2*l*.

2. CAPACITANCE OF A TWO-DIMENSIONAL *p*–*n* JUNCTION

Knowing the potential distribution and the surface-charge value per unit junction length

$$Q_S = \int_0^\infty |\rho(x)|dx, \tag{15}$$

we can also calculate the specific capacitance of the 2D *p*–*n* junction:

$$C = \frac{dQ_S}{dV_c}. \tag{16}$$

Taking into account (10), it is easy to obtain

$$Q_S = \frac{\varepsilon}{4\pi}V_c - \frac{e^2 m_p}{\pi^2\hbar^2}2\gamma_p\int_l^\infty \arctan\frac{l}{\sqrt{x^2-l^2}}dx. \tag{17}$$

As can be seen, the distribution of charge Q_S diverges logarithmically at large distances. The cause of such a divergence is the slow falloff of potential outside the surface-charge region. It is easy to show from (12) that the drop of potential away from the surface-charge region ($x \gg l$, $y \gg l$) follows the hyperbolic law:

$$\begin{aligned}\varphi(x, y = \text{const}) &\approx V_c\left(1 - \frac{l}{\pi x}\right), \quad x \gg l,\\ \varphi(x = \text{const}, y) &\approx \frac{V_c}{2}\left(1 + \frac{l}{\pi y}\right), \quad y \gg l.\end{aligned} \tag{18}$$

However, it is clear that, in a real situation, there are always physical causes leading to the "cutoff" of the potential at a certain length $L \gg l \gg a_B$. For this reason, we can write the following expression for Q_S:

$$Q_S = \frac{\varepsilon}{2\pi^2}V_c\left[\beta\arctan\frac{1}{\sqrt{\beta^2-1}} + \ln(\beta + \sqrt{\beta^2-1})\right]. \tag{19}$$

Here, $\beta = L/l$.

Consequently, for the specific capacitance of the junction, we have

$$C = \frac{\varepsilon}{2\pi^2}f(\beta), \tag{20}$$

where

$$f(\beta) = \beta\arctan\frac{1}{\sqrt{\beta^2-1}} + \ln(\beta + \sqrt{\beta^2-1}) \tag{21}$$

is a numerical factor that weakly depends on the parameter β.

As can be expected, the specific capacitance of the 2D *p*–*n* junction is virtually independent of the voltage across the junction and is determined only by the ambient permittivity.

3. DISCUSSION OF RESULTS

In Fig. 2, we show the behavior of the potential along the *x* axis both in the plane ($y = 0$) of the 2D gas and at certain distances from it ($y = l$ and $y = 2l$). Contrary to the conventional 3D *p*–*n* junction, the built-in electric field of the 2D *p*–*n* junction also exists outside the space-charge region ($|x| > l, y, z$), which is a result of a weak screening in the 2D case.

From relationship (8), it can be seen that, in contrast to the conventional *p*–*n* junction, the width of the space-charge region depends on the potential-barrier height not by the square-root law, but by a stronger linear law. It is for this reason that the capacitance (20) of the 2D *p*–*n* junction is independent of the external bias. In its turn, the average electric-field strength $\bar{E}_x$ in the *p*–*n* junction plane also depends weakly on the external bias. It is easy to show that, in the Schottky approximation,

$$E_x(x, 0) = -\frac{V_c}{2\pi l}\ln\frac{l + \sqrt{l^2 - x^2}}{l - \sqrt{l^2 - x^2}}, \tag{22}$$

and the average value of the electric-field strength is given by the surface density of ionized impurities

$$\bar{E}_x = \frac{1}{l}\int_0^l E_x(x, 0)dx = -\frac{2\pi eN}{\varepsilon} \equiv \text{const}(V). \tag{23}$$

As was mentioned above, the depletion-region width in the 2D *p*–*n* junction is always larger (due to the weakness of the screening) than in the conventional 3D case for comparable levels of bulk doping $N_D = N_S/d$. From (8), it follows that

$$L_{3D} = \sqrt{\frac{\varepsilon V_c}{4\pi e N_D}} = \sqrt{ld} \ll L_{2D}. \tag{24}$$

For example, according to (1) and (8), $V_c = 1.53$ V, $L_{2D} \approx 2.2$ μm, and $L_{3D} \approx 0.1$ μm in the quantum-dimen-

sional film of gallium arsenide (E_g = 1.43 eV, ε = 12.85, $m_n = 0.067m_0$, and $m_p = 0.48m_0$) for $N_S = 10^{11}$ cm^{-2} and d = 80 Å. Since $E_{Fp} \ll E_{Fn} \approx 3.6$ meV in this case and $a_{Bn} \approx 100$ Å, the conditions $eV_c \gg E_{Fn}$ and $L_{2D} \gg a_B \approx d$ used in deriving all of the above formulas are certainly satisfied. In addition, we may conclude that the condition $L_{2D} \gg a_B$ makes it possible to apply the Schottky-layer approximation for describing various properties of 2D *p–n* junctions, in particular, for calculating their current–voltage characteristics.

ACKNOWLEDGMENTS

This study was supported by the International Science and Technology Center, grant no. A-322.

REFERENCES

1. S. G. Petrosyan and A. Ya. Shik, Zh. Éksp. Teor. Fiz. **96**, 2229 (1989) [Sov. Phys. JETP **69**, 1261 (1989)].
2. A. Ya. Shik, Fiz. Tekh. Poluprovodn. (St. Petersburg) **29**, 1345 (1995) [Semiconductors **29**, 697 (1995)].
3. B. Gelmont, M. Shur, and C. Moglestue, IEEE Trans. Electron Devices **39** (5), 1216 (1992).
4. W. Porod, H. Harbury, and S. Goodnick, Appl. Phys. Lett. **61** (15), 1823 (1992).
5. H. Hasegawa, T. Hashizume, H. Okada, and K. Jinushi, J. Vac. Sci. Technol. B **13** (4), 1744 (1995).
6. M. Horstman, K. Scheimpt, M. Marso, *et al.*, Electron. Lett. **32**, 732 (1996).
7. W. C. B. Peatman, T. W. Crowe, and M. Shur, IEEE Electron Device Lett. **13**, 11 (1992).
8. M. Marso, M. Horstmann, H. Hardtdegen, *et al.*, Solid-State Electron. **41** (1), 25 (1997).

Translated by V. Bukhanov

Semiconductors, Vol. 36, No. 8, 2002, pp. 908–915. Translated from Fizika i Tekhnika Poluprovodnikov, Vol. 36, No. 8, 2002, pp. 974–980.

LOW-DIMENSIONAL SYSTEMS

Calculations of the Charge-Carrier Mobility and the Thermoelectric Figure of Merit for Multiple-Quantum-Well Structures

D. A. Pshenaĭ-Severin* and Yu. I. Ravich**

** Ioffe Physicotechnical Institute, Russian Academy of Sciences, Politekhnicheskaya ul. 26, St. Petersburg, 194021 Russia*

*** St. Petersburg State Technical University, Politekhnicheskaya ul. 29, St. Petersburg, 195251 Russia*

Submitted December 13, 2001; accepted for publication January 10, 2002

Abstract—The thermoelectric figure of merit of structures with multiple quantum wells (MQWs) was calculated taking into account the variations in the relaxation time of charge carriers compared to that in a bulk sample. The mechanisms of scattering by acoustic phonons, at the short-range impurity potential, and the polar scattering in the approximation of the isotropic parabolic dispersion law of the charge carriers were taken into account. The model used is based on the assumption that the phonon spectrum in the MQW structures is no different from the spectrum of the bulk crystal. In addition, the scattering is assumed to be elastic and the relaxation-time approximation was used for all three mechanisms of scattering. A comparison with the results of calculations for a bulk sample shows that the expression for thermoelectric figure of merit is exactly the same for a MQW structure as for a bulk sample if the decrease in the charge-carrier relaxation time in MQW structures is taken into account. The magnitude of the figure of merit for a MQW structure is found to be equal to that for a bulk sample if the chemical potential in each of the cases is chosen from the condition for the highest figure of merit. © *2002 MAIK "Nauka/Interperiodica".*

INTRODUCTION

Intensive theoretical and experimental studies concerned with quantum-well (QW) structures, which have been performed in recent decades, have attracted attention to the possibility of using these structures to increase the thermoelectric figure of merit Z. The studies in this field started with the publication by Hicks and Dresselhaus [1], in which it was shown by calculation that the value of Z can be increased by two–three times or more by preparing a thermoelectric material in the form of structures with multiple quantum wells (MQWs). The main gain in the thermoelectric figure of merit was attained owing to an increase in the density of states of the charge carriers in the vicinity of the band edges in two-dimensional (2D) systems compared to three-dimensional (3D) systems. It was assumed [1] that the dimensional quantization does not result in changes in the charge-carrier mobility in the layer planes. Layered structures consisting of PbTe-based QWs separated by $Pb_{1-x}Eu_xTe$ barriers were studied by Hicks *et al.* [2]. The mobility of charge carriers in QWs was assumed to be the same as in a bulk sample (as was done in [1]). The results of measuring the thermoelectric power α and the electron concentration n showed that the $\alpha^2 n$ factor increases with increasing width a of the QWs. Based on these data, it was concluded that it is possible to increase Z in such structures.

However, as was noted in [3, 4], the same effect of an increase in the density of states, which ensures an increase in concentration for the given chemical potential, results in an inevitable decrease in mobility; this is supported by numerical calculation for a specific semiconductor (PbTe). The figure of merit and the $\alpha^2 n$ quantity were calculated numerically in [4]. The dependence of $\alpha^2 n$ on a is consistent with experimental data [2]. At the same time, numerical calculation of the figure of merit [4] shows that a corresponding increase in Z with decreasing QW width is not observed. This indicates that one should be careful while inferring about an increase in the figure of merit based on the data on the $\alpha^2 n$ quantity due to variation in the charge-carrier mobility in such structures.

Therefore, it seems worthwhile to consider again the problem of the thermoelectric figure of merit for multilayered structures taking into account a decrease in mobility using the simplest but realistic model, which makes it possible to perform the calculation in an analytical form for arbitrary parameters of the semiconductor. This model is based on the assumption that the phonon spectrum is not changed much when we perform the transition to a multilayered structure; i.e., it is assumed that phonons remain the same as in the bulk. In addition, the temperature is assumed to be sufficiently higher than the Debye temperature, so that scattering by the acoustic and optical phonons, as well as by

the impurity centers, is elastic; this means that the relaxation-time approximation can be used in all cases under consideration. We will analyze the charge-carrier scattering by acoustic phonons, polar scattering by optical phonons, and scattering by the short-range potential of impurity atoms in the approximation of the conventional (isotropic parabolic) dispersion law for charge carriers.

The main objective of the calculation was to clarify whether a variation in the electron-state density under the conditions of dimensional quantization can basically bring about an increase in the thermoelectric figure of merit.

2. RELAXATION TIME IN THE CASE OF SCATTERING BY ACOUSTIC PHONONS

If a layer is sufficiently thin and constitutes a QW for electrons, all electrons are located near the bottom of the lower dimensional-quantization band. If the potential barriers are fairly high, the electron wave function can be represented as

$$\Psi_{\mathbf{k}_\parallel}(\mathbf{r}) = \sqrt{\frac{2}{a}}\sin\left(\frac{\pi a}{z}\right)\frac{1}{\sqrt{S}}e^{i\mathbf{k}_\parallel\boldsymbol{\rho}}, \quad (1)$$

where $\mathbf{k}_\parallel$ is the wave vector of an electron in the QW plane; the coordinate $\mathbf{r}$ has the components $\boldsymbol{\rho}$ (in the QW plane) and z (in the direction which is perpendicular to the QW plane); and a and S are the layer thickness and area, respectively. According to the deformation-potential method, the potential energy of interaction between electron and acoustic phonons can be expressed as [5]

$$U(\mathbf{r}) = \varepsilon_1 \mathrm{div}\mathbf{u}(\mathbf{r}) = \frac{i\varepsilon_1}{\sqrt{NM_0}}\sum_{\mathbf{q}} q[a_{\mathbf{q}}e^{i\mathbf{qr}} + a_{\mathbf{q}}^* e^{-i\mathbf{qr}}], \quad (2)$$

where ε_1 is the deformation-potential constant; $\mathbf{u}(\mathbf{r})$ is the displacement of the point $\mathbf{r}$ in the crystal (this displacement accounts for acoustic lattice vibrations in the continual approximation); N is the number of unit cells in the crystal volume; M_0 is the unit-cell mass; $\mathbf{q}$ is the wave vector of a phonon; and $a_{\mathbf{q}}$ are the complex normal coordinates. It is assumed that phonons are not susceptible to the effect of inhomogeneities, which give rise to QWs for electrons; i.e., these are conventional phonons in a 3D crystal with the volume $V = Sa$. Then, using formulas (1) and (2), we can derive the following expression for the matrix element of the electron transition between the states with the wave vectors $\mathbf{k}_\parallel$ and $\mathbf{k}_\parallel'$ in the lower subband of dimensional quantization with the participation of an acoustic phonon with the wave vector $\mathbf{q}$:

$$M_{\mathbf{k}_\parallel\mathbf{k}_\parallel'} = \int_V d^3r[\Psi^*_{\mathbf{k}_\parallel'}(\mathbf{r})U(\mathbf{r})\Psi_{\mathbf{k}_\parallel}(\mathbf{r})]. \quad (3)$$

After integration, the matrix element is represented as

$$M_{\mathbf{k}_\parallel\mathbf{k}_\parallel\pm\mathbf{q}_\parallel} = MY^{\pm}(q_z), \quad (4)$$

where the indices (+) and (–) correspond to the transitions of an electron to the state $\mathbf{k}_\parallel' = \mathbf{k}_\parallel + \mathbf{q}_\parallel$ with the absorption of a phonon and to the state $\mathbf{k}_\parallel' = \mathbf{k}_\parallel - \mathbf{q}_\parallel$ with the emission of a phonon, respectively. The factor M is equal to the conventional matrix element, which appears in the deformation-potential theory in the 3D case, and the function $Y^{\pm}(q_z)$ is the result of integration with respect to the variable z; i.e.,

$$Y^{\pm}(q_z) = \frac{2}{a}\int_0^a \sin^2\left(\frac{\pi}{a}z\right)e^{\pm iq_z z}dx = \frac{e^{\pm i\pi x}\sin\pi x}{\pi x(1-x^2)}, \quad (5)$$

where the following designation was introduced:

$$x = \frac{a}{2\pi}q_z. \quad (6)$$

The matrix element M is independent of the phonon wave vector $\mathbf{q}$ and is given by

$$M = \sqrt{\frac{\varepsilon_1^2 k_0 T}{2NM_0 v_0^2}}, \quad (7)$$

where k_0 is the Boltzmann constant, T is absolute temperature, and v_0 is the velocity of sound. The reciprocal relaxation time in the 2D case is expressed as

$$\tau_{2D}^{-1} = -\frac{2\pi}{\hbar}\sum_{\mathbf{q}}|M|^2\frac{q_\chi}{k_\chi}[|Y^+(q_z)|^2\delta(\varepsilon(\mathbf{k}_\parallel+\mathbf{q}_\parallel)-\varepsilon(\mathbf{k}_\parallel)) - |Y^-(q_z)|^2\delta(\varepsilon(\mathbf{k}_\parallel-\mathbf{q}_\parallel)-\varepsilon(\mathbf{k}_\parallel))], \quad (8)$$

where $\varepsilon(\mathbf{k}_\parallel)$ is the energy of an electron with the wave vector $\mathbf{k}_\parallel$; and q_χ and k_χ are the components of the wave vectors of a phonon and an electron along the vector $\boldsymbol{\chi}$, which determines the direction of the generalized force (the electric-field vector or the temperature gradient).

Replacing summation by integration in (8) and performing the latter, we obtain

$$\tau_{2D}^{-1} = \frac{2\pi}{\hbar}|M|^2 V g_{2D} X, \quad (9)$$

where $g_{2D} = m^*/(2\pi\hbar^2)$ is the 2D density of electronic states, m^* is the effective electron mass, and X is the

quantity that is obtained from (5) by integrating with respect to q_z; i.e.,

$$X = \int_{-\infty}^{\infty} |Y^{\pm}(q_z)|^2 \frac{dq_z}{2\pi} = \frac{1}{a}\int_{-\infty}^{\infty}\left(\frac{\sin\pi x}{\pi x(1-x^2)}\right)^2 dx = \frac{3}{2}a^{-1}. \quad (10)$$

The derived expression for τ_{2D} coincides with that reported previously [6–8] and should be compared with the corresponding relaxation time for a 3D crystal,

$$\tau_{3D}^{-1} = \frac{2\pi}{\hbar}|M|^2 V g_{3D}, \quad (11)$$

$$g_{3D} = \frac{m^* k}{2\pi^2\hbar^3}. \quad (12)$$

The comparison shows that, in a dimensional-quantized layer, the relaxation time for scattering by acoustic phonons is proportional to the small thickness a and is much shorter than in a 3D crystal; i.e.,

$$\frac{\tau_{2D}}{\tau_{3D}} = \frac{2ka}{3\pi}. \quad (13)$$

In what follows, after obtaining similar results for two other mechanisms for scattering, we will show that factor (13) completely compensates variations in both the kinetic coefficients and the thermoelectric figure of merit; these variations are caused by modifications in the form of the function of density of states under the conditions of dimensional quantization.

3. RELAXATION TIME UNDER THE CONDITIONS OF SCATTERING BY THE SHORT-RANGE POTENTIAL OF IMPURITIES AND DEFECTS

A variation in the density of states due to dimensional quantization brings about an increase in the charge-carrier concentration for a given chemical potential, which necessitates an increase in the concentration of the electrically active impurity. We assume that the impurity atoms reside in conducting layers and effectively scatter the charge carriers. Although there is a method for reducing the scattering at impurities by doping the barriers between QWs [9] (so that the charge carriers and impurities become spatially separated), the specific realization of one or another scattering mechanism is of secondary importance to us, since the main objective of this study was to clarify the issue concerning the effect of a modification in the density of states on the transport phenomena for various scattering mechanisms.

In many thermoelectric materials (e.g., PbTe [10]), the Coulomb potential of ionized impurities and point defects has a low efficiency from the standpoint of scattering; thus, scattering predominantly occurs at the inner portion of the impurity-atom potential. We may assume that the short-range potential $U(\mathbf{r})$ has an effective radius r_0, which is on the order of the interatomic distance.

In order to calculate the matrix element of interaction between an electron and an impurity atom in a 3D sample with volume V, we use the Bloch function

$$\Psi_{\mathbf{k}}(\mathbf{k}) = \frac{1}{\sqrt{V}} e^{i\mathbf{kr}} u_{\mathbf{k}}(\mathbf{r}). \quad (14)$$

The matrix element of an electron transition from a state with the wave vector $\mathbf{k}$ to a state with the wave vector $\mathbf{k}'$ as a result of scattering by the short-range potential of an impurity atom, the center of which is at the point $\mathbf{r}_i$, has the following form:

$$M_{\mathbf{kk}'} = \frac{1}{V}\int_V d^3r [e^{-i\mathbf{k}'\mathbf{r}} u^*_{\mathbf{k}'}(\mathbf{r}) U(\mathbf{r}-\mathbf{r}_i) e^{i\mathbf{kr}} u_{\mathbf{k}}(\mathbf{r})]. \quad (15)$$

Changing the variable $\mathbf{r}$ to $\mathbf{r} = \mathbf{r}' + \mathbf{r}_i$ and using the periodicity property of the Bloch amplitude $u_{\mathbf{k}}(\mathbf{r}) = u_{\mathbf{k}}(\mathbf{r}')$, we obtain

$$M_{\mathbf{kk}'} = \frac{e^{-i\mathbf{r}_i(\mathbf{k}'-\mathbf{k})}}{V} \times \int_V d^3r' [e^{-i\mathbf{k}'\mathbf{r}'} u^*_{\mathbf{k}'}(\mathbf{r}') U(\mathbf{r}') e^{i\mathbf{kr}'} u_{\mathbf{k}}(\mathbf{r}')]. \quad (16)$$

Since the short-range potential differs from zero only in a small region, $\Omega_0 \sim r_0^3$, in the vicinity of an impurity atom, the domain of integration in (16) can be replaced by Ω_0. Then, we have $kr' \ll 1$ for the scattering of charge carriers with small k and for all $r' \le r_0$, because r_0 is on the order of the lattice constant. In this case, all exponential functions under the integral in (16) are close to unity. In addition, for small values of k, the dispersion law for electrons is almost parabolic; therefore, in the same approximation, it may be assumed that the Bloch amplitudes $u_{\mathbf{k}}(\mathbf{k})$ depend only slightly on $\mathbf{k}$ and are equal to $u_0(\mathbf{r})$. Taking this into account, we obtain

$$M_{\mathbf{kk}'} = \frac{e^{-i\mathbf{r}_i(\mathbf{k}'-\mathbf{k})}}{V} C, \quad (17)$$

where the quantity C is independent of the wave vectors $\mathbf{k}$ and $\mathbf{k}'$ and is given by

$$C = \int_{\Omega_0} u_0^*(\mathbf{r}') U(\mathbf{r}') u_0(\mathbf{r}') d^3r'. \quad (18)$$

Thus, the squared matrix element (as in the case of scattering by acoustic phonons) is independent of the electron wave vector and is expressed as

$$|M_{\mathbf{k}\mathbf{k}'}|^2 = \frac{|C|^2}{V^2}. \quad (19)$$

The reciprocal relaxation time for scattering by a single impurity atom in a bulk sample is given by (11), in which $|M|^2$ should be replaced by $|C|^2/V^2$. If electrons are scattered independently by impurity atoms, which are distributed uniformly over the sample volume V, the reciprocal relaxation time for scattering by a single impurity atom should be multiplied additionally by the number of impurity atoms N_I; i.e.,

$$\tau_{3D}^{-1} = N_I \frac{2\pi}{\hbar}|M_{\mathbf{k}\mathbf{k}'}|^2 V g_{3D} = \frac{2\pi}{\hbar}|C|^2 n_I g_{3D}, \quad (20)$$

where $n_I = N_I/V$ is the impurity concentration and g_{3D} is defined, as before, by formula (12).

Taking into account the Bloch factor, we can represent the wave function of an electron in a QW as

$$\Psi_{\mathbf{k}}(\mathbf{r}) = \sqrt{\frac{2}{a}}\sin\left(\frac{\pi}{a}z\right)\frac{1}{\sqrt{S}}e^{i\mathbf{k}_\parallel\boldsymbol{\rho}}u_{\mathbf{k}}(\mathbf{r}). \quad (21)$$

The matrix element of transition for scattering by an impurity atom residing at the lattice site $\mathbf{r}_i$ within the QW is given by

$$M_{\mathbf{k}_\parallel\mathbf{k}'_\parallel} = \frac{2}{V}\int_S d^3\rho \int_0^a dz\left[e^{-i\mathbf{k}'_\parallel\boldsymbol{\rho}}\sin\left(\frac{\pi z}{a}\right)\right. \times u^*_{\mathbf{k}'}(\mathbf{r})U(\mathbf{r}-\mathbf{r}_i)e^{i\mathbf{k}_\parallel\boldsymbol{\rho}}\left.\sin\left(\frac{\pi z}{a}\right)u_{\mathbf{k}}(\mathbf{r})\right]. \quad (22)$$

Performing the calculations similarly to the above-considered case of a 3D sample in the same approximation of small wave vectors of electrons, we obtain the following expression for the squared modulus of the matrix:

$$|M_{\mathbf{k}_\parallel\mathbf{k}'_\parallel}|^2 = \frac{4|C|^2}{V^2}\sin^4\left(\frac{\pi}{a}z_i\right). \quad (23)$$

Here, z_i is the component of the impurity-atom coordinate $\mathbf{r}_i$ along the z-axis.

The reciprocal relaxation time of charge carriers in the QW can be determined using expression (23) and the formula

$$\tau_{2D}^{-1} = -\frac{2\pi}{\hbar}\int_V d^3r_i \times\left\{n_I\sum_{\mathbf{k}'_\parallel}\left[|M_{\mathbf{k}_\parallel\mathbf{k}'_\parallel}|^2\frac{k'_\chi - k_\chi}{k_\chi}\delta(\varepsilon(\mathbf{k}'_\parallel)-\varepsilon(\mathbf{k}_\parallel))\right]\right\}, \quad (24)$$

where the vector χ and $\varepsilon(\mathbf{k}_\parallel)$ have the same meaning as in (8) and n_I is the volume concentration of impurity atoms.

Since the dependence of τ_{2D} on the impurity-atom coordinate appears in (24) only in terms of matrix element (23), then, for the uniform distribution of independent scattering centers throughout the QW volume, the integration over the coordinates of the impurity atoms contributes to the reciprocal relaxation time in the form of a factor which is equal to

$$\int_V d^3r_i\left(n_I\sin^4\left(\frac{\pi}{a}z_i\right)\right) = n_I S\int_0^a \sin^4\left(\frac{\pi}{a}z_i\right)dz_i = \frac{3}{8}n_I V. \quad (25)$$

As a result, by performing summation over $\mathbf{k}'_\parallel$ in (24), we obtain

$$\tau_{2D}^{-1} = \frac{2\pi}{\hbar}|C|^2 n_I g_{2D}\frac{3}{2}a^{-1}. \quad (26)$$

A comparison of relaxation times for scattering by a short-range potential in a bulk sample (20) and in a layered sample with QWs (26) again yields formula (13); i.e., the ratio between the relaxation times τ_{2D} and τ_{3D} for scattering by acoustic phonons and by the short-range impurity potential has the same form.

4. RELAXATION TIME IN THE CASE OF POLAR SCATTERING BY OPTICAL PHONONS

In both above-considered cases, the matrix element in a bulk sample was independent of the electron and phonon wave vectors; therefore, it is of interest to clarify the issue of whether the derived equality (13) for the ratio τ_{2D}/τ_{3D} is a consequence of the specific form of the matrix element and to consider the case of polar scattering, for which the matrix element is inversely proportional to the wave vector of the optical phonon.

Polar optical phonons are more sensitive to inhomogeneities, which arise in a layered structure with QWs. Calculations of optical-phonon spectra with allowance made for the spatial quantization of phonons were performed in a number of studies (see, for example, review [11] and the references therein). A comparison of various models of charge-carrier scattering by optical phonons in structures with QWs showed [12–15] that discrepancies between the results obtained using the optical-phonon spectra of the bulk type and those obtained using the spectra calculated in accordance with more sophisticated models are not large. Taking this into account, we will consider the scattering of electrons by the bulk optical phonons in a layered structure with QWs using the continual approximation.

In this approximation, the potential of interaction between electrons and polar optical phonons is given by [5]

$$U(\mathbf{r}) = i\sqrt{\frac{4\pi e^2\omega_l^2}{V\varepsilon^*}}\sum_{\mathbf{q}}\frac{1}{q}[a_{\mathbf{q}}e^{i\mathbf{qr}} - a_{\mathbf{q}}^* e^{-i\mathbf{qr}}]. \quad (27)$$

Here, ω_l is the highest frequency of longitudinal optical phonons and

$$(\varepsilon^*)^{-1} = \varepsilon_\infty^{-1} - \varepsilon_0^{-1},$$

where ε_∞ and ε_0 are the high-frequency and static dielectric constants, respectively.

The matrix element corresponding to scattering by optical phonons and accounting for the variation (from $N_{\mathbf{q}}$ to $N'_{\mathbf{q}}$) in the number of phonons with the wave vector $\mathbf{q}$ can be expressed as

$$M_{\mathbf{k}_\parallel\mathbf{k}'_\parallel} = \langle N'_{\mathbf{q}}, \mathbf{k}'_\parallel|U(\mathbf{r})|N_{\mathbf{q}}, \mathbf{k}_\parallel\rangle. \quad (28)$$

Using the electron wave function given by (1), we obtain

$$M_{\mathbf{k}_\parallel\mathbf{k}'_\parallel} = i\sqrt{\frac{4\pi e^2\omega_l^2}{V\varepsilon^*}}\sum_{\mathbf{q}}\frac{1}{q}[\langle N'(\mathbf{q})|a_{\mathbf{q}}|N(\mathbf{q})\rangle Y^+(q_z)$$

$$\times\frac{1}{S}\int_S e^{i(\mathbf{k}_\parallel+\mathbf{q}_\parallel-\mathbf{k}'_\parallel)\boldsymbol{\rho}}d^2\rho - \langle N'(\mathbf{q})|a_{\mathbf{q}}^*|N(\mathbf{q})\rangle Y^-(q_z) \quad (29)$$

$$\times\frac{1}{S}\int_S e^{i(\mathbf{k}_\parallel-\mathbf{q}_\parallel-\mathbf{k}'_\parallel)\boldsymbol{\rho}}d^2\rho],$$

where the functions $Y^\pm(q_z)$ are defined, as before, by formula (5); integration over the coordinate $\boldsymbol{\rho}$ yields the delta functions, which express the law of conservation of the quasi-momentum in the plane of the layers; and the matrix elements of $a_{\mathbf{q}}$ and $a_{\mathbf{q}}^*$, which are related to the absorption and emission of a phonon, are different from zero and are given, respectively, by

$$\langle N'(\mathbf{q})|a_{\mathbf{q}}|N(\mathbf{q})\rangle = \sqrt{\hbar N_{\mathbf{q}}/2\omega_l} \quad \text{for} \quad N'_{\mathbf{q}} = N_{\mathbf{q}} - 1$$

and

$$\langle N'(\mathbf{q})|a_{\mathbf{q}}^*|N(\mathbf{q})\rangle = \sqrt{\hbar(N_{\mathbf{q}}+1)/2\omega_l} \quad \text{for} \quad N'_{\mathbf{q}} = N_{\mathbf{q}} - 1.$$

As a result, we obtain the following expression for the matrix element:

$$M_{\mathbf{k}_\parallel\mathbf{k}_\parallel\pm\mathbf{q}_\parallel} = M^\pm(q)Y^\pm(q_z). \quad (30)$$

Here, $M^\pm(q)$ is the well-known matrix element for polar scattering in the 3D case and is defined as

$$M^\pm(q) = \pm i\sqrt{\frac{2\pi e^2\hbar\omega_l}{V\varepsilon^*}}\frac{1}{q}\begin{cases}\sqrt{N_{\mathbf{q}}},\\ \sqrt{N_{\mathbf{q}}+1},\end{cases} \quad (31)$$

where the sign + (–) and the upper (lower) line on the right correspond to the absorption (emission) of a phonon. At temperatures such that $k_0T \gg \hbar\omega_l$, the number of phonons is equal to $N_{\mathbf{q}} = k_0T/\hbar\omega_l \gg 1$; therefore, the squared modulus of the bulk-related matrix element can be represented as

$$|M^\pm(q)|^2 = |M(q)|^2 = \frac{2\pi e^2 k_0 T}{V\varepsilon^*}\frac{1}{q^2}. \quad (32)$$

The expression for the reciprocal relaxation time can be written similarly to (8), with $|M|^2$ being replaced by $|M(q)|^2$ from (32). The calculation of τ_{2D}^{-1} presents more difficulties than in the case of scattering by acoustic phonons because integration over the components $\mathbf{q}_\parallel$ and q_z of the wave vector in (8) cannot be separated owing to the fact that $q^2 = q_\parallel^2 + q_z^2$ appears in the expression for the squared matrix element (32). However, by integrating first with respect to the direction and magnitude of the vector $\mathbf{q}_\parallel$ in the plane of the layers and then with respect to q_z, we can perform the calculations analytically. As a result, we obtained the following formula:

$$\tau_{2D}^{-1} = \frac{2\pi}{\hbar}|M(k)|^2 V g_{2D}\frac{3}{2}a^{-1}. \quad (33)$$

Here, the expression for $|M(k)|^2$ is given by formula (32).

The relaxation time for polar scattering in a 3D sample is given by [5]

$$\tau_{3D}^{-1} = \frac{2\pi}{\hbar}|M(k)|^2 V g_{3D}. \quad (34)$$

A comparison of (33) and (34) again yields formula (13). Thus, within the limits of the approximations employed, the calculations show that, for the mechanisms of scattering by acoustic phonons, by the short-range impurity potential, and by polar optical phonons, the ratio between the relaxation times in the 2D and 3D cases is the same [see (13)], and τ_{2D} decreases in proportion to the (small) thickness a of the quantum-dimensional layer.

5. THE THERMOELECTRIC FIGURE OF MERIT

Using the above expressions for the relaxation times τ_{2D} (9), (26), and (33), we can calculate the electrical conductivity σ_{2D} of a multilayered system, which consists of QWs and the separating barriers. In the expression derived by ignoring the variation in the relaxation time as a result of dimensional quantization [1], the electrical conductivity σ_{2D} is, in particular, inversely proportional to a, which represents the main cause of an increase in the thermoelectric figure of merit. The presence of the parameter a in the formulas we derived for τ_{2D} compensates this effect. Moreover, the expressions for σ_{2D} coincide with those for the electrical conductiv-

ity of a bulk sample σ_{3D} for each of the above-considered mechanisms of scattering.

Indeed, the expression for the electrical conductivity of a bulk sample can be written as

$$\sigma_{3D} = \frac{4e^2}{3m^*}\int_0^\infty\left(-\frac{\partial f_0}{\partial\varepsilon}\right)\tau_{3D}g_{3D}\varepsilon d\varepsilon, \quad (35)$$

where f_0 is the equilibrium Fermi–Dirac distribution function. The expressions for the reciprocal relaxation time for all three scattering mechanisms are similar [see (11), (20), (34)]; specifically, these reciprocal relaxation times are proportional to the squared matrix element and the density of states g_{3D}. Therefore, substituting in (35) the relaxation time given, e.g., by (11), we obtain

$$\sigma_{3D} = \frac{2e^2\hbar}{3\pi m^*}\int_0^\infty\left(-\frac{\partial f_0}{\partial\varepsilon}\right)\frac{\varepsilon}{|M|^2V}d\varepsilon. \quad (36)$$

In the 2D case, the following expression can be derived for the electrical conductivity of a multilayered system:

$$\sigma_{2D} = \frac{2e^2}{m^*}\int_0^\infty\left(-\frac{\partial f_0}{\partial\varepsilon}\right)\tau_{2D}\frac{g_{2D}}{a}\varepsilon d\varepsilon. \quad (37)$$

Then, after substituting the expression for the relaxation time τ_{2D} (9) into (37), we obtain a formula for σ_{2D}, which coincides with (36).

Expressions for the thermoelectric power and electronic thermal conductivity (the Lorentz number) of a multilayered system also coincide with the corresponding expressions for a bulk sample.

For further presentation, it is convenient to rewrite the expressions for the relaxation times in a bulk sample and in a MQW structure in the following form:

$$\tau_{3D} = \tau_0\left(\frac{\varepsilon}{k_0T}\right)^r, \quad (38)$$

$$\tau_{2D} = a\frac{2\sqrt{2m^*k_0T}}{3\pi\hbar}\tau_0\left(\frac{\varepsilon}{k_0T}\right)^{r+\frac{1}{2}}. \quad (39)$$

Here, r is the scattering parameter for a bulk sample; and τ_0 is a constant, which is independent of the electron energy. Distinctions between the scattering parameters in the 3D (r) and 2D ($r + 1/2$) cases are due to the different energy dependence of the density of states. The parameters r and τ_0 are expressed as

$$r = -\frac{1}{2}, \quad \tau_0 = \frac{2\pi\hbar^4M_0Nv_0^2}{\varepsilon_1^2V(2m^*k_0T)^{3/2}} \quad (40)$$

for scattering by acoustic phonons;

$$r = -\frac{1}{2}, \quad \tau_0 = \frac{\pi\hbar^4}{|C|^2n_Im^*\sqrt{2m^*k_0T}} \quad (41)$$

for scattering at the short-range potential; and

$$r = \frac{1}{2}, \quad \tau_0 = \frac{\hbar^2\varepsilon^*}{e^2\sqrt{2m^*k_0T}} \quad (42)$$

for polar scattering by optical phonons.

If the energy dependences of the relaxation times obey the power law given by (38) and (39), we can use expressions (40)–(42) for τ_0 and r to derive the expressions

$$\sigma = \frac{2^{3/2}e^2(m^*)^{1/2}(k_0T)^{3/2}}{3\pi^2\hbar^3}\tau_0\left(r+\frac{3}{2}\right)F_{r+1/2}(\xi^*) \quad (43)$$

for electrical conductivity;

$$\alpha = -\frac{k_0}{e}\left(\frac{r+5/2}{r+3/2}\frac{F_{r+3/2}(\xi^*)}{F_{r+1/2}(\xi^*)}-\xi^*\right) \quad (44)$$

for thermoelectric power; and

$$\kappa = \frac{2^{3/2}(m^*)^{1/2}(k_0T)^{5/2}k_0}{3\pi^2\hbar^3}\tau_0 \times\left((r+7/2)F_{r+5/2}(\xi^*)-\frac{(r+5/2)^2F_{r+3/2}^2(\xi^*)}{r+3/2}\frac{}{F_{r+1/2}(\xi^*)}\right) \quad (45)$$

for electronic thermal conductivity.

Here, $\xi^* = \xi/k_0T$, where ξ is the chemical potential; and $F_\nu(\xi^*)$ is the Fermi integral of the νth order.

Expressions (43)–(45) are found to be valid both for a MQW system and for a bulk (3D) crystal if the corresponding chemical potentials are used for the quantity ξ^* with the origin of energies in a 2D system being chosen at the bottom of the first subband of dimensional quantization.

Thus, if we assume that the phonon-related thermal conductivity κ_{ph} is the same in a 2D system as in a bulk sample, the expressions for the thermoelectric figure of merit $Z = \alpha^2\sigma/(\kappa + \kappa_{ph})$, which can be derived using (44)–(45), will have the following identical form for both the 2D and 3D cases:

$$ZT = \frac{\left[\left(r+\frac{5}{2}\right)F_{r+3/2}(\xi^*)-\xi^*\left(r+\frac{3}{2}\right)F_{r+1/2}\right]^2}{A+B}. \quad (46)$$

Here, the terms A and B in the denominator are given by

$$A = \frac{3\pi^2\hbar^3\left(r+\frac{3}{2}\right)F_{r+1/2}(\xi^*)\kappa_{ph}}{2^{3/2}(m^*)^{1/2}k_0(k_0T)^{5/2}\tau_0},$$

$$B = \left(r+\frac{7}{2}\right)\left(r+\frac{3}{2}\right)F_{r+5/2}(\xi^*)F_{r+1/2}(\xi^*) - \left(r+\frac{5}{2}\right)F^2_{r+3/2}(\xi^*).$$

If, in both cases, we now choose the chemical potential from the condition for the largest figure of merit, we find that the optimal chemical potential ξ^* and the largest value of Z for a bulk sample and for a structure with QWs are the same; however, the largest values of Z are attained in a 2D structure at higher concentrations of charge carriers and lower mobilities compared to what is typical of a bulk sample.

6. CONCLUSION

Thus, as the calculation of the figure of merit with allowance made for the distinction between the relaxation times in the 2D and 3D systems showed, the notion that it is possible to increase the thermoelectric figure of merit in the form suggested by Hicks and Dresselhaus [1] is unrealistic. Alternative considerations are required in order to render this possibility feasible.

In particular, such considerations were advanced by Ivanov *et al*. [16]. It turns out that, due to the dimensional quantization, inelasticity of scattering manifests itself in 2D structures at higher temperatures than in 3D crystals. In addition, the effects related to drag can also become more important in multilayered structures.

Spatial quantization of phonons can also be assigned to the factors that positively influence the value of Z in 2D systems. Notwithstanding the fact that a distinction between the phonon and bulk modes does not appreciably affect the charge-carrier scattering in QW structures, it can reduce the phonon-related thermal conductivity, which, in turn, causes the value of Z to increase [17].

However, there are a number of factors that adversely affect the thermoelectric figure of merit in 2D structures. Thus, for example, it is well known that tunneling of electrons through barriers, which separate the QWs, reduces the thermoelectric figure of merit; the same is true for thermal conductivity over the layers, which act as barriers. In addition, certain mechanisms of the charge-carrier scattering, which are not possible in the bulk samples, can give rise to more intense scattering in a 2D system. One of the scattering mechanisms, which is characteristic of thin layers, consists in the Coulomb scattering of charge carriers in QWs by charged impurity centers located in the barrier layers [18].

We would like to draw attention to another specific mechanism of scattering; this mechanism is operative in the layers with a thickness which only slightly exceeds the lattice constant. If the layer thickness is small, fluctuations of the thickness Δa are inevitable; these fluctuations affect the charge-carrier energy at $\mathbf{k}_\parallel = 0$. The energy corresponding to the bottom of the first (lowest) subband is equal to $\varepsilon_1 = \pi^2\hbar^2/(2m^*a^2)$. As the layer thickness increases by Δa, a decrease in this energy amounts to

$$\Delta\varepsilon = \frac{\hbar^2\pi^2}{2m^*}\left[\frac{1}{(a+\Delta a)^2} - \frac{1}{a^2}\right] = -\frac{\hbar^2\pi^2}{m^*a^2}\frac{\Delta a}{a}\frac{1+\Delta a/2a}{(1+\Delta a/a)^2}. \quad (47)$$

A variation in the energy $\Delta\varepsilon$ acts as the scattering potential for charge carriers. The effect of the scattering mechanism under consideration on mobility depends on the spatial scale of fluctuations and on the number of regions in which changes in the thickness occur. If this effect is pronounced, it results in the intensification of scattering and a decrease in the thermoelectric figure of merit.

ACKNOWLEDGMENTS

This study was supported by the program “Integration,” project no. 75.

REFERENCES

1. L. D. Hicks and M. S. Dresselhaus, Phys. Rev. B **47**, 12727 (1993).
2. L. D. Hicks, T. C. Harman, X. Sun, and M. S. Dresselhaus, Phys. Rev. B **53**, 10493 (1996).
3. T. L. Reinecke and D. A. Broido, Mater. Res. Soc. Symp. Proc. **487**, 161 (1997).
4. D. A. Broido and T. L. Reinecke, Appl. Phys. Lett. **70**, 2834 (1997).
5. A. I. Anselm, *Introduction to Semiconductor Theory* (Nauka, Moscow, 1978; Prentice-Hall, Englewood Cliffs, 1981).
6. B. K. Ridley, J. Phys. C **15**, 5899 (1982).
7. B. A. Tavger and V. Ya. Demikhovskiĭ, Usp. Fiz. Nauk **96**, 61 (1968).
8. A. Ya. Shik, Fiz. Tekh. Poluprovodn. (Leningrad) **7**, 261 (1973) [Sov. Phys. Semicond. **7**, 187 (1973)].
9. H. L. Stormer, A. C. Gossard, W. Wiegmann, *et al.*, Appl. Phys. Lett. **39**, 912 (1981).

10. Yu. I. Ravich, B. A. Efimova, and I. A. Smirnov, *Semiconducting Lead Chalcogenides* (Nauka, Moscow, 1968; Plenum, New York, 1970).
11. B. K. Ridley, Rep. Prog. Phys. **54**, 169 (1991).
12. H. Rücker, E. Molinary, and P. Lugli, Phys. Rev. B **44**, 3463 (1991).
13. H. Rücker, E. Molinary, and P. Lugli, Phys. Rev. B **45**, 6747 (1992).
14. N. A. Zakhleniuk, C. R. Benett, N. C. Constantinov, *et al.*, Phys. Rev. B **54**, 17838 (1996).
15. N. Nishiguchi, Phys. Rev. B **54**, 1494 (1996).
16. Yu. I. Ivanov, M. V. Vedernikov, and Yu. I. Ravich, Pis'ma Zh. Éksp. Teor. Fiz. **69**, 290 (1999) [JETP Lett. **69**, 317 (1999)].
17. A. Balandin, Phys. Low-Dimens. Struct. **1/2**, 1 (2000).
18. K. Hess, Appl. Phys. Lett. **35**, 484 (1979).

Translated by A. Spitsyn

Semiconductors, Vol. 36, No. 8, 2002, pp. 916–920. Translated from Fizika i Tekhnika Poluprovodnikov, Vol. 36, No. 8, 2002, pp. 981–985.

LOW-DIMENSIONAL SYSTEMS

Nonlinear Response and Nonlinear Coherent Generation in Resonant-Tunneling Diode in a Broad Frequency Range

V. F. Elesin, I. Yu. Kateev, and A. I. Podlivaev

Moscow State Institute of Engineering Physics (Technical University), Moscow, 115409 Russia

Submitted January 16, 2002; accepted for publication January 22, 2002

Abstract—Nonlinear response and coherent generation in a resonant-tunneling diode within a broad range of frequencies and field amplitudes are theoretically studied for real structures under dc bias voltage. The results are shown to be in a good qualitative agreement with the idealized model if the widths of the resonance level Γ are identical for both quantum wells. Thus, the generation of high-power terahertz-frequency fields within the quantum mode is possible under real conditions. It is explicitly shown that the transient time of current in resonant-tunneling diodes is equal to the reciprocal of Γ. © *2002 MAIK "Nauka/Interperiodica".*

1. INTRODUCTION

Resonant-tunneling diodes (RTD) are believed to be promising for numerous applications and for high-frequency electromagnetic generation in particular. For example, generation at the frequency of 712 GHz was obtained in [1], but the power was rather low. The problem of power enhancement is related, in particular, to the lack of theory on RTD generation.

An exact analytic expression for the polarization currents in the linear approximation in a high-frequency field was derived in [2] within a consistent model. It was shown in [2] that there is no limit on the generation frequency, and a new "quantum" mode of generation at the frequency ω, which significantly exceeds the resonance level width Γ, can be achieved under certain conditions. It should be recalled that some authors assert (see, for example, [3–5]) that there exists a limiting generation frequency, which is approximately equal to Γ (here and below $\hbar = 1$).

A nonlinear analytic theory of RTD generation at frequencies $\omega \ll \Gamma$ was developed in [6]. A hysteretic mode of generation was shown to exist. Polarization currents were calculated, and the generation in a broad range of frequencies and field amplitudes was described by numerically solving the Schrödinger equation in [7]. With good accuracy, the numerical results comply with the analytic ones from [2, 6] in the linear and low-frequency nonlinear cases. High-power generation at the frequency $\omega \gg \Gamma$ was shown to be possible in [7].

However, in [7], a simplified model of the structure (delta-barriers) was considered, and the role of the dc bias voltage was played by the energy of electrons arriving from the emitter.

The aim of this work is to generalize the results of [7] to the case of a real structure and to take into account the external bias electric field. We calculated the response and generation so that the results will be easy to compare with [7].

2. STATEMENT OF THE PROBLEM. BASIC EQUATIONS

Let us consider a one-dimensional quantum well (QW) with two rectangular barriers. A time-independent flux of electrons with energy E, with an intensity proportional to q^2, is fed to the QW from the emitter on the left (q is the value characterizing the electron flow density). The ac electric field is present in the QW region; the interaction energy of an electron with the field reads

$$V_{ac}(x, t) = \begin{cases} -\dfrac{e\mathcal{V}x\cos(\omega t)}{L}\Theta(x), & x < L \\ -e\mathcal{V}\cos(\omega t), & x > L, \end{cases} \quad (1)$$

where $\Theta(x)$ is the unit step function, L is the structure length, and $\mathcal{V}$ is the dc voltage amplitude. The one-particle electron wave function $\Psi(x, t)$ satisfies the time-dependent Schrödinger equation

$$i\frac{\partial\Psi}{\partial t} = -\frac{1}{2m^*}\frac{\partial^2\Psi}{\partial x^2} + [V_s(x) + V_{dc}(x)]\Psi(x, t) + V_{ac}(x, t)\Psi(x, t), \quad (2)$$

where

$$V_{dc}(x) = \begin{cases} -\dfrac{eV_0x}{L}\Theta(x), & x < L \\ -eV_0, & x > L. \end{cases} \quad (3)$$

1063-7826/02/3608-0916$22.00

Here $V_s(x)$ is the potential distribution across the quantum structure, e is the electron charge, and V_0 is the dc voltage.

The calculation of the dynamic characteristics of RTD is carried out similarly to [7]. The ac field induces the polarization current

$$J_c(x, t) = -ie\left\{\Psi^*(x, t)\frac{\partial\Psi(x, t)}{\partial x} - \Psi(x, t)\frac{\partial\Psi^*(x, t)}{\partial x}\right\} \quad (4)$$

$$= J_c(x)\cos\omega t + \sum_{k=2} J_k(x)\cos k\omega t.$$

The spatially averaged current is calculated [8] as

$$J_c = \frac{1}{L}\int_0^L J_c(x)dx. \quad (5)$$

Boundary conditions for the Schrödinger equation can be written similarly to [2]

$$\begin{cases}\Psi(0, t) + \dfrac{1}{ik_1}\dfrac{\partial\Psi(0, t)}{\partial x} = 2q\exp(-iEt),\\ \Psi(L, t) - \dfrac{1}{ik_2}\dfrac{\partial\Psi(L, t)}{\partial x} = 0,\end{cases} \quad (6)$$

where $k_1 = \sqrt{2m^*E}$ and $k_2 = \sqrt{2m^*(E + eV_0)}$ are, respectively, electron wave vectors to the left and to the right of the structure, and m^* is the effective electron mass in the structure. The boundary conditions (6) describe the incident from the left electron flow, as well as their reflection and transfer into the region $x > L$. They are valid if $\omega \ll E + eV_0$ and $ev \ll E + eV_0$.

For calculations we chose a structure which has shown record-breaking experimental results for generation [9] (a well width of 45.2 Å, a barrier thickness of 22.6 Å, and a barrier height of 1.2 eV). The energy E of the monoenergetic incident electron beam is assumed to equal 82 meV, the effective mass $m^* = 0.042m_e$ (m_e is the free electron mass), and the voltage $V_0 = V_R + \delta_V/e$, where $V_R = 280$ mV is the resonance voltage at which the transmission coefficient dependence on the voltage V_0 has a maximum at the chosen energy E and for the given structure parameters. The half-width of the resonance level Γ equals 1.66 meV at the given voltage $V_0 \approx V_R$.

3. LINEAR AND NONLINEAR RESPONSE OF THE RESONANT-TUNNELING DIODE

The linear response was shown in [2] to have a peak at $\omega = 0$ ("classical" mode) if $\delta < \Gamma$ ($\delta = E - E_R$). If $\delta > \Gamma$, a new peak at the frequency ω_m($\omega_m^2 = \delta^2 - \Gamma^2$) appears, which corresponds to the "quantum" mode [2]. This is caused by quasi-resonance transitions between the states with energies E and E_R. If we fix the energy of electrons arriving from the emitter and change the dc electric field, then the role of $\delta = E - E_R$ in [7] is played here by $\delta_V = e(V_0 - V_R)$. The resonance level is known to be shifted approximately by half of the voltage; i.e., we can assume that $\delta_V = 2\delta$. This is why the "classical" mode is observed for $\delta_V < 2\Gamma$.

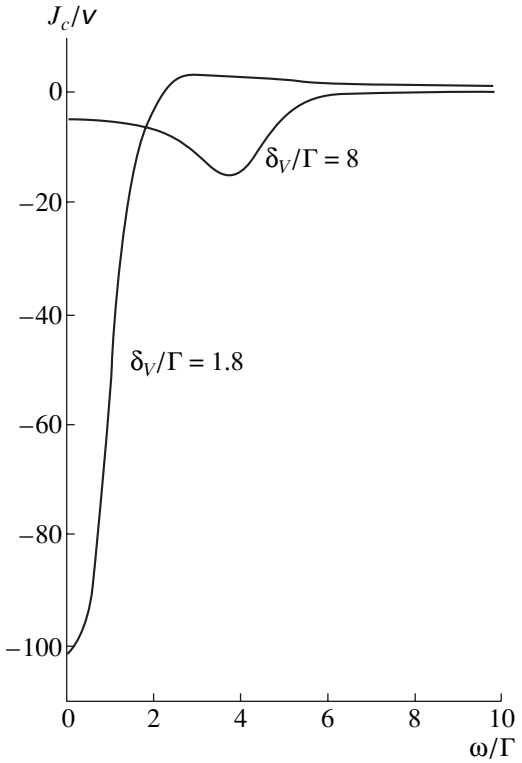

Fig. 1. Frequency dependence of the amplification coefficient J_c/v in the "quantum" and "classical" generation modes.

The dependence of the amplification coefficient J_c/v on the frequency ω for $\delta_V = 1.8\Gamma$ and $\delta_V = 8\Gamma$ at $ev = 0.01\Gamma$ (the weak field case) is presented in Fig. 1. The choice of the parameter δ_V is similar to that in [7], where δ is equal, respectively, to 0.9Γ and 4Γ. It is seen from Fig. 1 that there are peaks at the frequency $\omega = 0$ for $\delta_V = 1.8\Gamma$ and at ω_m, which correspond to $\omega_m^2 = (\delta_V/2)^2 - \Gamma^2$, for $\delta_V = 8\Gamma$. Comparison of the plots in Fig. 1 and [7] (Fig. 3) indicates that their behavior is qualitatively the same.

Mention should, however, be made of one essential distinction in the behavior of amplification in the classical mode for a frequency exceeding Γ. Indeed, the current J_c changes its sign at $\omega \approx 2\Gamma$ (i.e., amplification gives way to absorption), while in the model [2, 7] the sign of the current does not change over the entire frequency range. The sign changes because the bias field

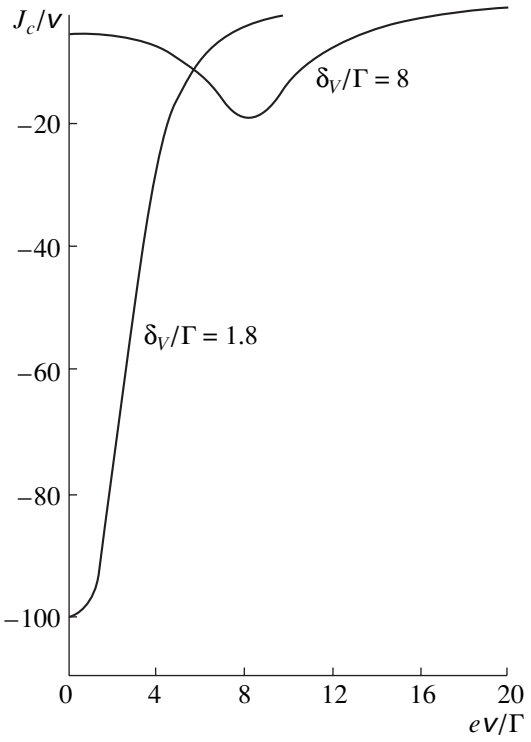

Fig. 2. Dependence of the amplification coefficient J_c/V on the dc voltage amplitude V in the low-frequency range. $\omega/\Gamma = 0.17$.

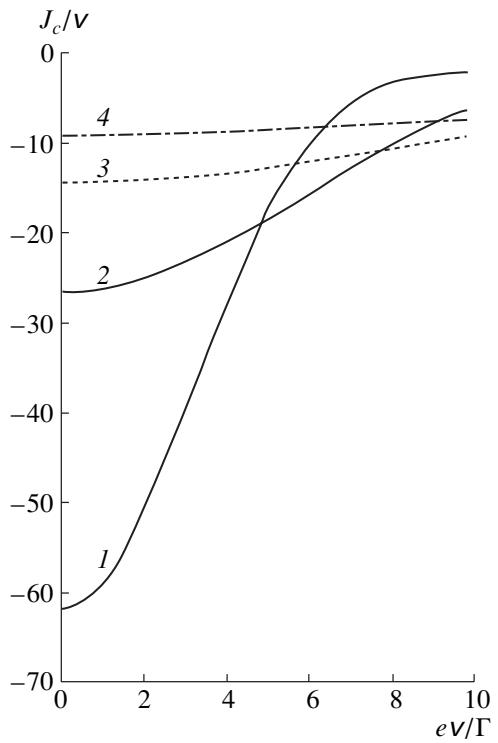

Fig. 3. Dependence of the amplification coefficient J_c/V on the dc voltage amplitude in the "quantum" generation mode. (*1*) $\delta_V/\Gamma = 2$, $\omega/\Gamma = 1$; (*2*) $\delta_V/\Gamma = 5$, $\omega/\Gamma = 2$; (*3*) $\delta_V/\Gamma = 8.2$, $\omega/\Gamma = 4$; and (*4*) $\delta_V/\Gamma = 12$, $\omega/\Gamma = 6$.

not only reduces the resonance level energy, but also lowers the collector-barrier height.

Nonlinear response was studied within a broad frequency range. The dependence of J_c/V on the dimensionless field eV/Γ in the low-frequency limit $\omega = 0.17\Gamma$ is presented in Fig. 2 ($\delta_V/\Gamma = 1.8$ and $\delta_V/\Gamma = 8$). One can see an essential distinction in the dependence of J_c/V in these cases, similarly to [6, 7]. In the first case ($\delta_V/\Gamma > 2$), a rise of the amplification is observed in the beginning and, when the peak is reached, its descent is observed. The dependence in Fig. 2 agrees qualitatively with Figs. 4 and 5 in [6, 7]. The nonmonotonic behavior of the amplification leads to the hysteretic generation mode (see below).

A typical dependence of the amplification J_c/V on the field amplitude eV/Γ for high frequencies ($\omega > \Gamma$) at the satisfied quasi-resonance condition $\delta_V = 2\omega$, i.e., in the quantum mode, is presented in Fig. 3. Noteworthy are the features of these plots, which are qualitatively similar to [7]: first, there is a steady amplification drop J_c/V with the field; and second, there is a decrease in the rate of this drop with increasing frequency. This means that high fields can be reached at high frequencies in the "quantum" mode.

4. GENERATION IN THE RESONANT-TUNNELING DIODE IN A BROAD FREQUENCY RANGE

Following [2, 7], we find the field generated by RTD from the equation

$$\frac{\tilde{E}}{\tau_0} = \frac{4\pi}{\kappa} J_c, \qquad (17)$$

where τ_0 is the time characterizing resonator losses, and κ is the dielectric constant.

The dependences of the low-frequency ($\omega = 0.17\Gamma$) generated field on the reduced pumping current Q is presented in Fig. 4. It is seen that the field steadily rises with Q at $\delta_V = 1.8\Gamma$ ($\delta_V/\Gamma < 2$). If $\delta_V/\Gamma > 2$ ($\delta_V/\Gamma = 8$), the hysteretic mode is observed. The results are again in good qualitatively agreement with [6, 7].

The Q dependence of the generated field for a large collection of parameters is presented in Fig. 5. A comparison of the results for the "classical" and "quantum" modes is given in Fig. 6. It is seen that the field in the "quantum" mode ($\omega = 4\Gamma$) significantly exceeds the one in the "classical" mode ($\omega = 0.17\Gamma$) at $Q > 0.07$. Again, the results obtained are in good agreement with [6, 7].

The steady state generation is considered in [2, 6]. It exists due to the finite lifetime of an electron in the QW:

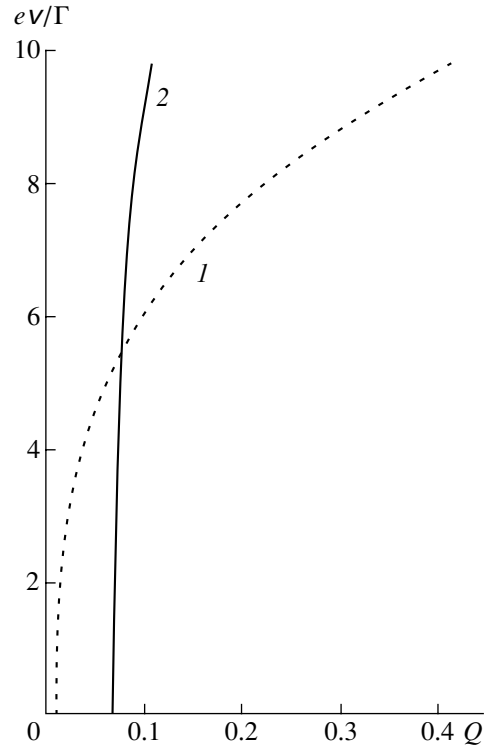

Fig. 4. Dependence of the generated field on the reduced pumping current Q in the "classical" (*1*) and "quantum" (*2*) generation modes in the low-frequency range. (*1*) $\delta_V/\Gamma = 1.8$, $\omega/\Gamma = 0.17$; (*2*) $\delta_V/\Gamma = 8.2$, $\omega/\Gamma = 4$.

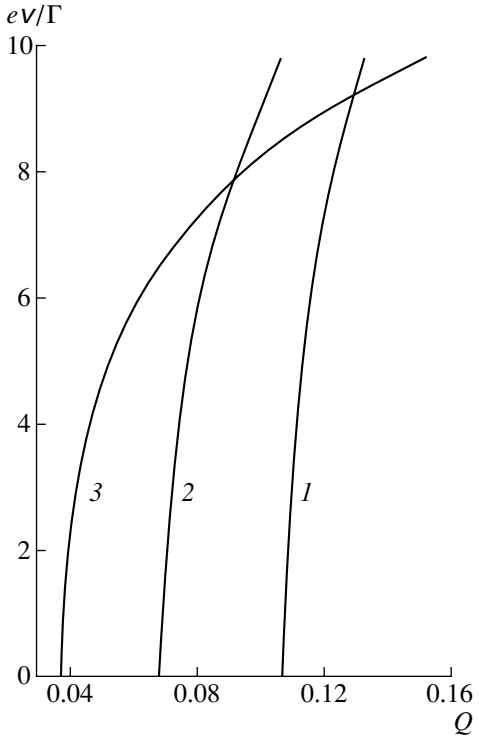

Fig. 5. Dependence of the generated field on the reduced pumping current Q in the "quantum" mode at high frequency ω and large parameter δ_V (*1*) $\delta_V/\Gamma = 12$, $\omega/\Gamma = 6$; (*2*) $\delta_V/\Gamma = 8.2$, $\omega/\Gamma = 4$; and (*3*) $\delta_V/\Gamma = 5$, $\omega/\Gamma = 2$.

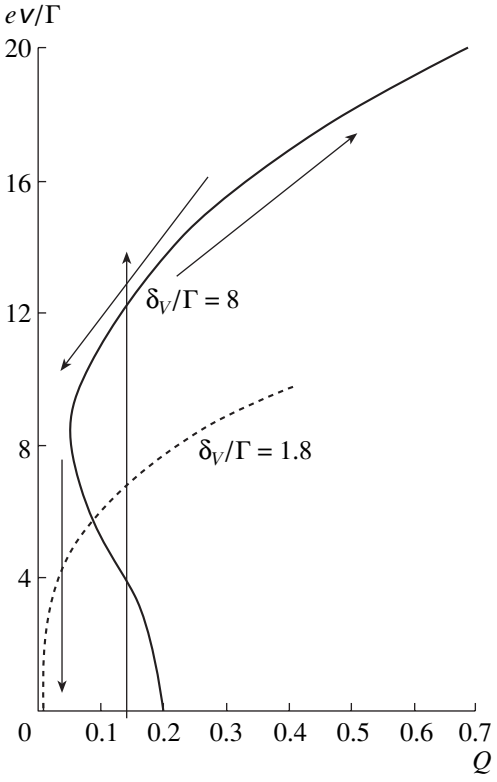

Fig. 6. Dependence of the generated field on the reduced pumping current Q: comparison of the "quantum" and "classical" modes. $\omega/\Gamma = 0.17$.

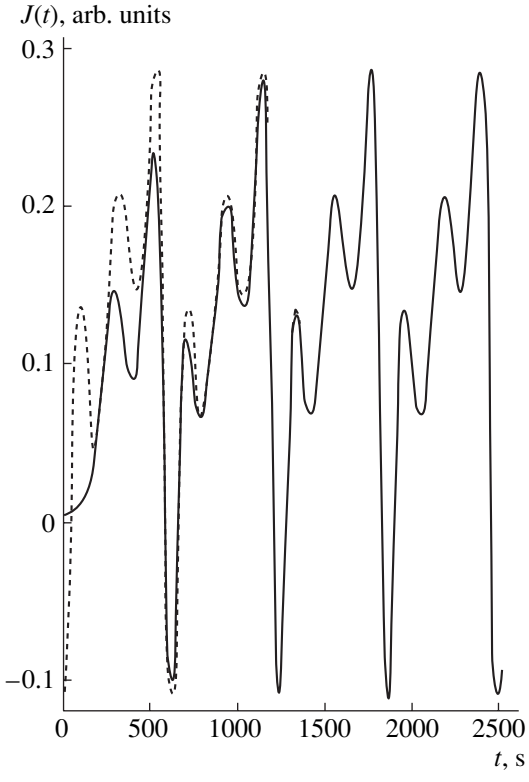

Fig. 7. Dependence of the electron current J through RTD (solid line) on time t for $\omega/\Gamma = 4$ and $\delta_V/\Gamma = 8.2$ at $eV/\Gamma = 20$. Dashed line: see text.

$\tau \sim 1/\Gamma$. It is of interest to study the transient process and to determine the transient time for current in RTD. The dependence of the electron current J through the RTD (solid line) on time t for $\omega/\Gamma = 4$ and $\delta_V/\Gamma = 8.2$ at $eV/\Gamma = 20$ is presented in Fig. 7. The frequency ω and parameter δ_V correspond to the "quantum" generation mode. An external dc electric field was assumed to be switched on at the instant of time $t = 0$. The steady-state current through RTD is depicted with the dashed line under the assumption that there is no transient process and that the steady-state current is attained instantaneously. It is seen that the real transient process occupies almost three periods of the external harmonic field, i.e., the transient time $T = 3(2\pi/\omega) = 3(2\pi/4\Gamma) \approx 1/\Gamma$. Thus, the transient time of the current in RTD does not depend on external field parameters, rather, it is determined by the halfwidth of the resonance level Γ and is approximately equal to the electron lifetime τ in a QW, as was assumed in [2, 6].

5. CONCLUSION

In this communication, coherent generation in RTD within a broad range of frequencies and fields for a real structure with rectangular barriers and with nonzero voltage is described by solving a time-dependent Schrödinger equation with approximate boundary conditions.

It is shown that, in this case too, "classical" and "quantum" generation modes occur in which high frequency and power are achieved. We have ascertained that the generation features are determined by the halfwidth of the resonance level Γ and not by the barrier configuration.

It is found that the transient process in RTD terminates during the time $T \approx 1/\Gamma$; i.e., again, it depends only on Γ.

ACKNOWLEDGMENTS

We thank Yu.V. Kopaev for his helpful participation in discussions.

This study was supported by the special federal program "Integratsiya" (project no. A0133), by the "Solid-State Nanostructures" program of the Ministry for Science and Technology of the Russian Federation (project no. 99-1140), and by the project "Development of the Theory of Interaction of Strong High-Frequency Electromagnetic Fields with a System of Resonant-Tunneling Diodes and Lasers."

REFERENCES

1. E. R. Brown, T. C. L. G. Sollner, C. D. Parker, *et al.*, Appl. Phys. Lett. **55**, 1777 (1989); E. R. Brown, J. R. Söderstrom, C. D. Parker, *et al.*, Appl. Phys. Lett. **58**, 2291 (1991).
2. V. F. Elesin, Zh. Éksp. Teor. Fiz. **116**, 704 (1999) [JETP **89**, 377 (1999)].
3. R. K. Mains and G. I. Haddad, J. Appl. Phys. **64**, 3564 (1988).
4. R. K. Mains and G. I. Haddad, J. Appl. Phys. **64**, 5041 (1988).
5. H. C. Liu, Phys. Rev. B **43**, 2097 (1991).
6. V. F. Elesin, Phys. Low-Dimens. Struct. **1/2**, 55 (2000).
7. V. F. Elesin, I. Yu. Kateev, and A. I. Podlivaev, Fiz. Tekh. Poluprovodn. (St. Petersburg) **34**, 1373 (2000) [Semiconductors **34**, 1321 (2000)].
8. V. I. Saforev, *Radio Receiving Equipments* (Nauka, Moscow, 1954).
9. T. Inata, S. Muto, Y. Nakata, *et al.*, Jpn. J. Appl. Phys. **26**, L1332 (1987).

Translated by S. Ktitorov

Semiconductors, Vol. 36, No. 8, 2002, pp. 921–923. Translated from Fizika i Tekhnika Poluprovodnikov, Vol. 36, No. 8, 2002, pp. 986–988.

LOW-DIMENSIONAL SYSTEMS

Anomalies of the Fractional Quantum Hall Effect in a Wide Ballistic Wire

Z. D. Kvon[1]*, E. B. Olshanetsky[1], A. E. Plotnikov[1], A. I. Toropov[1], and J. C. Portal[2, 3, 4]

[1] *Institute of Semiconductor Physics, Siberian Division, Russian Academy of Sciences, pr. Akademika Lavrent'eva 13, Novosibirsk, 630090 Russia*

**e-mail: kvon@thermo.isp.nsc.ru*

[2] *Grenoble High Magnetic Fields Laboratory, MPI-FKF and CNRS, B.P.166, F-38042 Grenoble, France*

[3] *INSA 135, Avenue de Rangueil, 31077 Toulouse, Cedex 4, France*

[4] *Institut Universitaire de France*

Submitted January 14, 2002; accepted for publication January 22, 2002

Abstract—Magnetotransport in a ballistic wire under the conditions of integer and fractional quantization was studied experimentally. A nonlinear magnetic-field dependence of filling factor (ν) of the Landau level was observed; this dependence arises if the self-consistent electrostatic potential of the wire has a specific form. It is assumed that the observed effect results from the influence of interaction between electrons at the partially occupied Landau level on this potential, which brings about a decrease in the electron concentration in the wire as the magnetic field increases in the case of $\nu < 1$. © *2002 MAIK "Nauka/Interperiodica".*

After the first relevant publication [1] and subsequent experiments, there is no doubt that, in a number of cases, the charge transport under the conditions of the integer and fractional Hall effect is controlled by the edge current states. These are represented by both the broad bands (their width far exceeds the corresponding magnetic length) of compressible electron liquid and the much narrower incompressible bands located at the sample edges. The effect of wide compressible bands was first demonstrated by Hwang *et al.* [2]. However, only the two-terminal resistance of the wire was studied [2], whereas an important and interesting issue concerning the behavior of the Hall (R_H) and longitudinally dissipative (R_L) components of wire resistance for magnetotransport effected by the edge current states whose width is comparable with the wire width has remained open. The quantities R_H and R_L were measured simultaneously for the first time in a thick ballistic wire ($L_H \ll W \ll l$, where L_H is the magnetic length and l is the free-path length) by Kvon *et al.* [3]; a number of anomalies in the behavior of R_H and R_L were observed [3] and attributed to the existence of compressible electron-liquid bands, the width of which was comparable to the wire thickness.

In this paper, we report on another anomaly which arises in a wide ballistic wire under the conditions of fractional Hall quantization; we refer to the nonlinear dependence of the filling factor ν of the Landau level on the magnetic field for $\nu < 1$. It is assumed that this nonlinearity is related to the effect of a magnetic field on the self-consistent electrostatic potential of the wire, which brings about a decrease in the electron concentration in the wire with increasing magnetic field under the conditions of the ultraquantum limit ($\nu < 1$).

The samples used in this study were wires with potentiometric contacts. The wire structures were fabricated using electron lithography with subsequent plasma-chemical etching (schematic representation of a wire and its lithographic dimensions are illustrated in the inset in Fig. 1). As the starting material, we used a AlGaAs/GaAs heterojunction with two-dimensional

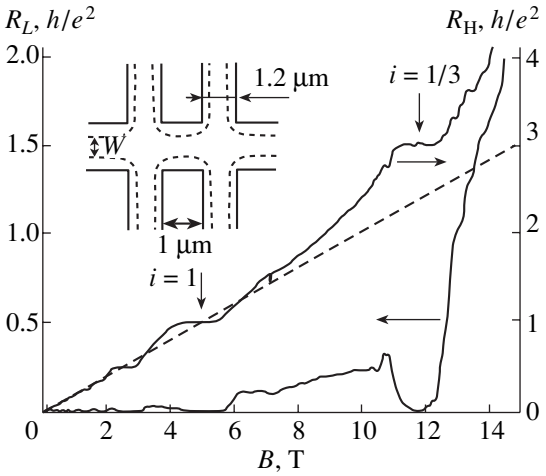

Fig. 1. Dependences of the Hall $R_H(B)$ and longitudinal $R_L(B)$ components of the wire resistance on the magnetic field for V_g = –0.35 V and T = 50 mK (the dashed line represents the dependence $R_H = B/eN_s$). Schematic representation of the wire is shown in the inset.

1063-7826/02/3608-0921$22.00 © 2002 MAIK "Nauka/Interperiodica"

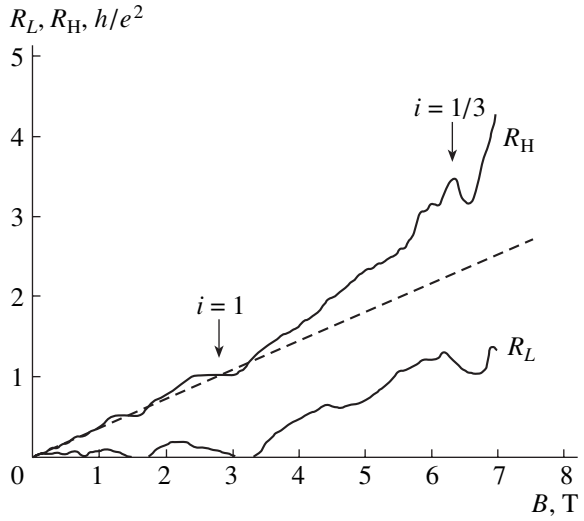

Fig. 2. The magnetic-field dependences of the Hall $R_H(B)$ and longitudinal $R_L(B)$ components of the wire resistance at $V_g = -0.5$ V and $T = 60$ mK (the dashed line represents the dependence $R_H = B/eN_s$).

(2D) electron gas, which had an electron mobility $\mu = 10^6$ cm^2/(V s), an electron density $N_s = 2 \times 10^{11}$ cm^{-2} (the corresponding free path length was $l_e = 8$ μm), and was located at a distance of 150 nm from the structure surface. It is noteworthy that the etching depth was no larger than 50 nm; as a result, the surface subjected to the plasma treatment was separated from the 2D electron gas by a distance larger than the spacer thickness ($d_{sp} = 60$ nm). Consequently, an appreciable effect of the fluctuation potential at the wire boundaries was eliminated. After fabrication of the wire, a metallic gate contact was formed by spraying TiAu on the wire surface; the electron concentration in the wire was varied by applying a voltage to the gate. Measurements were conducted using the conventional four-point probe method at temperatures of 0.04–1 K in magnetic fields as high as 16 T. The current during measurements was no higher than 1 nA, in order to eliminate the effects of heating.

In Fig. 1, we show the results of measuring the dissipative R_L and the Hall R_H components of the wire's magnetoresistance for the gate voltage $V_g = -0.35$ V. At first glance, Fig. 1 demonstrates a conventional pattern of behavior of R_L and R_H under the conditions of the quantum Hall effect. In the magnetic-field range corresponding to the integer filling factor ν, the minima in R_L and the corresponding plateaus in the Hall quantization are observed, whereas, for filling factor $\nu < 1$, minima in the dependence $R_L(B)$ and the plateaus in the dependence $R_H(B)$, which correspond to $\nu = 1/3$, are observed. However, closer inspection reveals a deviation from this pattern. The dashed straight line in Fig. 1 corresponds to the dependence $R_H = B/eN_s$ ($N_s = 1.2 \times 10^{11}$ cm^{-2}). It can be clearly seen that, in the range of weak fields, the experimental data precisely fit this dependence, whereas, in the region where the plateaus of the integer quantization are observed, the dependence runs approximately through the middle of these plateaus. It is this pattern that is observed for a macroscopic 2D electron gas under the conditions of both the quantum Hall effect and the fractional quantum Hall effect. However, it can be seen from Fig. 1 that, in the magnetic fields corresponding to the ultraquantum limit, i.e., for $\nu < 1$ (for the magnetic fields exceeding 5 T), experimental dependence $R_H(B)$ starts to deviate from the straight line and runs above this line. This fact gives us cause to assume that, under these conditions, the linear dependence of the occupancy of the Landau level on the magnetic field, which is observed in all macroscopic 2D systems, is upset. However, the very fact that the dependence $R_H(B)$ is nonlinear cannot be used to unambiguously advance the above assumption. A valid conclusion can be made on the basis of the position of the plateau of the fractional Hall quantization, which makes it possible to determine the occupancy of the Landau level unambiguously. In Fig. 1, a well-pronounced plateau of the Hall quantization corresponding to the filling factor $\nu = 1/3$ can be clearly seen. The middle of this plateau corresponds to the magnetic-field strength of $B = 11.7$ T; the latter value is much smaller than that following from the conventional linear dependence, which yields $B = 15$ T. We note that a minimum in the $R_L(B)$ dependence is also located at $B = 11.7$ T, rather than at $B = 15$ T. Thus, the above experimental data on the fractional Hall quantization unambiguously indicate that a nonlinear dependence of the occupancy of the Landau level on the magnetic field comes into existence in the wire. This nonlinearity gives rise to the fact that a specific value of ν in the ultraquantum limit is attained at a smaller value of the magnetic field than in the case of conventional linear dependence. This behavior can be explained only if we assume that the electron concentration in the wire begins to decrease with increasing magnetic field as soon as the filling factor becomes smaller than unity. This means that, under certain conditions fulfilled in our experiment (including partial occupation of the Landau level), a magnetic field can affect the self-consistent electrostatic potential of the wire. This inference is also supported by experimental data that were obtained at a lower electron concentration. In Fig. 2, we show the dependences $R_H(B)$ and $R_L(B)$ measured at the gate voltage $V_g = -0.5$ V. The dependence $R_H = B/eN_s$ for a much lower electron density ($N_s = 7 \times 10^{10}$ cm^{-2}) is also shown in Fig. 2 by the dashed straight line. It can be seen that the dependence $R_H(B)$ starts to deviate from this straight line as soon as the magnetic field becomes higher than 3 T, i.e., when the occupancy of the Landau level becomes smaller than unity. This is also supported by the positions of both a plateau of the fractional Hall quantization (also corresponding to $\nu = 1/3$) and a minimum in the dependence $R_L(B)$. In fact, the plateau is already distorted by mesoscopic fluctuations, and the minimum is shifted to higher fields in reference to the plateau. Nevertheless,

this does not prevent one from determining the filling factor with satisfactory accuracy and from recognizing the same nonlinearity in the $\nu(B)$ dependence. Thus, irrespective of the electron concentration in the zero magnetic field, a nonlinear dependence $\nu(B)$ arises as soon as the partially occupied Landau level appears in the wire, with the degree of nonlinearity remaining virtually the same for both values of N_s. It is noteworthy that the aforementioned nonlinearity is not observed in all wires. In the wires with lower threshold voltages, this effect was not observed and the behavior of the filling factor was the same as in the macroscopic case. Hence, it follows that the existence of nonlinearity largely depends on the form of the electrostatic potential well which is present in the wire under consideration.

We now discuss the above results. They indicate that, under certain conditions, the occupancy of the partially occupied Landau level in a wide ballistic wire increases with the magnetic field superlinearly (the linear dependence is typical of macroscopic samples). The most probable explanation for the observed effect is based on the assumption that the 2D electron concentration at the partially occupied Landau level in a wide ballistic wire starts to decrease with increasing magnetic field. Basically, it is hardly surprising that a magnetic field can affect N_s. Qualitatively, the mechanism of this phenomenon may be conceived in the following way. Evidently, the self-consistent electrostatic potential formed in the wire is the result of the summation of electrostatic fields related to the charges of the spacer, the metallic gate, the surface states, and, of most importance, the screening charge of electrons at the partially occupied Landau level. It is these factors that give rise to the compressible and incompressible electron-liquid bands in the wire. The formation of the aforementioned self-consistent potential depends to a great extent on the characteristics of the electron–electron interaction at this level, which, in turn, depends on the occupancy of this level and on N_s. It is this effect that can give rise to the effect of a magnetic field on electron concentration. However, an unambiguous solution of the formulated problem can only be obtained by deriving a consistent theory of the partially occupied Landau level in a ballistic wire; this theory should account for all the above factors.

REFERENCES

1. D. B. Chklovskii, B. I. Shklovskii, and L. I. Glazman, Phys. Rev. B **46**, 4026 (1992).
2. S. W. Hwang, D. C. Tsui, and M. Shayegan, Phys. Rev. B **48**, 8161 (1993).
3. Z. D. Kvon, E. B. Olshanetsky, M. Casse, *et al.*, Physica B (Amsterdam) **298**, 155 (2001).

Translated by A. Spitsyn

Semiconductors, Vol. 36, No. 8, 2002, pp. 924–928. Translated from Fizika i Tekhnika Poluprovodnikov, Vol. 36, No. 8, 2002, pp. 989–992.

LOW-DIMENSIONAL SYSTEMS

Special Features of Electrical Conductivity in a Parabolic Quantum Well in a Magnetic Field

E. P. Sinyavskii* and R. A. Khamidullin

Institute of Applied Physics, Academy of Sciences of Moldova, Chisinau, 277028 Moldova

** e-mail: arusanov@mail.ru*

Submitted November 8, 2001; accepted for publication January 29, 2002

Abstract—The Kubo formula was used to derive a general expression for static electrical conductivity in a magnetic field directed parallel to the surface of a parabolic quantum well. Conditions for the applicability of the relaxation-time approximation for the calculation of the correlation functions were formulated using the cumulant-averaging method. The tensors of longitudinal and transverse conductivities in the dimensionally confined system under consideration, with allowance made for the interaction of electrons with acoustic and optical vibrations, were calculated. It is shown that the transverse conductivity in quantum-well systems is much higher (by several orders of magnitude) than in the bulk samples. The dependence of longitudinal conductivity on the magnetic field was studied for a highly degenerate electron gas. © *2002 MAIK "Nauka/Interperiodica".*

1. Studies of transport phenomena in systems with quantum wells (QWs) are important because, due to the dispersion relation for the band charge carriers, such quantum-mechanical systems are promising for the development of devices with unique characteristics. For a degenerate two-dimensional (2D) electron gas, the kinetic coefficients and optical characteristics vary nonmonotonically with decreasing thickness of a spatially confined system [1, 2]. The description of the electron-transport phenomena in various dimensionally quantized systems (QWs, quantum wires, and superlattices) has been mainly based on the solution of the Boltzmann equation with allowance made for scattering of charge carriers by point defects [3–6].

In this study, general relations for the conductivity tensor were used to gain insight into special features of electrical conductivity in parabolic QWs in a transverse magnetic field. We consider the cases of a degenerate and a nondegenerate electron gas which interacts with acoustic and optical vibrations. Some of the results are compared with experimental data.

2. Using the secondary-quantization representation and the Kubo formula [7], we can express the static electrical conductivity as

$$\sigma_{ij} = \frac{\beta_0 e^2}{2Vm^2}\sum_{\alpha\beta\alpha_1\beta_1} p^{(i)}_{\alpha\beta}p^{(j)}_{\alpha_1\beta_1}\int\limits_{-\infty}^{\infty} dt\langle a^+_\alpha(t)a_\beta(t)a^+_{\alpha_1}a_{\beta_1}\rangle. \quad (1)$$

Here, $a^+_\alpha(a_\alpha)$ are the operators of creation (annihilation) of the charge carriers with the charge e and the effective mass m in the state α; $\beta_0 = 1/k_0T$ (T is the temperature expressed in absolute degrees); V is the volume of the quantum-mechanical system,

$$a^+_\alpha(t) = \exp\left(\frac{i\hat{H}t}{\hbar}\right)a^+_\alpha\exp\left(\frac{i\hat{H}t}{\hbar}\right); \quad (2)$$

and $\langle\ldots\rangle$ in (1) denotes averaging with the equilibrium density matrix of the system under investigation, which is described by the Hamiltonian $\hat{H}$.

The matrix elements of the momentum operator $p^{(i)}_{\alpha\beta}$ acting on the wave functions of an electron in a parabolic QW in a magnetic field directed parallel to the surface of the QW system [8, 9] are calculated directly; i.e.,

$$p^{(x)}_{\alpha\beta} = \hbar k_x\delta_{\alpha\beta}, \quad (3)$$

$$p^{(y)}_{\alpha\beta} = \hbar\left(\frac{\omega}{\omega_0}\right)^2 k_y\delta_{\alpha\beta} - \frac{m\omega_c}{\sqrt{2\lambda}}\delta_{k_x,k'_x}\delta_{k_y,k'_y} \times\{\sqrt{n}\delta_{n,n_1+1} + \sqrt{n+1}\delta_{n,n_1-1}\}, \quad (4)$$

where ω is the dimensional-quantization frequency, ω_c is the cyclotron frequency, $\lambda = m\omega_0/\hbar$, k_x and k_y are the components of the electron quasi-momentum, and $\omega_0^2 = \omega^2 + \omega_c^2$.

It follows from (3) that, for the electric field direction parallel to the magnetic field, the matrix element of the momentum operator differs from zero if $\alpha = \beta$. For transverse electrical conductivity, the matrix element of the generalized-momentum operator has both diagonal components [the first term in (4)] and nondiagonal components with reference to the quantum number n.

It is noteworthy that the diagonal matrix element appears only in quantum-mechanically confined systems (for $\omega \longrightarrow 0$, the corresponding term in (4) is absent). It is this circumstance that gives rise to special features in the dimensionally quantized systems, i.e., to a significant increase in transverse electrical conductivity compared to that in the bulk materials.

We now consider the interaction of charge carriers with phonons, i.e.,

$$\hat{H} = \hat{H}_0 + \hat{V},$$
$$\hat{H}_0 = \sum_{\alpha} E_\alpha a_\alpha^+ a_\alpha + \sum_{\mathbf{q}} \hbar\omega_{\mathbf{q}} b_{\mathbf{q}}^+ b_{\mathbf{q}}, \quad (5)$$
$$\hat{V} = \sum_{\alpha\beta\mathbf{q}} C_{\mathbf{q}} V_{\alpha\beta}(\mathbf{q})(b_{\mathbf{q}} + b_{-\mathbf{q}}^+) a_\alpha^+ a_\beta.$$

Here, $b_{\mathbf{q}}^+(b_{\mathbf{q}})$ are the operators of creation (annihilation) of phonons with energy $\hbar\omega_{\mathbf{q}}$ and the wave vector $\mathbf{q}$, $C_{\mathbf{q}}$ is the coefficient function of the electron–phonon coupling, and $V_{\alpha\beta}(\mathbf{q}) = \langle\alpha|e^{i\mathbf{qr}}|\beta\rangle$ is the matrix element of $e^{i\mathbf{qr}}$ in the wave functions of the band electrons in a parabolic QW in a magnetic field,

$$E_\alpha = \frac{\hbar^2 k_x^2}{2m} + \frac{\hbar^2 k_y^2}{2m}\left(\frac{\omega}{\omega_0}\right)^2 + \hbar\omega_0\left(n + \frac{1}{2}\right). \quad (6)$$

According to (2), $a_\alpha^+(t)$ satisfy the following equation of motion:

$$\dot{a}_\alpha^+(t) = \frac{i}{\hbar}\left\{E_\alpha a_\alpha^+(t) + \sum_{\beta\mathbf{q}} C_{\mathbf{q}} V_{\beta\alpha}(\mathbf{q}) a_\beta^+(t)[b_{\mathbf{q}} e^{-i\omega_{\mathbf{q}}t} + b_{-\mathbf{q}}^+ e^{i\omega_{\mathbf{q}}t}]\right\}. \quad (7)$$

When writing Eq. (7), we ignored the effect of electrons on the phonon spectrum [10]; i.e.,

$$b_{\mathbf{q}}(t) + b_{-\mathbf{q}}^+(t) \approx b_{\mathbf{q}} e^{-i\omega_{\mathbf{q}}t} + b_{-\mathbf{q}}^+ e^{i\omega_{\mathbf{q}}t}.$$

In this natural approximation, the solution to Eq. (7) has the following form [11]:

$$a_\alpha^+(t) = \exp\left(i\frac{E_\alpha}{\hbar}t\right)\sum_\beta a_\beta^+ \times\left\langle\beta\left|\exp\left(i\frac{t}{\hbar}(\tilde{H}_0 + \tilde{V})\right)\exp\left(-i\frac{t}{\hbar}\tilde{H}_0\right)\right|\alpha\right\rangle. \quad (8)$$

Here,

$$\tilde{H}_0 = \hat{H}_e + \sum_{\mathbf{q}} \hbar\omega_{\mathbf{q}} b_{\mathbf{q}}^+ b_{\mathbf{q}}, \quad \tilde{V} = \sum_{\mathbf{q}} C_{\mathbf{q}} e^{i\mathbf{qr}}(b_{\mathbf{q}} + b_{-\mathbf{q}}^+),$$

where $\hat{H}_e$ is the Hamiltonian for free charge carriers in the coordinate representation ($\hat{H}_e\Psi_\alpha = E_\alpha\Psi_\alpha$).

Similarly, we can derive an expression for $a_\beta(t)$. After substitution of $a_\alpha^+(t)$ and $a_\beta(t)$ into (1), the electrical-conductivity tensor can be expressed as

$$\sigma_{ij} = \frac{\beta_0 e^2}{2Vm^2}\sum_{\alpha\beta\gamma\alpha_1\beta_1\gamma_1} p_{\alpha\beta}^{(i)} p_{\alpha_1\beta_1}^{(j)} \times\int_{-\infty}^{\infty} dt\left\{\left\langle\gamma\left|\exp\left(i\frac{t}{\hbar}(\tilde{H}_0 + \tilde{V})\right)\right|\alpha\right\rangle \times\left\langle\beta\left|\exp\left(-i\frac{t}{\hbar}(\tilde{H}_0 + \tilde{V})\right)\right|\gamma_1\right\rangle\right\}_0 \langle a_\gamma^+ a_{\gamma_1} a_{\alpha_1}^+ a_{\beta_1}\rangle_0. \quad (9)$$

When deriving (9), we ignored the polaronic effect. This means that the operations of averaging over the electron subsystem $\langle\ldots\rangle_0$ and the phonon subsystem $\{\ldots\}_0$ are performed independently.

In the lowest approximations with respect to the electron concentration n_e, which is valid for a nondegenerate electron gas, we have

$$\langle a_\gamma^+ a_{\gamma_1} a_{\alpha_1}^+ a_{\beta_1}\rangle_0 \approx n_\gamma^0 \delta_{\gamma\beta_1}\delta_{\gamma_1\alpha_1}, \quad (10)$$

where n_γ^0 is the equilibrium distribution function for the band charge carriers in a parabolic QW with width a_0 in a transverse magnetic field; i.e.,

$$n_\gamma^0 = \frac{2\pi\beta_0\hbar^2 a_0\omega}{m\omega_0} n_e \sinh\left(\frac{\beta_0\hbar\omega_0}{2}\right)\exp(-\beta_0 E_\alpha). \quad (11)$$

We perform averaging over a system of a free phonon field using the cumulant averaging procedure [12] and restricting ourselves to the lowest approximation. If, for simplicity, we consider only the diagonal matrix elements of the momentum operator (4), the sought-for expression for the conductivity tensor (1) for a nondegenerate electron gas can be rewritten as

$$\sigma_{ij} = \frac{\beta_0 e^2}{2Vm^2}\sum_\alpha p_{\alpha\alpha}^{(i)} p_{\alpha\alpha}^{(j)} n_\alpha^0 \int_{-\infty}^{\infty} dt \exp\{g_{\alpha\alpha}(t)\}. \quad (12)$$

Here,

$$g_{\alpha\alpha}(t) = -\frac{2}{\hbar^2}\int_0^t dt_1 \int_0^{t_1} dt_2 \sum_{\gamma\mathbf{q}} |C_{\mathbf{q}}|^2 |V_{\alpha\gamma}(\mathbf{q})|^2 \times\exp\left(i\frac{t_2}{\hbar}(E_\alpha - E_\gamma)\right)[(N_{\mathbf{q}} + 1)e^{-i\omega_{\mathbf{q}}t_2} + N_{\mathbf{q}} e^{i\omega_{\mathbf{q}}t_2}], \quad (13)$$

where $N_{\mathbf{q}} = [e^{\beta_0\hbar\omega_{\mathbf{q}}} - 1]^{-1}$ is the distribution function for nonequilibrium phonons.

Integration with respect to t_1 and t_2 in (13) is performed easily. If we take into account that

$$\left.\frac{1-e^{i\alpha t}}{\alpha^2}\right|_{t\to\infty} = \pi|t|\delta(\alpha),$$

we obtain

$$g_{\alpha\alpha}(t) = -\frac{2\pi|t|}{\hbar}\sum_{\gamma\mathbf{q}}|C_{\mathbf{q}}|^2|V_{\alpha\gamma}(\mathbf{q})|^2\{(N_{\mathbf{q}}+1) \times \delta(E_\alpha - E_\gamma - \hbar\omega_{\mathbf{q}}) + N_{\mathbf{q}}\delta(E_\alpha - E_\gamma + \hbar\omega_{\mathbf{q}})\} \equiv -\frac{|t|}{\tau_\alpha}, \quad (14)$$

where τ_α corresponds to the relaxation time related to scattering by the lattice vibrations.

In view of (14), expression (12) can be rewritten as

$$\sigma_{ij} = \frac{\beta_0 e^2}{Vm^2}\sum_\alpha p^{(i)}_{\alpha\alpha}p^{(j)}_{\alpha\alpha}n^0_\alpha\tau_\alpha. \quad (15)$$

3. We now calculate the electrical conductivity in a parabolic QW for the situation where acoustic (long-wavelength) vibrations are involved in the process of scattering; we have

$$|C_{\mathbf{q}}|^2 = \frac{E_1^2\hbar q}{2B\rho v}. \quad (16)$$

Here, E_1 is the deformation-potential constant, ρ is the quantum-system density, and v is the velocity of sound in the material. If electrons are scattered elastically [i.e., if we ignore the electron energy $\hbar\omega\mathbf{q} = \hbar vq$ in the delta functions in (14)] and if we are concerned with high temperatures, we obtain

$$N_{\mathbf{q}} \approx \frac{k_0T}{\hbar vq} \gg 1 \quad \text{and} \quad \left(\frac{\omega_c}{\omega}\right)^2\frac{k_0T}{\hbar\omega_0} \ll 1$$

(the charge carriers are at the bottom of the lowest dimensionally quantized band; i.e., we have $n = 0$). It is then easy to obtain

$$\frac{1}{\tau_\alpha} = \frac{1}{\tau} = \sqrt{\frac{\lambda}{2\pi}}\frac{E_1^2mk_0T\omega_0}{\hbar^3v^2\rho\omega}. \quad (17)$$

Correspondingly, according to (15),

$$\sigma_{xx}(H) = \frac{e^2n_e}{m}\tau, \qquad \sigma_{xx}(H) \propto T^{-1}(\omega \gg \omega_c), \qquad \sigma_{xx}(H) \propto T^{-1}H^{-3/2}(\omega_c \gg \omega). \quad (18)$$

In the absence of a magnetic field ($\omega_c = 0$), we use formulas (17) and (15) to derive the following expression for electrical conductivity in a parabolic QW:

$$\sigma_{xx}(0) = \frac{e^2n_e}{m}\tau(0), \quad \frac{1}{\tau(0)} = \frac{E_1^2mk_0T}{\hbar^3v^2\rho}\sqrt{\frac{m\omega}{2\pi\hbar}}. \quad (19)$$

Consequently,

$$\sigma_{xx}(H) = \sigma_{xx}(0)(\omega/\omega_0)^{3/2}. \quad (20)$$

Since $(\omega/\omega_0)^{3/2} < 1$, the electrical conductivity decreases in the presence of a magnetic field. This is caused by the fact that the charge carriers are localized in the QW to a larger extent in a magnetic field; as a result, the scattering of charge carriers by phonons is predominant. An effective intensification of electron scattering with increasing magnetic field in the ultraquantum limit was reported by Peters *et al.* [13]. A decrease in electrical conductivity with increasing temperature [as follows from (19)] was experimentally observed in GaAs–GaAlAs heterostructures [14].

We can similarly calculate the transverse electrical conductivity (the electric field is perpendicular to the magnetic field); this conductivity is given by the first term in (4); i.e.,

$$\sigma_{yy}(H) = \sigma_{xx}(0)(\omega/\omega_0)^{7/2}. \quad (21)$$

Since $(\omega/\omega_0)^{7/2} < 1$, the transverse electrical conductivity is always lower than the longitudinal one. This is related to the fact that, according to the dispersion law (6), the effective electron mass m along the k_x direction is smaller than the effective mass m^* along the k_y axis [$m^* = m(\omega_0/\omega)^2$].

It is easy to show that the contribution of the second term in (4) to the transverse electrical conductivity (21) is insignificant if $\tau\omega_C \gg 1$.

Using realistic parameters of a GaAs/$Ga_{1-x}Al_xAs$ parabolic QW, i.e., $m = 0.06m_0$, $\rho = 5.4$ g/cm^3, $v = 3\times10^5$ cm/s, and $E_1 = 7$ eV for $a_0 = 10^3$ Å, $T = 100$ K, and $\omega = \omega_c$, we obtain $\tau\omega_c \approx 10^2$. Consequently, the transverse electrical conductivity is always much higher in quasi-2D systems than in bulk semiconductor materials.

We now study the behavior of the conductivity tensor in relation to temperature and magnetic field in the situation where an electron interacts with optical phonons. We have

$$|C_{\mathbf{q}}|^2 = \frac{2\pi e^2\hbar\tilde{\omega}c_0}{q^2}; \quad c_0 = \frac{1}{\varepsilon_\infty} - \frac{1}{\varepsilon_0},$$

where ε_0 and ε_∞ are the low- and high-frequency dielectric constants, respectively; and $\hbar\tilde{\omega}$ is the highest frequency of the optical phonon. At low temperatures ($\hbar\tilde{\omega} \gg k_0T$), in which case electrons are located at the

bottom of the quantum-dimensional band ($n = 0$), we obtain the following expression if $\delta_0 = \dfrac{\hbar\tilde{\omega} - n_1\hbar\omega_0}{\hbar\omega_0} \ll 1$ (in the resonance approximation):

$$\frac{1}{\tau^{(\mathrm{opt})}} = \frac{2me^2\tilde{\omega}c_0N_0}{\hbar^2}\sqrt{\frac{\pi}{2\lambda}}\frac{\omega}{\omega_0}\frac{(2n_1-3)!!}{n_1!2^{n_1}}. \qquad (22)$$

Consequently, the conductivity tensor does not feature any singularities in the resonance approximation if the interaction of electrons with optical phonons is taken into account; these singularities do arise in a three-dimensional semiconductor material [15]. We now calculate the longitudinal electrical conductivity in a parabolic QW for a degenerate electron gas. According to the Wick theorem, the correlation function given by (10) can be represented as

$$\begin{aligned}&\langle a_\gamma^+ a_{\gamma_1} a_{\alpha_1}^+ a_{\beta_1}\rangle_0 \\ &= n_\gamma^0(1-n_{\gamma_1}^{(0)})\delta_{\gamma\beta_1}\delta_{\gamma_1\alpha_1} + n_\gamma^{(0)}n_{\alpha_1}^{(0)}\delta_{\gamma\gamma_1}\delta_{\alpha_1\beta_1},\end{aligned} \qquad (23)$$

where $n_\gamma^{(0)}$ is the equilibrium distribution function for electrons,

$$n_\gamma^{(0)} = [e^{\beta_0(E_\gamma-\xi)}+1]^{-1}.$$

For a degenerate electron gas (the chemical potential $\xi > 0$), in which case the charge carriers reside in the lowest quantum-dimensional band (the ultraquantum limit), we can easily find that

$$\xi_0 = \frac{1}{\beta_0}\ln[e^{n_0}-1]. \qquad (24)$$

Here, $\xi_0 = \xi - \hbar\omega_0/2$ is the chemical potential measured from the bottom of the lowest band; and

$$n_0 = \frac{\pi\hbar^2\tilde{n}_e^{(0)}\beta_0\omega}{m\omega_0},$$

where $\tilde{n}_e^{(0)}$ is the surface density of the electron gas. For $n_0 \gg 1$, we have

$$\xi_0 = \frac{n_0}{\beta_0} = \frac{\pi\hbar^2\tilde{n}_e^{(0)}\omega}{m\omega_0}. \qquad (25)$$

Let us calculate the electrical conductivity σ_{xx} taking into account the first term in (23). It is easy to verify that the second term does not contribute to the longitudinal electrical conductivity; thus,

$$\sigma_{xx}^{(\mathrm{deg})} = \frac{\beta_0e^2\hbar^2}{2Vm}\sum_\alpha k_x^2 n_\alpha^{(0)}(1-n_\alpha^{(0)})\tau_\alpha. \qquad (26)$$

In further calculations, we use the approximate equality

$$n_\alpha^{(0)}(1-n_\alpha^{(0)}) \approx \delta\{\beta_0(E_\alpha-\xi)\},$$

which is certainly valid for a degenerate electron gas at low temperatures. As a result, we obtain

$$\sigma_{xx}^{(\mathrm{deg})} = \frac{e^2\tau\omega_0n_0}{\pi a\beta_0\hbar^2\omega}. \qquad (27)$$

If there is no magnetic field ($\omega_c = 0$, $\omega_0 = \omega$), we can use formula (27) to derive the following expression for electrical conductivity in a parabolic QW in the case of a degenerate electron gas:

$$\begin{aligned}\tilde{\sigma}_{xx}(0) &= \frac{e^2\tau^{(0)}\tilde{n}_0}{\pi a\beta_0\hbar^2}, \\ \tilde{n}_0 &= \frac{\pi\hbar^2\tilde{n}_e^{(0)}\beta_0}{m}.\end{aligned} \qquad (28)$$

Consequently, for an equal concentration of charge carriers, we have

$$\frac{\sigma_{xx}^{(\mathrm{deg})}}{\tilde{\sigma}_{xx}(0)} = \left(\frac{\omega}{\omega_0}\right)^{3/2}. \qquad (29)$$

Since $\omega_0 > \omega$, the electrical conductivity in a magnetic field is always lower than in the absence of this field.

As directly follows from formula (27), we have $\sigma_{xx}^{(\mathrm{deg})} \propto \omega/\omega_0$ in the quantum limit; i.e., the specific magnetoresistance increases with increasing magnetic field. Such behavior of the resistivity in a magnetic field for quantum-confined GaAs/Al_xGa_{1-x}As systems was observed experimentally [16] at a low temperature (T = 1.3 K).

Using formula (15), one can easily derive an expression for the longitudinal electrical conductivity $\sigma_{xx}^{(0)}(H)$ in a bulk material in a magnetic field [15]. In the quantum limit ($\beta\hbar\omega_c > 1$), we have

$$\frac{\sigma_{xx}^{(0)}(0)}{\sigma_{xx}^{(0)}(H)} = \frac{2}{3}\beta\hbar\omega_c, \qquad (30)$$

where $\sigma_{xx}^{(0)}(0)$ is the conductivity tensor for a bulk semiconductor material in the absence of a magnetic field [17].

It directly follows from expressions (30), (18), and (19) that

$$\begin{aligned}&\sigma_{xx}^{(0)}(0) > \sigma_{xx}(0) > \sigma_{xx}^{(0)}(H) > \sigma_{xx}(H) \\ &\qquad (\text{for } \beta\hbar\omega_x > 8\sqrt{2}).\end{aligned} \qquad (31)$$

Consequently, a decrease in the "dimensionality" of a quantum system, i.e., an increase in the degree of localization of charge carriers in the bands, brings about a decrease in the longitudinal electrical conductivity.

REFERENCES

1. D. G. Cantrell and P. N. Butcher, J. Phys. C **18**, L587 (1985).
2. B. E. Sernelius, K.-F. Berggren, M. Tamak, and C. Mc. Fadden, J. Phys. C **18**, 225 (1985).
3. D. G. Cantrell and P. N. Butcher, J. Phys. C **18**, 5111 (1985).
4. Hui Tang and P. N. Butcher, J. Phys. C **21**, 3313 (1988).
5. E. Yu. Safronov and E. P. Sinyavskii, Phys. Status Solidi B **180**, 377 (1993).
6. V. A. Geĭler, V. A. Margulis, and L. I. Filina, Zh. Éksp. Teor. Fiz. **113**, 1376 (1998) [JETP **86**, 751 (1998)].
7. R. Kubo, J. Phys. Soc. Jpn. **12**, 570 (1957).
8. B. A. Tavger and M. Sh. Erukhimov, Zh. Éksp. Teor. Fiz. **51**, 528 (1966) [Sov. Phys. JETP **24**, 354 (1967)].
9. E. P. Sinyavskii, S. M. Sokovnich, and F. I. Pasechnik, Phys. Status Solidi B **209**, 55 (1998).
10. É. P. Sinyavskiĭ and E. I. Grebenshchikova, Zh. Éksp. Teor. Fiz. **116**, 2069 (1999) [JETP **89**, 1120 (1999)].
11. É. P. Sinyavskiĭ and E. I. Grebenshchikova, Zh. Éksp. Teor. Fiz. **119** (3), 527 (2001) [JETP **92**, 493 (2001)].
12. R. Kubo, J. Phys. Soc. Jpn. **17**, 1100 (1962).
13. P. J. Peters, P. Schehzger, M. J. Lea, *et al.*, Phys. Rev. B **50**, 11570 (1994).
14. X. L. Lei, J. Phys. C **18**, L993 (1985).
15. B. M. Askerov, *Kinetic Effects in Semiconductors* (Nauka, Leningrad, 1970), p. 303.
16. M. Shayegan, T. Sajoto, M. Santos, and C. Silvestre, Appl. Phys. Lett. **53**, 791 (1988).
17. A. I. Anselm, *Introduction to Semiconductor Theory* (Nauka, Moscow, 1978; Prentice-Hall, Englewood Cliffs, 1981).

Translated by A. Spitsyn

Semiconductors, Vol. 36, No. 8, 2002, pp. 929–931. Translated from Fizika i Tekhnika Poluprovodnikov, Vol. 36, No. 8, 2002, pp. 993–995.

LOW-DIMENSIONAL SYSTEMS

Manifestation of *A*(+) Centers in the Luminescence of Two-Dimensional GaAs/AlGaAs Structures

Yu. L. Ivanov, N. V. Agrinskaya, P. V. Petrov, V. M. Ustinov, and G. É. Tsyrlin

Ioffe Physicotechnical Institute, Russian Academy of Sciences, ul. Politekhnicheskaya 26, St. Petersburg, 194021 Russia

Submitted January 31, 2002; accepted for publication January 31, 2002

Abstract—Photoluminescence of GaAs/AlGaAs multiple-quantum-well structures incorporating positively charged beryllium-impurity shallow-level acceptors (the so-called *A*(+) centers) was investigated. A novel luminescence line, which originated from radiative recombination of free electrons with *A*(+) centers, was observed. It was shown that its spectral position is determined uniquely by the binding energy of *A*(+) centers. It was also ascertained that the binding energy of *A*(+) centers increases with a decrease in the quantum-well width when the latter is comparable to the radius of *A*(+) centers. © *2002 MAIK "Nauka/Interperiodica".*

1. INTRODUCTION

It is well known by now that, at low temperatures, neutral donor and acceptor impurities can capture, respectively, an electron or a hole to form charged centers referred to as *D*(–) and *A*(+) centers. In a bulk material like GaAs, their binding energy amounts to a fraction of a millielectronvolt; however, in two-dimensional (2D) structures it increases considerably as compared to the three-dimensional case, which makes these centers easier to study. In addition, a stationary population of *D*(–) and *A*(+) centers can readily be obtained in 2D structures using so-called dual selective doping (simultaneous doping of the quantum wells (QWs) and the barriers) [1]. Investigation of negatively charged shallow-level donors (*D*(–) centers) was the subject of quite a number of publications (see, e.g., [2, 3]). At the same time, studies of similar states of shallow-level acceptors (*A*(+) centers) are limited to just several theoretical papers [4]. Recently, we experimentally observed *A*(+) centers in 15-nm-wide GaAs/AlGaAs QWs and carried out preliminary investigations of their properties. The energy and the Bohr radius of *A*(+) centers were determined from measurements of the Hall effect [5] and low-temperature hopping transport via *A*(+) bands [6].

Significant additional information about the nature of *A*(+) centers can be provided by the analysis of their luminescence properties. In this paper, we report on the studies of photoluminescence (PL) spectra of *p*-type GaAs/AlGaAs QWs incorporating *A*(+) centers, which were obtained by dual selective doping with a Be shallow-level acceptor impurity.

2. EXPERIMENT

The GaAs/$Al_{0.3}Ga_{0.7}As$ multiple-QW structures under study were grown by molecular-beam epitaxy. The luminescence spectra of the structures with a well width of 15 nm and those with a well width of 9 nm were compared. In both cases, two types of selectively doped structures were investigated: doping was introduced either in the QWs only (then, the wells incorporate *A*(0) centers) or both in the QWs and in the barriers (then, the wells incorporate *A*(+) centers). All structures contained ten QWs separated from each other by 20-nm-wide $Al_{0.3}Ga_{0.7}As$ barriers; the QWs were spaced from the substrate by a 100-nm-wide $Al_{0.3}Ga_{0.7}As$ layer and from the surface by a 200-nm-wide $Al_{0.3}Ga_{0.7}As$ layer (to prevent the effect of the surface field on the energy band structure of the wells). A 5-nm-wide layer at the center of each QW (or at each QW and each barrier) was doped with shallow-level Be impurity to a density of $(3–5) \times 10^{17}$ cm^{-3}. The impurity density was chosen to be, on the one hand, lower than the critical density for the insulator–metal transition but, on the other hand, sufficiently high to observe the impurity luminescence. The PL was excited by an LGN-215 He–Ne laser; the sample was exposed to the laser beam and the luminescence was collected through a glass optical fiber. The maximum power density on the sample at the output of the fiber was 10 mW/mm^2. The PL was detected by a cooled FEU-62 photomultiplier operating in the photon-counting mode. Measurements were performed with the sample under study immersed in liquid helium.

A typical PL spectrum of a structure with a well width of 15 nm is shown in Fig. 1. Curve *1* represents the spectrum of a structure with *A*(0) centers. Four lines can be seen. The one at 1.5352 eV corresponds to the free exciton; it is observed only under the highest pump level attainable in these experiments, which is due to the quadratic dependence of its intensity on the pump. Taking into account the QW width, the position of this line agrees with the published data [7] and the binding energy is 7.6 meV. The line at 1.5287 eV corresponds

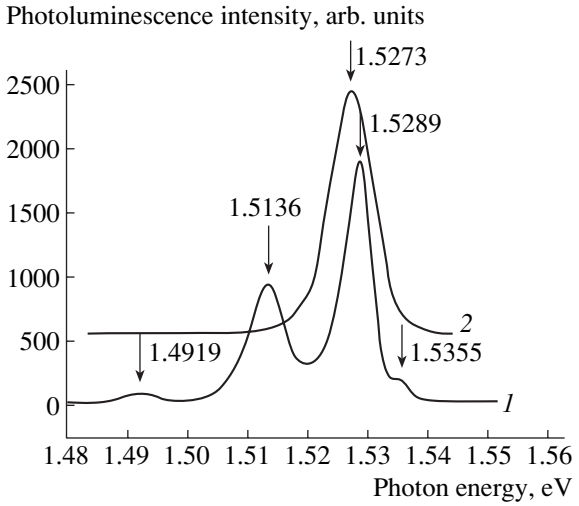

Fig. 1. Photoluminescence of the structures with 15-nm-wide quantum wells.

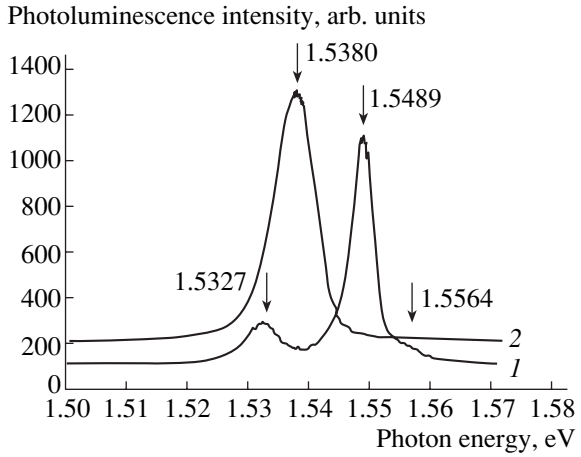

Fig. 2. Photoluminescence of the structures with 9-nm-wide quantum wells.

to an impurity-bound exciton with a binding energy of 9 meV. Its intensity depends linearly on the pump, which is expected for the bound state. The line at 1.5136 eV originates from radiative recombination via impurities. It is shifted to lower energies by ~ 14 meV from the bound-exciton line and by ~ 21 meV from the free-exciton line. Its intensity depends sublinearly on the pump. Its energy position is determined by the binding energy of the $A(0)$ center; the latter amounts to ~ 30 meV, which is in agreement with the published data [8]. The line at 1.4919 eV, which is present in all spectra, corresponds to the PL of the bulk GaAs substrate material. Curve *2* in Fig. 1 represents the spectrum of a structure with $A(+)$ centers. A characteristic feature of this spectrum is the absence of the conventional impurity line. The free- and bound-exciton lines are hardly observed; the main peak at 1.5278 eV is ~ 1 meV lower in energy than the bound-exciton peak.

A typical PL spectrum of a structure with a well width of 9 nm is shown in Fig. 2. Here, curve *1* also represents the spectrum of a structure with $A(0)$ centers, and the spectrum of a structure with $A(+)$ centers is given by curve *2*. In spectrum *1*, the free-exciton peak is fairly weakly exhibited; actually, one observes only the bound-exciton line and, nearly 16 meV lower in energy, the line of impurity-mediated radiative recombination. Just as in Fig. 1, the impurity line seen in spectrum *1* is not observed in spectrum *2*. Also, similarly to Fig. 1, spectrum *2* has only one peak; however, in contrast to the case of 15-nm QWs, the spacing between this peak and the bound-exciton peak is 11 meV; i.e., it becomes 10 meV greater.

3. DISCUSSION

The absence of the usual impurity PL peak in the spectra of the structures with $A(+)$ centers is explained by the absence of impurities in the neutral state. In other words, the $A(+)$ center represents a common multicharge center, similar to compensated Cu in germanium [9]. Under nearly equilibrium conditions, only the upper level of this center is important for its optical properties. In the case of $A(+)$ centers in 15-nm QWs, this level is spaced by 7–8 meV from the valence-band edge, which we established previously from the Hall-effect measurements [5]. Thus, the ground impurity level, spaced from the valence-band edge by 30 meV, cannot be seen; more exactly, it arises only under sufficiently high excitation levels, when $A(+)$ centers capture nonequilibrium electrons. However, there is uncertainty in the nature of the peak related to $A(+)$ centers: it can originate from radiative recombination through $A(+)$ centers or be related to excitons bound to $A(+)$ centers.

As was mentioned above (and demonstrated in [5]), due to the confinement, the binding energy of $A(+)$ centers in the QWs is higher than that in the bulk and is anticipated to increase with a decrease in the well width in a certain range. One can expect that the binding energy in 9-nm-wide QWs will be higher than that in 15-nm-wide QWs. In fact, we do find that the peak related to $A(+)$ centers is spaced from the bound-exciton peak by 1 meV in the structures with 15-nm QWs and by 11 meV in the structures with 9-nm QWs, the shift in the peak position in the two structures thus being equal to 10 meV. It is reasonable to assume that the PL peak in the structures with $A(+)$ centers originates from the radiative recombination via this center. Then, the optical binding energy of $A(+)$ centers can be determined from the peak position. This assumption is corroborated by the data presented in the table, where the positions of all peaks in the structures with 15-nm and 9-nm QWs are listed. For each peak, the shift in its position resulting from an increase in the band gap with

Table

Well width, nm; peak energy shift, eV	9	15	Δε
Energy of the free-exciton peak ε, eV	1.5564	1.5355	0.0209
Energy of the bound-exciton peak ε, eV	1.5489	1.5289	0.0200
Energy of the impurity-mediated radiative recombination peak ε, eV	1.5327	1.5136	0.0191
Energy of the *A*(+)-center-mediated radiative recombination peak ε, eV	1.5380	1.5273	0.0107

decreasing well width is given in the fourth column. The energy difference for the free-exciton peak is the largest, while that for the bound-exciton and impurity-transition peaks is somewhat smaller. This can be attributed to the more pronounced increase in the binding energy of impurity states in comparison to the exciton states. Indeed, according to the published data, the free-exciton binding energy increases by 0.8 meV with a decrease in the QW width from 15 to 9 nm [10], whereas the Be-impurity binding energy increases by about 2 meV [8]. At the same time, the shift of the free- and bound-exciton peaks and the impurity peak is, on the average, two times larger than the shift of the *A*(+)-center peak. If the above assumption, which assigns this peak to radiative recombination of electrons at *A*(+) centers, is correct, this means that the *A*(+)-center level becomes deeper in 9-nm QWs. The Hall-effect measurements carried out previously did indicate that the *A*(+)-center binding energy increases to 14 meV in 9-nm-wide QWs in comparison to 7 meV in 15-nm-wide QWs. It should be noted that the binding energies obtained from the Hall-effect measurements may differ from their true values by $1/2W$ (where W is the impurity-band width) [5]. Taking this into account, we conclude that there is rather good agreement between the values of the shift in the *A*(+)-center energy position determined from luminescence and thermal measurements.

These experimental results indicate that the PL peak related to *A*(+) centers does originate from the radiative recombination of electrons with these centers.

4. CONCLUSION

Thus, in this study we observed a new luminescence line originating from the radiative transitions of electrons to *A*(+) centers. Its energy position is determined uniquely by the energy position of the *A*(+) center and depends heavily on the QW width when the latter is comparable to the hole localization radius at *A*(+) centers.

ACKNOWLEDGMENTS

This study was supported by the Russian Foundation for Basic Research (project no. 01-02-17917) and the program "Physics of Solid-State Nanostructures" ("Optical and Nonlinar-Optical Properties of Nanostructures").

REFERENCES

1. S. Huant, S. P. Najda, and B. Etienne, Phys. Rev. Lett. **65**, 1486 (1990).
2. S. Huant, A. Mandray, J. Zhu, *et al.*, Phys. Rev. B **48**, 2370 (1993).
3. D. Mikhailov, F. J. Betancur, J. H. Marin, and L. E. Oliveira, Phys. Status Solidi B **210**, 605 (1998).
4. I. N. Yassievich, K. Schmalz, M. A. Odnobludov, and M. S. Kagan, Solid-State Electron. **40**, 97 (1996).
5. N. V. Agrinskaya, Yu. L. Ivanov, V. M. Ustinov, and D. V. Poloskin, Fiz. Tekh. Poluprovodn. (St. Petersburg) **35**, 571 (2001) [Semiconductors **35**, 550 (2001)].
6. N. V. Agrinskaya, Yu. L. Ivanov, V. M. Ustinov, *et al.*, Zh. Éksp. Teor. Fiz. **120**, 480 (2001) [JETP **93**, 424 (2001)].
7. A. C. Ferreira, P. O. Holtz, B. E. Sernelius, *et al.*, Phys. Rev. B **54**, 16989 (1996).
8. W. T. Masselink, Yia-Chung Chang, and H. Morkoc, Phys. Rev. B **32**, 5190 (1985).
9. Yu. L. Ivanov and S. M. Ryvkin, Fiz. Tverd. Tela (Leningrad) **4**, 1482 (1962) [Sov. Phys. Solid State **4**, 1089 (1963)].
10. Y. Fu and R. A. Chao, Phys. Rev. B **43**, 12626 (1991).

Translated by M. Skorikov

Semiconductors, Vol. 36, No. 8, 2002, pp. 932–935. Translated from Fizika i Tekhnika Poluprovodnikov, Vol. 36, No. 8, 2002, pp. 996–1000.

LOW-DIMENSIONAL SYSTEMS

One-Dimensional Photonic Crystal Obtained by Vertical Anisotropic Etching of Silicon

V. A. Tolmachev*^, L. S. Granitsyna*, E. N. Vlasova, B. Z. Volchek**, A. V. Nashchekin*, A. D. Remenyuk*, and E. V. Astrova***

** Ioffe Physicotechnical Institute, Russian Academy of Sciences, St. Petersburg, 194021 Russia*
^e-mail: tva@pop.ioffe.rssi.ru
*** Institute of Macromolecular Compounds, Russian Academy of Sciences, St. Petersburg, 199004 Russia*
Submitted February 4, 2002; accepted for publication February 14, 2002

Abstract—The potentialities of vertical anisotropic etching of (110) silicon for the fabrication of one-dimensional photonic crystal with a high refractive index contrast have been studied. It is shown that advances toward the near-IR spectral range are limited by the mechanical strength of thin silicon walls. The device structures obtained consist of 50 trenches, 114 μm deep, with 1.8-μm-thick Si walls (structure period 8 μm). Their reflectance spectra in the wavelength range 2.5–16.5 μm show good agreement with calculation results, although the main photonic band gap at $\lambda \approx 28 \pm 10$ μm remained outside the spectral region of measurements. *© 2002 MAIK "Nauka/Interperiodica".*

Multilayer dielectric mirrors and Fabry–Perot resonators are well-known optical elements. Recently, these devices have aroused much interest in connection with studies in the field of photonic crystals [1]. One-dimensional (1D) photonic crystals can be obtained in the form of a structure containing alternating layers with high and low refractive indices, N_H and N_L, with the optimal optical thickness of each layer equal to $\lambda/4$, where λ is a prescribed wavelength. However, neither the conventional methods of thin layer deposition, nor the new technique, which creates layers of microporous Si with varied porosity by electrochemical etching [2, 3], can ensure high contrast in refractive indices, N_H/N_L, which is an essential characteristic of photonic crystals. High contrast enables reduction of the number of layers necessary for a wide band gap with sharp edges to be formed, and it is also advantageous in the production of composite materials, since introduction of a filler with $N > 1$ necessarily reduces the contrast.

The technology of etching vertical-wall trenches in single-crystal (110) Si has been developed quite some time ago [4], but it is not widely used in the production of optical elements, despite the possibility of fabricating periodic structures with high index ratio (N_H/N_L = 3.42) and mirror-smooth wall surfaces in the silicon transparency range ($\lambda > 1.1$ μm). The main problems are associated with the formation of short-period structures and the input of light into the lateral face of the structure. The goal of this study was to investigate the applicability of deep anisotropic etching of Si to the fabrication of 1D photonic crystals.

Anisotropic etching of (110) silicon wafers with 100-Ω-cm resistivity was performed in a 44% aqueous solution of KOH at 70°C for 1–4 h, depending on the needed depth. A 0.8- to 0.9-μm-thick layer of thermal oxide, in which the device pattern was formed by standard photolithography with positive photoresist, served as the etching mask. The photomask included three types of device structures consisting of 2-mm-long alternating bright and dark stripes of equal width. The periods of stripe alternation were different (see table),

Parameters of device structures

Device type	Period of structure, a, μm	Width of dark stripe on photomask, D_0, μm	Trench depth L, μm	Thickness of Si wall in device fabricated, D_H, μm
1	16	8	43	5.6
			114	5.3
			232	4.8
2	8	4	43	2.5
			114	1.8
			232	0
3	4	2	43	0.25
			114	0
			232	0

1063-7826/02/3608-0932$22.00

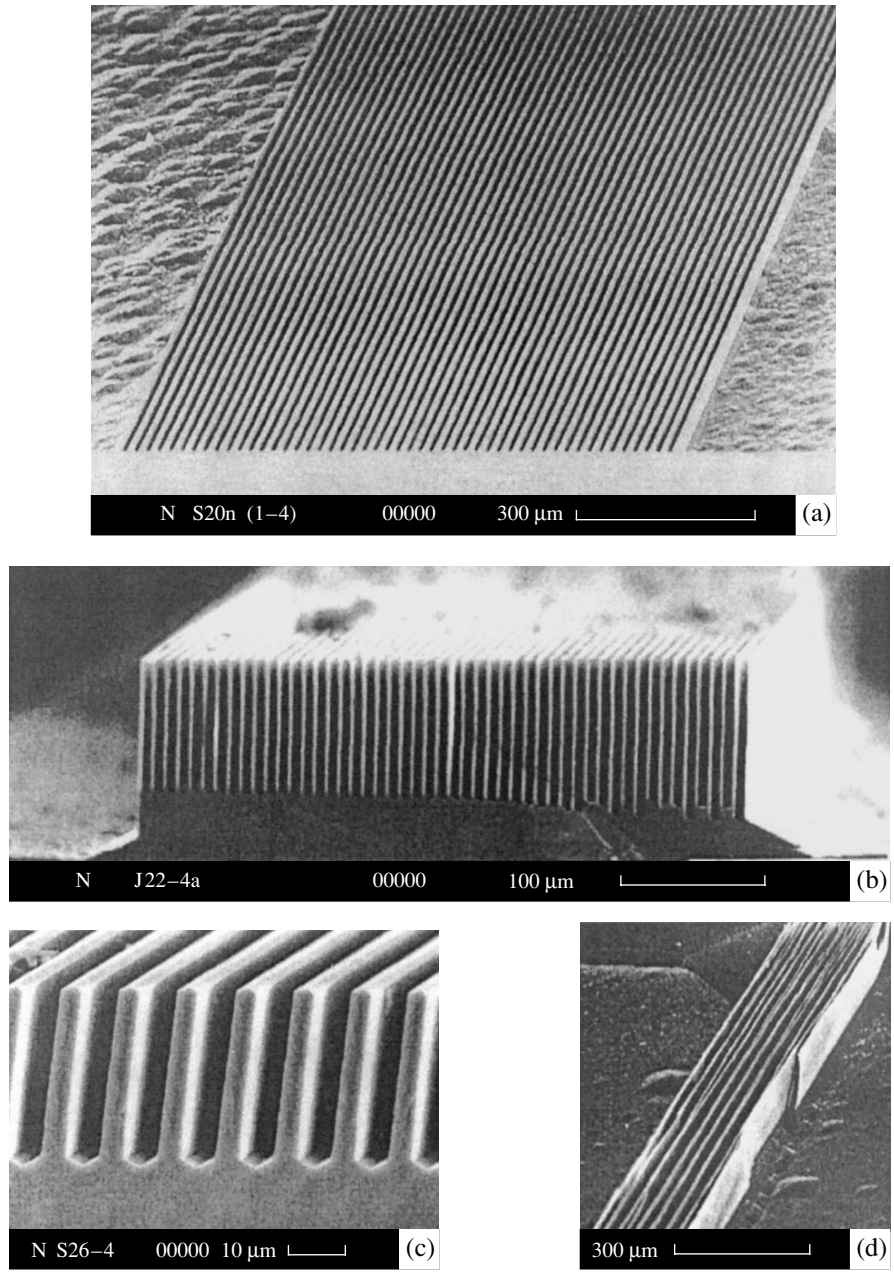

Fig. 1. SEM images of 1D photonic crystal structures: (a) plan view of a type-1 device structure with a period of 16 μm, (b) cross-sectional view of type-2 structure with a period of 8 μm and a trench depth of 114 μm, (c) cross-sectional view of the same kind of type-2 structure with a period of 8 μm and a trench depth of 28 μm, (d) type 3 structure with a period of 4 μm.

but the number of periods was 50 in each type of device. To ensure precise alignment of the stripes with the ⟨111⟩ direction in the wafer plane, we used preliminary deep etching of special alignment marks arranged at different angles to form a fan [5]. The width of dark stripes, D_0, varied between the different types of device structures, being equal to 8, 4, and 2 μm. Figure 1a shows a plan view of a type-1 device. The depth of trench etching and the thickness of silicon walls were measured by optical and scanning electron microscopy (SEM). Figures 1b and 1c present cross-sectional SEM images of type-2 structures of different depths. It is necessary to note that the fabrication of small-period structures is hindered by lateral etching ("undercutting") and by the mechanical strength of silicon walls. The walls are thinned both through undercutting of the photoresist in the buffer etchant at the window-opening stage in the oxide and because of a certain deviation from verticality during the deep etching of silicon. As a result, walls were retained only upon etching to a depth of <50 μm in type-3 devices, and to <150 μm in type-2 devices. This is seen in Fig. 2, which demonstrates how

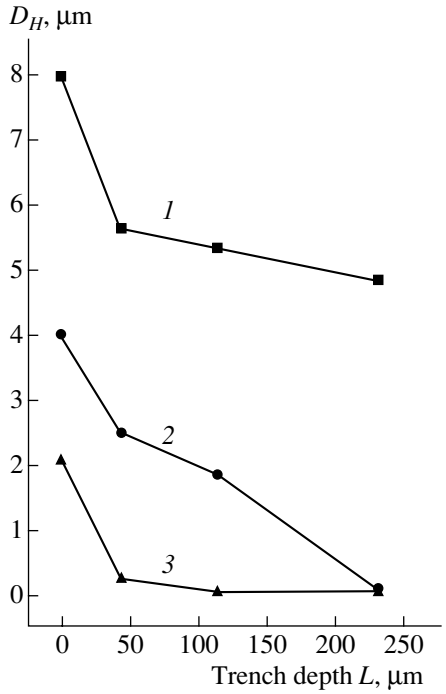

Fig. 2. Thickness of silicon walls, D_H, vs. depth L of anisotropic etching for device structures of different types. D_0: (*1*) 8, (*2*) 4, and (*3*) 2 μm.

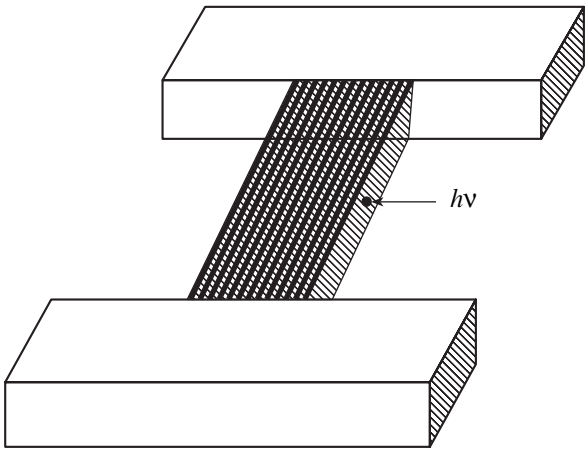

Fig. 3. Optical configuration used in studying a 1D photonic crystal.

the silicon wall thickness varies between devices with different initial widths D_0 of the dark stripe in the photomask. The silicon wall thicknesses D_H presented in the table and in Fig. 2, and used in calculations of the reflectance spectra, correspond to the thickness measured in the structure at a medium depth. In type-3 devices, which have the thinnest walls, we observed partial wall destruction and sag, which leads to the adhesion of adjacent planes (Fig. 1d).

The parameters Δ and ψ were measured on one of the side walls of the structure using multiple-angle-of-incidence ellipsometry on an LEF-3m ellipsometer (λ = 0.63 μm). The null method used in the recording allowed us to evaluate the degree of depolarization of the reflected beam. No depolarization was observed at any of the used angles of incidence (φ = 60–78°), which indicates high perfection of the surface of the vertical walls produced by anisotropic etching. The measured Δ and ψ values corresponded to the optical constants of Si.

The optical characteristics of 1D photonic crystals were studied with a Bruker Fourier spectrometer. The light beam was focused with a microscope onto a spot 60 μm in diameter and directed onto the lateral face of the device structure, as shown in Fig. 3. The reflectance spectra were recorded in the range λ = 2.5–16.5 μm. Of those fabricated, structures with $L > 100$ μm were suitable for these studies. Reproducible results with nearly optimal wall thicknesses were obtained for the structure with a period $a = 8$ μm and a trench depth of 114 μm (Fig. 1b).

The reflectance spectra of such a 1D photonic crystal were calculated using the method of characteristic matrices [6] for $N_H = 3.42$, $N_L = 1$, and the absorption coefficient $k = 0$ for both layers. The layer thicknesses used in the calculation, $D_H = 1.8$ μm and $D_L = 6.2$ μm, corresponded to the fabricated structure. Figure 4a presents a calculated reflectance spectrum with a clearly seen wide band of high reflectance at λ = 18–39 μm (main photonic band gap) and several narrower secondary bands near λ = 8 and 5 μm. Figure 4b shows a normalized experimental reflectance spectrum and a fragment of the calculated spectrum. Good coincidence between the calculated and experimental dependences is seen in the accessible spectral range, which suggests that the formulated problem has been resolved successfully.

In order to shift the main photonic band gap to the near-IR range, it is necessary to reduce the structure period. Among the untapped resources in this context are the reduction of the length of trenches, which would enhance their mechanical strength, and also the diminishing of the undercutting by using dry etching of the oxide mask. The micro-optical devices under development are well compatible with standard silicon technology, and they can be fabricated in the same chip with the electronic components of an integrated circuit. Moreover, *p–n* junctions can be formed directly in their single-crystal walls. In contrast to microporous silicon devices, they are not subject to aging. Therefore, the above-listed properties indicate that wet anisotropic etching is promising for the fabri-

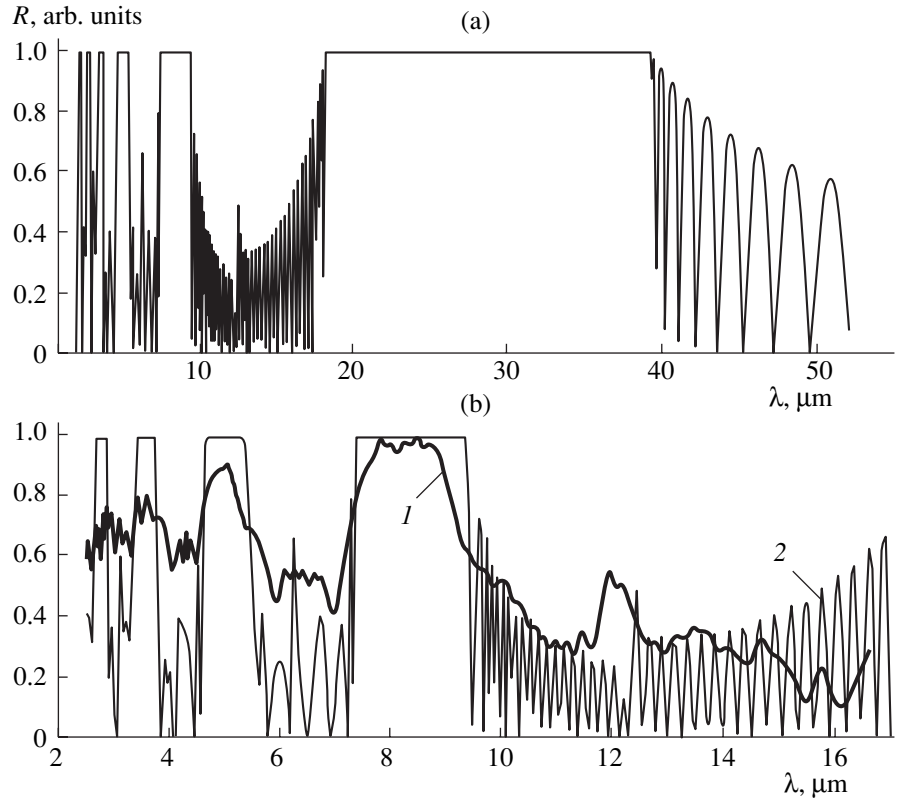

Fig. 4. Reflectance spectra of 1D photonic crystal with a period $a = 8$ μm and a Si wall thickness $D_H = 1.8$ μm: (a) overall calculated spectrum and (b) (*1*) experimental and (*2*) part of the calculated dependence.

cation of such micro-optical devices as filters, dielectric mirrors, waveguides, anti-reflection elements, resonators, etc.

ACKNOWLEDGMENTS

This study was supported by the Russian Foundation for Basic Research (project no. 00-15-96770), the St. Petersburg Scientific Center program "Low-Dimensional Quantum Structures," and the Ministry of Industry, Science, and Technology under the programs "Physics of Nanostructures" and "Design of Components of Communication Networks, Software, and Databases for Fundamental Science and Education."

REFERENCES

1. J. D. Joannopoulos, R. D. Meade, and R. D. Winn, *Photonic Crystals* (Princeton Univ. Press, Princeton, 1995).
2. M. G. Berger, M. Thonissen, R. Arens-Fisher, *et al.*, Thin Solid Films **255**, 313 (1995).
3. L. Pavesi and V. Mulloni, J. Lumin. **80**, 43 (1998).
4. D. L. Kendall, Annu. Rev. Mater. Sci. **9**, 373 (1979).
5. E. G. Guk, A. G. Tkachenko, N. A. Tokranova, *et al.*, Pis'ma Zh. Tekh. Fiz. **27** (9), 64 (2001) [Tech. Phys. Lett. **27**, 381 (2001)].
6. R. M. Azzam and N. M. Bashara, *Ellipsometry and Polarized Light* (North-Holland, Amsterdam, 1977; Mir, Moscow, 1981).

Translated by D. Mashovets

Semiconductors, Vol. 36, No. 8, 2002, pp. 936–940. Translated from Fizika i Tekhnika Poluprovodnikov, Vol. 36, No. 8, 2002, pp. 1001–1005.

AMORPHOUS, VITREOUS, AND POROUS SEMICONDUCTORS

Gamma-Irradiation-Induced Metastable States of Undoped Amorphous Hydrogenated Silicon

M. S. Ablova, G. S. Kulikov, and S. K. Persheev

Ioffe Physicotechnical Institute, Russian Academy of Sciences, Politekhnicheskaya ul. 26, St. Petersburg, 194021 Russia

Submitted February 4, 2002; accepted for publication February 5, 2002

Abstract—The conductivity of intrinsic amorphous hydrogenated silicon (*a*-Si:H) becomes higher upon gamma irradiation. This effect is due to an increase in the number of metastable D^+ states in the mobility gap. At the same time, the conductivity of extrinsic (undoped) irradiated *a*-Si:H decreases. Most likely, gamma irradiation creates hydrogen-containing complexes in this material. The results obtained are discussed in comparison with the known data for B- or P-doped *a*-Si:H. © *2002 MAIK "Nauka/Interperiodica".*

1. INTRODUCTION

To date, a great number of studies concerned with metastable defects in amorphous hydrogenated silicon (*a*-Si:H) have been published. This is associated with the important part played by defects of this kind in the material used to fabricate solar cells and other devices. It is for this reason that studies of the physical mechanism of defect formation in *a*-Si:H are still of much scientific interest. Among the external actions used to create metastable states in *a*-Si:H in scientific investigations are, mainly, exposure to visible light, which causes fatigue (Staebler–Wronski effect), as well as UV irradiation, bombardment with electrons and ions, and irradiation with X-rays and gamma rays. A relatively small number of studies have been concerned with gamma-ray-induced states in *a*-Si:H. This study attempts, to a certain extent, to fill this gap. In contrast to our preceding publication [1], which was devoted to the study of the influence exerted by gamma irradiation on the properties of doped *a*-Si:H [*a*-Si:(B,H) and *a*-Si:(P,H)], the present communication reports the results of similar investigations on undoped *a*-Si:H.

2. EXPERIMENTAL

The films to be studied were prepared by the decomposition of monosilane in high-frequency glow discharge and the deposition of *a*-Si:H onto a quartz substrate at 290–330°C. The content of hydrogen in the films was, according to IR spectral data, 10–12%. The film thickness was 0.2–0.5 μm. In accordance with currently accepted concepts (see, e.g., [2–4]), films of undoped hydrogenated amorphous silicon can be divided into two groups: those of intrinsic and undoped (extrinsic) *a*-Si:H. There is no clear distinction between their properties, and the existing difference is determined by the number N of defects formed in film deposition: $N \sim 10^{15}$–10^{16} cm^{-3} for the intrinsic, and $\sim 10^{17}$ cm^{-3} for the extrinsic (undoped) material. Selected basic properties of the samples studied in these two groups are presented in Table 1.

The temperature dependence of the dark conductivity of the samples, $\sigma_d = f(1/T)$, was studied in the temperature range 20–230°C. Measurements of each sample were taken before and after its exposure to gamma radiation. The type of conduction (*n* or *p*) was judged

Table 1. Basic parameters of films of intrinsic and undoped (extrinsic) amorphous hydrogenated silicon *a*-Si:H

Parameters	State of a sample			
	Intrinsic *a*-Si:H		Undoped (extrinsic) *a*-Si:H	
	before gamma irradiation	after gamma irradiation	before gamma irradiation	after gamma irradiation
σ_d^{300}, S/cm	1.0×10^{-11}	1.0×10^{-8}	5.0×10^{-7}	7.0×10^{-9}
E_A, eV	1.04	0.54	0.68	0.77; 1.5
T_E, °C*	208	208	162	156
Sign of charge carriers	weak *n*-type	*p*-type	*n*-type	

* Temperature of transition to thermodynamically equilibrium state [5, 6].

1063-7826/02/3608-0936$22.00 © 2002 MAIK "Nauka/Interperiodica"

from the room-temperature thermoelectric power. Irradiation with gamma quanta was performed in a reactor in air at room temperature under a flux $W = 7.7 \times 10^{11}$ photon cm^{-2} s^{-1} from a ^{60}Co source. It was found that heating a sample above 150°C compensates (totally or in part) for the changes caused by gamma irradiation; i.e., defects generated by gamma irradiation and those induced thermally are mutually exclusive. Therefore, for experimental results to be reliable, it was necessary to ensure continuous irradiation without intermediate heating. For this purpose, samples were prepared as follows: a 15 × 15-mm^2 *a*-Si:H film was cut in two and contacts were deposited onto each half. The dependences $\sigma_d = f(1/T)$ for such half-samples usually coincided. Then, both halves of a sample were placed in a reactor for irradiation. The irradiation doses were determined from the time of sample residence in the reactor. The first batch of film halves was removed from the reactor after exposure to a dose of 5.1×10^{17} photon cm^{-2}. The second batch of half-samples was left in the reactor until a dose of 1.43×10^{18} or 2.1×10^{18} photon cm^{-2} was given. Thus, both halves of each sample were subjected to different doses of continuous irradiation.

It was important to know the type of conduction of the material. However, determining the thermoelectric power by the standard procedure (temperature gradient ~20°, distance between probes ~0.5 mm) failed to ensure reliable quantitative measurements of this parameter. This is due to the low conductivity of the undoped material, which results from the low carrier mobility $\mu < 1$ cm^2 V^{-1} s^{-1}. We could only determine the type of conduction from the sign of the thermoelectric power.

3. RESULTS

Figure 1a presents $\sigma_d = f(1/T)$ curves obtained for intrinsic *a*-Si:H. It can be seen that curve *1* for an unirradiated sample at 20–208°C is characterized by a single activation energy E_A = 1.04 eV (the bend in the curve at T_E = 208°C corresponds to a transition to a thermodynamically equilibrium state [5, 6] with activation energy E_A^σ = 0.43 eV). Thermoelectric power measurements at room temperature revealed a weakly pronounced *n*-type conduction in such samples. The conductivity of the films grows with increasing irradiation dose. Upon irradiation, the activation energy decreases from 1.04 to 0.54 eV. According to thermoelectric power measurements, the type of conduction of the samples changes to *p*-type after irradiation.

The change in the type of conduction of the intrinsic *a*-Si:H as a result of gamma irradiation is also accompanied by a decrease in the coefficient σ_0 (Fig. 2) in the expression for the electrical conductivity $\sigma = \sigma_0 \exp(-E_A/kT)$. A similar decrease in σ_0 upon a change

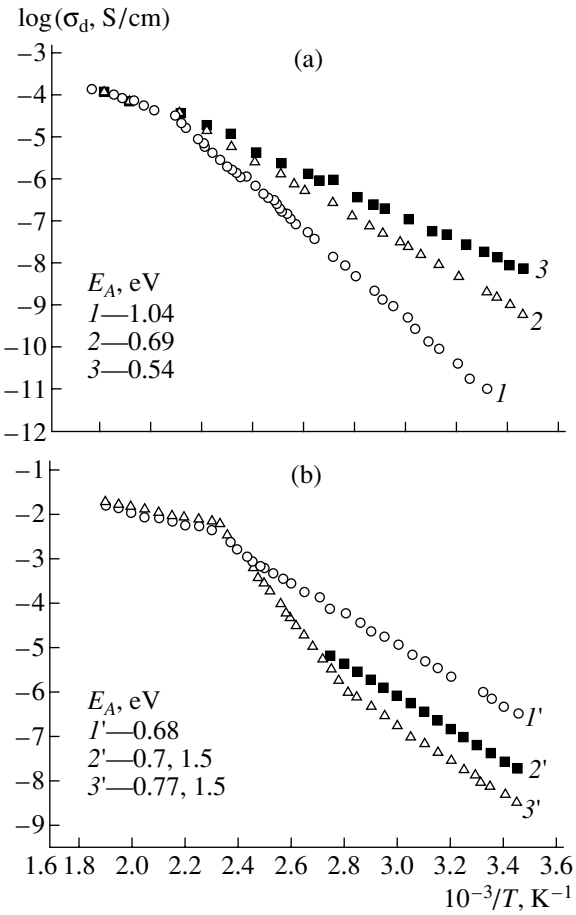

Fig. 1. Effect of gamma irradiation on temperature dependences of dark electrical conductivity $\sigma_d = f(1/T)$ of undoped samples of amorphous hydrogenated silicon: (a) intrinsic *a*-Si:H and (b) undoped (extrinsic) *a*-Si:H. (*1*, *1*') Before irradiation; after irradiation with a dose: (*2*, *2*') 5.1×10^{17}, (*3*) 1.43×10^{18}, and (*3*') 2.1×10^{18} photon cm^{-2}. The activation energies E_A are indicated in the figure.

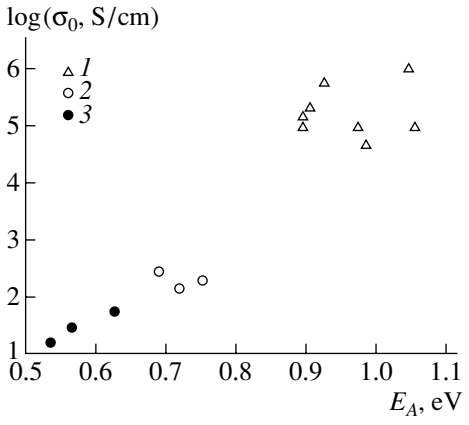

Fig. 2. Meyer–Neldel $\sigma_0 = f(E_A)$ curve for unirradiated and irradiated *a*-Si:H samples. (*1*) Before irradiation; after irradiation with a dose: (*2*) 5.1×10^{17} and (*3*) 1.43×10^{18} photon cm^{-2}.

Table 2. Defect state density distribution in the mobility gap of *a*-Si:H [3, 4]

Type of defect	Parameter	State of a sample			
		Intrinsic *a*-Si:H		Undoped *a*-Si:H*	
		annealed	irradiated with visible light	annealed	irradiated with visible light
D^+	$E–E_V$, eV	1.28	1.28	~1.36	~1.22
	N_{D^+}, cm^{-3}	3.0×10^{15}	6.0×10^{16}	6.0×10^{16}	1.1×10^{17}
D^0	$E–E_V$, eV	0.78	0.78	0.78	0.78
	N_{D^0}, cm^{-3}	4.5×10^{15}	1.0×10^{17}	8.0×10^{15}	1.4×10^{17}
D^-	$E–E_V$, eV	0.5	0.5	~0.56	~0.48
	N_{D^-}, cm^{-3}	3.0×10^{15}	6.0×10^{16}	6.0×10^{16}	1×10^{17}

* Substrate temperature T_S = 280°C.

of the conduction from *n*- to *p*-type was observed by Spear [7].

The effect of gamma irradiation on the conductivity of undoped (extrinsic) *a*-Si:H has a different nature (Fig. 1b). The dependence $\sigma_d = f(1/T)$ obtained prior to irradiation (curve *1*') is characterized by two activation energies of 0.68 and 0.91 eV in the temperature range 20–162°C (the bend at T_E = 162°C corresponds to a transition to an equilibrium state with activation energy E_A^σ = 0.3 eV). Measurements on irradiated samples of this material (Fig. 1b, curves *2*' and *3*') revealed a decrease in conductivity by approximately 2 orders of magnitude, compared with its original value, and an increase in the activation energy to 0.77 eV in the range of 20–97°C and to 1.5 eV in the range of 97–156°C. In this case, a transition to the equilibrium state occurred in irradiated samples at a lower temperature (T_E = 156°C) than in unirradiated samples, which may be due to an increase in the number of defects as a result of gamma irradiation. Noteworthy is the appearance upon irradiation of the high activation energy of 1.5 eV, which is untypical of *a*-Si:H. The type of conduction remained electronic upon irradiation of extrinsic material samples.

4. DISCUSSION

The change in the conductivity of *a*-Si:H films under gamma irradiation can be attributed to defect states in the mobility gap of both intrinsic and undoped (extrinsic) materials.

Let us evaluate the results obtained in terms of modern concepts concerning the distribution of the defect state density $g(E)$ in the mobility gap of undoped *a*-Si:H. Despite intensive long-term studies (which began in the 1970s), for quite some time ambiguity remained over the question of energy states near the midgap of *a*-Si:H, and data obtained by different authors were contradictory. The situation changed in the 1990s. It was revealed that charged defect states, originally attributed to only doped *a*-Si:H, are always present in the mobility gap of the undoped material as well. Three density-of-states peaks were found in the gap [3, 4]: D^+, D^0, and D^-. The corresponding defect concentrations and peak positions are presented in Table 2, which was compiled using the results of Wronski *et al.* [3, 4]. It can be seen that, in the undoped material, the defect concentration varies over a narrow range (8×10^{15}–10^{17} cm^{-3}); however, as shown in [3, 4], even minor variations of charged defects markedly affect the properties of *a*-Si:H, especially its electrical and optical properties. The reason is that silicon dangling bonds, D^0, which appear in *a*-Si:H in the course of film growth or under external effects on the film, are easily converted through interaction with free carriers into other states by the reactions

$$D^0 + h \longrightarrow D^+, \quad (1)$$

$$D^0 + e \longrightarrow D^-, \quad (2)$$

$$D^+ + 2e \longrightarrow D^-, \quad (3)$$

$$D^- + 2h \longrightarrow D^+. \quad (4)$$

Thus, all three types of defects, D^+, D^0, and D^-, may become traps both for electrons and for holes.

For intrinsic *a*-Si:H, we observed on irradiated samples an increase in the dark conductivity and a decrease in the activation energy, as well as a change of the conduction from *n*- to *p*-type (Fig. 1a). Taking into account the last circumstance, we believe that gamma photons create holes in the material being irradiated and the number of these holes grows as the irradiation dose increases. This is in agreement with the results obtained by Imagawa *et al.* [8], who established that gamma irradiation creates silicon dangling bonds with a predominance of D^+ defects [see reactions (1) and (4)].

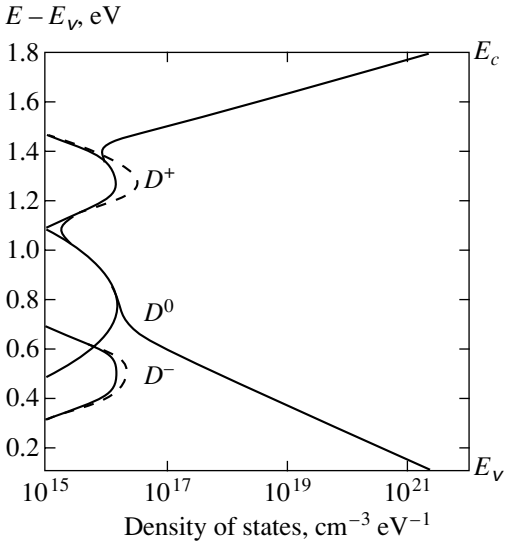

Fig. 3. Energy distribution of the density of D^+, D^0, and D^- defect states in the mobility gap established for undoped *a*-Si:H in [3, 4]. Dashed lines show the assumed changes in the concentration of D^+ and D^- defects upon gamma irradiation of our samples with account of the data of [8].

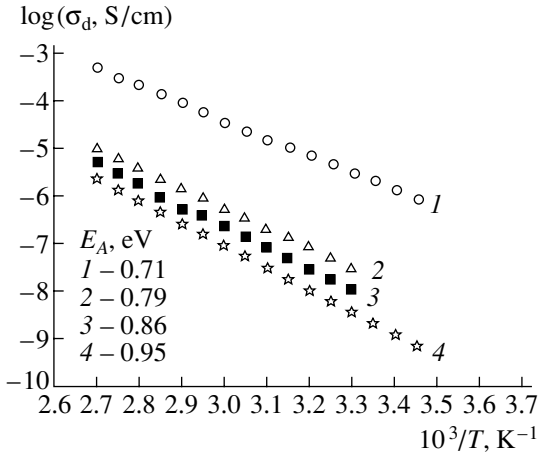

Fig. 4. Staebler–Wronski effect in undoped samples of extrinsic *a*-Si:H: (*1*) before exposure to white light and (*2–4*) after exposure. Time of exposure: (*2*) 3, (*3*) 8, and (*4*) 60 min. The activation energies are indicated in the figure.

If we now pass to a consideration of the band diagram and take into account the data of [3, 4], it may be assumed that the density of states at a deep acceptor level increases in gamma-irradiated samples (Fig. 3). The energy difference $E_c - E_{D^+}$ approximately corresponds to the activation energies observed in our experiments (~0.6 eV).

In the quasi-equilibrium state, the equality $N_{D^+} = N_{D^-}$ is valid. Since D^+ defects predominate in the case of gamma irradiation, it should be assumed that this equality is broken down, so that $N_{D^+} > N_{D^-}$ and the Fermi level is shifted upwards. Figure 3 shows the band diagram of *a*-Si:H according to [3, 4]. The dashed line in the diagram shows the assumed changes in the density of D^+ states as a result of gamma irradiation. Thus, the whole set of data for intrinsic *a*-Si:H suggests that gamma irradiation introduces asymmetry into the densities of states of charged defects D^+ and D^- in the mobility gap and leads to a more significant departure of the sample from equilibrium (compared, e.g., with the case of exposure to light).

The results of gamma irradiation of extrinsic *a*-Si:H (Fig. 1b) markedly differ from the above data for the intrinsic material (Fig. 1a). Upon gamma irradiation, the conductivity of the extrinsic sample decreases and the activation energy exceeds 1 eV, with the conduction remaining *n*-type. It may be assumed that the interaction of gamma photons with the amorphous matrix of *a*-Si:H gives rise to electrically active centers that capture free carriers.

Along with studying the effect of gamma irradiation on the electrical conductivity of undoped (extrinsic) *a*-Si:H, we previously investigated, on samples of the same batch, the influence exerted by white light on the dependence $\sigma_d = f(1/T)$ (Staebler–Wronski effect) under conditions which are standard for the observation of this effect (the light of a KGM-300 tungsten lamp was filtered so as to pass photons in the wavelength range 600–900 nm; the incident power ~50 mW cm^{-2}). The results obtained are presented in Fig. 4. Noteworthy is the similarity of the curves in Figs. 4 and 1b, which describe the temperature dependence of electrical conductivity. This suggests that the mechanisms of defect formation are similar for these two kinds of irradiation. The nature of the Staebler–Wronski effect is sufficiently well understood [3, 4, 8, 9]. It has been established that *a*-Si:H exposure to visible light leads to the rupture of Si=Si bonds and, especially, weak Si~Si bonds to give D^0 defects (Table 2) which favor the formation of electrically active hydrogen-containing complexes. Upon heating the samples for electrical conductivity measurements, such complexes completely disintegrate and liberate hydrogen, since the $\sigma_d = f(1/T)$ curve returns to its initial state both for samples irradiated with gamma quanta and for those exposed to light.

5. CONCLUSION

To conclude, we note the similarity of the results presented in this communication with the data of our previous study on gamma irradiation of doped *a*-Si:H samples [1]. The effect of gamma irradiation on the electrical conductivity of an intrinsic material is qualitatively similar to its action on a boron-doped material: in both cases, gamma quanta make the conductivity of films higher (true, in different temperature ranges),

leaving the conduction *p*-type. The qualitative similarity of the results obtained for the intrinsic and doped *p*-type materials gives reason to believe that gamma irradiation leads to the recharging of dangling bonds, with the predominance of D^+ states.

Another pair of materials being compared comprises undoped (extrinsic) and phosphorus-doped *a*-Si:H. The effects of gamma irradiation on the electrical conductivity of these materials exhibit even more pronounced similarities: (i) a substantial decrease in conductivity, (ii) invariable type of conduction, and (iii) appearance of a high activation energy (> 1 eV). It may be assumed that the similarities of the effects produced by gamma irradiation on this pair of materials is due to the formation of hydrogen-containing complexes and their disintegration upon being heated above 150°C.

The aforesaid suggests that a more important factor in gamma irradiation of doped samples is, presumably, the presence of D^+, D^0, and D^- defects, as well as hydrogen, rather than the presence of the impurity itself.

REFERENCES

1. M. S. Ablova, G. S. Kulikov, and S. K. Persheev, Fiz. Tekh. Poluprovodn. (St. Petersburg) **32**, 245 (1998) [Semiconductors **32**, 222 (1998)].
2. O. A. Golikova, Fiz. Tekh. Poluprovodn. (St. Petersburg) **31**, 281 (1997) [Semiconductors **31**, 228 (1997)].
3. M. Gunes, C. R. Wronski, and T. J. McMahon, J. Appl. Phys. **76**, 2260 (1994).
4. M. Gunes and C. R. Wronski, J. Appl. Phys. **81**, 3526 (1997).
5. R. A. Street, J. R. Kakalios, C. C. Tsaj, and T. M. Hayes, Phys. Rev. B **35**, 1316 (1987); Phys. Rev. B **34**, 3030 (1986).
6. *Advances in Disordered Semiconductors*, Vol. 1: *Amorphous Silicon and Related Materials*, Ed. by H. Fritzsche (World Scientific, Singapore, 1989; Mir, Moscow, 1991).
7. N. F. Mott and E. A. Davis, *Electronic Processes in Non-Crystalline Materials* (Clarendon, Oxford, 1979; Mir, Moscow, 1982), Vol. 2.
8. O. Imagawa, K. Yasuda, and A. Yoshida, J. Appl. Phys. **66**, 4719 (1989).
9. D. L. Staebler and C. R. Wronski, J. Appl. Phys. **51**, 3262 (1980).

Translated by M. Tagirdzhanov

Semiconductors, Vol. 36, No. 8, 2002, pp. 941–943. Translated from Fizika i Tekhnika Poluprovodnikov, Vol. 36, No. 8, 2002, pp. 1006–1009.

AMORPHOUS, VITREOUS, AND POROUS SEMICONDUCTORS

Fabrication and Properties of Amorphous Hydrogenated Boron Carbide Films

A. S. Anan'ev*, O. I. Kon'kov*, V. M. Lebedev, A. N. Novokhatski*, E. I. Terukov*, and I. N. Trapeznikova***

** Ioffe Physicotechnical Institute, Russian Academy of Sciences, Politekhnicheskaya ul. 26, St. Petersburg, 194021 Russia*

*** Konstantinov Institute of Nuclear Physics, Russian Academy of Sciences, Gatchina, St. Petersburg, 188350 Russia*

Submitted December 5, 2001; accepted for publication February 11, 2002

Abstract—Boron carbide films were grown using glow discharge decomposition of $C_2B_{10}H_{12}$ powder sublimation products. The film composition found as *a*-$B_{0.52}C_{0.48}$:H using nuclear reaction and infrared spectroscopy techniques was shown to depend weakly on the discharge gas (Ar or He) and the substrate temperature (20–100°C). The optical band gap was found to be about 3.8 eV; the resistivity varied from 10^6 to 10^5 Ω cm as the substrate temperature increased. Weak photoluminescence with a peak at 475 nm indicates that there is an acceptor level in the band gap which correlates with the conduction activation energy. © *2002 MAIK "Nauka/Interperiodica".*

INTRODUCTION

The crystal structure of boron-enriched solids contains icosahedral fragments that are tightly bonded to each other and form a rhombohedral lattice skeleton. In crystalline boron carbide ($B_{12}C_3$), carbon plays an important role in the lattice skeleton formation, since it eliminates three-center bonds between neighboring icosahedral fragments and forms a rhombohedral skeleton with ordinary covalent bonds. In this case, carbon atoms are considered as a component of the lattice structure; as a result, the introduced carbon fraction is limited to about 20% [1]. However, this limitation is removed in amorphous boron carbide. Almost any carbon composition can be obtained by plasmochemical deposition. In specific cases, the carbon fraction can exceed the limiting one for the crystal [2]. In this case, the role of carbon is significantly changed and its incorporation into the amorphous boron network has different effects on the optical and electrical properties of the material. In the case of the production of hydrogenated amorphous films of boron carbide, their structure contains a great number of hydrogen atoms bonded to both boron and carbon, which also has an effect on the physical properties of films.

In the synthesis of *a*-B_xC_y:H films, the method of high-frequency (HF) glow discharge [3] is rather widely used; a mixture of methane (CH_4) and diborane (B_2H_6) is, as a rule, employed as the working gas. However, operation with highly toxic diborane is a disadvantage of this synthesis and imposes specific requirements on the vacuum system. Boron carbide films may also be produced by the decomposition of the sublimation products of $C_2B_{10}H_{12}$ powder in dc glow discharge plasma [4–6].

FABRICATION TECHNOLOGY

In this study, amorphous hydrogenated boron carbide films were produced from the decomposition of the sublimation products of $C_2B_{10}H_{12}$ powder (heated to 45°C) in HF glow discharge plasma. Fragments of the primary decomposition (sublimation) of the powder were bombarded with HF plasma electrons; then, the chemically active products of this reaction were deposited onto a substrate. Argon or helium was used as the carrier gas. The films were deposited in a conventional capacitive system with a bottom HF electrode and a heated grounded top electrode. The substrates were placed on the grounded electrode with the temperature being varied from ~20 to 100°C. The discharge frequency and power were 40 MHz and 20 W, respectively. The interelectrode spacing was 35 mm. Active $C_2B_{10}H_{12}$ material was introduced into the reactor center through the bottom HF electrode. The deposition rate (2–4 μm h^{-1}) decreased as the substrate temperature was elevated. Single-crystal silicon wafers, fused quartz, and glass were used as substrates. The typical thickness of the studied samples was 1–3 μm.

RESULTS AND DISCUSSION

Figure 1 displays a typical infrared (IR) transmission spectrum of an amorphous hydrogenated boron carbide sample produced by the described method. Variations in fabrication conditions, i.e., carrier gas (Ar or He) and the substrate temperature, had an insignifi-

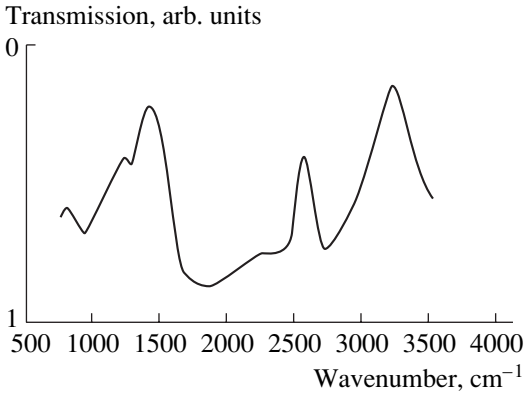

Fig. 1. Typical IR transmission spectrum of amorphous boron carbide film produced by decomposition of the sublimation products of $C_2B_{10}H_{12}$ powder in high-frequency glow discharge plasma.

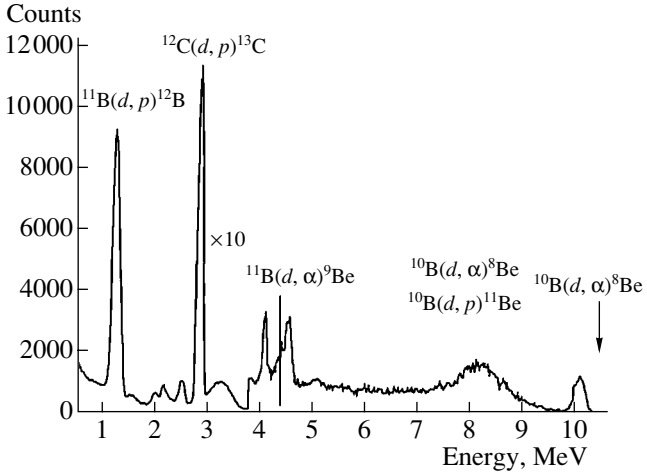

Fig. 2. Spectrum of protons and α-particles produced from the nuclear reactions ^{12}C(d, p)^{13}C, ^{10}B(d, p)^{11}B, ^{11}B(d, p)^{12}B, ^{10}B(d, α)^{8}Be, and ^{11}B(d, α)^{9}Be in the amorphous boron carbide film irradiated with deuterons of energy E_d = 1 MeV. The proton detector is positioned at an angle θ = 135° to the beam and is covered by an aluminum absorber 11 μm thick.

cant effect on the spectrum. An analysis of the IR spectra shows that a great amount of hydrogen is bonded to both boron (the band at 2560 cm^{-1}) and carbon, which is indicated by the broad absorption band in the region of 2800–3500 cm^{-1} with a peak at 3270 cm^{-1}; this band is related to the C–H_n bond stretching mode [4]. The absorption band with a peak in the region of 1350–1450 cm^{-1} is also related to C–H_n bonds and is interpreted as the bending mode. This is confirmed by the data of [1], where a broad absorption band with a peak near 1510 cm^{-1} was observed in carbon-reach samples; this band was related to either free carbon or graphite-like inclusions. The pronounced absorption band with a peak near 1200 cm^{-1} is related to the B–C bond. This band is usually observed in polycrystalline boron carbide samples [7, 8] and is explained by the motion of boron and carbon atoms either in an isolated B–C bond [1] or in the unit cell of the boride–carbide icosahedron [9]. It is also worth mentioning that this line is shifted to longer wavelengths in similar films produced by glow discharge in a methane and diborane mixture, which is explained by an increase in the carbon concentration in the material [9]. The "pure" B–B bond (an absorption band near 800 cm^{-1}) is also observed in the IR spectra of the studied films. In our opinion, this indicates the presence of boride icosahedra. The hydrogen concentration in the films, which was roughly estimated according to [10], is 40–50 at. %.

The elemental composition of the films was determined by deuteron nuclear reactions [11] at the energy E_d = 1 MeV. The detector of the reaction products was positioned at an angle of 135° to the deuteron beam direction. The detector was protected against scattered deuterons by an aluminum filter 11 μm thick. The measured spectrum of protons and α-particles is shown in Fig. 2. One can see a number of peaks corresponding to deuteron nuclear reactions with carbon and boron isotopes. The carbon and boron concentrations were determined from the ^{12}C(d, p)^{13}C and ^{10}B(d, α_0)^{8}Be reactions with cross sections $\sigma_C = 29 \times 10^{-27}$ and $\sigma_B = 3 \times 10^{-27}$ cm^2 sr^{-1} and peaks at 2.8 and 10 MeV, respectively [11]. The ratio of the carbon and boron concentrations in the film C_C/C_B was determined from the ratio S_C/S_B of the corresponding areas under the peaks taking into account the ^{10}B and ^{12}C abundances, which were equal to 19.61 and 98.892%, respectively; i.e.,

$$C_C/C_B = 0.1961(S_C/S_B).$$

Thus, in the absence of accurate data on the hydrogen concentration, the film composition can be written as a-$B_{0.52}C_{0.48}$:H.

The optical absorption edge $\alpha(\hbar\omega)$ (α is the absorptivity) was studied with a two-beam spectrometer in the wavelength range of 200–1200 nm. Figure 3 displays the corresponding absorption spectrum as well as the result of its processing by the Tauc law

$$(\alpha\hbar\omega)^{1/2} = B(\hbar\omega - E_g^{\text{opt}}).$$

The optical band gap determined with the absorptivity $\alpha = 10^3$ cm^{-1}, as well as by linear extrapolation of the dependence $\sqrt{\alpha\hbar\omega}$ on $\hbar\omega$, is $E_g^{\text{opt}} \approx 3.8$ eV.

The photoluminescence (PL) spectrum was measured at room temperature using excitation with the ultraviolet radiation of a pulsed nitrogen laser at a wavelength of 337 nm and a pulse duration of 10 ns. The spectra were measured using an MDR-3 grating monochromator, a FEU-79 photomultiplier, and a pulse synchronous detector. The spectrum has a pronounced peak at a wavelength of 470 nm (2.64 eV) and is similar to that with a peak near 490 nm, which we previously observed in films of tetrahedral amorphous carbon [12]. The energy position of the peak does not correlate with

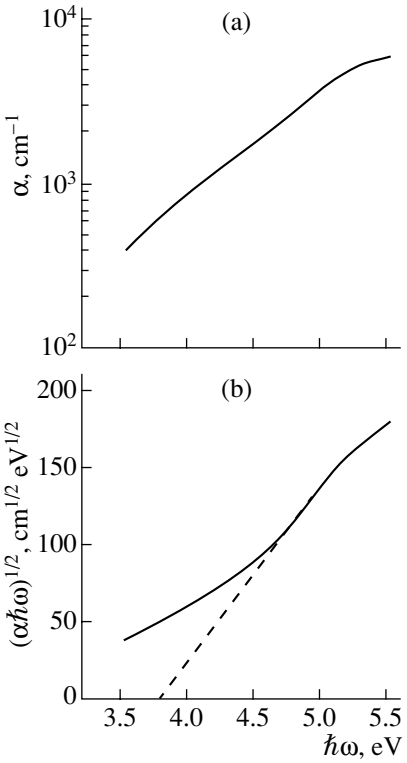

Fig. 3. (a) Optical absorption edge of the amorphous boron carbide film and (b) the spectral region approximation according to the Tauc law.

the probable band-to-band transition and suggests the presence of an impurity level in the band gap. This assumption is confirmed by the low resistivity of the films, which varied from 10^6 to 10^5 Ω cm as the substrate was heated from room temperature to 100°C. In this case, the conductivity activation energy is 0.79 eV, which also correlates with the impurity level position.

Based on the above experimental data, we attempt to answer the following question: which subsystem—carbon or boron—controls the physical properties of the produced films? Our studies of amorphous hydrogenated carbon films [12] show that samples with a similar band gap can be produced within this system by glow discharge. However, all samples had high resistivity, and the problem of their doping has not yet been solved. At the same time, different stoichiometric boron carbide films are characterized by a band gap no wider than 3.8 eV [3]; therefore, it is difficult to explain the observed properties only by the pure boron or pure carbon subsystems. The observed properties are probably controlled by the composite structure of the produced films, which may be conceived as a host of the carbon–boron skeleton of icosahedra bonded by C–H_n groups (n = 2, 3) and BH_2 groups. These factors are responsible for the formation of a material whose properties differ from those of the crystalline phases possible in this system. Thus, many problems, such as the band gap formation and the conduction mechanism, call for further investigations.

CONCLUSION

The properties of amorphous hydrogenated boron carbide films produced in neutral glow HF discharge plasma using $C_2B_{10}H_{12}$ powder as the boron and carbon source were studied. The composition of the films produced depended only slightly on the neutral gas (argon or helium) and the substrate temperature (in the range from 20 to 100°C). The film composition, which was determined using nuclear reaction and IR spectroscopy methods, was described by the formula a-$B_{0.52}C_{0.48}$:H. The films were characterized by a complex microstructure, which included icosahedra of both boron carbide and boron, as well as a high hydrogen concentration in the form of CH_n and BH_2 groups.

REFERENCES

1. K. Shirai, S. Emura, S. Gonda, and Y. Kumashiro, J. Appl. Phys. **78** (5), 3392 (1995).
2. K. Shirai, S. Ae, and S. Gonda, in *Boron-Rich Solids: Proceedings of the 10th International Symposium on Boron, Borides and Related Compounds, 1987*, Ed. by H. Werheit, p. 336.
3. B. Silvester, Shu-Han Lin, and B. J. Feldman, Solid State Commun. **93**, 969 (1995).
4. J. Ristein, R. T. Steif, and L. Ley, J. Appl. Phys. **87**, 3836 (1998).
5. V. M. Sharapov, V. E. Golant, V. K. Gusev, and A. N. Novokhatski, J. Nucl. Mater. **220–222**, 730 (1995).
6. V. K. Gusev, V. E. Golant, E. Z. Gusakov, *et al.*, Zh. Tekh. Fiz. **69** (9), 58 (1999) [Tech. Phys. **44**, 1054 (1999)].
7. V. K. Gusev, S. V. Alexandrov, T. A. Burtseva, *et al.*, in *Proceedings of the 18th Fusion Energy Conference, Sorrento, 2000*, paper EXP01/03.
8. H. Stein, T. Aselage, and D. Emin, in *Boron-Rich Solids: Proceedings of the 10th International Symposium on Boron, Borides and Related Compounds, 1987*, Ed. by H. Werheit, p. 322.
9. Shu-Han Lin and B. J. Feldman, Solid State Commun. **107**, 239 (1998).
10. N. A. Blum, C. Feldman, and F. G. Satkiewicz, Phys. Status Solidi A **41**, 481 (1977).
11. G. Giorginis, L. Persson, M. Hult, *et al.*, Nucl. Instrum. Methods Phys. Res. B **136–138**, 258 (1998).
12. O. I. Kon'kov, E. I. Terukov, and I. N. Trapeznikova, Fiz. Tekh. Poluprovodn. (St. Petersburg) **30**, 2183 (1996) [Semiconductors **30**, 1138 (1996)].

Translated by A. Kazantsev

Semiconductors, Vol. 36, No. 8, 2002, pp. 944–949. Translated from Fizika i Tekhnika Poluprovodnikov, Vol. 36, No. 8, 2002, pp. 1010–1015.

PHYSICS OF SEMICONDUCTOR DEVICES

Lattice-Matched GaInPAsSb/InAs Structures for Devices of Infrared Optoelectronics

M. Aĭdaraliev*, N. V. Zotova*, S. A. Karandashev*, B. A. Matveev*, M. A. Remennyi*, N. M. Stus'*, G. N. Talalakin*, V. V. Shustov*, V. V. Kuznetsov, and E. A. Kognovitskaya****

** Ioffe Physicotechnical Institute, Russian Academy of Sciences, Politekhnicheskaya ul. 26, St. Petersburg, 194021 Russia*

e-mail: bmat@iropt3.ioffe.rssi.ru

*** St. Petersburg State Electrotechnical University, St. Petersburg, 197376 Russia*

Submitted January 23, 2002; accepted for publication January 29, 2002

Abstract—It is reported that a $Ga_{0.92}In_{0.08}P_{0.05}As_{0.08}Sb_{0.87}$ quinary solid solution, which is lattice-matched to InAs, with a band gap of 695 meV (77 K) and 640 meV (300 K) is obtained. It is demonstrated that a heterojunction of type II is realized in the $InAs/Ga_{0.92}In_{0.08}P_{0.05}As_{0.08}Sb_{0.87}$ structure. The solid solution obtained was used for the development of prototypes of light-emitting diodes and photodiodes with the highest intensity of emission and photosensitivity in the vicinity of 1.9 μm. © *2002 MAIK "Nauka/Interperiodica".*

1. INTRODUCTION

Multicomponent ternary (InAsSb, InGaAs) and quaternary (InGaAsSb, InAsSbP) solid solutions are widely used for the production of optoelectronic devices for the spectral range of 2–5 μm. Quinary solid solutions (for example, GaInPAsSb [1–9]) have been investigated in substantially less detail, although their obvious advantage is the possibility of the independent variation of three parameters. The control of the band gap, the lattice constant, and the coefficient of thermal expansion permits one to develop heterostructures without lattice mismatch under the growth temperature and under the temperature of device operation. This leads to a decrease in the probability of defect formation and, correspondingly, to the improvement of luminescence characteristics and extension of the service life of the device. The control of the band gap, the lattice constant, and the refractive index, apparently, will be a fundamental prerequisite for the development of lasers operating at elevated temperatures.

The purpose of this study was to obtain a $Ga_xIn_{1-x}P_yAs_zSb_{1-y-z}$ quinary solid solution with a band gap of 600–700 meV on an InAs substrate and to develop prototypes of a light-emitting diode (LED) and a photodiode with the highest intensity of emission and photoresponse in the vicinity of 1.9 μm at 300 K.

2. METHODS FOR FORECAST, GROWTH, AND INVESTIGATION

The effective design of modern semiconductor heterostructures based on multicomponent solid solutions is a methodologically complex process. The reliability of calculations is determined by the correctness of the models applied and the adequacy of the parameters used. In this study, in order to forecast the technology process, the following methodology was used. The composition of the required quinary $Ga_xInP_yAsSb_z$ solid solution was determined through the linear interpolation of the lattice constants of binary components using the published data [2].

The band gap of the GaInPAsSb quinary solid solution was interpolated over the band gap of two GaPAsSb and InPAsSb quaternary systems with the substitution of components over the sites of the metal sublattice while making allowance for the nonlinear contribution of mixing effects [2].

The determination of the parameters of the liquid-phase heteroepitaxial process for obtaining the GaInPAsSb solid solution in the range of compositions lattice-matched to InAs was carried out based on an analysis of the liquid–solid phase equilibria in the context of the model of simple solutions. The method for this analysis and basic data for the calculations are given in [2–6]. The choice of uncertain excess molar energies of mixing (interaction parameters) was justified as follows. The parameters of interaction between the metal and metalloid components are obtained from the analysis of phase diagrams for corresponding binary systems in the relevant temperature range. These parameters are justifiably considered as self-consistent based on the generality of the applied thermodynamic model [3]. However, the parameters of interaction between elements in the liquid phase have not been reliably deter-

Table

Composition of the liquid phase				Composition of the layer deposited (1, calculation; 2, experiment)			
$x^l_{Ga} \times 10^3$, atomic fractions	$x^l_P \times 10^3$, atomic fractions	$x^l_{As} \times 10^2$, atomic fractions	$x^l_{Sb} \times 10$, atomic fractions		*x*, molar fractions	*y*, molar fractions	*z*, molar fractions
3.03	1.63	3.24	3.77	1	0.06	0.12	0.77
				2	0.08	0.08	0.81
				2	0.072	0.09	0.78
273	0.122	0.245	1.28	1	0.89	0.021	0.153
				2	0.92	0.012	0.165
				2	0.91	0.011	0.160

mined separately for Group III and Group V elements, such as P–As, P–Sb, As–Sb, and, partially, between the components of the solid phase, namely, GaP–GaSb and InP–InSb. In addition, for P-containing and Sb-containing systems, a considerable positive deviation from the Raoult law is observed. This primarily affects the magnitudes of the corresponding excess molar energies of mixing and, consequently, the results of calculations [3, 6]. The situation is additionally complicated by the fact that a very strong association of components in the liquid phase is observed for the III–Sb systems, which restricts the applicability of the model.

In order to adapt the model used, the above-mentioned parameters were corrected using test experiments for the $Ga_{0.06}In_{0.94}P_{0.12}As_{0.8}Sb_{0.08}$ solid-phase composition (see table). We used reasonable values of excess molar energies of mixing. This permitted us to calculate the temperatures and compositions of the liquidus and solidus in the temperature range of epitaxy along the isoperiod of InAs on both sides of the binodal space. The results of calculations, in comparison with subsequent experiments, are given in the table.

The epitaxy was carried out according to the following procedure. The InAs substrates, which had a ⟨111⟩ orientation and were 400 μm thick, were chemically etched in HCl for 1–2 s before the process. After that, the substrates were rinsed in distilled water and dried in a thermostat at 60°C.

For the formation of the liquid phase, the following substances were used: Sb (SU-000); In (IN-000); Ga (GL-000); InAs (IME-1); and undoped InP. In order to remove the oxide film, In was etched in a mixture of HNO_3 : HF at a ratio of 8 : 1 at room temperature for 1–2 min. After rinsing in distilled water, all the materials, except for Ga, were dried in the thermostat at 60–70°C.

Components of the charge and substrates were placed into a translatory graphite cartridge. After blowing with H_2, the cartridge was heated to 993 K and kept for 90 min at this temperature in order to homogenize the melt. After that, the temperature was lowered to 925–920 K and the liquid phase was brought into contact with the substrate for 1–3 min. The thickness of the layers obtained varied from 2 to 10 μm.

The compositions of the initial charge were selected so that the liquid phase was supercooled relative to the liquidus temperature by 5–9 K at the temperature of epitaxy.

In order to obtain a *p–n* heterojunction, the solid solution was doped with Zn (acceptor) or Te (donor). In the Te–In charge, Te was introduced directly into the solution before carrying out the epitaxy. Doping with Zn was performed from the gas phase by introducing the In–Zn alloy into the reactor zone at a prescribed temperature. The Zn content in the melt was governed by the partial pressure of Zn vapors, which were controlled by the temperature of the source zone. The charge-carrier density in the layers obtained was 5×10^{17} cm^{-3}.

The composition of solid solutions, which were measured using a CAMEBAX X-ray microanalyzer, as well as the compositions of the solutions–melts, from which they were obtained, are given in the table (entries 2, experiment). The content of the components in the liquid phase in equilibrium with the given solid solutions, which was calculated from the equations of the phase diagram, are also given there (entries 1, calculation).

The methods for the investigation of epitaxial structures included photoluminescence (PL), electroluminescence (EL), and spectral measurements of photosensitivity. The measurements were carried out at temperatures of 77 (PL and EL) and 296 K (EL, photosensitivity). The EL and photosensitivity were measured on chips 0.5×0.5 mm^2 in size with a point contact to the epitaxial layer and with a massive contact to the InAs substrate.

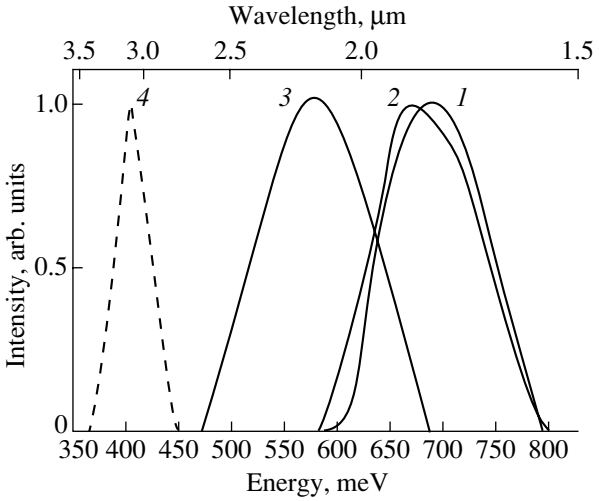

Fig. 1. Photoluminescence spectra (77 K) of solid solutions (*1*) with no intentional doping, (*2*) Zn-doped, and (*3*) Te-doped; (*4*) the photoluminescence spectrum of *n*-InAs substrate.

3. RESULTS AND DISCUSSION

3.1. Photoluminescence of the $Ga_{0.92}In_{0.08}P_{0.05}As_{0.08}Sb_{0.87}$ Solid Solution

The PL spectra of the InAs/GaInPAsSb structure with a nominally undoped solid solution (curve *1*), doped with Zn (curve *2*), and doped with Te (curve *3*) are shown in Fig. 1. The spectrum involves a PL line from the solid solution with a peak energy $h\nu$ = 580–690 meV and a PL line from the *n*-InAs substrate with a peak at $h\nu$ = 400 meV (curve *4*).

The $Ga_{0.92}In_{0.08}P_{0.05}As_{0.08}Sb_{0.87}$ solid solution is close to binary GaSb and $Ga_{0.8}In_{0.2}As_{0.22}Sb_{0.78}$ quaternary solid solutions in its composition and band gap [11, 12]. These latter are of *p*-type conduction due to native structural defects of the V_{Ga} or $V_{Ga}Ga_{Sb}$ types, which induce doubly charged acceptor levels with an ionization energy of 30 and 90 meV in the band gap. For undoped GaSb and $Ga_{0.8}In_{0.2}As_{0.22}Sb_{0.78}$, it is these acceptor levels that are involved in recombination, since all shallow levels, both donor and acceptor, are ionized even at 77 K [13]. We believe that the PL in the quinary solid solution without intentional doping ($h\nu$ = 690 meV) is also determined by transitions between the conduction band and a doubly charged acceptor. This is confirmed by the large half-width of the spectrum ($\Delta h\nu$ = 100 meV).

Doping of the solid solution with the Zn acceptor impurity leads to recombination at a deeper acceptor level and to a shift of the spectral band to lower energies by ~20 meV at the same spectrum half-width.

Doping of the solid solution with the Te donor impurity leads to the compensation of *p*-type conduction and the emergence of weakly pronounced electron conduction. The electrons from the donor levels occupy the shallow acceptor levels, which leads to the recombination via deeper acceptor states. For example, the radiative transition between the conduction band and a deep acceptor level with an activation energy of ~122 meV, which is associated with V_{Ga}Te complexes, was observed for the $Ga_{0.8}In_{0.2}As_{0.2}Sb_{0.8}$ quaternary solid solution [12]. With respect to the band gap, this solid solution is close to the material investigated. In our case, the PL peak for the Te-doped solid solution is shifted to energies ($h\nu$ = 580 meV) that are lower by 110 meV relative to the nominally undoped solid solutions. This is very close to the ionization energy of the V_{Ga}Te complex in $Ga_{0.8}In_{0.2}As_{0.22}Sb_{0.78}$. The band gap of the $Ga_{0.92}In_{0.08}P_{0.05}As_{0.08}Sb_{0.87}$ solid solution can be estimated as 695 meV (77 K).

3.2. Electroluminescence of InAs/GaInPAsSb Heterostructures

In order to interpret the experimental data, we accepted, as a basis, the luminescence mechanism in a broken-gap heterojunction of type II. The solid solution investigated is close to the GaSb binary compound in its composition and band gap. The latter compound forms a broken-gap heterojunction of type II with InAs. In this case, the valence band top for the wide-gap semiconductor is above the conduction band bottom for the narrow-gap semiconductor. On both sides of the heterointerface, deep quantum wells (QWs) are formed for electrons and holes and their wave functions overlap appreciably [13]. Applying an external electric field to the heterointerface, we can vary the relative position of energy bands close to the heterointerface and the carrier population of QWs. Under certain conditions, this can lead to a high probability of indirect radiative recombination, which is caused by tunnel transitions through the heterointerface. Due to the low effective mass of charge carriers in the system under investigation compared with, for example, GaAs/GaAlAs, the requirements for the abruptness of the heterointerface are less stringent for the formation of QWs. In this case, interface radiative recombination is observed in the structures with the lattice mismatch $\Delta a/a \le 10^{-3}$.

In order to investigate the EL, we used both substrate–epilayer heterojunctions and structures with *p–n* homojunctions in the bulk of the solid solution itself: *n*-InAs/*P*-GaInPAsSb/*N*-GaInPAsSb. The current–voltage characteristics of the structures *p–P*, *n–N*, and *n–P* varied only slightly in the temperature range of 77–300 K, which is indicative of tunnel current flow. Isotypic *p–P* and *n–N* structures had rectifying characteristics and showed EL in the range of 77–300 K, whereas the *n–P* structure was characterized by the absence of both rectification and an EL signal. This indicates that a broken-gap heterojunction of type II is formed in the InAs/GaInPAsSb structure [10].

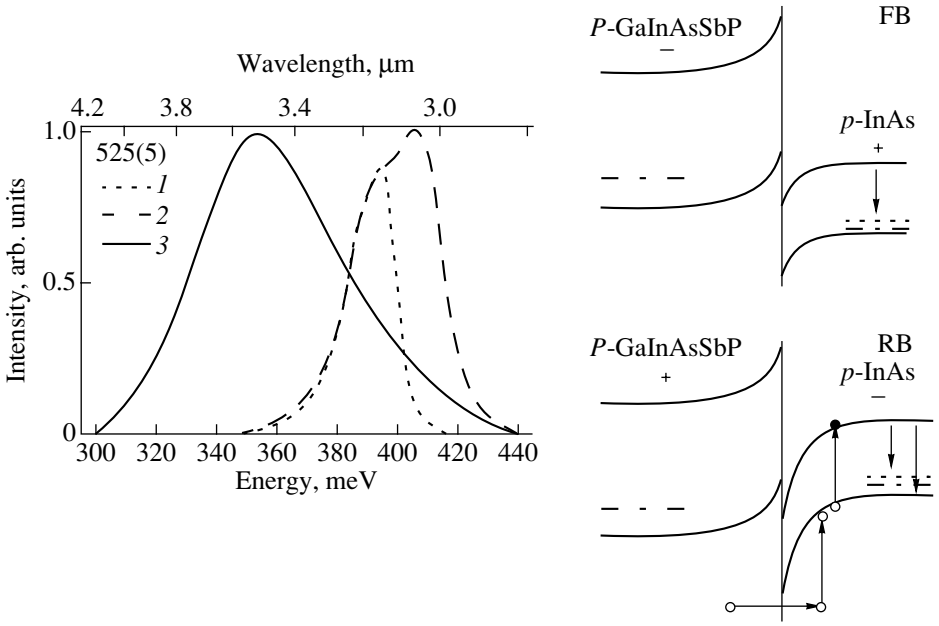

Fig. 2. Electroluminescence spectra of an isotype *p–P* junction for forward bias (FB: "plus" is at *p*-InAs, curve *1*) and reverse bias (RB: "minus" is on *p*-InAs, curve *2*) at 77 and 300 K (RB, curve *3*). On the right: energy diagrams of the heterojunction for the forward and reverse biases.

3.2.1. The EL of the isotypic P–p heterojunction

The EL spectra with forward ("+" on *p*-InAs) and reverse ("–" on *p*-InAs) biases at 77 and 300 K are shown in Fig. 2. The shape of the spectra for both polarities of the bias applied is similar, and the band positions actually coincide. For the forward bias, a band with a peak at 395 meV (77 K) is observed (curve *1*), and for the reverse bias, two close bands at 405 and 395 meV are observed (curve *2*). A broad ($\Delta h\nu$ = 48 meV) line with a peak at 352 meV is observed at 300 K (curve *3*). The coincidence of the spectra for different polarities indicates that carrier recombination occurs in the same region of the heterostructure. The emergence of nonequilibrium electrons in the *p–P* junction can be explained by the following model [14]. With zero bias, the two-dimensional electron gas exists in the QW on the InAs side close to the heterointerface due to the electron transition from the valence band of the wide-gap material to the conduction band of InAs. If negative bias is applied, the energy bands at the heterointerface shift so that the energy bands of InAs ascend, whereas the energy bands of the solid solution descend. Space charge is mainly localized in the region of the narrow-gap material. This leads to pronounced band bending close to the heterointerface and the absence of free holes close to the interface, which could recombine with localized electrons in the QW. The application of negative bias leads to effective electron tunneling from the valence band of the solid solution to the valence band of InAs. A tunneled hole loses energy due to the Auger process, which is accompanied by the excitation of a nonequilibrium electron from the valence band of InAs to the conduction band and a hole transition to the valence band top. The electron in the conduction band undergoes radiative recombination in the region of flat bands of InAs with holes at the acceptor level (395 meV) or in the valence band (405 meV). A broad peak is observed close to 352 meV at 300 K, which corresponds to the band-to-band transition. The temperature variation of the peak energy agrees well with the coefficient of temperature variation of the band gap for InAs (3×10^{-4} eV/K).

Upon applying a forward bias which exceeds the contact potential difference, electrons can tunnel from the valence band of the solid solution to the conduction band of InAs and recombine at the acceptor level in the bulk (395 meV). The energy diagrams of such transitions are shown to the right of Fig. 2.

3.2.2. The EL of the isotypic N–n heterojunction

Let us consider the isotypic *N–n* structure, which also demonstrates rectifying properties for the case of a misaligned junction. The EL spectra of such a structure, which is biased in the forward direction at 77 and 300 K, are shown in Fig. 3. A single narrow band ($\Delta h\nu$ = 20 meV) with a spectral peak at 402 meV (77 K) and 344 meV (300 K), which corresponds to band-to-band transitions in *n*-InAs, is observed.

The *P–p* structure exhibits metallic behavior in a wide range of temperatures and currents. Thus, the *I–V* characteristics and EL properties of the InAs/GaInPAsSb structure indicate that this is a broken-gap junction of type II.

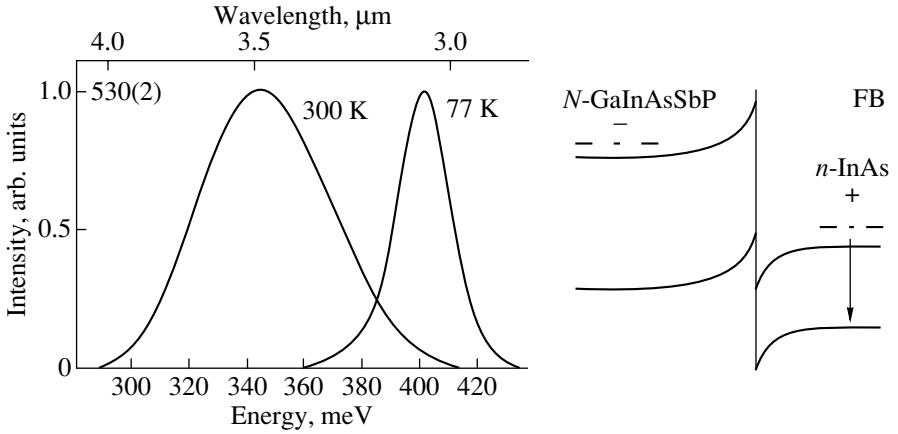

Fig. 3. On the left: electroluminescence spectra of the *N–n* structure shifted in the forward direction (FB: "plus" is on *n*-InAs) at 77 and 300 K. On the right: the energy diagram of the heterojunction.

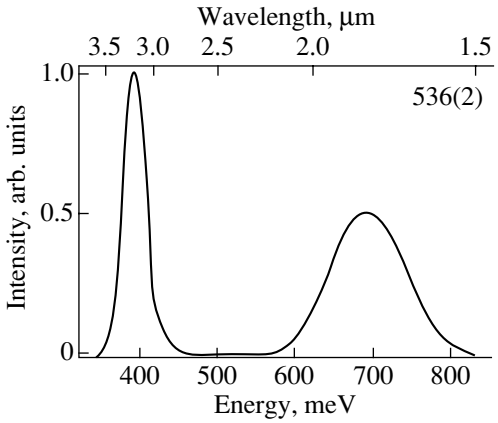

Fig. 4. Electroluminescence spectra of the *n–N–P* structure (77 K).

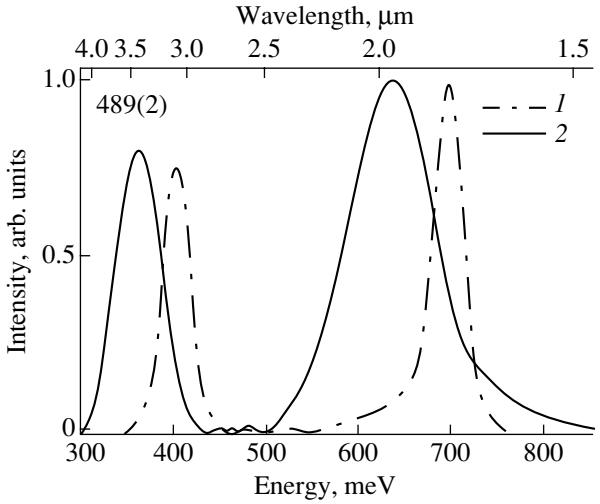

Fig. 5. Electroluminescence spectra of the *n–P–N* structure (*1*—77 K, *2*—300 K).

3.2.3. The EL of the P–N homojunction in the bulk of the solid solution.

Let us consider the EL of the *P–N* homojunction in the bulk of the epilayer of the solid solution. The *P–N* junction was formed by introducing a Te impurity into the p-type layer of the solid solution with no intentional doping. The EL spectra of the *n–N–P* (77 K) and *n–P–N* structures (77, 300 K) are shown in Figs. 4 and 5, respectively. In both cases, the spectra consist of two bands. These are a short-wavelength band (685–695 meV, $\Delta h\nu$ = 40 meV, 77 K) and a long-wavelength band (400 meV, $\Delta h\nu$ = 35 meV, 77 K). The former band is caused by radiative recombination in the solid solution, and the latter band is caused by radiative recombination in the substrate. At 300 K, the EL peaks are at 640 and 360 meV. The temperature shift of the peaks corresponds to the temperature variation of the band gap for InAs, namely, 3×10^{-4} eV/K. This is indicative of the high crystalline quality of the epilayer. It is assumed that the emitting region of the *p–n* homojunction of the solid solution, similarly to InAs, is the *p* region, since the diffusion length of electrons is much larger than the diffusion length of holes. This is also confirmed by the coincidence of the PL spectra of the *p*-type material of the solid solution with the EL spectra of the *P–N* junction.

Based on the *p–n* homojunction in the solid solutions, LEDs with an emission peak wavelength of 1.9 μm and a half-width of 0.3 μm were fabricated.

3.2.4. Photoresponse of the P–N homojunction in the bulk of the solid solution.

The photosensitivity spectra of the *P–N* homojunction in the bulk of the solid solution at 300 K are shown in Fig. 6. The photosensitivity peak coincides with the EL peak (300 K) and corresponds to λ = 1.94 μm. The shape of the spectral curve depends on the *P–N* junction depth relative to the illuminated surface and becomes

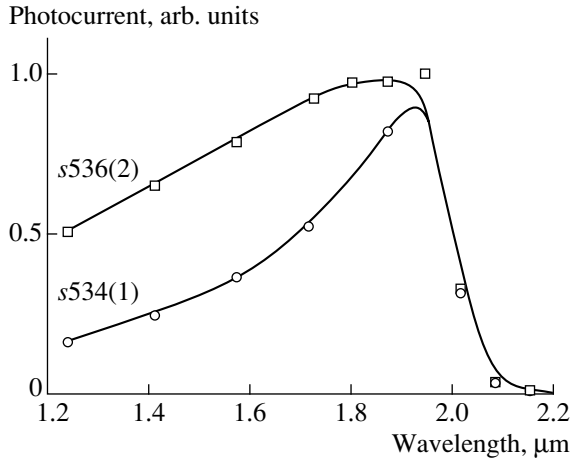

Fig. 6. Photocurrent spectra of the *n–P–N* structure (300 K).

less steep in the short-wavelength region as the *P–N* junction approaches the surface [structure *s*536(2)].

4. CONCLUSION

A $Ga_{0.92}In_{0.08}P_{0.05}As_{0.08}Sb_{0.87}$ quinary solid solution with a band gap of 695 meV (77 K) and 640 meV (300 K), which is lattice-matched to InAs, was obtained for the first time. It is demonstrated that a heterojunction of type II is realized in the $InAs/Ga_{0.92}In_{0.08}P_{0.05}As_{0.08}Sb_{0.87}$ structure. The solid solution obtained was used for the development of prototypes of a LED and a photodiode with the highest emission intensity and photosensitivity in the vicinity of 1.9 μm.

ACKNOWLEDGMENTS

We thank R. N. Kyutt for X-ray diffraction measurements of the samples used in this study.

This study was supported by the Schlumberger Oilfield Services corporation, the program on Optics of Nanostructures, and the Civil Research and Development Foundation (USA).

REFERENCES

1. N. A. Charykov, A. M. Litvak, M. P. Mikhaĭlova, *et al.*, Fiz. Tekh. Poluprovodn. (St. Petersburg) **31**, 410 (1997) [Semiconductors **31**, 344 (1997)].
2. V. V. Kuznetsov, É. R. Rubtsov, and V. S. Sorokin, Zh. Fiz. Khim. **71**, 415 (1997).
3. V. V. Kuznetsov, P. P. Moskvin, and V. S. Sorokin, in *Nonequilibrium Phenomena During Liquid Heteroepitaxy of Semiconductor Solid Solutions* (Metallurgiya, Moscow, 1991).
4. V. V. Kuznetsov and É. R. Rubtsov, Izv. Vyssh. Uchebn. Zaved., Mater. Élektron. Tekh., No. 2, 48 (1998).
5. V. V. Kuznetsov, É. R. Rubtsov, and O. A. Lebedev, Neorg. Mater. **34** (5), 525 (1998).
6. V. V. Kuznetsov, N. M. Stus', G. N. Talalakin, and É. R. Rubtsov, Kristallografiya **37**, 998 (1992) [Sov. Phys. Crystallogr. **37**, 530 (1992)].
7. V. L. Vasil'ev, M. V. Baidakova, E. A. Kognovitskaya, *et al.*, in *Abstracts of the 3rd International Conference on Mid-IR Optoelectronic Materials and Devices, Aachen, Germany, 1999*, p. 9.
8. V. L. Vasil'ev, S. N. Losev, V. M. Smirnov, *et al.*, in *Proceedings of the 5th Conference on Intermolecular Interaction in Matter, Lublin, Poland, 1999*, p. 96.
9. V. L. Vasil'ev, D. Akhmedov, G. S. Gagis, *et al.*, in *Abstracts of the 4th International Conference on Mid-IR Optoelectronic Materials and Devices, Montpellier, France, 2001*, p. 97.
10. M. P. Mikhaĭlova, G. G. Zegrya, K. D. Moiseev, *et al.*, Fiz. Tekh. Poluprovodn. (St. Petersburg) **29**, 687 (1995) [Semiconductors **29**, 357 (1995)].
11. M. P. Mikhailova, K. D. Moiseev, Y. A. Berezovets, *et al.*, IEE Proc.: Optoelectron. **145**, 269 (1998).
12. K. D. Moiseev, A. A. Toropov, Ya. V. Terent'ev, *et al.*, Fiz. Tekh. Poluprovodn. (St. Petersburg) **34**, 1432 (2000) [Semiconductors **34**, 1376 (2000)].
13. M. P. Mikhailova and A. N. Titkov, Semicond. Sci. Technol. **9**, 1279 (1994).
14. N. L. Bazhenov, G. G. Zegrya, V. I. Ivanov-Omskiĭ, *et al.*, Fiz. Tekh. Poluprovodn. (St. Petersburg) **31**, 1216 (1997) [Semiconductors **31**, 1046 (1997)].

Translated by N. Korovin

Semiconductors, Vol. 36, No. 8, 2002, pp. 950–951. Translated from Fizika i Tekhnika Poluprovodnikov, Vol. 36, No. 8, 2002, pp. 1016–1017.

PERSONALIA

Viktor Il'ich Fistul'
(on his 75th birthday)

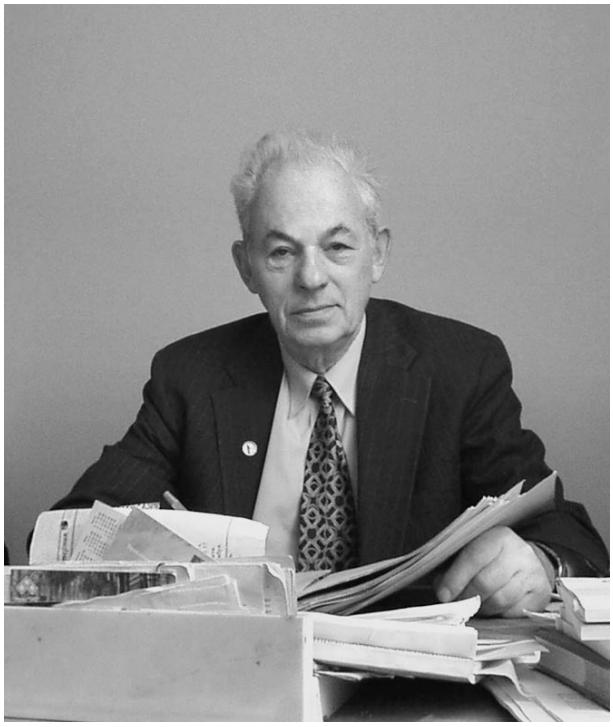

Viktor Il'ich Fistul' celebrated his 75th birthday on May 1, 2002. He is a full member of the Russian Academy of Natural Sciences, Doctor of Physics and Mathematics, and professor at the Lomonosov State Academy of Fine Chemical Technology (Moscow).

After graduating in 1949 from the Physics and Mechanics Department of the Leningrad Polytechnical Institute, V.I. Fistul' worked as a technical-control inspector, an engineer, and a chief engineer at the laboratory of the Uraléektroapparat plant in Sverdlovsk (now, Yekaterinburg). From 1952 to 1964, he worked at the Research Institute of the Electronics Industry, and, from 1964 to 1977, he was with the State Research Institute for the Rare-Metals Industry (Giredmet), first as a senior researcher and finally as the head of the physics department.

Starting in the late 1950s, we observed a rapid progress of semiconductor electronics in this country. From 1959, the scientific interests of Fistul' became indissolubly and permanently centered around semiconductors. The latter represent a class of materials in the studies of which the linkage between the two most important natural sciences—physics and chemistry—manifests itself most clearly. The characteristics of semiconductors depend on the type and amount of impurities. This dependence attracted the attention of Fistul'; as a result, his scientific activity became predominantly devoted to the studies of the state and behavior of impurities in semiconductor crystals.

His studies of heavily doped semiconductors are internationally known. These studies led Fistul' to the discovery and explanation of the polytropy of impurities in semiconductors. The results of the relevant studies were generalized by Fistul'in two monographs: "Heavily Doped Semiconductors" (1967) and "Decomposition of Supersaturated Semiconducting Solid Solutions" (1977). Fistul' supervised the studies of impurity atoms with partially filled electronic shells in diamond-like semiconductors and in III–V compounds. These studies made it possible to ascertain the basic trends in the behavior of the above impurities; the results were embodied in the monograph "The Transition-Metal Impurities in Semiconductors" (1983) written jointly by Fistul' and É.M. Omel'yanovskiĭ, his student and follower.

Studies of gaseous impurities in the diamond-like semiconductor crystals resulted in the discovery of a deep level of hydrogen in the band gaps of germanium and silicon (USSR Inventor's Certificate no. 259, 1983). A large contribution was made by Fistul' and his followers to the understanding of the behavior of amphoteric and isovalent impurities in the III–V crystals. In 1992, Fistul' published the monograph "Amphoteric Impurities in Semiconductors."

Starting in 1962, Fistul' combined scientific activity at Giredmet with teaching at the Moscow Institute of Fine Chemical Technology, where, in 1977, he was appointed head of the department "Technology of Semiconducting Materials". In 1985, Fistul' initiated the foundation of the department of "Physics and Chemistry of Solids" in the above institute; he was the head of this department until 1991, and now continues his activity at this department as a professor.

Fistul' showed himself as an outstanding teacher. In fact, he became a founder of a scientific–pedagogical school in the field of semiconductor-materials science at the Moscow Institute of Fine Chemical Technology; this school served as an excellent source of qualified scientists and teachers.

Six doctoral and 47 candidate dissertations were completed and defended under Fistul's supervision.

1063-7826/02/3608-0950$22.00 © 2002 MAIK "Nauka/Interperiodica"

Fistul' is the author of 225 papers, 8 monographs, 4 textbooks for higher education, and a scientific textbook for high-school seniors. His two-volume textbook "Physics and Chemistry of the Solid State" (1995) received wide recognition by specialists in this field.

For his scientific achievements, Fistul' was granted the title of "Renowned person involved in science and technology in the Russian Federation." He was also awarded state prizes of the USSR in the field of science and technology (1975, 1987); the medals named after Academicians Kurnakov (1985) and Kapitsa (1995) and Peter the Great (1996); and a diploma "For Scientific Achievements" (2000) from the International Biographic Center. In 1998, the International Biographic Center granted Fistul' the honorary title of "Man of the Year." He is a professor emeritus of Hanoi Technical University.

From the first volumes of "Fizika i Tekhnika Poluprovodnikov," Fistul' has been a member of the editorial board of this journal.

At present, he is still active in science, the training of specialists in science and engineering, and in publishing.

Fistul' is a highly educated and charming person and is respected by all who work with him.

We wish Fistul' health, optimism, and long years of creative activity.

Colleagues from the Moscow Institute of Fine Chemical Technology and the Editorial Board of the journal "Fizika i Tekhnika Poluprovodnikov."

Translated by A. Spitsyn